UNIVERSIDADE TÉCNICA DE LISBOA
INSTITUTO SUPERIOR TÉCNICO

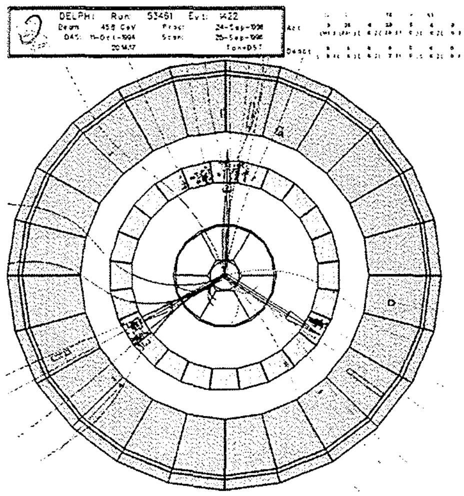

Particles identified with the DELPHI detector in hadronic events at LEP

Rosa Paula Infante Henriques

Orientador: Professor Doutor Mário João Martins Pimenta
Co-Orientador: Professor Licenciado Alessandro De Angelis
Constituição Do Júri:

Presidente:

Reitor da Universidade Técnica de Lisboa

Vogais:

Professor Doutor Carlos Pajares
Professor Doutor Gustavo da Fonseca Castelo Branco
Professor Doutor Jorge Venceslau Comprido Dias de Deus
Professora Doutora Maria da Conceição Abreu e Silva
Professor Doutor Mário João Martins Pimenta
Professor Licenciado Alessandro De Angelis

Junho de 1998

To Erwin

Rosa Paula Infante Henriques

Orientada por

Professor Mário João Martins Pimenta

Professor Associado do Instituto Superior Técnico

Doutoramento em Física

submetido ao

Departamento de Física do Instituto Superior Técnico,

Universidade Técnica de Lisboa

em

Janeiro de 1998

com o Título:

Particles identified with the DELPHI detector
in hadronic events at LEP

Abstract

In this thesis final states of charged particles (unresolved) and of hadrons (protons, charged kaons, K^0 and Λ) identified with the DELPHI detector at LEP were analysed. The final states were selected in quark and gluon jets from the symmetric topologies Mercedes and Y (at LEP I energies), and in $q\overline{q}$ events (at higher energies). The aim was to test some of the phenomenological models proposed, in particular the JETSET and HERWIG models, based on string and cluster fragmentation, respectively, and to check, using the distribution ξ^* versus $\sqrt{s}$ for identified hadrons, the validity of the MLLA+LPHD approach in this context.

The high statistics collected at LEP (170 pb^{-1} per detector at and around the Z^0 peak; $\sim$ 12 pb^{-1} between 130 GeV and 140 GeV; $\sim$ 10 pb^{-1} at 161 GeV; $\sim$ 10 pb^{-1} at 172 GeV and $\sim$ 50 pb^{-1} at 183 GeV) allows precision measurements of QCD parameters, as well as the study of non-perturbative effects, such as aspects related to the parton hadronization.

The evolution with momentum of the multiplicity ratio of identified particles (protons, charged kaons, K^0 and Λ) in gluon jets relative to quark jets was measured. It was observed that both models, JETSET and HERWIG, give a satisfactory description of the data.

The enhancement of identified particles' production (protons, charged kaons, K^0 and Λ) in gluon jets relative to quark jets was observed to be consistent with the corresponding enhancement for all charged particles (unresolved). This is in disagreement with HERWIG predictions for protons in Y events (1.5σ difference) and charged kaons in both Y (5σ difference) and Mercedes (2.5σ difference) events. Also JETSET is in disagreement with the proton results in Y events by 2 to 3σ.

The distribution of multiplicity and of $\xi_p = -\log(\frac{2p}{\sqrt{s}})$ for identified hadrons (protons, charged kaons, K^0 and Λ) in $q\overline{q}$ events at energies above the Z^0 resonance are satisfactorily reproduced by the Monte Carlo programs JETSET and HERWIG. However the K^0 multiplicity at 183 GeV is 3.4 standard deviations (2.4 standard deviations) below the HERWIG (JETSET) predictions; HERWIG underestimates the results for protons at 133 GeV and overestimates the results for charged kaons at 161 GeV by 2 standard deviations.

The parameter $\Lambda_{eff} \sim 0.07$ was obtained from the data by fitting the evolution ξ^* versus $\sqrt{s}$ (ξ^* is the peak of the ξ_p distribution) to the MLLA+LPHD predictions. This Λ_{eff} corresponds to a value of $\alpha_s \sim 0.1$ when plugged in the evolution equation at leading order. This suggests that MLLA+LPHD could possibly give a quantitative description of the observed particle spectra.

Keywords

LEP; DELPHI; QCD; Hadronization; Identified particles; Charged particles; KNO

Resumo

Nesta tese analisaram-se estados finais de partículas carregadas em geral e de partículas identificadas (protões, kaões carregados, K^0 e Λ), usando dados adquiridos pela experiência DELPHI em LEP. Estes estados finais foram seleccionados em jets de quarks e gluões em topologias simétricas do tipo Mercedes e Y (em LEP I) e em acontecimentos $q\bar{q}$ (a energias superiores a 91 GeV). O objectivo consiste em testar alguns dos modelos fenomenológicos propostos, nomeadamente os modelos JETSET e HERWIG que se baseiam, respectivamente, nos modelos de hadronização por cordas e *cluster*, e verificar, usando a distribuição ξ^* em função de $\sqrt{s}$ para partículas identificadas, a validade da aproximação MLLA+LPHD no âmbito deste contexto.

A elevada estatística acumulada por LEP ($\sim$ 170 pb^{-1} no pico do Z^0; $\sim$ 12 pb^{-1} entre 130 GeV e 140 GeV; $\sim$ 10 pb^{-1} a 161 GeV; $\sim$ 10 pb^{-1} a 172 GeV e $\sim$ 50 pb^{-1} a 183 GeV) permite realizar testes precisos dos parâmetros da QCD, para além de permitir ainda estudar efeitos da fase não-perturbativa, tais como aspectos relacionados com a hadronização.

Neste trabalho mediu-se a evolução com o momento, da razão da multiplicidade de partículas identificadas entre quarks e gluões. Constatou-se que os modelos JETSET e HERWIG reproduzem satisfatoriamente os dados.

Verificou-se que o aumento da produção de partículas identificadas em jets de gluões, relativamente a jets de quarks, é consistente com o respectivo aumento observado para partículas carregadas. Esta medida está em desacordo com as previsões do modelo HERWIG para protões em acontecimentos Y (a diferença é de 1.5σ) e para kaões carregados tanto em acontecimentos Y (a diferença é de 5σ) como em acontecimentos Mercedes (a diferença é de 2.5σ). As previsões de JETSET também estão em desacordo com os resultados para protões em acontecimentos Y (a diferença é de 2 a 3σ).

Os programas JETSET e HERWIG reproduzem satisfatoriamente as distribuições de multiplicidade e $\xi_p = -\log(\frac{2p}{\sqrt{s}})$ para hadrões identificados em acontecimentos $q\bar{q}$, a energias superiores a 91 GeV. No entanto, a multiplicidade de K^0 a 183 GeV está 3.4σ abaixo das previsões de HERWIG; o modelo HERWIG subestima a multiplicidade de protões a 133 GeV e sobrestima os resultados para kaões carregados a 161 GeV por 2σ.

Através do fit das previsões do modelo MLLA+LPHD à distribuição ξ^* em função de $\sqrt{s}$ (ξ^* é o pico da distribuição ξ_p), obteve-se o parâmetro $\Lambda_{eff} \sim 0.07$. Este valor corresponde a $\alpha_s \sim 0.1$ quando inserido na equação de evolução em primeira aproximação. Este resultado sugere que o modelo MLLA+LPHD pode dar uma descrição quantitativa do espectro de partículas observadas.

Palavras Chave

LEP; DELPHI; QCD; Hadronização; Partículas identificadas; Partículas carregadas; KNO

Acknowledgments

The subject of this thesis and the development of the work here presented were suggested, accompanied and supervised by Professor Mário Pimenta and Professor Alessandro De Angelis.

To Mário, with whom I have worked during the last six years, I thank all the support, time dedicated and specially the motivation and the dynamism he was always able to input to this work in particular and to the LIP/DELPHI group in general. Finally I thank him for the friendship and support always present.

I thank Alessandro for the dedication, effort, dynamism and time spent to make this work feasible and competitive. I thank him for the friendship and fruitful discussions.

To Professor Jorge Dias de Deus I thank the useful discussions, the advice and the good suggestions.

I thank to Professor Gaspar Barreira and to Professor Mário Pimenta the support from LIP (Laboratório de Instrumentação e Partículas), the institute in which this work was developed.

I thank JNICT (within the founding program PRAXIS XXI) for the financial support.

To the DELPHI people at CERN I thank the opportunity given to develop this work within the group.

I thank my colleagues Fernando Barão, Pedro Abreu, Maria Catarina, Patrícia Gonçalves, Lorenzo Vitale, Luís Peralta, and professor Amélia Maio, for the friendship and fruitful discussions. I specially thank Pedro with whom I have worked directly and from whose knowledge and help I have profit during this work.

I thank my family for all the support. A special thank to Ana and João for all the patience and warmth.

Finally my special "thanks" to Erwin, for the love, support, friendship and motivation always present.

Contents

1 Introduction **1**

2 Underlying physics processes **5**

2.1 Electroweak processes 8

2.2 Perturbative QCD 11

2.2.1 QCD Bremsstrahlung 15

2.2.2 Running of α_s 17

2.2.3 Jet physics 19

2.2.3.1 Jet clustering 25

2.2.4 Measurements of $\alpha_s(Q^2 = M^2_{Z^0})$ 27

2.3 Hadronization 28

2.3.1 Fragmentation functions 30

2.3.2 Independent fragmentation model 34

2.3.3 String hadronization model 34

2.3.4 Cluster fragmentation 37

2.3.5 Monte Carlo event generators 37

2.4 Multiplicity 40

2.4.1 KNO scaling 42

2.5 Multiplicity of identified final states 45

3 Experimental setup **49**

3.1 The LEP collider 49

3.2 Luminosity 51

3.3 Components of the DELPHI detector 52

3.3.1 Tracking detectors 55

3.3.2 Calorimeters 58

3.3.3 Ring Imaging Čerenkov detectors 61

4 Particle identification **65**
4.1 Charged particle identification 65
4.1.1 dE/dX identification 65
4.1.1.1 Pion, kaon and proton identification 67
4.1.2 RICH identification 68
4.1.2.1 Pion, kaon and proton identification 72
4.2 V^0 Reconstruction 76
4.2.1 Efficiency matrix from the data 81
4.3 b-Tagging 86
4.3.1 Primary vertex fit 86
4.3.2 Secondary vertex fit 91

5 Analysis **95**
5.1 Event selections - LEP I 95
5.1.1 Hadronic event selections 95
5.1.2 Three-jet event selections 97
5.1.3 Selection of gluon and b jets 99
5.1.4 Selection of particle flavors 104
5.1.4.1 Pion, kaon and proton selections 104
5.1.4.2 K^0_S and Λ selections 105
5.1.5 Correction method 105
5.1.5.1 Unfolding of the jet flavors 105
5.1.5.2 Efficiency and contamination of the particle tagging 106
5.1.5.3 Multiplicity matrix unfolding 107
5.2 Event selections - LEP II 110
5.2.1 Initial state radiation 110
5.2.2 Hadronic event selections 112
5.2.3 Selection of particle flavors 115
5.2.4 Correction method 115

6 Results **121**
6.1 Identified particles in jets at LEP I 121
6.2 KNO distribution in jets at LEP I 127
6.3 Identified hadrons at LEP II 132
6.3.1 ξ^* distribution 134
6.3.2 Average multiplicity 139

7 Conclusions **149**

Chapter 1

Introduction

To the present knowledge, the building blocks of matter are the fermions and the bosons (mediators of the interactions). All the phenomena of particle physics can be explained in terms of the interactions between the fermions and the bosons. Quantum ChromoDynamics (QCD) is the fundamental theory of strong interactions. Formulated in analogy to Quantum ElectroDynamics (QED), QCD is a gauge theory describing the strong interactions between quarks through the exchange of massless gauge bosons, the gluons. The main difference between QCD and QED relies on the fact that in QED there is only one charge, while in QCD there are three types of strong charge called colour. Moreover, the gauge bosons of QCD, the gluons, carry colour charge and therefore couple among them (contrary to the QED boson).

Hadronic final states of highly energetic e^+e^- annihilation are an ideal laboratory for performing precise tests of the strong interaction, compared to processes like hadron-hadron collisions or lepton-nucleon scattering, due to the absence of beam and target remnants. In e^+e^- annihilations there is in addition the capability to tune the center of mass energy to sit exactly on a resonance which decays approximately at rest in the laboratory frame.

At LEP, the **L**arge **E**lectron **P**ositron collider located at CERN, electron and positron beams circulate in opposite directions inside the ring and are forced to collide in four points in which detectors are located. The four detectors operating at LEP are ALEPH, OPAL, L3 and DELPHI. For the production of Z^0 bosons in the first phase of LEP, LEP I, the center of mass energy of the e^+e^- collision ($\sqrt{s}$) was set to 91 GeV; for the production of W^+W^- pairs in the second phase of LEP, LEP II, the energy was raised to $\sqrt{s} > 160$ GeV (with intermediate data taking at energies between 130 GeV and 140 GeV).

Between 1989 and 1997 LEP delivered an integrated luminosity of about 170 pb^{-1} per detector at and around the Z^0 peak; $\sim$ 12 pb^{-1} between 130 GeV and 140 GeV; $\sim$ 10 pb^{-1} at 161 GeV; $\sim$ 10 pb^{-1} at 172 GeV and $\sim$ 50 pb^{-1} at 183 GeV. These high statistics enables precision measurements of QCD parameters, as well as the study of non-perturbative effects, such as aspects related to the parton hadronization.

DELPHI is one of the four experiments of LEP. It is a general purpose detector for e^+e^- physics, designed to provide high granularity over a 4π solid angle and with special emphasis on particle identification. DELPHI is the leading experiment in charged particle identification, thanks to the RICHs (Ring Imaging Čerenkov) detectors.

In the process $e^+e^- \to \gamma^*/Z^0 \to q\bar{q}$ at small momentum scales (large distances) the strong coupling constant, α_s, becomes large and at this stage the free quarks organize themselves into strongly bound clusters, ultimately the hadrons we observe. The confinement transition from the quark and gluon degrees of freedom, appropriate in perturbative theory, to the hadrons observed by real world experiments is complex and not entirely understood by present theories.

To describe this region of phase space (hadronization) non-perturbative phenomenological models, mostly relying on mathematical constructs such as clusters and strings, were developed. The hadronization is modelled to an extent which allows the connection to be made between the properties of hadrons and the dynamics of the parton cascade predicted by perturbative QCD. In this picture, implemented via Monte Carlo simulations, the hadronization of a $q\bar{q}$ pair is split into phases. In a first phase, gluon emission and parton branching of the original $q\bar{q}$ pair take place. In a second phase, at a certain virtuality Q_0, quarks and gluons produced in the first phase transform into mesons and baryons. In the third phase the unstable states decay into hadrons which can be observed or identified by the detector.

The hadronization models account correctly for the average multiplicity and the momentum spectrum of identified particles in $q\bar{q}$ events up to the Z^0 energy; with LEP II, the energy range spanned in e^+e^- interactions is doubled. It is important to check the validity of these models through the analysis of observables which probe certain aspects of the fragmentation of quarks and gluons into hadrons, their evolution with the center of mass energy and the way quarks differ from gluons.

Compared to the phenomenological models, a different and purely analytical approach giving quantitative predictions of hadronic spectra are QCD calculations using the so-called Modified Leading Logarithmic Approximation (MLLA) under the assumption of Local Parton Hadron Duality (LPHD). In this model the particle yield is described by a parton cascade; at the end of the parton cascade it is assumed that a calculated spectrum for partons can be related to the spectrum of real hadrons by simple normalization constants. The momentum spectra of particles produced can be calculated as a function of the variable $\xi_p = -\log(\frac{2p}{\sqrt{s}})$ (p is the momentum of the particle and $\sqrt{s}$ is the center of mass energy). The model predicts the evolution of the peak ξ^* of this distribution with $\sqrt{s}$.

In this thesis the final states of charged particles (unresolved) and of hadrons (protons, charged kaons, K^0 and Λ) identified with the DELPHI detector at LEP are analysed in quark and gluon jets at LEP I energies, and in $q\overline{q}$ events at higher energies. The aim is to test some of the phenomenological models proposed, in particular the JETSET and HERWIG models, based on string and cluster fragmentation, respectively.

The multiplicity ratio of identified particles in gluon jets relative to quark jets (and its evolution with momentum) and the momentum spectrum of charged particles (unresolved) in the KNO form ($< n > P$ versus $z = n / < n >$, where P is the probability to have an hadronic Z^0 decay with n charged particles and $< n >$ is the average multiplicity) are measured for LEP I energies. Quark and gluon jets are selected among three jet events of the Y and Mercedes topologies, so that the gluon and at least one quark jet are symmetrical. These results are compared to the model predictions.

The multiplicity of identified hadrons (protons, charged kaons, K^0 and Λ) in $q\overline{q}$ events is measured for center of mass energies above the Z^0 resonance. The distribution ξ^* versus $\sqrt{s}$ is measured for the identified particles: protons, charged kaons, K^0 and Λ, and the results are compared with the MLLA+LPHD predictions.

The thesis is organized as follows. In chapter 2 the underlying physics processes are specified. The components of the DELPHI detector and the particle identification are described in chapters 3 and 4. In chapters 5, 6 and 7 the analysis, results and conclusions, respectively, are presented.

The work developed throughout this thesis was subject to publication, and presentation in conferences.

Presentations in Conferences:

1. **February 1996:** Participation in the conference "Hadron Structure'96", held at Stará Lesná in High Tatra Mountains, in Slovak Republic. The contributing paper published in the proceedings of the conference: "Preliminary Results on the Identification of Particles in Quark and Gluon Jets Using the DELPHI Detector at LEP".

2. **September 1996:** Participation in the conference "XXVI International Symposium on Multiparticle Dynamics", held at Algarve in Portugal. The contributing paper published in the proceedings of the conference: "Multiplicity of Particles and Bose-Einstein Correlation in Quark and Gluon Jets".

3. **September 1997:** Participation in the conference "XXVII International Symposium on Multiparticle Dynamics", held at Frascati in Italy. The contributing paper to be published in the proceedings of the conference: "Multiplicity of identified particles in e^+e^- at the Z^0".

Publications:

1. "Charged Particle Multiplicity in e^+e^- interactions at $\sqrt{s} = 130$ GeV", DELPHI collab., P. Abreu *et al.*, Phys. Lett. **B372** (1996) 172.

2. "Identified Particles in Quark and Gluon Jets", DELPHI collab., P. Abreu *et al.*, Phys. Lett. **B401** (1997) 118.

DELPHI Notes:

1. "SPRIME A Package for Estimating the Effective $\sqrt{s'}$ center of Mass Energy in $q\bar{q}\gamma$ Events " , P. Abreu, D. Fassouliotis, A. Grefrath, R.P. Henriques and L. Vitale, DELPHI note 96-124 PHYS-632 (1996).

2. "Charged particle multiplicity in e^+e^- annihilations a $\sqrt{s}$=161 GeV ", P. Abreu, A. De Angelis, R.P. Henriques, M. Pimenta, 96-144 PHYS-642 (1996).

3. "Charged particle multiplicity in e^+e^- annihilations into $q\bar{q}$ at $\sqrt{s}$=172 GeV ", P. Abreu, A. De Angelis, R.P. Henriques, M. Pimenta, L. Vitale, 97-21 PHYS-677 (1997).

4. "Multiplicity of particles and Bose-Einstein correlations in quark and gluon jets ", R.P. Henriques, 97-38 PHYS-691 (1997).

5. "Particle identification and V^0 reconstruction, comparison between 94B3 and 94C2 ", P. Abreu, A. de Angelis, R.P. Henriques, D. Liko, M. Pimenta, L. Vitale, 97-50 PHYS-702 (1997).

Chapter 2

Underlying physics processes

To the present knowledge, the building blocks of matter are the fermions and the bosons (carriers of the forces between the fermions). All the phenomena of particle physics can be explained in terms of the properties and interactions between fermions and bosons.

There are two classes of fermions: leptons and quarks. The charged leptons interact via both the electromagnetic and weak forces whereas the neutral leptons interact only via weak interactions. The quarks and their bound states, the hadrons, can interact via weak, electromagnetic and strong interactions.

The mediators of the forces, the gauge bosons, are the photon (γ), responsible for the electromagnetic force; the $W^{\pm}$ and Z^0, responsible for the weak interactions; the gluons (eight in total) are the mediators of the strong interaction. A boson called graviton should mediate the gravitational force. This force is however too weak to play an important role in elementary particle physics.

All particle interactions can be dictated by symmetry principles, in particular by *local gauge symmetries*, which reflect the idea that the conservation of physical quantities holds in local regions in space. Group theory is the underlying mathematical framework for dealing with symmetries (U(1) for electromagnetic interactions, SU(2) for weak interactions and SU(3) for strong interactions).

In table 2.1 and table 2.2 the main properties of the particles (fermions and bosons) are presented [1].

The connection between symmetries and conservation laws is better understood in the framework of the *lagrangian field theory*. The perturbative approach follows directly from the lagrangian through the Feynman rules. These are derived by associating to each term of the lagrangian a set of propagators (the force carriers) and vertex factors (which reflect the couplings) and allow easy and straightforward matrix element derivations, and subsequent calculation of cross sections and other related quantities. The fundamental vertices of the electromagnetic and weak interactions are indicated in figure 2.1, in the form of Feynman diagrams, together with their contributing factors for the cross section.

FERMIONS			
Particle	Charge	Mass	Decay Modes
Quarks			
u	+2/3	2 to 8 MeV/c^2	-
d	-1/3	5 to 15 MeV/c^2	-
s	-1/3	100 to 300 MeV/c^2	-
c	+2/3	1.0 to 1.6 GeV/c^2	-
b	-1/3	4.1 to 4.5 GeV/c^2	-
t	+2/3	173.1±5.4 GeV/c^2	-
Leptons			
e	-1	0.51099907 ± 0.00000015MeV/c^2	-
ν_e	0	~0	-
μ	-1	105.658389 ± 0.000034MeV/c^2	$e\nu_\mu\overline{\nu_e}$
ν_μ	0	< 0.17MeV/c^2	-
τ	-1	$1777.00^{+0.30}_{-0.27}$MeV/c^2	$\mu\nu_\tau\overline{\nu_\mu}$ $e\nu_\tau\overline{\nu_e}$,$\rho\nu_\tau$
ν_τ	0	< 24 MeV/c^2	-

Table 2.1: Fermion properties. The charge is expressed in units of the electron charge.

BOSONS				
Particle	Charge	Mass	Interaction	underlying theory
Gluon (g)	0	0	Strong	QCD
Photon (γ)	0	0	Electromagnetic	QED
W$^\pm$	±	80.35± 0.12	Charged weak	Electroweak
Z^0	0	91.1863±0.0019	Neutral weak	Electroweak

Table 2.2: Boson properties. The charge is expressed in units of the electron charge, the mass in GeV/c^2.

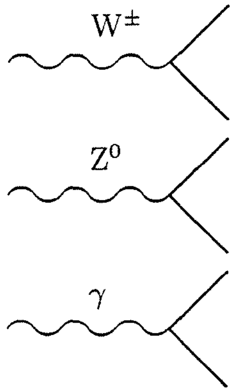

$$\leftarrow ie\gamma_\mu(1-\gamma_5)\frac{1}{2\sqrt{2}sin\theta_W} \qquad \text{(a)}$$

$$\leftarrow ie\gamma_\mu(v_f - a_f\gamma_5) \qquad \text{(b)}$$

$$\leftarrow ieQ_f\gamma_\mu \qquad \text{(c)}$$

Figure 2.1: Feynman diagrams representing the fundamental vertices of the weak (a) and b)) and electromagnetic (c)) interactions.

$v_f = \frac{I_3^f - 2Q_f sin^2\theta_W}{2sin\theta_W cos\theta_W}$ is the vector coupling and $a_f = \frac{I_3^f}{2sin\theta_W cos\theta_W}$ the axial coupling. I_3^f and Q_f denote the third isospin component and the electric charge of a given fermion species f, e is the electric charge and θ_W represents the Weinberg angle.

The focus in this thesis will be the study of several relevant quantities for the understanding of strong interaction phenomena involving quarks and gluons. Aspects of the reaction $e^+e^- \to Z^0 \to q\bar{q} \to hadrons$, like inclusive (charged) and identified particle multiplicity distributions and spectra of identified particles, will be discussed.

Between 1989 and 1995, the Large Electron Positron collider (LEP) at CERN delivered an integrated luminosity of about 170 pb^{-1} per detector at and around the Z^0 peak, providing each of its four dedicated experiments, ALEPH, DELPHI, L3 and OPAL, with some 6 million e^+e^- annihilation events, 70% of which are multihadronic. These high statistics enables precision measurements of Quantum ChromoDynamics (QCD) parameters, as well as the study of non-perturbative effects, such as aspects related to the parton hadronization.

Hadronic final states of highly energetic e^+e^- annihilation have proved already to be an ideal laboratory for performing precise tests of the strong interaction. The main advantages of e^+e^- annihilations, compared to processes like hadron-hadron collisions or lepton-nucleon scattering, for performing precise tests of QCD, come from the fact that the process is clean, due to the absence of beam and target remnants. In e^+e^- annihilations there is in addition the capability to tune the center of mass energy to sit exactly on a resonance which decays approximately at rest in the laboratory frame.

In the reaction $e^+e^- \to Z^0 \to q\bar{q}$ the final states observed after the Z^0 boson decay to a primary quark-antiquark pair correspond to hadrons, which at high enough energies emerge as "jets" of collimated particles, reflecting the direction of the primary partons. The mechanisms through which the primary partons transform to final state hadrons ("hadronization") is complex and still not understood.

The whole process can be modelled through four stages which underline different physics processes (figure 2.2). Initially the Z^0 resonance decays into a highly virtual quark-antiquark pair. This stage, along with possible photon radiation, is well described by the standard model of electroweak interactions. In the second stage the quark and the antiquark radiate gluons, a process which is well described within the framework of perturbative QCD. In the third stage the partons transform into colour-neutral hadrons (non-perturbative process) and finally in the fourth stage the decay of short lived hadrons occurs.

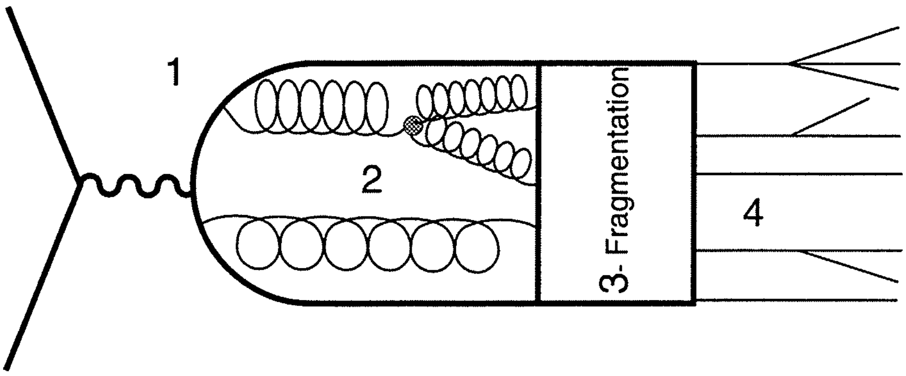

Figure 2.2: The reaction $e^+e^- \to Z^0 \to q\bar{q} \to hadrons$ viewed in four stages.

For experimental studies of hadron production and of QCD, model calculations which generate complete final states of hadrons are an essential tool. These QCD plus hadronization models are implemented via Monte Carlo event generators.

In the following sections these stages will be detailed separately.

2.1 Electroweak processes

In this stage, the generation of $q\bar{q}$ pairs from the annihilation $e^+e^- \to \gamma^*/Z^0 \to q\bar{q}$ occurs, where the angular orientation as well as the relative flavour composition of the overall event sample are determined by the electroweak couplings of the exchanged vector bosons.

The differential cross section for production of a fermion-antifermion pair for both Z^0 and photon exchange is given by [2]:

(2.1)

$$\frac{d\sigma}{d\Omega} = \frac{\alpha^2}{4s} N_c^f \times$$
$$\sqrt{1-4\mu_f} \times [G_1(s)(1+cos^2\theta) + 4\mu_f G_2(s) sin^2\theta + \sqrt{1-4\mu_f} G_3(s) \times 2cos\theta]$$

where the colour factor $N_c^f = 1$ (leptons), $N_c^f = 3$ (quarks) distinguishes between the final state fermions. The angle θ represents the polar angle between the fermion and the incoming electron from the beam, $\mu_f = m_f^2/s$, $\sqrt{s}$ is the center of mass energy and m_f is the mass of the fermion. The functions G_i in equation 2.1 are given by:

$$\left[\begin{array}{c} G_1(s) = Q_f^2 - 2v_e v_f Q_f Re\chi_0(s) + (v_e^2 + a_e^2)(v_f^2 + a_f^2 - 4\mu_f a_f^2)|\chi_0(s)|^2 \\ G_2(s) = Q_f^2 - 2v_e v_f Q_f Re\chi_0(s)(v_e^2 + a_e^2)v_f^2|\chi_0(s)|^2 \\ G_3(s) = -2a_e a_f Q_f Re\chi_0(s) + 4v_e a_e v_f a_f|\chi_0(s)|^2 \\ \chi_0(s) = \frac{s}{s-M_{Z^0}^2+iM_{Z^0}\Gamma_{Z^0}} \end{array}\right]$$

with:

$$\Gamma_{Z^0} = \sum_f N_c^f \frac{\alpha}{3} M_{Z^0}\sqrt{1-\frac{4m_f^2}{s}}\left(v_f^2(1+\frac{2m_f^2}{s}) + a_f^2(1-\frac{4m_f^2}{s})\right) \tag{2.2}$$

The total cross section $\sigma_{e^+e^-\to q\bar{q}}$ may be expressed as:

$$\sigma_{e^+e^-\to q\bar{q}}(s) = \frac{sN_c}{(s-M_{Z^0}^2)^2+M_{Z^0}^2\Gamma_{Z^0}^2}\left[\frac{12\pi\Gamma_e\Gamma_{q\bar{q}}}{M_{Z^0}^2 N_c}\right] + \frac{4\pi\alpha^2}{3s}Q_q^2 N_c + Interference\ terms \tag{2.3}$$

with the partial width $\Gamma_{q\bar{q}}$ ($Z^0 \to q\bar{q}$) given by:

$$\Gamma_{q\bar{q}} = \frac{N_c\alpha M_{Z^0}}{3} \times \sqrt{1-\frac{4m_q^2}{s}}\left(v_q^2(1+\frac{2m_q^2}{s}) + a_q^2(1-\frac{4m_q^2}{s})\right), \tag{2.4}$$

M_{Z^0} is the mass of the Z^0 boson. The first term in equation 2.3 represents the Z^0 exchange diagram contribution to the total cross section, the second term the photon exchange and there is a small contribution at the Z^0 peak due to the interference between both diagrams. In figure 2.3 [3] the cross section for e^+e^- annihilation into hadronic final states is shown.

For energies close to the Z^0 resonance, the e^+e^- annihilation through Z^0 boson exchange dominates over photon exchange, and the hadronic branching fraction is $\sim 70\%$ of the total annihilation cross section.

Comparing the partial widths $\Gamma_{q\bar{q}}$ to Γ_{Z^0} leads to relative hadronic branching ratios of $\sim 17\%$ for up-type quarks and $\sim 22\%$ for down-type quarks at the Z^0. In figure 2.4 [4] the fractions of charm and bottom quark production in e^+e^- annihilation as a function of the center of mass energy are shown. Far below the Z^0 mass the cross section is dominated by the photon exchange diagram (with a probability proportional to the square of the electric charge, equation 2.3) which leads to a higher charm production relative to the bottom quark production. As the center os mass energy increases, the Z^0 exchange diagram starts to be relevant (for energies higher than ~ 40 GeV) and becomes dominant around the Z^0 mass. At this energy the bottom quark production is higher than the charm production (equation 2.4). Above the Z^0 mass, the Z^0 width is still relevant to the cross section, and the balance with the photon exchange contribution leads to the increase of the charm production relative to the bottom quark production.

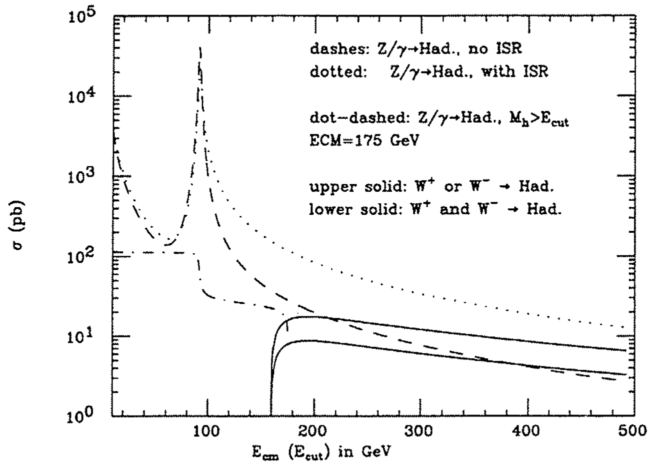

Figure 2.3: Cross section for the generation of multihadronic final states in e^+e^- annihilations, as a function of the centre of mass energy.

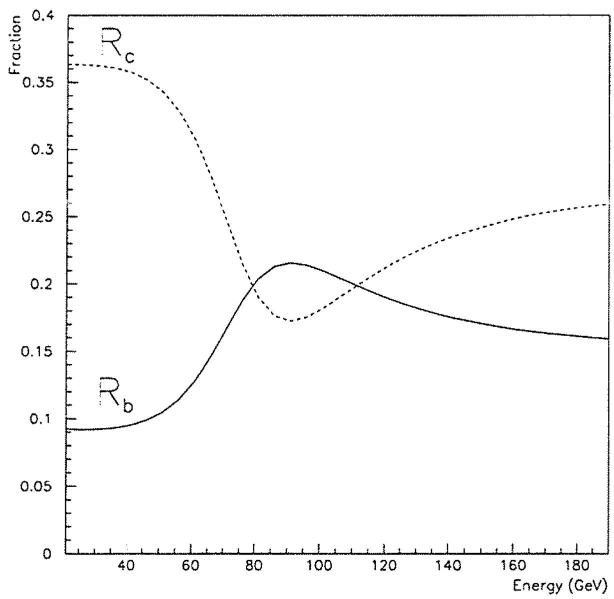

Figure 2.4: The relative branching fractions of charm and bottom quarks in e^+e^- annihilation as a function of the center of mass energy.

In the e^+e^- continuum, *i.e.* away from any resonance, the lowest order cross section for the process $e^+e^- \to \gamma^* \to q\bar{q} \to hadrons$, compared to $e^+e^- \to \gamma^* \to \mu^+\mu^-$ is given by the ratio [5]:

$$R = \frac{\sigma(e^+e^- \to \gamma^* \to hadrons)}{\sigma(e^+e^- \to \gamma^* \to \mu^+\mu^-)} = 3\sum_q e_q^2 \qquad (2.5)$$

where q runs over all quark flavors active for a given center of mass energy and the factor 3 comes from the three internal degrees of freedom for the quarks, associated with the colour charges of QCD.

From the measurement of the ratio R (equation 2.5) it is possible to deduce the number of quark flavors and colours. The experimental results point to a typical value $\sim 11/3$ for energies higher than 10 GeV (figure 2.5 [6]). This value is predicted from equation 2.5, for 2 quark flavors with charge 2/3 and 3 flavors with charge 1/3, which confirms the hypothesis of three colour degrees of freedom. The increase of R at high energies ($\sim$ 40 GeV) starts to reflect the contribution of the Z^0 exchange diagram to the total cross section.

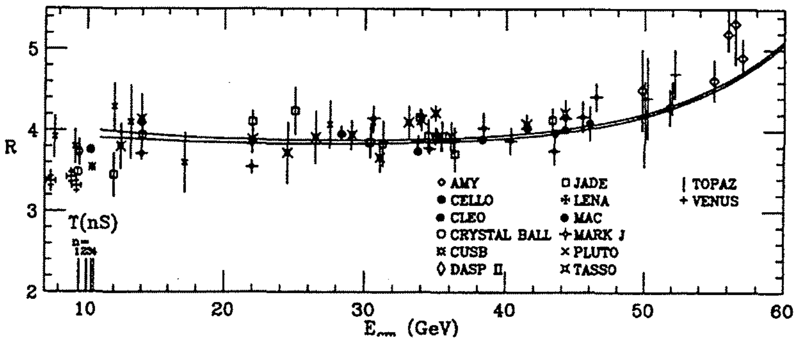

Figure 2.5: Ratio R (equation 2.5) as a function of the total e^+e^- center of mass energy E_{cm}.

2.2 Perturbative QCD

Due to its large success in describing strong interaction phenomena, QCD is commonly accepted as the fundamental theory of strong interactions. QCD was formulated in analogy to Quantum ElectroDynamics (QED) as a gauge theory describing the strong interactions between quarks through the exchange of massless gauge bosons, the gluons. The main difference between QCD and QED relies on the fact that in QED there is only one charge, while in QCD there are three types of strong charge called colour. Moreover, the gauge bosons of QCD, the gluons, carry colour charge and therefore couple among them (figure 2.6), contrary to the QED boson. This feature turns QCD into a non-Abelian gauge theory, in contrast with QED.

A comparison between the non-Abelian gauge theory of QCD with the (Abelian) gauge theory of QED is given in table 2.3.

	QED	QCD
fermions	leptons (e,μ,τ) quarks (u,d,s,c,b,t)	quarks (u,d,s,c,b,t)
force couples to	electric charge	3 colour charges
exchange quantum	photon (γ) (carries no charge)	gluons (g) (carry 2 colour charges) $\Rightarrow$ gluon self couplings
coupling constant	$\alpha^{-1}(Q^2 = M_{Z^0}) = 128.896 \pm 0.090$ Increases with Q^2	$\alpha_s(Q^2 = M_{Z^0}) = 0.120 \pm 0.003$ Decreases with Q^2
theory	perturbative theory; calculations up to $O(\alpha^4)$	pert. theory to $O(\alpha_s^2)$ (some to $O(\alpha_s^3)$) leading log approximation

Table 2.3: Basic properties and features of Quantum ElectroDynamics (QED) and Quantum ChromoDynamics (QCD).

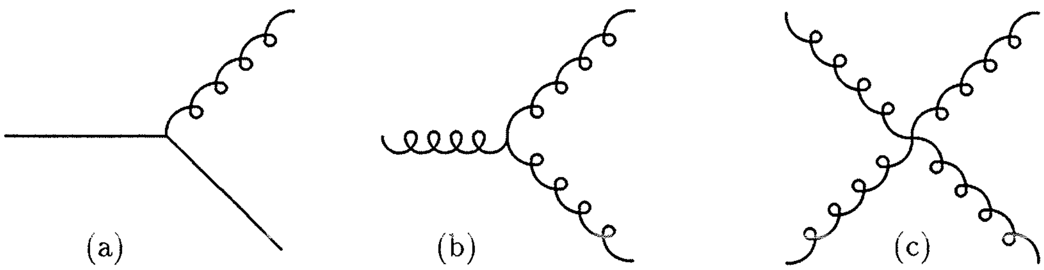

Figure 2.6: Elementary vertices of QCD: (a) quark-gluon vertex, (b) triple gluon vertex, (c) four-gluon vertex.

In QED the strength of the electromagnetic coupling between two quarks is given by $e_1 e_2 \alpha$, where e_i is the electric charged and α the fine structure constant. Similarly, in QCD, the strength of the (strong) coupling for single-gluon exchange between two colour charges is $\frac{1}{2}c_1 c_2 \alpha_s$, with c_1 and c_2 the two colour coefficients associated with the vertices. It has become conventional to call $C_F = \frac{1}{2}|c_1 c_2|$ the colour factor associated to the branching $q \to qg$ and C_A (T_F) the corresponding colour factor in the branching $g \to gg$ ($g \to q\bar{q}$). The sum over all possible colour combinations for final state partons leads to the following coefficients:

$$q \to qg \;\sim \alpha_s \times C_F \;,\; C_F = \frac{4}{3}$$

$$g \to gg \sim \alpha_s \times C_A \ , \ C_A = 3$$

$$g \to q\bar{q} \sim \alpha_s \times T_F \ , \ T_F = \frac{1}{2}$$

The fragmentation involves the primary parton emitting soft gluons, therefore the properties of quark jets are determined by the qqg coupling, while the properties of gluon jets are determined by the ggg coupling. As $C_A > C_F$, the ggg coupling is stronger than qqg, from which it is expected that the gluons will radiate more subsequent gluons in a parton shower. This leads to the anticipation that gluon jets, as compared to quark jets, will have: higher multiplicity and softer momentum spectrum.

The above anticipation is a consequence of the assumption that the hadronization and resonance decays, taking place after the parton shower development from an initial parton, cause little disruption on the features already established by the parton cascade. In the absence of a well developed theory of hadronization this is the minimum requirement for perturbative QCD calculations (see section 2.3 for a detailed description of the hadronization process). This idea has become known as *Local Parton-Hadron Duality* (LPHD) and represents the simplest working hypothesis to describe and predict the effects of the hadronization.

In this scenario the parton hadronization is local, so that it is the quantum numbers of a few nearby partons which determine the properties of a produced hadron. On one hand this leaves little space for long range-effects, on the other hand approximate local conservation of flavour and baryon number, for instance, follow naturally. Therefore hadronization should not significantly alter an event's angular structure or its energy and multiplicity distributions or their correlations, but only provide a "correction".

Although the concept is quite attactive due to its simplicity and predictive power, care must be taken when applying it blindly. Experimental results on "hard event properties" indicate that this hypothesis is not sufficient to explain all the hadronization related phenomena, and less trivial, non-perturbative models of hadronization are needed (section 2.3).

Concerning the hadron multiplicity in jets, we could naively expect a multiplicity ratio between gluon and quark jets, $r = < n >_{gluon} / < n >_{quark}$, of the order $\sim C_A/C_F = \frac{9}{4} = 2.25$. However this result is hidden by higher order corrections as well as by hadronization effects. At order $\alpha_s(Q^2)$ *Gaffney and Mueller* [7] have obtained r depending on the energy, through $\alpha_s(Q^2)$, given by:

(2.6)

$$r = \frac{9}{4}\left[1 - \left(1 + \frac{N_f}{C_A} - \frac{2N_f C_F}{C_A^2}\right)\left[\sqrt{\frac{\alpha_s C_A}{18\pi}} + \frac{\alpha_s C_A}{18\pi}\left(\frac{25}{8} - \frac{3}{4}\frac{N_f}{C_A} - \frac{N_f C_F}{C_A^2}\right)\right]\right]$$

where N_f is the number of quark flavors. This result lowers the value $r = 2.25$ by $\sim 10\%$ (considering 5 flavors and $\alpha_s(Q^2)$ at $Q^2 = M_{Z^0}$).

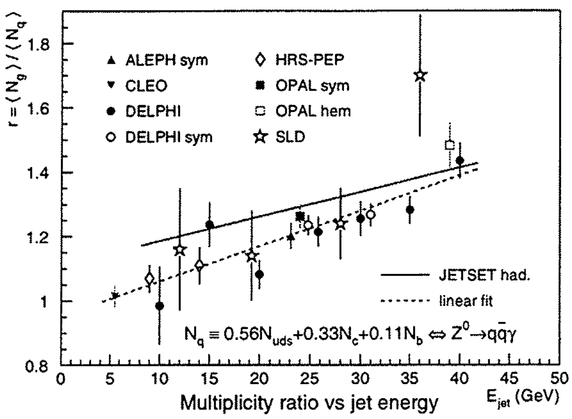

Figure 2.7: Multiplicity ratio r as a function of the jet energy. The solid line represents the results from the Monte Carlo program JETSET. Values corresponding to the same energy are separated for having a better display.

Though the average multiplicity depends strongly on the running property of the coupling constant, the ratio $r = < n >_{gluon} / < n >_{quark}$ turns out to be instead more sensitive to a proper treatment of energy conservation [8]. After incorporating energy conservation into the parton shower branching process, r ranges from about 1.6 to 1.8 [8].

It should be noted that the values reported above refer to the ratio of the number of partons in jets. In order to compare the results at parton level with the observations, Monte Carlo computation, using definite hadronization schemes, is used to recalculate partonic ratios to the hadronic ratios observed by the experiments. The measured ratio, has been obtained from quark and gluon jet samples selected in three jet symmetric events (in two and three-fold symmetric topologies) [9], [10], [11]. Typical values at LEP I energies fall in the range 1.1-1.3. Monte Carlo results, including the perturbative QCD expansion together with the hadronization of the partons into the observed hadrons, are shown in figure 2.7 [12]). The results presented were based on the $q\bar{q}\gamma$ analysis from DELPHI, which rescale the results taking into account for all samples the same b and c quark content as the one present in the $q\bar{q}\gamma$ sample. All other results are corrected from their original values to account for the same quark mixture.

Recently it has been pointed out that special care must be taken in comparing directly the analytic calculations with the observations. These analytic predictions are made for back-to-back pairs of quark or gluon jets, but growing evidence suggests that the relative topology of a jet is important in determining the appropriate scale [13].

The OPAL collaboration has performed an analysis in which the gluon jet is identified with all the particles observed in one hemisphere opposite to that containing the two quark jets [14]. This analysis yields an inclusive gluon jet definition which resembles more the one used in analytic calculations, moreover these results are only weakly dependent on the jet finding algorithm, therefore allowing a direct test of those calculations. The result obtained, $r = 1.552 \pm 0.041 \pm 0.060$ (for a jet energy of 39.2 GeV), agrees with the predictions of analytic calculations which incorporate energy conservation into the parton shower branching process.

2.2.1 QCD Bremsstrahlung

The cross-section for the process $e^+e^- \rightarrow q\overline{q}g$ is calculable analytically using either the matrix element approach, or alternatively the so called Altarelli-Parisi-Weizsäcker-Williams technique. The exact $O(\alpha_s)$ result from matrix element calculation is given by [5]:

$$\frac{1}{\sigma_{q\overline{q}}}\frac{d\sigma}{dx_q dx_{\overline{q}}} = \frac{2\alpha_s}{3\pi}\frac{x_q^2 + x_{\overline{q}}^2}{(1-x_q)(1-x_{\overline{q}})}, \tag{2.7}$$

where $x_i = 2E_i/E_{cm}$ are the energy fractions of the partons, E_{cm} is the center of mass energy and $\sigma_{q\overline{q}}$ is the total cross section for production of a $q\overline{q}$ pair. From energy-momentum conservation, the sum of all energy fractions must add up to $\sum_i x_i = 2, i = q, \overline{q}, g$.

The integration of equation 2.7, leads to infrared as well as "collinear" divergences through the factor $(1 - x_q)$:

$$(1 - x_q) = \frac{2}{Q^2}E_{\overline{q}}E_g(1 - cos\theta_{\overline{q}g}), \tag{2.8}$$

valid for massless partons. $\theta_{\overline{q}g}$ is the angle in space between the $\overline{q}$ and the gluon. From equation 2.8 the divergences occur when the gluon is emitted with energy $E_g \rightarrow 0$ (*infrared divergency*) and when the quark and gluon are very close together (*collinear divergency*).

When this kind of calculations is implemented via Monte Carlo programs, these divergences are removed via cutoff procedures. These concern either cuts on the minimum invariant mass between the partons, or direct cuts on the angle between them, or also a transverse momentum cut.

The alternative way to calculate this cross section, using the Altarelli-Parisi-Weizsäcker-Williams technique, leads to the following result for the cross-section expressed in terms of the transverse momentum fractions, $x_T = \frac{2p_T}{E_{cm}}$, of the parton emitting the gluon:

$$\frac{1}{\sigma_{q\overline{q}}}\frac{d\sigma}{dx_T^2} = \frac{4\alpha_s}{3\pi}\frac{1}{x_T} \times \log(\frac{1}{x_T^2}) \tag{2.9}$$

or in terms of the transverse momentum itself:

$$\frac{1}{\sigma_{q\bar{q}}}\frac{d\sigma}{dp_T^2} = \frac{\alpha_s}{p_T^2} \times \log(\frac{E_{cm}^2}{4p_T^2}) \tag{2.10}$$

The exact matrix elements have been computed only to second order in α_s, and can be found in [15]. This describes a maximum of four partons in the final state, as shown in figure 2.8.

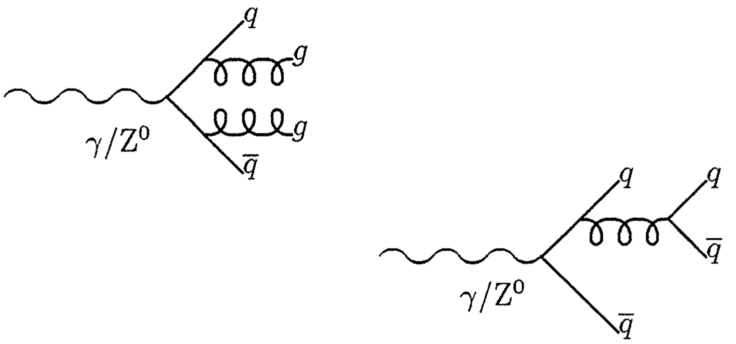

Figure 2.8: Four parton final states corresponding to $q\bar{q}gg$ and $q\bar{q}q\bar{q}$.

For predictions with any number of final state partons, two basic classes of QCD calculations are used: fixed order calculations, and the parton shower approach.

Fixed order QCD models are based on the complete QCD matrix element for $q\bar{q}$, $q\bar{q}g$, $q\bar{q}gg$ and $q\bar{q}q\bar{q}$. A complication arises in this approach, because tree-level diagrams diverge whenever external partons become soft or collinear and other divergences arise also in virtual (loop) diagrams (in addition to ultraviolet divergences). In sufficiently inclusive measurements such as the total hadronic cross section it is guaranteed that the two sets of divergences cancel, but in more exclusive quantities, such as some event shapes, the cancellation is no longer complete. Cutoff procedures are thus still needed.

QCD parton shower models are based on calculations which derive probabilities for the process $q \to qg$, $g \to q\bar{q}$ and $g \to gg$. The perturbation series is rearranged in terms of powers of $\alpha_s \log(Q^2/Q_0^2)$: $\sum_n a_n(\alpha_s \log(Q^2/Q_0^2))^n + \alpha_s(Q)\sum_n b_n(\alpha_s \log(Q^2/Q_0^2))^n + ...$ The first infinite set of terms represents the leading logarithm approximation (LLA), then the α_s-suppressed next-to-LLA and so on. Many of these terms have been identified and summed using renormalization group techniques. The result for the cross-section can be reinterpreted as a sequence of parton branching (shower): $q \to qg$, $g \to gg$ and $g \to q\bar{q}$.

The probability $P_{a\to bc}$ for the branching $a \to bc$, taking place during a small change dt, is expressed through the Altarelli-Parisi equation [16]:

$$\frac{dP_{a\to bc}}{dt} = \int dz \frac{\alpha_s}{2\pi} P_{a\to bc}(z) \tag{2.11}$$

where z gives the sharing of energy and momentum with fraction z being taken by b and $1-z$ by c. In the above equation the probabilities $P_{a\to bc}$ are the Altarelli-Parisi splitting functions [17], which are given by:

$$\left[\begin{array}{c} P_{q\to qg} = C_F \frac{1+z^2}{1-z} \\ P_{g\to gg} = C_A \frac{(1-z(1-z))^2}{z(1-z)} \\ P_{g\to q\bar{q}} = T_F(z^2+(1-z)^2) \end{array}\right].$$

QCD parton shower models are somewhat superior compared to fixed order QCD models, since the latter cannot generate events with more than four partons.

2.2.2 Running of α_s

The scaling of R mentioned in section 2.1 is violated when higher order QCD corrections are considered. In $O(\alpha_s^3)$ the ratio R of equation 2.5 is given by [18]:

$$R = \frac{\sigma(e^+e^-\to hadrons)}{\sigma(e^+e^-\to\mu^+\mu^-)} = 3\sum_q e_q^2 \times \left(1+\frac{\alpha_s(Q^2)}{\pi}+1.4(\frac{\alpha_s(Q^2)}{\pi})^2-12.8(\frac{\alpha_s(Q^2)}{\pi})^3+O(\alpha_s^4)\right) \quad (2.12)$$

The scaling is now violated logarithmically through the $\log(Q^2)$ behaviour of α_s, as will be specified below.

The dependency of α_s on the energy scale Q is ultimately the consequence of quantum fluctuations which lead to a variation in the interaction strength with distance (or energy). These quantum fluctuations are mainly vacuum polarization corrections which, at higher order, must be considered for the one gluon exchange diagram. If only quark loops were induced, this would lead to an interaction growing stronger at short distances as in QED. However the effect of diagrams including gluon loops leads to an antiscreening effect, which causes the interaction to grow weaker at short distances, since the effect of the gluon self coupling contributions is bigger than the contribution from vacuum polarization diagrams involving quarks. All these contributions are ultraviolet divergent and renormalization leads to a running coupling $\alpha_s(Q^2)$ where Q^2 is the renormalization scale.

The scale dependence of $\alpha_s(Q^2)$ is given by the *renormalization group equation*:

$$Q^2\frac{\partial\alpha_s}{\partial Q^2} = \beta(\alpha_s) = -\beta_0\alpha_s^2+\beta_1\alpha_s^3+O(\alpha_s^4) \quad (2.13)$$

The right hand side of equation 2.13 is the β function of QCD. The coefficients β_0 and β_1 do not depend on the *renormalization scheme* used. These are given by:

$$\beta_0 = \frac{11C_A-2N_f}{12\pi}$$

$$\beta_1 = \frac{17C_A^2-5C_AN_f-3C_FN_f}{24\pi^2}$$

(N_f is the number of active quark flavors *i.e.* flavors with mass m_q small compared to the energy scale of the process so that they contribute to quark loop corrections).

In solving this equation for α_s, a constant of integration is introduced in order to "absorb" the ultraviolet divergences mentioned above. This constant is not predicted theoretically: it is the one fundamental parameter of QCD which must be deduced from experiment. The most common procedure is to introduce a parameter, Λ, whose definition is arbitrary. One way to define it is in the so-called $\overline{MS}$ (modified minimal subtraction) scheme [1], where the solution of equation 2.13 is written as an expansion in inverse powers of $\log(Q^2)$. In second order expansion the solution of equation 2.13 is given by:

(2.14)

$$\alpha_s(Q) = \frac{12\pi}{(33-2N_f)\times\log(Q^2/\Lambda^2_{\overline{MS}})}\left(1 - 6\frac{153-19N_f}{(33-2N_f)^2}\frac{\log(\log(Q^2/\Lambda^2_{\overline{MS}}))}{\log(Q^2/\Lambda^2_{\overline{MS}})} + O(\alpha_s^3)\right).$$

The measured dependency of α_s on Q is shown in figure 2.9 [1].

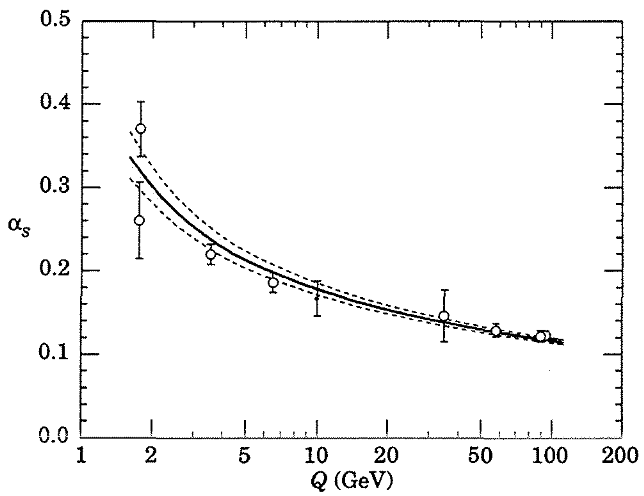

Figure 2.9: Summary of the values of $\alpha_s(Q)$. The lines show the central values and the $\pm 1\sigma$ limits of the average. The figure clearly shows the decrease of $\alpha_s(Q)$ with increasing Q.

The confinement and the asymptotic freedom are implicit in the Q dependence of α_s (equation 2.14). For $Q \gg \Lambda$, which happens for large momentum transfers or short distances, α_s is small (asymptotic freedom) and a perturbative description in terms of quarks and gluons interacting weekly is possible. For Q of the order of Λ and as it decreases further, α_s becomes large. At this stage the quarks and gluons are going to arrange themselves into strongly bound clusters, namely the hadrons (confinement). For this reason, quarks and gluons are not observed as free entities but instead always confined inside the hadrons in colour singlet structures.

The mass scale Λ defines in this way a borderline between the world of quasi-free quarks and gluons, and the world of hadrons.

2.2.3 Jet physics

The genesis of jets is on the parton cascade. The $q\bar{q}$ pairs, generated after the primary quarks and gluons in the reaction $e^+e^- \to q\bar{q}, q\bar{q}g, \ldots$ are produced along the direction of the initial quarks and gluons with a limited transverse momentum relative to their directions (Bremsstrahlung process). Moreover, the average transverse momentum of hadrons with respect to the direction of the quark or gluon motion is basically independent of the energy of the parton, which, at large energies, ultimately leads to the jet structure of the observed hadrons (the particles are more or less collimated around the direction of the quark or gluon).

The first evidence for jets was observed in hadron production in e^+e^- annihilation [19]. The jet structure manifested itself as a decrease of the mean sphericity (S) with respect to energy increase. The sphericity is defined by:

$$S = \frac{3}{2} Min \left(\frac{\sum_i p_{Ti}^2}{\sum_i p_i^2} \right) \tag{2.15}$$

i runs over all charged hadrons, p_{Ti} is the transverse momentum of the hadrons, relative to the axis which minimizes the sphericity itself, and p_i their momentum. For spherical events $S \to 1$, whereas $S \to 0$ for events with bound transverse momentum (collimated jets). The observations by the MARK II collaboration are shown in figure 2.10 [19].

From the figures the expected decrease in the mean sphericity with the beam energy is clearly seen.

For higher energies a significant fraction of events deviate from a simple linear configuration, which constitutes evidence for gluon radiation. At the Z^0, hard non-collinear gluon radiation is manifested in multi-jet event structures. As an example in figure 2.11 the structures of a two and three jet event as observed by the DELPHI detector at LEP are shown.

Other event shape variables, besides sphericity, have been developed to be sensitive to the "jetness" of an event, these are divided into two categories:

- Variables linear in momentum ("Thrust family")
- Variables quadratic in momentum ("Sphericity family")

Thrust family: (*Thrust, Major and Oblateness*)

Thrust (T) is defined by:

$$T = Max \left(\frac{\sum_i |\vec{p_i} \cdot \vec{n}_{thrust}|}{\sum_i p_i} \right) \tag{2.16}$$

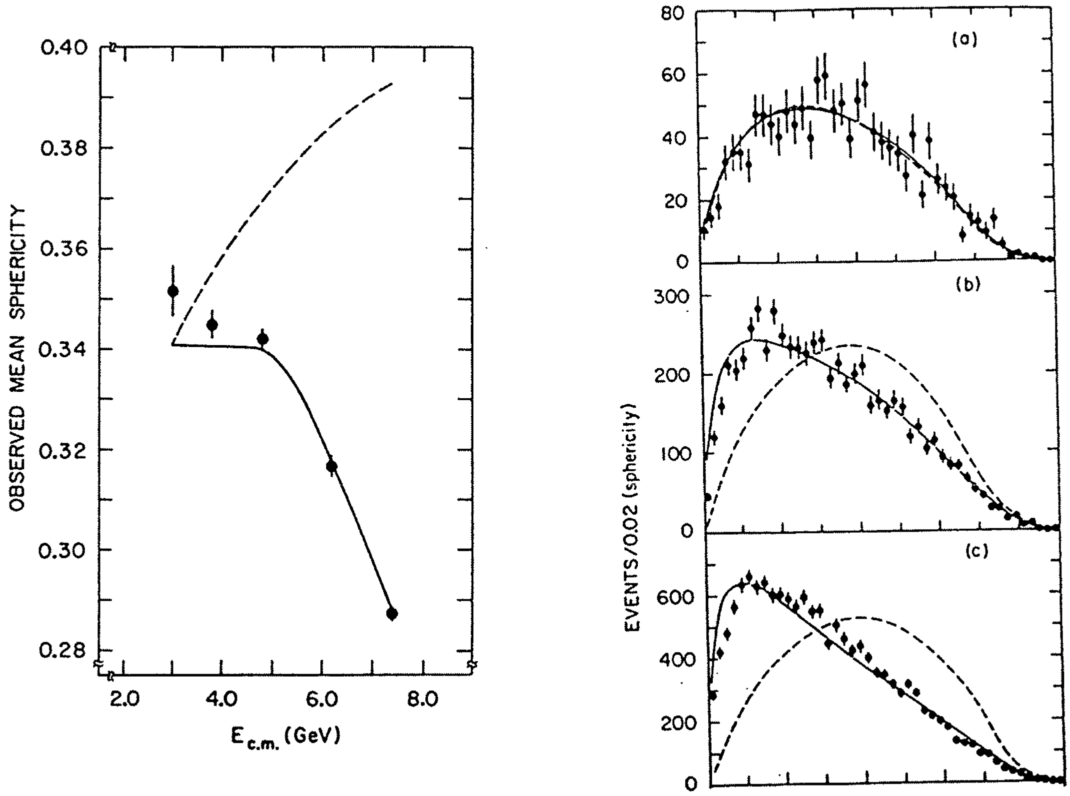

Figure 2.10: Left hand side graph: Observed mean sphericity versus the center-of-mass energy E_{cm} for data, jet model with $< p_T >= 315$ MeV/c (solid curve), and phase space model (dashed curve). Right hand side graph: Observed sphericity distributions for data, jet model with $< p_T >= 315$ MeV/c (solid curves), and phase space model (dashed curves): for (a) $E_{cm} = 3.0$ GeV; (b) $E_{cm} = 6.2$ GeV; (c) $E_{cm} = 7.4$ GeV.

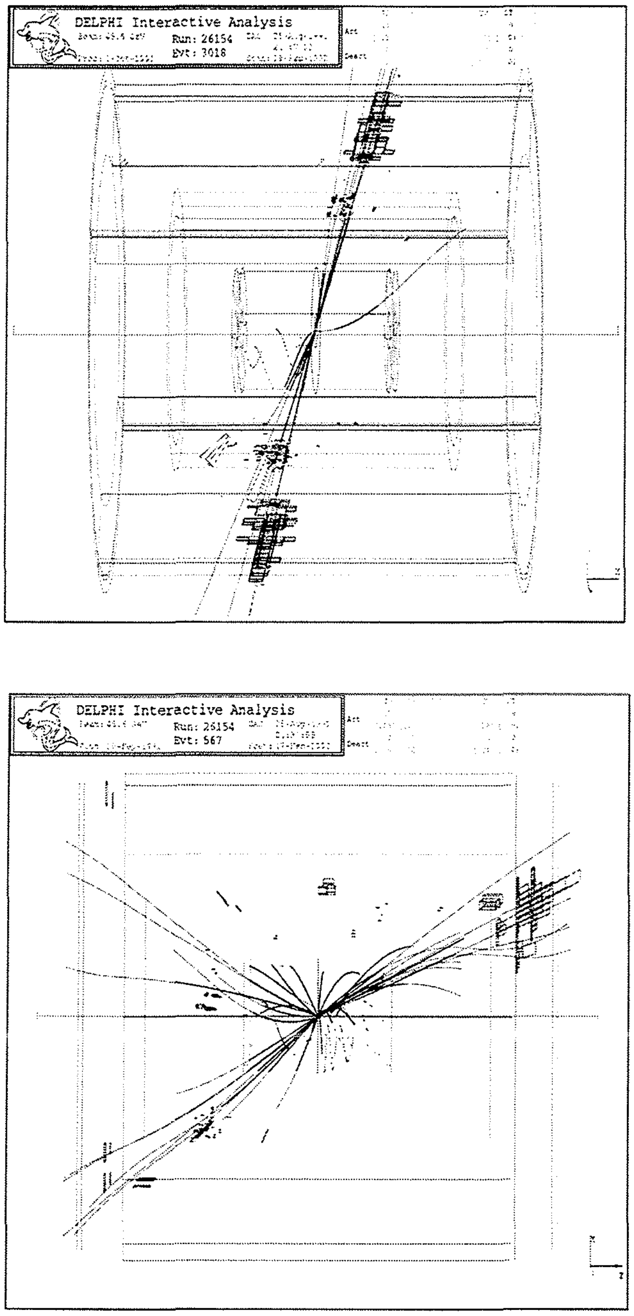

Figure 2.11: A two jet event (upper display) and three jet event (lower display) at the Z^0 peak.

where the thrust axis, $\vec{n}_{thrust}$, is defined as the axis which maximizes the above expression. For spherical events $T \to 1/2$, and $T \to 1$ for events with two collimated jets.

Major (F_{major}) is defined by:

$$F_{major} = Max\left(\frac{\sum_i |\vec{p_i} \cdot \vec{n}_{major}|}{\sum_i p_i}\right) \tag{2.17}$$

with $\vec{n}_{major}$ a unitary vector orthogonal to $\vec{n}_{thrust}$. For spherical events $F_{major} \to 1/2$, and $F_{major} \to 0$ for events with two collimated jets.

Oblateness O is another conveniently chosen variable to define the jet-like structure of an event. It is defined by:

$$O = F_{major} - F_{minor} \tag{2.18}$$

where $F_{minor} = Max\left(\frac{\sum_i |\vec{p_i} \cdot \vec{n}_{minor}|}{\sum_i p_i}\right)$, $\vec{n}_{minor} = \vec{n}_{thrust} \times \vec{n}_{major}$. $O \to 0$ for both spherical events and for events with two collimated jets.

Sphericity family: (*Sphericity, Aplanarity and Planarity*). The variables from this family depend quadratically on the particle's momentum and are thus not infra-red safe.

Ordering the eigenvalues λ of the quadratic momentum tensor:

$$M^{\alpha\beta} = \sum_{i=1}^{N_{particles}} p_i^{\alpha} p_{i\beta} (\alpha, \beta = 1, 2, 3) \tag{2.19}$$

$\lambda_1 > \lambda_2 > \lambda_3$, with $\lambda_1 + \lambda_2 + \lambda_3 = 1$, the sphericity is expressed as:

$$S = \frac{3}{2}(\lambda_2 + \lambda_3) \tag{2.20}$$

(which coincides with expression 2.15). The Aplanarity is defined by:

$$A = \frac{3}{2}\lambda_3 \tag{2.21}$$

and the Planarity is:

$$P = \frac{2}{3}(S - 2A). \tag{2.22}$$

For spherical events $A \to 1/2$, and $A \to 0$ for events with two collimated jets.

The main advantage of the linear variables relies on the fact that they are invariant with respect to decays, whereas the main advantages attached to the quadratic variables rely on the fact that they are easy to compute. The last are however not reliable for some measures, since they are not infra-red safe.

Establishing agreement between the predictions of event generator programs and data for event shape variables is widely used for confirming the ability to model QCD as a whole and has led to a first generation tuning of Monte Carlo models. The shape variables are used as well for α_s measurements from the energy dependence of these variables, as it will be detailed in section 2.2.4. As an example in figure 2.12 [20] distributions for the linear shape variables for two energies at LEP (133 GeV and the Z^0 peak) are shown together with model predictions.

QCD predicts scaling violations for observables which do not depend on absolute energies or momenta, as for instance the variables from the Thrust family indicated in figure 2.12. These scaling violations are caused by the energy dependence of α_s, which determines the amount of gluon radiation. At leading order, the probability of gluon radiation is proportional to α_s. It is thus expected that fewer 3-jet and multi-jet events should be observed at higher center-of-mass energies, and that event shape distributions evolve towards the 2-jet limit. This behaviour is represented in figure 2.12 (lower insets) where it is shown that the amount of two jet events is higher at 133 GeV than at the Z^0 peak.

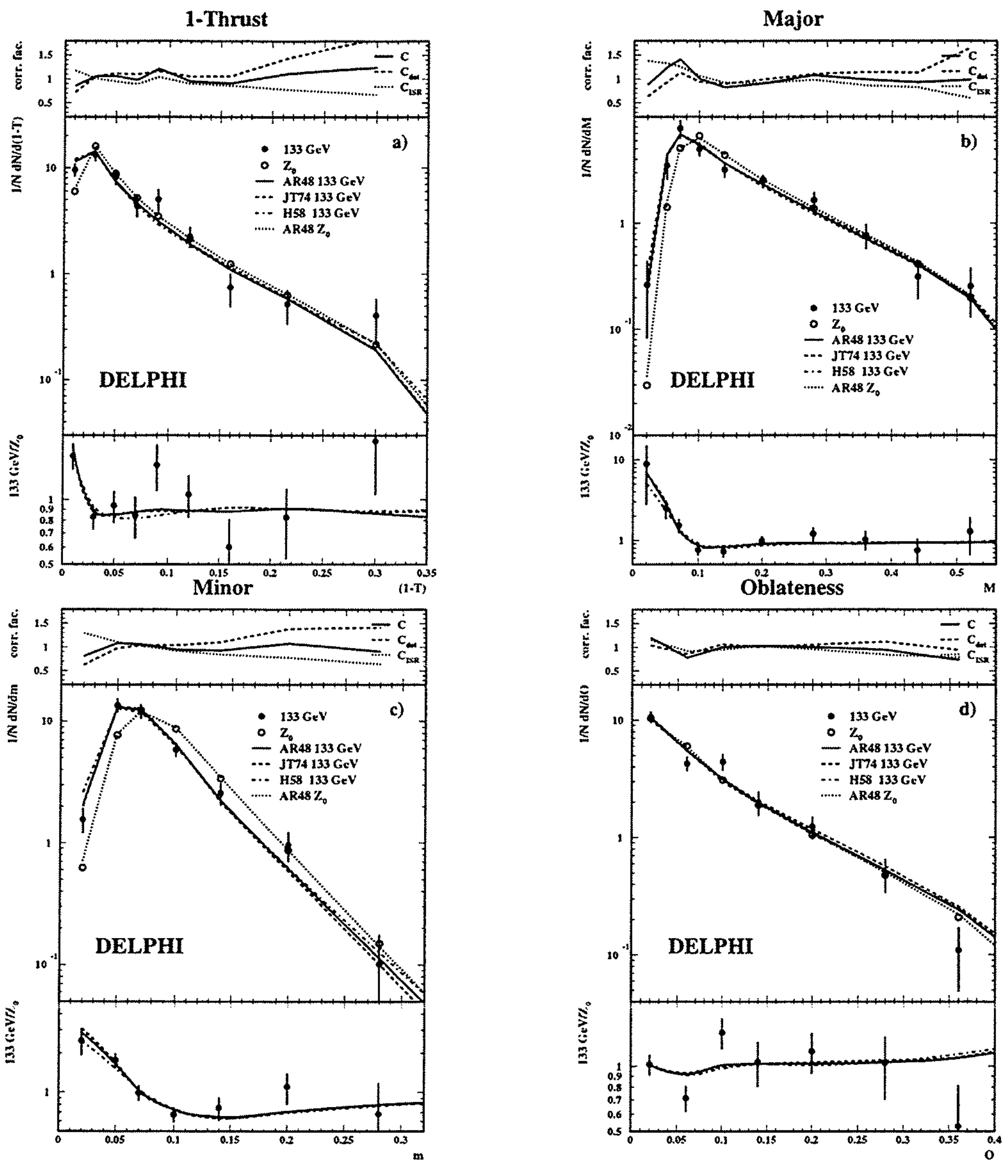

Figure 2.12: a) 1-Thrust, b) Major (F_{major}), c) Minor (F_{minor}) and d) Oblateness distributions at 133 GeV (full circles) and at the Z^0 peak (open circles). The curves show the predictions of the Monte Carlo simulation ARIADNE 4.8 (full curve at 133 GeV, dotted for the Z^0) and, for 133 GeV only, from JETSET 7.4 (dashed) and HERWIG 5.8 (dot-dashed). The upper insets display the correction factors, the dashed line is for the detector corrections (related to the limited detector acceptance and limited resolution), the dotted line shows the ISR (initial state radiation) corrections and the full line represents the total correction. The lower insets show the ratio of the 133 GeV data to the Z^0 data and the corresponding model predictions.

2.2.3.1 Jet clustering

Quantitative studies of jet production require an exact definition of the jet itself, which is usually given in terms of one or more resolution parameters. The kind of algorithms used to reconstruct jets define a measure of their "distance" y_{ij}, which is required to exceed a threshold value y_{cut} to consider two jets as separated.

In a recursive process, the pair of particles (or clusters of particles) which has the smallest value of y_{ij} is replaced by a single jet k with four-momentum $p_k = p_i + p_j$ (or other combination, depending on the scheme), as long as $y_{ij} < y_{cut}$. The procedure is repeated until all y_{ij} are larger than the jet resolution parameter y_{cut}; the remaining clusters are the jets. In table 2.4 the most widely used jet algorithms are summarized.

Algorithm	Resolution	Combination
E	$\frac{(p_i+p_j)^2}{E^2_{vis}}$	$p_k = p_i + p_j$
p	$\frac{(p_i+p_j)^2}{E^2_{vis}}$	$\vec{p_k} = \vec{p_i} + \vec{p_j}$; $E_k = \lvert\vec{p_k}\rvert$
E0 (JADE)	$\frac{(p_i+p_j)^2}{E^2_{vis}}$	$E_k = E_i + E_j$; $\vec{p_k} = \frac{E_k(\vec{p_i}+\vec{p_j})}{\lvert\vec{p_i}+\vec{p_j}\rvert}$
DURHAM (k_T)	$\frac{2min(E_i^2,E_j^2)(1-cos\theta_{ij})}{E^2_{vis}}$	$p_k = p_i + p_j$

Table 2.4: Resolution criteria and recombination schemes of various jet algorithms. E_i and E_j are the particles' energies, θ_{ij} their opening angle, and E_{vis} the total visible (measured) energy of the event.

QCD matrix element predictions in complete $O(\alpha_s^2)$ perturbation theory [21] exist for all jet algorithms mentioned before. In order $O(\alpha_s^2)$, the jet production rates are quadratic functions of $\alpha_s(\mu)$:

$$\begin{aligned}
R_2(y_{cut},\mu) &= \tfrac{\sigma_2}{\sigma_{tot}} = 1 - A(y_{cut})\tfrac{\alpha_s(\mu)}{2\pi} - [B(y_{cut},x_\mu) + C(y_{cut})]\left(\tfrac{\alpha_s(\mu)}{2\pi}\right)^2 \\
R_3(y_{cut},\mu) &= \tfrac{\sigma_3}{\sigma_{tot}} = A(y_{cut})\tfrac{\alpha_s(\mu)}{2\pi} + B(y_{cut},x_\mu)\left(\tfrac{\alpha_s(\mu)}{2\pi}\right)^2 \\
R_4(y_{cut},\mu) &= \tfrac{\sigma_4}{\sigma_{tot}} = C(y_{cut})\left(\tfrac{\alpha_s(\mu)}{2\pi}\right)^2
\end{aligned}$$

where σ_{tot} is the total hadronic cross section, σ_n are the cross sections for n-parton event production, $\mu = x_\mu E_{cm}$ is the renormalization scale at which α_s is evaluated, and x_μ is the renormalization scale factor. A, B and C are parameters.

In figure 2.13 [18] for several algorithms the n-jet production rate (n=2,3,4 and ≥ 5) as a function of the jet resolution parameter y_{cut} is shown. The calculations are done with the JETSET QCD parton shower (PS) Monte Carlo plus string hadronization program, both for the quarks and gluons at the end of the parton shower, *"parton level"*, and for the particles after hadronization, *"hadron level"* (see section 2.3).

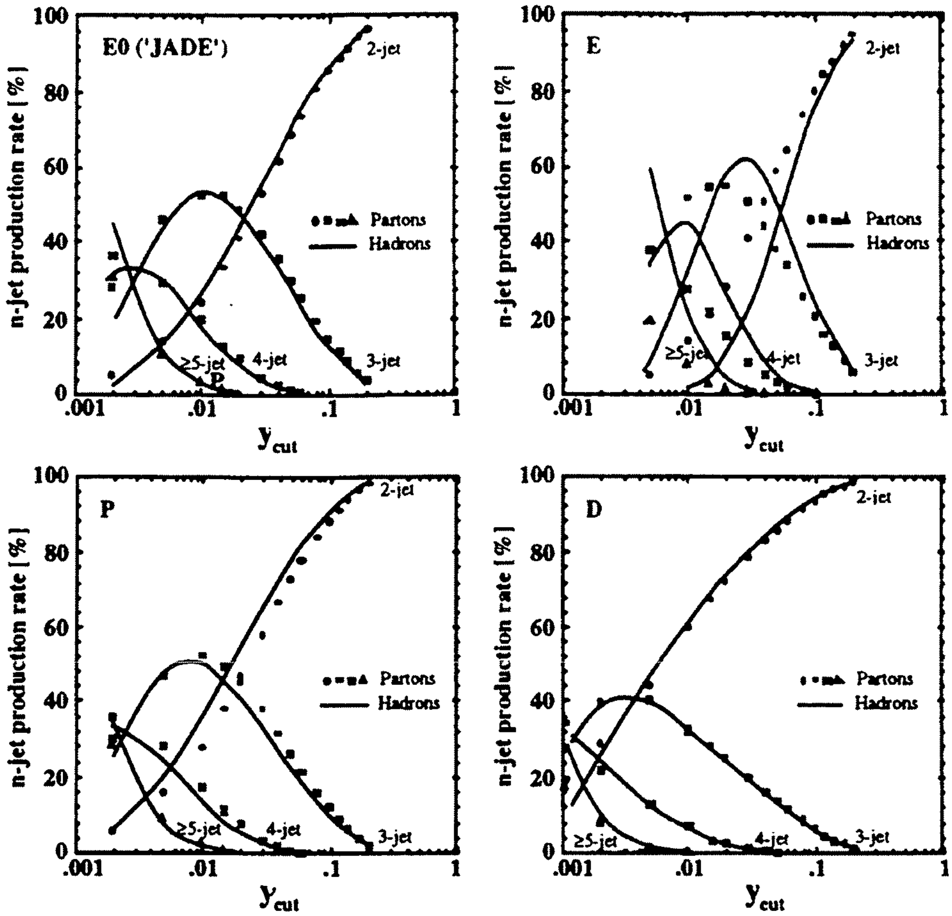

Figure 2.13: Jet rates as a function of y_{cut}, as predicted by the JETSET QCD shower model before (partons) and after (hadrons) the hadronization process ($E_{cm} = 91.2\text{GeV}$).

From figure 2.13, comparing the different algorithms, it can be seen that the size of the hadronization correction, *i.e.* the difference between the hadron and the parton levels, varies significantly. The hadronization corrections are smallest for the Durham and E0 (JADE) schemes, while they are largest for the E-scheme.

The production rate of three jet events at hadron level, compared to three jet events at parton level, is shown in figure 2.14 [18] as a function of the center of mass energy.

The JADE-scheme shows the smallest and more stable hadronization corrections at lower center of mass energies, however at higher energies (LEP I and above) the DURHAM algorithm has advantages over JADE, since its hadronization corrections start to be smaller.

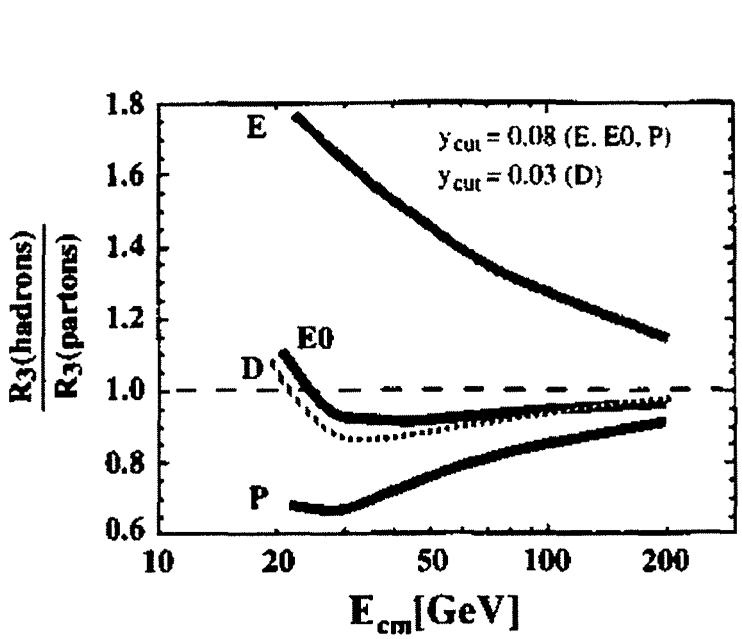

Figure 2.14: Energy dependence of the ratio between hadron and parton levels of three-jet event rates. The calculations were performed using the JETSET QCD shower model.

2.2.4 Measurements of $\alpha_s(Q^2 = M_{Z^0}^2)$

QCD contains one free parameter, the QCD scale Λ. Most QCD calculations of observables are performed using finite-order perturbation theory, and calculations beyond leading order depend on the renormalization scheme employed, implying a scheme dependent Λ. In the modified minimal subtraction scheme the strong coupling constant (α_s) and Λ are related through equation 2.14, so that Λ can be obtained from the measurement of α_s.

Tests of QCD are obtained through the consistency of the values of α_s obtained from different experiments. Such measurements have been performed in e^+e^- annihilation, hadron-hadron collisions, and deep-inelastic lepton-hadron scattering, covering a range of Q^2 from 1 to 10^5 GeV. Here only α_s measurements performed at LEP will be briefly referred.

The topology of hadronic events in e^+e^- collisions is modified by the effects of gluon radiation, which gives rise to events differing from the collimated two-jet topology ($e^+e^- \rightarrow q\bar{q}$). Since the amount of gluon radiation is directly proportional to the strong coupling constant, studying the topology of hadronic decays of the Z^0 boson or jet-rates (see section 2.2.3.1), for example, will provide a measurement of $\alpha_s(M_{Z^0})$. The strategy consists thus in finding variables which characterize the jetness of the event, like the shape variables described previously in chapter 2.2.3, and which are at the same time infra-red and collinear safe (variables from the sphericity family are thus not adequate for these kind of studies).

At LEP, the observables which lead to the measurement of α_s are divided into two categories:

- **inclusive.** These include the measurement of the total hadronic decay width of both the Z^0 boson and the tau lepton.
- **non-inclusive.** These include comparisons of measurements of jet-rates, global event shape variables, energy-energy correlations (*EEC*) and scaling violations in the fragmentation functions with the predictions of $O(\alpha_s^2)$ QCD plus hadronization models.

The observables on which the inclusive measurements are based are computed to complete $O(\alpha_s^3)$ (see for instance the ratio R_{Z^0} of the hadronic to leptonic widths from equation 2.12). In these measurements the non-perturbative contributions are expected to be small, so that in general no assumption is made on the hadronization process. These results however require large data samples, otherwise they will be subject to larger experimental or statistical uncertainties. Using τ decays, the ratio $R_\tau = \Gamma(\tau \to \nu_\tau hadrons)/\Gamma(\tau \to \nu_\tau l \nu_l)$ is measured and compared to QCD predictions to $O(\alpha_s^3)$ (similar to R_{Z^0}). Here non-perturbative effects might be important and thus must be taken into account.

The non-inclusive variables are in general more affected by the hadronization stage, so that the observables measured at hadron level must be translated, through Monte Carlo simulation programs, to the corresponding "observables" at parton level before reliable comparisons can be made with the QCD predictions.

Using the same data set, many different shape variables are combined in one analysis, in order to verify the size of the theoretical uncertainty. The QCD predictions for all the event shape variable distributions are known to second order in α_s [15]:

$$\frac{1}{\sigma}\frac{d\sigma}{dy} = \frac{\alpha_s(Q)}{2\pi}A(y) + \left(\frac{\alpha_s(Q)}{2\pi}\right)^2 \left[B(y) + 2\pi b_0 \log(\frac{Q^2}{s})A(y)\right] \tag{2.23}$$

where y represents the event shape variable, with $y = 0$ corresponding to the two jet limit, Q is the renormalization scale used in the calculation and $A(y)$ and $B(y)$ are specific for every event shape variable and contain the full information of the second order matrix element. To obtain a prediction for multi-hadronic final states, the above expression is convoluted with the predictions obtained from phenomenological hadronization models.

In figure 2.15 [1] a compilation of results obtained from several experiments for $\alpha_s(Z^0)$ is presented.

2.3 Hadronization

As mentioned in the previous section, at small momentum scales $\alpha_s(Q^2)$ becomes large and at this stage the free quarks organize themselves into strongly bound clusters, ultimately the hadrons we observe. The hadronization typically happens

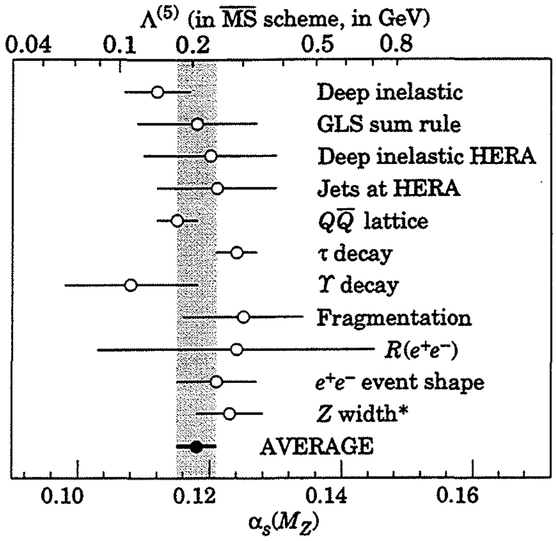

Figure 2.15: Summary of the values of $\alpha_s(M_{Z^0})$ and $\Lambda^{(5)}$ from various processes ordered from top to bottom by increasing energy scale of the measurements. The values shown indicate the process and the measured value of α_s extrapolated up to $Q = M_{Z^0}$. The error shown is the total error including theoretical uncertainties.

at energy scales smaller than or of the order of a few GeV, at the scale of hadron masses.

The confinement transition from the quark and gluon degrees of freedom, appropriate in perturbative theory, to the hadrons observed by real world experiments is poorly understood. In this region of phase space non-perturbative methods (models) are used, which to varying degrees reflect possible scenarios for the QCD dynamics.

Some phenomenological models, mostly relying on mathematical constructs such as clusters and strings, were developed to describe this hadronization process. In these models the hadronization is modelled to an extent which allows the connection to be made between measurements of hadrons and the dynamics of quarks and gluons predicted by perturbative QCD. Fragmentation functions (parameterizations) are used to describe which fraction of momentum (or energy) of the initial partons ends up in each of the produced hadrons. The event global features are manly provided by the parton shower, so that hadronization and resonance decays causes little disruption of the features already established by the cascade.

The last step of the non-perturbative stage is the decay of unstable hadrons. A large fraction of the primary hadrons produced are unstable resonances which decay into stable hadrons and leptons according to measured probabilities.

In the following sections the most widely used models for describing the QCD shower in connection with hadronization will be described.

2.3.1 Fragmentation functions

A typical hadronic final state in Z^0 decay contains about 20 stable charged particles (most of which are pions) and 10 neutral hadrons, mainly π^0's. The way these hadrons are obtained from the initial partons is not known and the analysis relies on parameterizations, adjusted to the data, of functions describing the distribution of an hadron in the debris of a parton carrying a fractions $x_E = \frac{E_h}{E_q}$ of its energy (E_h is the energy of the hadron and E_q the quark's energy)[1].

The differential cross section for the process $e^+e^- \rightarrow hX$, indicated in figure 2.16, is given by:

$$\frac{d\sigma}{dx_E}(e^+e^- \rightarrow hX) = \sum_q \sigma(e^+e^- \rightarrow q\overline{q}) \left[D_q^h(x_E) + D_{\overline{q}}^h(x_E)\right] \tag{2.24}$$

where $D_q^h(x_E)$ ($D_{\overline{q}}^h(x_E)$) describes the probability that a hadron h is produced anywhere in the jet with a fraction x_E of the initial quark (anti-quark) energy.

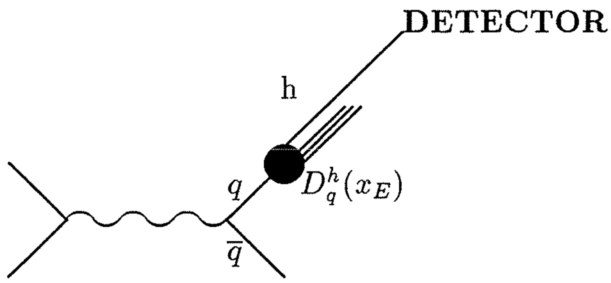

Figure 2.16: A hadron h observed with fraction x_E of the quark's energy, $x_E = \frac{E_h}{E_q}$.

The probability functions $D_{q(\overline{q})}^h$ are subject to constraints imposed by momentum and probability conservation:

$$\sum_h \int_0^1 x_E D_q^h(x_E) dx_E = 1 \; ; \tag{2.25}$$

this simply states that the sum of the energies of all hadrons produced is equal to the energy of the parent quark.

$$\sum_q \int_{x_E(min)}^1 \left[D_q^h(x_E) + D_{\overline{q}}^h(x_E)\right] dx_E = n_h \tag{2.26}$$

where $x_E(min)$ is the threshold energy for producing a hadron with mass m_h, $x_E(min) = \frac{m_h}{E_q}$, n_h is the average multiplicity of hadrons of type h.

[1]Generally the expression $x_E = \frac{(E+p_{||})_{hadron}}{(E+p_{||})_{quark}}$ is used instead ($p_{||}$ is the momentum component along the initial quark direction) since it is Lorentz invariant, whereas the previous definition of x_E is not.

The experimental measurement of the differential cross-section, $\frac{d\sigma}{dx_E}(e^+e^- \rightarrow hX)$ (equation 2.24), gives direct information on $D^h_{q(\overline{q})}$. Moreover, in processes involving three or more parton final states (with quarks and gluons), the analysis of the quark and gluon jet fragmentation functions (D^h_q, and D^h_g) can be translated into information on the properties and differences between quarks and gluons.

A priori these fragmentation functions, for quark and gluon jets, are expected to be different due to the fact that the underlying partons differ in their coupling strength to emit additional gluons, and in consequence their fragmentation (branching) is expected to be different as well. This behaviour is expected to be revealed through the structure and properties of the observed jets.

In figure 2.17 [22] results from DELPHI (LEP I energies) on the fragmentation function of quark and gluon jets are presented. The jets were selected from samples of symmetric three jet events, in fully symmetric topologies (*Mercedes type*), and two fold symmetric topologies (*Y type*). In the first topology all jets have the same energy ($\sim$ 30 GeV), in the last, two jets (one gluon and one quark jet) have equal energy ($\sim$ 24 GeV) and the remaining (quark) jet is more energetic ($\sim$ 43 GeV).

It is observed (figure 2.17) that gluon jets produce fragments with a softer energy spectrum than quarks jets of equivalent energy. This behaviour is a direct consequence of the fact that gluons branch more than quarks, thus leading to a higher number of particles produced with low energy inside gluon jets, relative to quark jets. Moreover, the extra suppression at high X_E (by almost one order of magnitude) in gluon jets relative to quark jets is expected because contrary to the quark case, the gluon cannot be present as a valence parton inside the produced hadron. In the figure results on the fragmentation functions of quark jets from lower energy data (AMY and TASSO) are also shown. Their fragmentation function lies in between the gluon and quark fragmentation functions obtained by DELPHI, which is due to the fact that the distributions at lower energies were normalized to the number of jets (assumed to be two). Therefore, particles from gluons are also added to the two quark jets. Details related to this analysis can be found in [22].

In figure 2.18 [23] a comparison between the fragmentation functions for two different quark energies (quarks from Mercedes events are compared with quarks from Y events, S_q, and quarks from two jet events from DELPHI compared to TASSO, S_e) is shown. As observed from the uppermost figure there is a scaling violation in the fragmentation function of quarks (there is a depletion at large energies and an increase at small energies), which is more pronounced for S_e than for S_q, due to the higher energy difference in the first case. This scaling violation is as well observed in gluon jets (S_g), in which the scaling is more pronounced than in quark jets. This is a consequence of the larger gluon splitting probability.

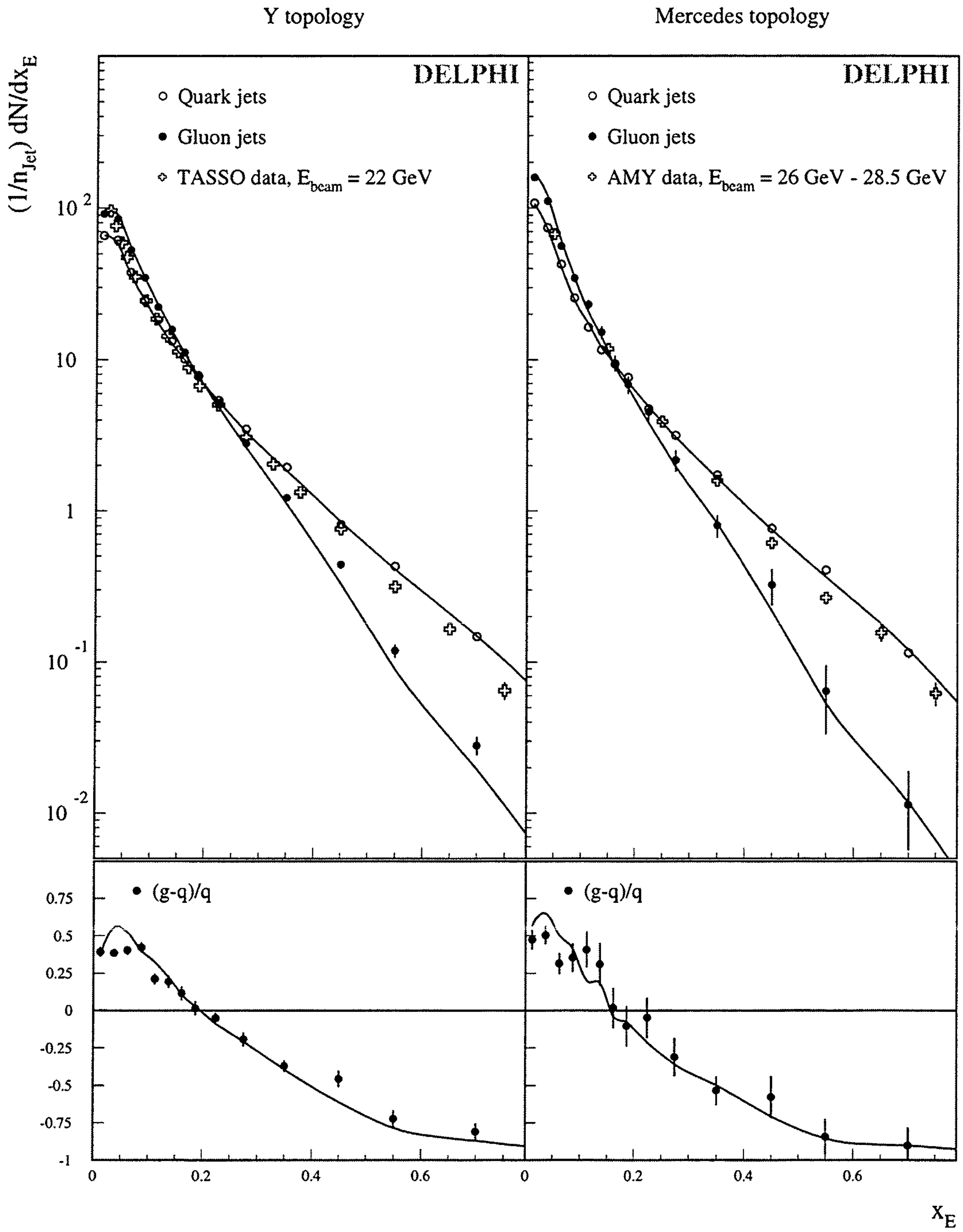

Figure 2.17: Scaled energy distributions, $X_E = \frac{E_{hadron}}{E_{jet}}$ (where "*hadron*" represents all stable hadrons produced in the jet), for Y and *Mercedes* type events, the curves are the corresponding Monte Carlo simulation (JETSET) predictions.

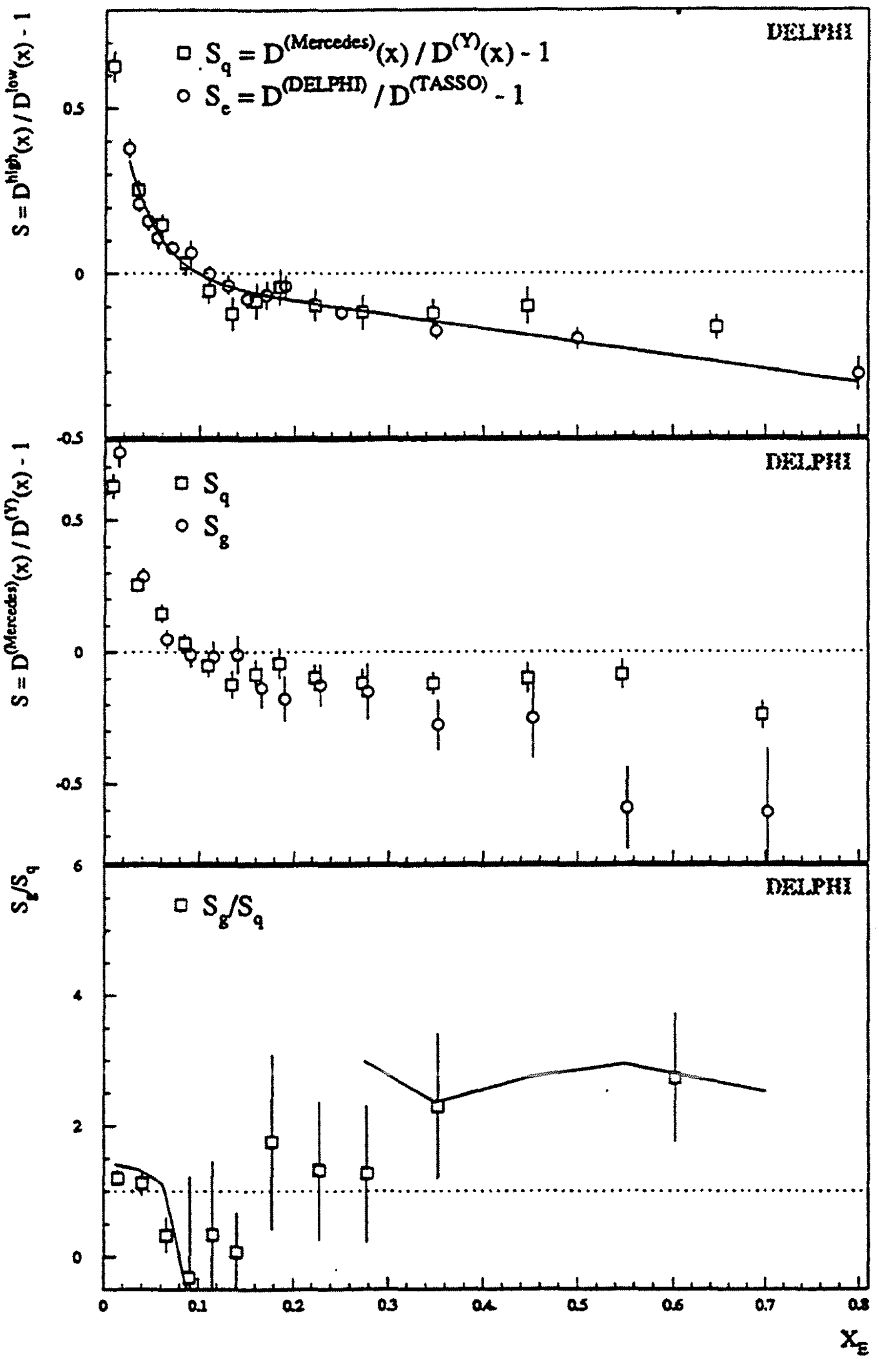

Figure 2.18: The upper plot shows the ratio S of quark fragmentation functions at different energies. The line is a fit to the DELPHI/TASSO data $(\frac{E_{jet}=45\text{GeV}}{E_{jet}=22\text{GeV}})$. The second plot compares S_q with S_g and the last plot represents the ratio presents the ratio $\frac{S_g}{S_q}$. The curve in the lower plot is a prediction of JETSET 7.3 as included in the DELPHI simulation.

2.3.2 Independent fragmentation model

In this model [24], each primary parton is treated independently, and the fragmentation proceeds according to the scheme indicated in figure 2.19. Each outgoing quark (antiquark) generates a chain of secondary quark pairs out of the vacuum and at each step in the chain, a meson is formed containing the initiating and one of the newly generated secondary antiquark. The meson gets an energy fraction z of the initial quark with probability $f(z)$ given by:

$$f(z) = 1 - a + a(1+b)(1-z)^b, \tag{2.27}$$

where a and b are free parameters. Special forms are employed in the case of heavy quarks where harder momentum spectra are expected.

A quark can as well combine with two others from diquark-antidiquark pairs generated out of the vacuum and thus form a baryon. Gluons are first split into $q\overline{q}$ pairs, according to the $g \to q\overline{q}$ Altarelli-Parisi splitting function [17], which then in turn fragment as before.

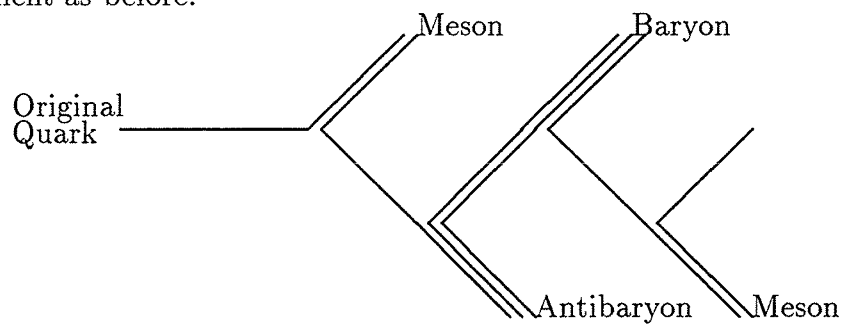

Figure 2.19: Independent jet fragmentation.

This model is not used nowadays for e^+e^- annihilation since it does not reproduce well the data at high energies. Today the best descriptions so far are obtained by models using the string or cluster fragmentation, which are discussed in the following sections.

2.3.3 String hadronization model

String hadronization models [25] are utilized both within shower and fixed order QCD models.

As the primary partons move apart, a colour flux tube ("string") stretches between them (figure 2.20). Neglecting a short-range Coulomb term, the potential energy in the string, supplied by the kinetic energy of the partons, rises linearly as the charges separate. In this situation the string has a constant energy density per unit length (k). Once the potential energy is sufficient to be able to create a quark-antiquark pair, the string may "break" into two separate strings (figure 2.20), which occurs for strings about $1-5$ fm long. If the invariant mass of the secondary strings is large enough they may break into further pieces (new $q\overline{q}$ pairs). The new pairs are formed in such a way as to conserve energy, momentum and internal quantum numbers. The process continues until only ordinary hadrons remain. Energy and momentum are conserved at each step of the string fragmentation.

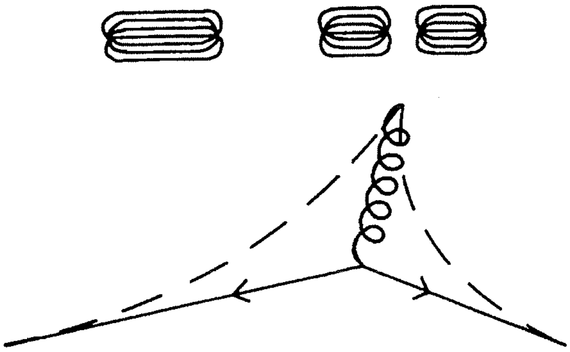

Figure 2.20: ChromoDynamic field lines produced by the strong interaction between two colour charges (upper display). The gluon as a "kink" in the string (lower display).

The Lund Group [26] introduced the concept of a hard gluon, as a "kink" in the colour string between the quark and antiquark (figure 2.20). The fragmentation of the gluon results from the breakup of two strings, stretched from quark to gluon and gluon to antiquark.

Hadron production results from a breaking of the string and baryon production is introduced by the creation of diquark-antidiquark pairs at some of the string breaks.

In the string model all vertices are treated identically, which lead the Lund group to the "left-right symmetric" fragmentation function (symmetric under the exchange $q \leftrightarrow \overline{q}$) [27]:

$$f(z) = \frac{(1-z)^a}{z} exp(-bM_T^2/z) \tag{2.28}$$

where $M_T^2 = M^2 + p_T^2$, with M the mass of the hadron and p_T its transverse momentum relative to the quark's direction. a and b are free parameters. However this function only describes well light flavors. For charm and bottom quarks the Peterson [28] function was introduced:

$$f(z) = \frac{1}{z(1-\frac{1}{z}-\frac{\varepsilon_q}{1-z})^2}; \tag{2.29}$$

here the parameter $\varepsilon_q \sim \frac{1}{m_q}$ (m_q is the quark's mass) gives the required mass dependence, with $\varepsilon_{b(c)}$ for b (c) quarks as free parameters. The Lund fragmentation function and the Peterson function are shown in figure 2.21.

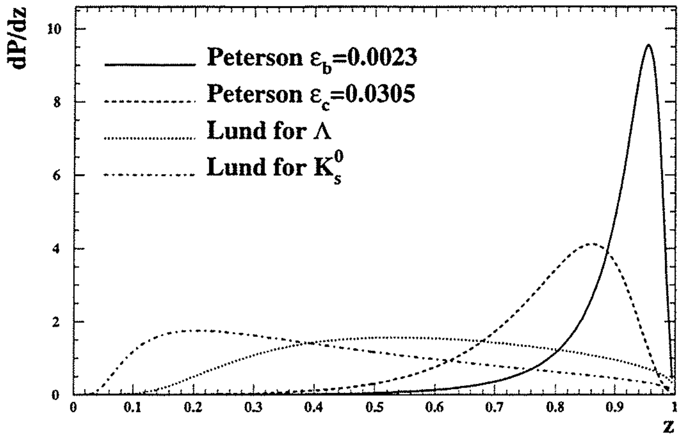

Figure 2.21: Fragmentation functions of Lund and Peterson.

The quark's transverse momentum is taken from a Gaussian probability distribution controlled by its width σ_q (a free parameter), and the transverse momentum of the hadrons is taken as the sum of the transverse momentum of its constituent quarks.

The probability to produce a quark of mass m_q is proportional to $exp(-\pi m_q^2/k)$, where k is the string tension, which leads to the following probabilities for the several quark flavors' production:

$$\gamma_u : \gamma_d : \gamma_s : \gamma_c \simeq 1 : 1 : 0.3 : 10^{-11} \tag{2.30}$$

The main free parameters of the model, besides the ones mentioned before, are the parameter $P/(P+V)$ (which controls the relative rates of vector (V) and pseudoscalar (P) meson production) and the suppression of diquark pair production relative to quark pairs, given by:

$$P(qq')/P(q) = exp\left[-\left(\frac{\pi(m_{qq'}^2 - m_q^2)}{k}\right)\right] \tag{2.31}$$

The string models became very popular, as compared to other models, since they reproduce effects like the so-called string effect (increase of hadron production in the region between a quark and a gluon relative to the region between two quarks). For string models, in $q\overline{q}g$ events, the fragmentation does not occur along the directions of the initial partons but along the directions of the strings which connect the quark-gluon and the gluon-antiquark. The primary hadrons tend to be distributed along a hyperbola on the gluon side of the event as shown in figure 2.20 (lower display) and consequently this leads to a depletion of particles in the $q\overline{q}$ region opposite to the gluon. Transverse momentum and resonance decays tend to wash out this effect.

In figure 2.22 [22] results are presented on the normalized differential particle flow as a function of the angle Ψ of the particles with respect to the direction of the most energetic quark as measured in symmetric three jet events of the Y type ($q\overline{q}g$ and $q\overline{q}\gamma$) and Mercedes type ($q\overline{q}g$)[2].

The particle flow in the interjet region between the two quarks ($N_{q\overline{q}}$) is suppressed relative to the particle flow in the interjet region between a quark and a gluon (N_{qg}), $R = \frac{N_{qg}}{N_{q\overline{q}}} \sim 2$. Moreover, comparing the particle flow in the $q\overline{q}$ interjet region in Y events of the type $q\overline{q}g$ with Y events of the type $q\overline{q}\gamma$, it is observed (figure 2.22) that the suppression is higher in the first case ($R = \frac{N_{q\overline{q}}(q\overline{q}g)}{N_{q\overline{q}}(q\overline{q}\gamma)} \sim 0.6$). These observations constitute good confirmation of the string model.

2.3.4 Cluster fragmentation

The cluster mechanism is mostly utilized in connection with QCD shower models. It is based on the preconfinment characteristics of QCD [29], which reflect the fact that at the end of the partonic cascade a parton is found neighbour in the phase space of another parton with colour charge opposite to it.

The partons at the end of the QCD shower are mostly gluons, which split into $q\overline{q}$ pairs. Since the colour charge of a parton is compensated by the colour charge of its neighboring parton, these $q\overline{q}$ pairs combine to form colour-neutral clusters. The schematic representation of the hadronization process in this approximation is shown in figure 2.23.

The hadrons result from cluster decays. These decays proceed isotropically and are governed by the phase space, which determines the decay probability into the several possible channels. This avoids the introduction of *ad hoc* parameters and enables a simple description of the fragmentation process. Very large clusters are broken into two smaller clusters before decaying to hadrons. The maximum allowed cluster mass, M_c, is taken as a free parameter in the model.

Cluster models contain very few free parameters. For example, transverse momentum in the hadronization, relative numbers of vector mesons and baryons are all controlled by the phase space decays of the clusters. The number of heavy hadrons (baryons) produced depends strongly on M_c.

2.3.5 Monte Carlo event generators

The most widely used Monte Carlo programs for e^+e^- annihilation are based on the QCD parton shower approach.

[2]Although Mercedes events are ideally fully symmetric events, the experimental selections might induce bias. Therefore the jets are energy ordered (although the difference in energy between them is minimal) and the most energetic jet is used as the reference for measuring the angle Ψ.

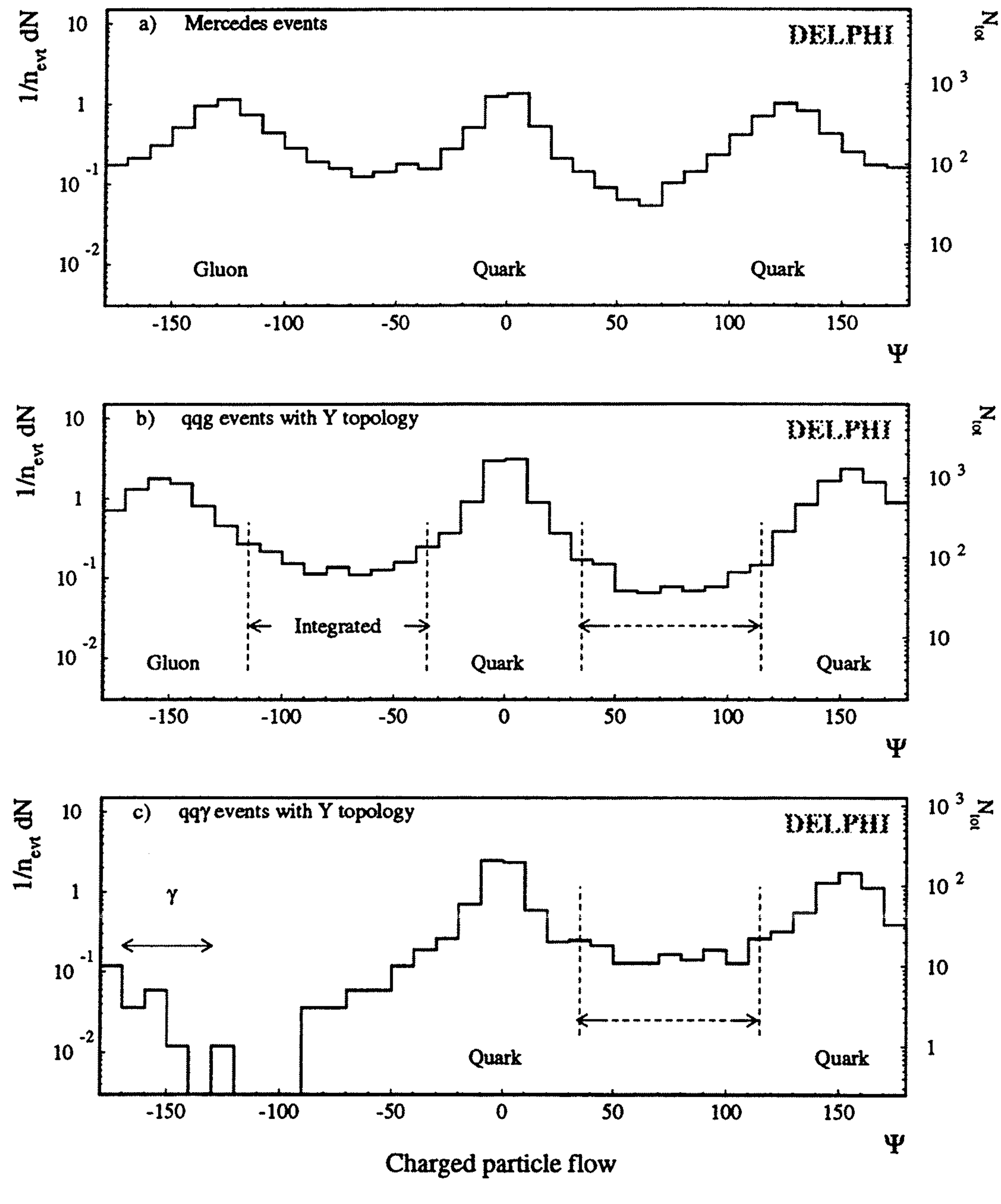

Figure 2.22: Charged particle flow for various three jet event configurations: a) Mercedes $q\bar{q}g$ events, b) Y $q\bar{q}g$ events and c) Y $q\bar{q}\gamma$ events. In all plots, the number of particles is also indicated by the vertical scale at the right side.

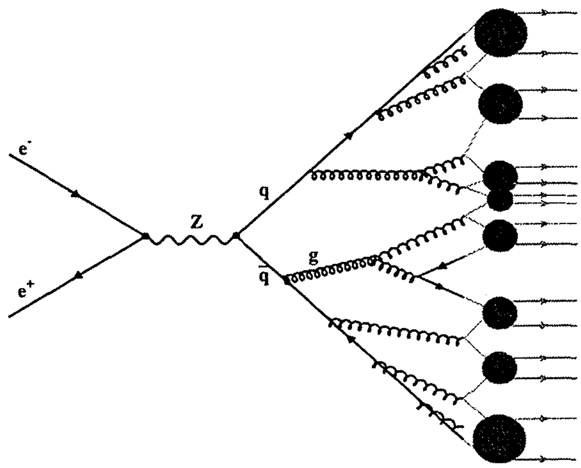

Figure 2.23: QCD cascade fragmentation with subsequent cluster formation using $q\overline{q}$ pairs from neighboring gluons.

As mentioned before (section 2.2.1), the probability for the branching $a \to bc$ to take place during a small change dt is described by the Altarelli-Parisi splitting functions in this approach. The interpretation of the evolution parameter t and the Q^2 scale dependence of the strong coupling constant are model dependent.

Soft gluon interference effects can be taken into account by ordering successive branching in terms of decreasing opening angle (figure 2.24).

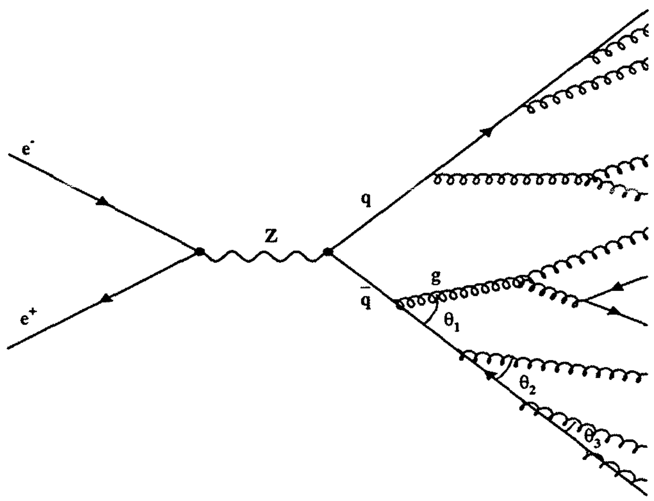

Figure 2.24: Angular ordering of parton branching. A branching cannot occur with an opening angle greater than a previous one ($\theta_1 > \theta_2 > \theta_3$).

Cluster models, together with parton shower cascade including angular ordering, are also able to reproduce the string effect. This suggests that the string effect can be interpreted as a manifestation of soft gluon interference which depletes the region between the quark and the antiquark.

Two widely used Monte Carlo implementations of the parton shower approach, HERWIG [30] and JETSET [31], are presented in table 2.5. HERWIG and JETSET use the Lund string fragmentation and cluster fragmentation, respectively, with free parameters, as mentioned before, for each of these mechanisms.

Model	QCD	Hadronization	Characteristics	
			evolution parameter t	Q^2 scale for α_s
JETSET	Parton shower	Lund String model	$t = \log(m_a^2/\Lambda^2)$; $\Lambda \sim 0.3$ GeV	$Q^2 = m_a^2$
HERWIG	Parton shower	cluster mechanism	$t = \log(\varepsilon_a^2/\Lambda^2)$; $\Lambda \sim 0.2$ GeV	$Q^2 = \varepsilon_a^2$

Table 2.5: Characteristics of the Monte Carlos JETSET and HERWIG. m_a is the parent parton's virtual mass in the branching $a \to bc$. $\varepsilon_a^2 = E_a^2(1 - cos\theta)$, where E_a is the energy of the parent parton and θ is the opening angle of the daughter partons.

The choice of Q^2 made in HERWIG accounts for the angular ordering. In JETSET the angular ordering is introduced by hand.

2.4 Multiplicity

The average multiplicity of a given species of hadron is obtained through the jet fragmentation function. Inspired by a function of the form used in *Independent fragmentation models* (section 2.3.2):

$$f(z) = (1 + \alpha)(1 - z)^\alpha, \tag{2.32}$$

where α is a parameter, the following parameterization is obtained for the total multiplicity of hadrons of type h, with mass M_h [32]:

$$< n_{ch} >= 2(1+\alpha)\left(\log\frac{s}{2M_h} + O(\frac{M_h}{s}).\right) \tag{2.33}$$

Hence one expects a logarithmic rise in multiplicity with increasing center of mass energy ($\sqrt{s}$). A fragmentation function of the simple form $(1 - z)^\alpha$ does not however reproduce well the data and QCD effects, such as hard gluon emission, which increase the multiplicity especially at low momenta, must be taken into account. More complicated forms for $f(z)$, including hard gluon emission effects, lead to parameterizations for the average charged particle multiplicity ($< n_{ch} >$) of the form:

$$< n_{ch} >= a + b\log s + c\log^2 s \tag{2.34}$$

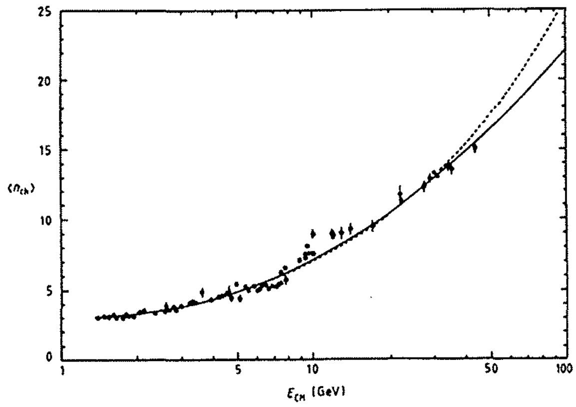

Figure 2.25: Charged multiplicity as a function of the centre of mass energy.

which were observed to fit better the multiplicity distributions at low energies (< 45 GeV). In figure 2.25, low energy data from PETRA on the charged particle multiplicity is presented, together with a fit using equation 2.34 (solid line), with parameters $a = 3.24 \pm 0.11$, $b = -0.34 \pm 0.08$ and $c = 0.26 \pm 0.01$ [33]. The dotted line in the figure is a parameterization motivated by QCD [32]:

$$< n_{ch} >= a + b\exp\left[c\log(\frac{s}{Q_0^2})^{1/2}\right] \tag{2.35}$$

with $Q_0 = 1$ GeV, $a = 2.56 \pm 0.10$, $b = 0.083 \pm 0.014$ and $c = 1.86 \pm 0.07$.

With the income of higher energy data it was observed that the simple parameterizations mentioned above no longer fit well the data. Including the resummation of leading (LLA) and next-to-leading (NLLA) corrections [34], the QCD prediction for charge multiplicity has been computed as a function of α_s:

$$< n_{ch} >= a\alpha_s(\sqrt{s})^b e^{c/\sqrt{\alpha_s(\sqrt{s})}}\left[1 + O(\sqrt{\alpha_s(\sqrt{s})})\right] \tag{2.36}$$

where s is the squared centre of mass energy and a is a parameter (not calculable from perturbation theory) whose value has been fitted from the data. The constants $b = 0.49$ and $c = 2.27$ are predicted by the theory [34].

In order to consider the effect of the higher order corrections to equation 2.36, an *ad hoc* parameter d is sometimes introduced [34] in the form:

$$< n_{ch} >= a\alpha_s(\sqrt{s})^b e^{c/\sqrt{\alpha_s(\sqrt{s})}}\left[1 + d \cdot \sqrt{\alpha_s(\sqrt{s})}\right] \tag{2.37}$$

A fit to the data using equation 2.37, with $\alpha_s(\sqrt{s})$ being expressed at next-to-leading order, a and d as free parameters, is shown in figure 2.26 [35] (the solid line), together with the average charged particle multiplicity results for different center of mass energies. The results of the fit are $a = 0.053 \pm 0.006$ and $d = 1.11 \pm 0.39$.

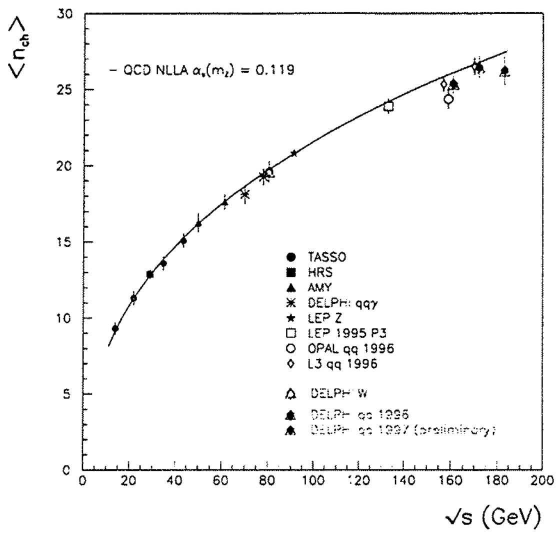

Figure 2.26: Measured average multiplicity as a function of the center of mass energy, together with a fit to a prediction from QCD in Next to Leading Order.

2.4.1 KNO scaling

Z. Koba, H.B. Nielsen and P. Olesen have shown that asymptotically $< n > \sigma_n(s)$ should be only a function of the scaled variable $z = \frac{n}{<n>}$ [36] (independent of the total energy), where n is the number of hadrons, $< n >$ its average and $\sigma_n(s)$ is the cross section of the n-particle production process at a center of mass energy $\sqrt{s}$. According to this hypothesis, known as KNO-scaling, asymptotically the multiplicity distribution is described by a function $\psi(n/ < n >)$ such that:

$$\psi(z) \equiv < n > P(n) \; ; \; z \equiv n/ < n > . \tag{2.38}$$

$P(n)$ is the multiplicity distribution:

$$P_n = \frac{\sigma_n(s)}{\sum_{n=0}^{\infty} \sigma_n(s)}; \tag{2.39}$$

the sum runs over all possible values of n so that:

$$\sum_{n=0}^{\infty} P_n = 1. \tag{2.40}$$

The normalization condition 2.40 leads to the normalization for the KNO-function: $\int_0^\infty z\psi(z)dz = 1$.

The average multiplicity $< n >$ is now expressed in terms of P_n through:

$$< n >= \sum_{n=0}^{\infty} = P_n n \tag{2.41}$$

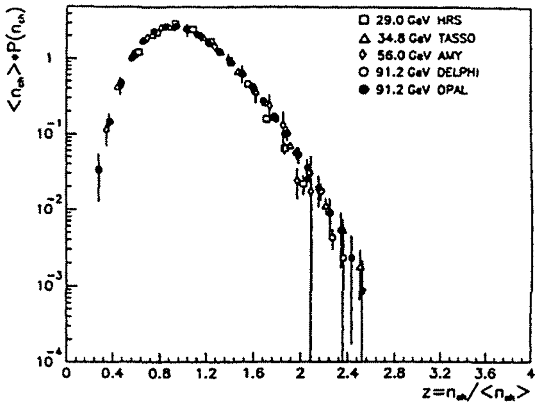

Figure 2.27: Distribution of the KNO variable $\frac{n}{<n>}$ for several center of mass energies indicated in the figure.

In figure 2.27 [37] the experimentally observed distributions of the KNO variable $(n/<n>)$ for different center of mass energies in e^+e^- annihilations is presented.

The energy dependence of the multiplicity distribution is often studied in terms of the dispersion D:

$$D = \sqrt{<n^2> - <n>^2} \tag{2.42}$$

Experimental results on charged particles show that D increases with energy but $\frac{<n>}{D} \sim$ *constant* as predicted (KNO scaling); this behaviour is presented in figure 2.28 [35] for several different e^+e^- center of mass energies. The experimental results (figure 2.28) are also consistent with the predictions of QCD including 1-loop Higher Order terms (H.O.) [38].

As mentioned in the previous sections, the charged particle multiplicity can be understood from the general properties of the branching processes which occur during fragmentation, and therefore is one of the most important features revealing the dynamics of the interaction. To describe the observed charged particle multiplicity distribution in e^+e^- annihilation, at a fixed center of mass energy, phenomenological approaches are used, which originate usually from simplified ideas about particle emission by several sources and exploit some distributions widely used in probability theory.

As an example, it was observed that a fit to a simple Poisson distribution:

$$P(n) = 2\frac{<n>^n e^{-<n>}}{n!} \tag{2.43}$$

does not agree well with the data, as might be expected from completely incoherent particle emission. In particular, this distribution does not obey KNO scaling. For

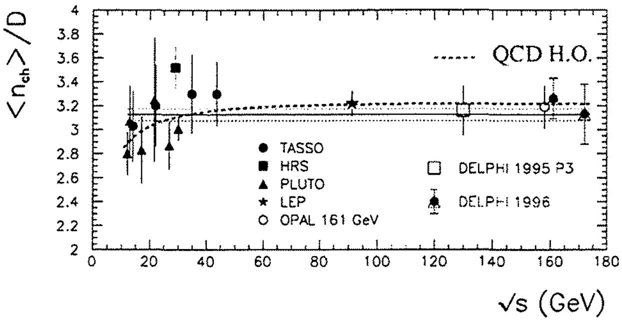

Figure 2.28: Measured ratio of the average multiplicity to the dispersion, for several e^+e^- center of mass energies up to 172 GeV (LEP II). The straight solid and dotted lines represent the weighted average and errors of the data points. The dashed line represents the prediction from QCD (see text).

a Poisson distribution, $D = \sqrt{<n>}$, therefore $\frac{<n>}{D} = \sqrt{<n>}$ should increase with energy (since $<n>$ does), contrary to the observations (figure 2.28).

The NBD (Negative Binomial Distribution) is one of the most popular distributions, as it describes reasonably well the experimental data for various reactions in wide energy intervals (when its parameters are fitted), however there are some discrepancies at high energies (for instance, the e^+e^- data at 91 GeV [39]). Moreover the interpretation of the NBD in terms of the mechanism for particle production, detailed in the previous sections, is not clear.

The NBD is given by:

$$P_n(k, <n>) = \frac{(n+k-1)!}{n!(k-1)!}(<n>/k)^n(1+<n>/k)^{-n-k} \tag{2.44}$$

k is an adjustable parameter with a physical meaning of the number of independent sources and $<n>$ represents the average multiplicity.

For a NBD the dispersion is related to the parameter k by:

$$\frac{D^2}{<n>^2} = \frac{1}{<n>} + \frac{1}{k} \tag{2.45}$$

It should be noted that the NBD with fixed parameter k possesses the asymptotical KNO-scaling, i.e. at average multiplicity tending to infinity $<n> \gg k$, $\frac{D^2}{<n>^2} = constant$. At finite energies $\frac{<n>}{D}$ increases with energy.

Apart from the NBD there are other forms which were proposed to fit e^+e^- annihilation data, as for instance the Generalized Multiplicity Distribution (GMD) [40], which is based on the underlying physics processes taking place during fragmentation. This multiplicity distribution is a solution to the stochastic branching equation proposed by Giovannini [41], which depicts the branching processes: $g \rightarrow gg$

$q \to qg$ and $g \to q\overline{q}$ with average probabilities A, $\overline{A}$ and B, respectively. The probability distribution of n gluons and fixed number of quarks m was obtained [40]:

$$P_n = \frac{(n+k-1)!}{(n-k')!(k'+k-1)!}\left(\frac{<n> -k'}{<n> +k}\right)^{n-k'}\left(\frac{k'+k}{<n> +k}\right)^{k'+k} \tag{2.46}$$

k is now a parameter related to the initial number of quarks by $k = m\frac{\overline{A}}{A}$ and k' is the initial number of gluons in the expression above. $<n> = (k'+k)e^{At} - k$ and $n > k'$, $t = \frac{6}{11N_c - 2N_f}\log\left[\frac{\log(Q^2/\mu^2)}{\log(Q_0^2/\mu^2)}\right]$, Q is the initial parton invariant mass, Q_0 is the scale were the hadronization starts and μ a QCD mass scale. This distribution fits well the data from e^+e^- annihilation as well as from pp and $p\overline{p}$.

A good way of parameterizing multiplicity distributions in e^+e^- annihilation and other processes, is by using the generalized Gamma function (Γ) for the KNO function [42]:

$$\psi(z) = \frac{\mu}{\Gamma(k)}\left[\frac{\Gamma(k+1/\mu)}{\Gamma(k)}\right]^{k\mu} z^{k\mu-1} exp\left(-(\frac{\Gamma(k+1/\mu)}{\Gamma(k)} \times z)^{\mu}\right) \tag{2.47}$$

k and μ are shape parameters. For $\mu = 1$ the generalized Gamma function reduces to the NBD. This functional form for the KNO-function is inspired in the parton QCD characteristics [42] and had its origin when the popular NBD failed in describing existing data.

2.5 Multiplicity of identified final states

The measurement of the production rate of different particles species probes the fragmentation process in great detail. For instance, the relative fractions of kaons and pions produced gives information about the rate of strange quark pair production during fragmentation, while the relative fractions of π and ρ production gives information about the spin structure of the quark pairs. Measurements of baryon production rates are interesting, because the baryon production mechanism in some models is different from the meson production mechanism and this gives information about possible diquark pair production.

The relative rate of pseudoscalar and vector meson production, controlled through the parameter $P/(P+V)$ in the Lund fragmentation models, can be obtained from the ratios in the c and b sectors (here the vector and pseudoscalar mass differences are smaller): $\frac{D^*}{D+D^*}$ and $\frac{B^*}{B+B^*}$, respectively. In the absence of mass effects $P/(P+V)$ may depend only on spin statistics, in which case $P/(P+V) = 3/4 = 0.75$. However feed-down from decays is also important and may obscure the interpretation of the experimental results. The average ratio for primary $\frac{B^*}{B+B^*}$ is found to be 0.75 ± 0.04 [43], in the charm sector the value found is 0.51 ± 0.04 [44]. The disagreement between the value measured in the c sector and the value expected from simple spin counting might arise from the incomplete knowledge of the production rate and decay modes of the D^{**} states, which are likely to feed down into D and D^* production. In the b sector the same could be expected for the B^{**}; here the production and decay rates of the four different J^P states might conspire to leave the value $P/(P+V)$ at 3/4. More measurements are needed before drawing definite conclusions.

To extract the strange quark suppression factor $\gamma_s = (s/u)$, which is an important parameter of string like models (section 2.3.3), the *primary* $K^0(s\bar{d})$ and $\pi^+(u\bar{d})$ rates can be compared. There is however an intrinsic problem about this measurement. About 75% of K^0 come from K^* and other decays and 85% of pions come from ρ, ω and other decays, therefore the direct ratio bears little relation to γ_s. In practice γ_s is varied in the Monte Carlo program until the ratio of final K^0 to $\pi^\pm$ after all decays agrees with the data.

The charmed particles D, D^*, D_s, D_s^* and Λ_c have been reconstructed and their charm fragmentation functions measured, more or less directly. Charmed particles can be identified by combining charged pions, kaons and protons and searching invariant mass plots for $D^0 \to K^-\pi^+$, $D^+ \to K^-\pi^+\pi^+$, $D_s^+ \to \phi\pi^+ \to K^+K^-\pi^+$, $\Lambda_c^+ \to pK^-\pi^+$ and their charge conjugates. D^{*+} candidates can be identified from the mass difference $D^{*+} - D^0$, which has a good mass resolution, whereas the mass resolution for $D^{*+} \to D^0\pi^+$, where $D^0 \to K^-\pi^+$, is poor.

It is normally assumed that only light quarks are produced during the fragmentation process. Although heavy quarks are copiously produced in e^+e^- annihilation, most of them originate from leading c and b quarks and it is difficult to isolate any contribution from these quarks produced during fragmentation (see 2.30). Therefore the hadrons containing heavy quarks can be assumed to contain the primary partons produced directly in the e^+e^- annihilation. A common method for studying heavy quark fragmentation consists in measuring the properties of hadrons containing heavy quarks.

A great number of particles have been identified in e^+e^- annihilations. Table 2.6 shows results from LEP on average hadron multiplicities, compared to model results [37].

The total charged particle multiplicity agrees with the data for both models, however it should be noted that the charged particle momentum distribution is used in the model tuning. The pseudoscalar and vector meson octets, are well described. For the mesons with orbital angular momentum little information is available, and therefore not much input to the models is provided. Here the predicted K_2^{*0} and f_0 rates are too small (f_0 is not at all generated in HERWIG). The octet baryons are well reproduced by both models, with the exception of Ξ^- where the rate in the HERWIG generator is twice as large as in the data. For the decuplet baryons the situation is worse. JETSET is closer to the data, while HERWIG overestimates the rate of strange baryons.

Particle	LEP I	JETSET 7.4	HERWIG 5.8
charged	20.94±0.19	20.59	20.67
$\pi^{\pm}$	17.05±0.43	16.86	17.26
π^0	9.38±0.45	9.65	9.61
$K^{\pm}$	2.11±0.008	2.14	2.08
K^0	2.009±0.027	2.083	2.044
η	0.953±0.076	1.062	0.990
η'	0.25±0.04	0.155	0.132
ρ^0	1.29±0.12	1.286	1.330
$K^{*\pm}$	0.713±0.039	0.774	0.692
K^{*0}	0.757±0.036	0.777	0.693
ω	1.11±0.10	1.261	0.861
ϕ	0.093±0.004	0.105	0.092
f_0	0.160±0.014	0.046	0.
f_2	0.119±0.016	0.209	0.226
f_2'	0.020±0.008	0.021	0.024
K_2^{*0}	0.24±0.09	0.127	0.131
p	1.04±0.04	1.068	1.047
Δ^{++}	0.087±0.033	0.159	0.234
Λ	0.370±0.010	0.379	0.461
Σ^0	0.071±0.013	0.087	0.063
$\Sigma^{\pm}$	0.175±0.029	0.167	0.145
Ξ^-	0.0264±0.0018	0.033	0.061
$\Sigma^{*\pm}$	0.0415±0.0067	0.068	0.159
Ξ^{*0}	0.0056±0.0011	0.0065	0.0322
Ω^-	0.0011±0.0003	0.0012	0.0096
D^0	0.450±0.022	0.500	0.556
$D^{\pm}$	0.182±0.015	0.219	0.252
$D^{*\pm}$	0.172±0.009	0.216	0.228
D^{**0}	0.097±0.040	0.038	0.020
J/ψ	0.0054±0.0003	0.0042	0.
ψ'	0.0023±0.0004	0.	0.
χ_c	0.0084±0.0026	0.0023	0.
$\Upsilon,\Upsilon',\Upsilon''$	0.00015±0.00006	0.000002	0.
Λ_c^+	0.075±0.024	0.034	0.023

Table 2.6: Average hadron multiplicities measured at LEP I in comparison with Monte Carlo models.

Chapter 3

Experimental setup

3.1 The LEP collider

The LEP (**L**arge **E**lectron **P**ositron) collider, with a circumference of 27 Km, is the largest collider ever built. It is located at CERN, in the border between France and Switzerland, at a depth of about 100 m. The electron and positron beams circulate in opposite directions in the ring with a revolution period of $\sim$ 88.9 μs. The beams collide in four points, inside a region of 300$\otimes$ 60$\otimes$ 2000 μm^3, in which the detectors are located. The four detectors now running at LEP are ALEPH, OPAL, L3 and DELPHI. In figure 3.1 a schematic view of the location of the accelerator and the four detectors is given.

The electrons are obtained through ionization and accelerated in the linear accelerator LIL (**L**inear **I**njector **LEP**) until a maximum energy of 600 MeV (see figure 3.1). The electron beam is used as well to produce positrons, through the collision with a tungsten target. Both e^- and e^+ are independently accelerated up to 600 MeV and stored in EPA (**E**lectron **P**ositron **A**cumulator). They reach the energy of 3.5 GeV in the PS (**P**roton **S**incrotron). In the SPS (**S**uper **P**roton **S**incrotron) they are accelerated until 20 GeV. Finally the beams are injected in LEP and accelerated until they reach their final energy.

The size of the ring is justified by the physics goals aimed: for the production of Z^0 bosons in the first phase of LEP (LEP I), the center of mass energy ($\sqrt{s}$) was set to 91 GeV; for the production of W^+W^- pairs in the second phase of LEP (LEP II), $\sqrt{s}$ >160 GeV. To allow a higher flexibility in this respect, the ring was designed to reach a center of mass energy of 200 GeV. Having this in mind, the radius of the ring was determined by the compromise between the minimization of the energy losses by sincrotron radiation ($\propto E^4/Radius$) and the minimization of the costs ($\propto Radius$).

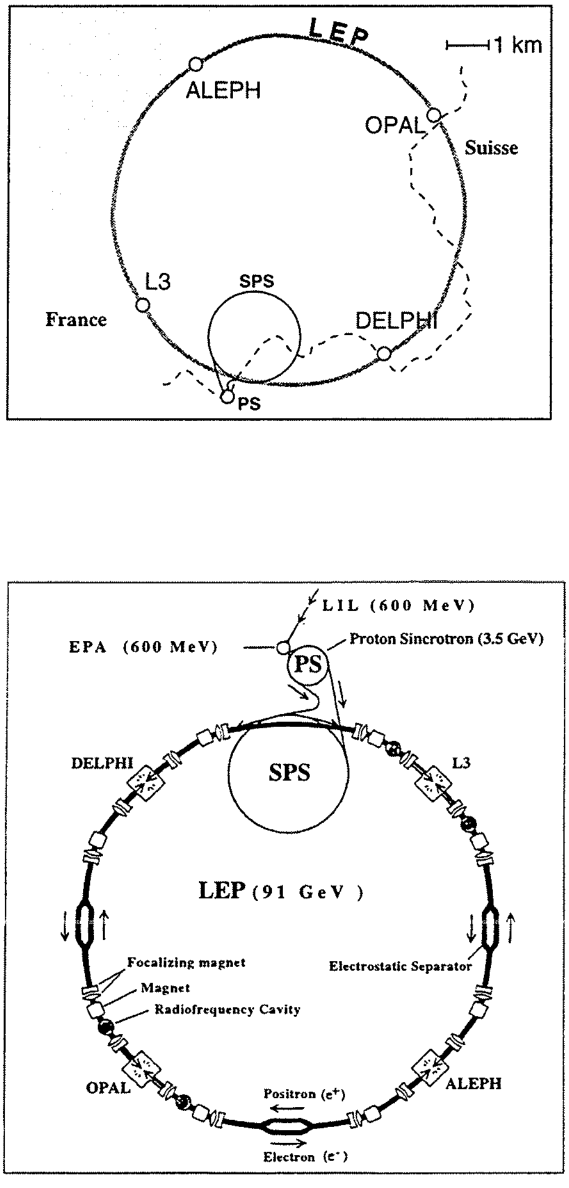

Figure 3.1: In the upper display an overview of the LEP collider is shown, the lower display represents the schematics of the beam injection at LEP.

3.2 Luminosity

The event rate per unit of cross section is given by the luminosity. The e^+ and e^- beams at LEP circulate in opposite directions inside the LEP ring and they are divided into bunches, each having a number of particles N^+ and N^- respectively. The luminosity L is given by:

$$L = n_b \times f \times \frac{N^+ \times N^-}{S}, \tag{3.1}$$

where n_b is the number of bunches of each type, f the frequency of revolution and S the bunch transverse area.

In fact, the luminosity at LEP is not determined through the above parameters, due to the difficulty in measuring, and rigorously controlling them. The luminosity measurement is instead performed by counting the Bhabha scattering events ($e^+e^- \to e^+e^-$) at low angles. In the Bhabha process the electron and positron interact by exchanging either a spacelike (s-channel) or a timelike (t-channel) photon and the first order cross section is given by:

$$\sigma_{Bhabha} = \frac{\alpha^2}{4s}\left((1+cos\theta^2) + 2\frac{(1+cos\theta)^2+4}{(1-cos\theta)^2} - 2\frac{(1+cos\theta)^2}{(1-cos\theta)}\right) \tag{3.2}$$

α is the fine structure constant, s the center of mass energy and θ the polar angle relative to the e^+e^- collision axis. The first contribution comes from the s-channel, the second from the t-channel (which dominates at small angles) and the third from the interference between the two.

For N particles measured with an efficiency ϵ, the luminosity is obtained through the relation:

$$N = L \times \sigma_{Bhabha} \times \epsilon \tag{3.3}$$

The choice of Bhabha scattering as the reference process for the luminosity measurement is due to the following reasons:

- it is mainly a QED process and therefore the cross section can be calculated with high precision;
- it has a large cross section, which ensures the statistical accuracy of the measurement and allows to study the systematics without any statistical limitation;
- it has a simple signature, allowing for a selection of the events with high efficiency and well known acceptance, which guarantees an accurate control of the systematics.

The experimental measure of the Bhabha process at small angles was performed by the detector SAT (**S**mall **A**ngle **T**agger), which was replaced at the end of 1993 by the new calorimeter STIC (**S**mall angle **TI**le **C**alorimeter). These calorimeters cover the low angular region of the detector (43 to 135 mrad in θ for the SAT and 29 to 185 mrad for the STIC). In figure 3.2 integrated luminosities taken by DELPHI from 1990 to 1994 are shown. In 1995 LEP entered its second phase at energies higher than the Z^0 peak. The high energy data taking in 1995 corresponded to an integrated luminosity of 2.85 pb^{-1} (at 130 GeV), 2.98 pb^{-1} (at 136 GeV) and 0.04 pb^{-1} (at 140 GeV). In 1996 the high energy data taking corresponded to 161 and 172 GeV, with integrated luminosities of 9.96 pb^{-1} and 10.14 pb^{-1}, respectively. In 1997 data was taken at 130 GeV and 183 GeV, with integrated luminosities of 6 pb^{-1} and 50.15 pb^{-1}, respectively.

3.3 Components of the DELPHI detector

DELPHI (**DE**tector with **L**epton, **P**hoton and **H**adron **I**dentification) is a general purpose detector for e^+e^- physics, designed to provide high granularity over a 4π solid angle and with emphasis on particle identification [45]. The measurement of the particle's Čerenkov angle distribution, using the Ring Imaging Čerenkov detectors of DELPHI (RICH), together with the ionization energy loss measurement in the Time Projection Chamber, provides a way for charged particle identification.

The DELPHI coordinate system is such that the z-axis coincides with the beam-axis where the positive z runs in the direction of the e^-. The x-axis is perpendicular to the z-axis and is directed towards the centre of the ring, the y-axis is perpendicular to the x and z-axes (see figure 3.3). In figure 3.4 a schematic view of the DELPHI detector is given.

The geometry of the several detectors is approximately cylindrical around the interaction point (barrel region), with two endcaps closing the extremes of the cylinder (forward region). The detector layers closest to the interaction point are composed of detectors aimed to measure the trajectory of charged particles (generally referred to as *tracks*); these are known as *tracking detectors.* The curvature of a particle's trajectory in the DELPHI magnetic field is used to obtain its momentum. The field is produced by a superconducting solenoid with a length of 7.4 m and an inner diameter of 5.2 m. The field strength produced is 1.2 T. Under the influence of the magnetic field, charged particles will follow an helical trajectory. If r is the radius of curvature and p_T the particle's transverse momentum relative to the beam direction, the relation is given by:

$$p_T = 0.3Br \tag{3.4}$$

where p_T is expressed in GeV/c, B in Tesla and r in meters. Unit charge is assumed.

The RICH detector is located externally to the first tracking subdetectors. The electromagnetic and hadronic calorimeters follow the RICH, these are designed

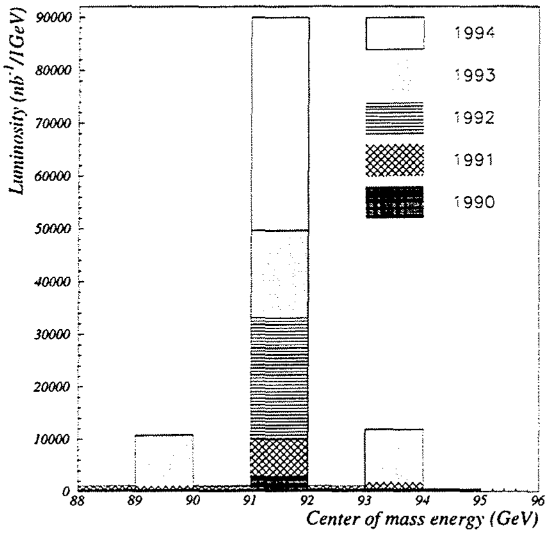

Figure 3.2: Integrated luminosity as a function of the center of mass energy.

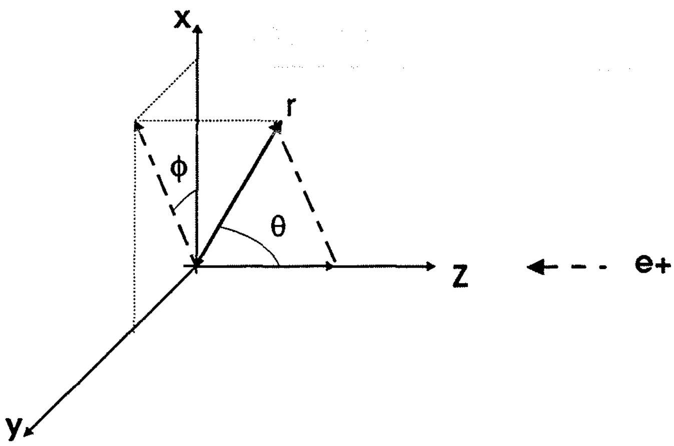

Figure 3.3: Coordinate system of the DELPHI detector.

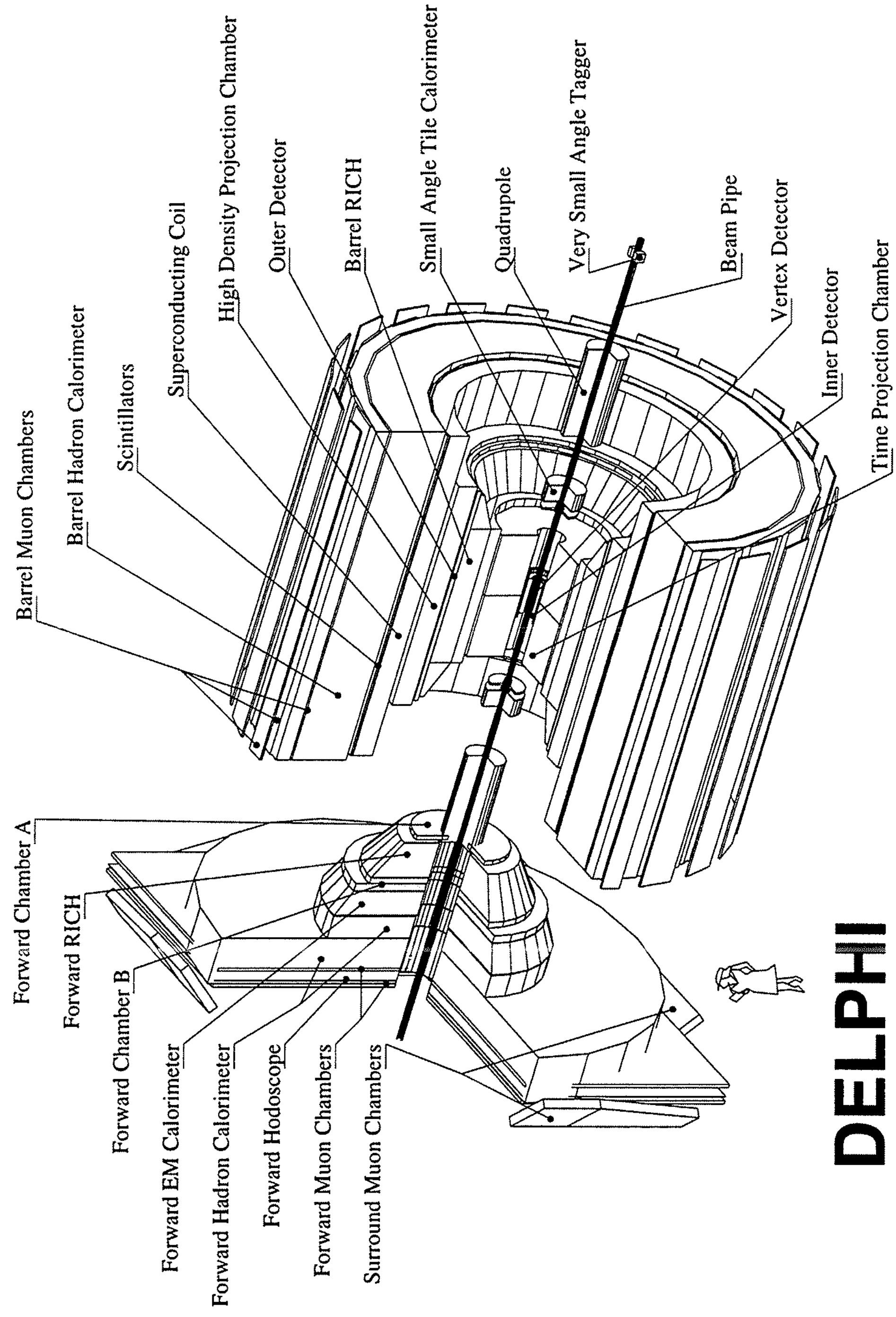

Figure 3.4: Schematic view of the DELPHI detector.

for the measurement of electromagnetic energy depositions and for hadron detection, respectively. Finally, the last shell of the detector is composed by the muon chambers. In this chapter the several detector components are described.

3.3.1 Tracking detectors

The **Vertex Detector (VD)** gives high precision measures of the position of particles near the primary vertex of the interaction.

It consists of three concentric layers of silicon micro strip detectors at radii 6.3 (first layer), 9.0 (second layer) and 10.9 cm (third layer). The polar angle coverage of the first layer of the detector extends from 25° to 155°. At the start of 1994 the first and third layers were equiped with double-sided silicon detectors, having strips orthogonal to each other on opposite sides of the detector wafer, providing measurements also in the z direction. The single hit precision is better than 10 μm in $r\phi$ and of the same order in z.

The physical motivation of this detector is to reconstruct tracks and in particular to give precise extrapolations to the interaction region. It allows the study of the spectroscopy of short lived particles as for instance τ leptons and systems of heavy quarks (see section 4.3).

The **Inner Detector (ID)** is located at a radius of 12 to 23 cm. This detector gives high redundancy for the vertex reconstruction; it is also specially used for the first level trigger, in order to select tracks coming from the interaction point.

It consists of two parts: a jet chamber and a set of trigger layers outside the jet chamber. The jet chamber is subdivided in 24 sectors in $r\phi$, subtending 15 ° each. Every sector has 24 sense wires, measuring drift times in the $r\phi$ direction. The single wire resolution varies from 75 μm to 125 μm. The resolution of a local track element in the Inner Detector is 50 μm in $r\phi$ and 1.5 mrad in ϕ.

The five trigger layers are cylindrical multi-wire proportional chambers (MWPC) with 192 anode wires parallel to the beam axis and 192 circular cathode strips perpendicular to the beam. Single plane resolution along the beam-axis varies from 0.5 to 1 mm for well isolated tracks depending on the angle of the track.

The **Time Projection Chamber (TPC)** is located at a radius of 29 to 122 cm. This detector is the main DELPHI detector for measuring the trajectory of charged particles. The detector is divided in two by a high voltage plate at $z = 0$ (where the interaction point is located). In both directions in z, the detector extends to 130 cm. In $r\phi$, the detector is divided in 6 sectors. When a particle traverses a sector, it ionizes the drift gas. Electrons drift to the end plates. There, they create an avalanche on the sense wires (192 per sector), and induce a signal on the cathode read out pads located behind the sense wires. There are 16 circular rows of pads, therefore up to 16 space points per track can be reconstructed. Each sector contains 1680 pads which allow a measurement in $r\phi$ with a single point resolution of about 250 μm. The resolution in z is close to 1 mm.

The TPC, in addition to providing three-dimensional track reconstruction, helps in charge particle identification by measuring the dE/dX (see section 4.1). The sense wires of its proportional chambers can provide up to 192 ionization measurements per track.

The **Outer Detector (OD)** is located at a radius of 198 cm to 206 cm. The aim of this detector is to give trigger information in $r\phi$ and z, as well as additional tracking information, which, together with the measurements from the TPC and ID, improves the momentum resolution. For this purpose it uses the basic principles of a drift chamber, working in the region of limited proportionality. It consists of 24 sectors in azimuth. Each sector measures 470 cm in z and contains 145 drift tubes in five layers. The layers are staggered in order to ensure a full coverage in azimuth. All layers give $r\phi$ information. The three middle layers also give z information by relative timing of signals at both ends. This fast z measurement is used in the trigger. The single point resolution in $r\phi$ is 110 μm per track, the precision in z is around 4 cm.

The **Barrel Muon Chambers (MUB)** are located in the outermost part of the DELPHI detector. They are arranged in three layers with full coverage in azimuth. Each separate layer contains multiple planes of drift chambers. Free electrons drift maximally 10 cm to an anode wire. Time differences between the signals at each end of the chamber provide a z measurement. The muon chambers measure about 3.7 m in z. The resolution obtained is 4 mm in $r\phi$ and about 2.5 cm in z. A signal measured in these chambers indicates the passage of a muon through them, since basically all other particles loose their energy before reaching it.

In the forward regions, tracking is performed by the **Forward Chambers A (FCA)**, **Forward Chambers B (FCB)** and the **Forward Muon Chambers (MUF)**. The principle of operation of these chambers does not differ in the essential from the other tracking detectors. Typical resolutions of the A and B chambers are about 300 μm in x and y. For the forward muon chambers it is an order of magnitude larger.

The combination of the information from the various tracking detectors is essential for the reconstruction of the trajectory of particles and to obtain a high momentum resolution. The momentum precision of the tracking system in the barrel region is illustrated in figure 3.5(a), which shows the measured inverse momenta of muons from $Z^0 \rightarrow \mu^+\mu^-$ events in which the acollinearity of the two muons is below 0.15° (to remove radiative Z^0 decays) and whose tracks contain

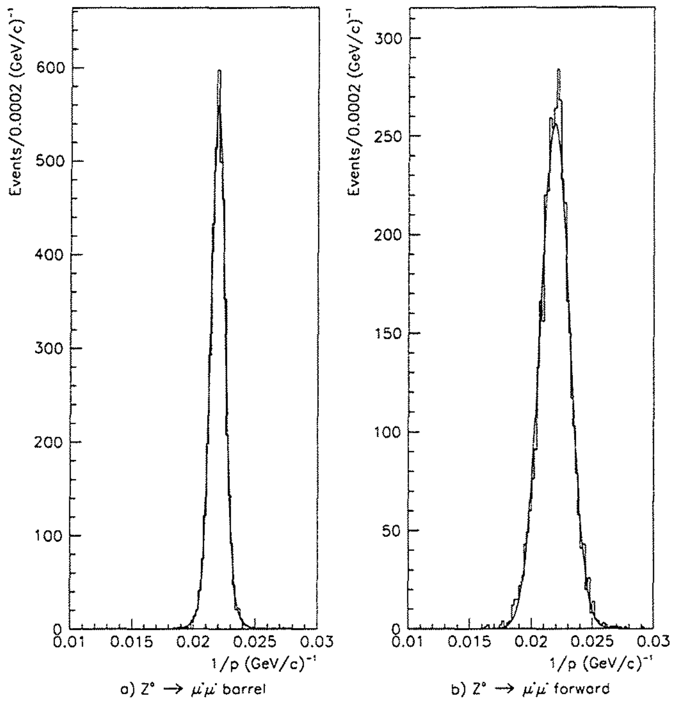

Figure 3.5: Inverse momentum distributions for collinear muons from $Z^0 \to \mu^+\mu^-$ decays: (a) tracks containing hits from VD, ID, TPC and OD, (b) tracks containing hits from VD and FCB at least.

information from all the barrel detectors (VD, ID, TPC, OD). The distribution can be fitted to the sum of two Gaussians. A width of

$$\sigma(1/p) = 0.57 \times 10^{-3}\ (\mathrm{GeV/c})^{-1} \tag{3.5}$$

is obtained for the narrower Gaussian. The tails of the distribution require the wider Gaussian. This has a peak value of about 8% with respect to the total peak, and a width of 1.04×10^{-3} $(\mathrm{GeV/c})^{-1}$.

A similar plot for muons in the forward region seen in at least the closer layer of the VD and in FCB is shown in figure 3.5(b), where a precision of

$$\sigma(1/p) = 1.31 \times 10^{-3}\ (\mathrm{GeV/c})^{-1} \tag{3.6}$$

is measured.

In table 3.1 is indicated the momentum measurement precision obtained for 45.6 GeV/c muons, by combining the information from the several tracking detectors.

The precisions obtained on the track parameters at other momenta can be estimated by comparing the simulated and reconstructed parameters in a sample of generated Z^0 hadronic decays. The behavior of the σ of the distribution of the difference between the reconstructed and simulated momenta as a function of the polar angle θ, for samples of tracks in different momentum intervals, is shown in

$\theta(°)$	Detectors	$\sigma(1/p)(GeV/c)^{-1}$
≥ 42	**VD+ID+TPC+OD**	0.6×10^{-3}
≥ 42	**ID+TPC+OD**	1.1×10^{-3}
≥ 42	**VD+ID+TPC**	1.7×10^{-3}
≤ 36	**VD+FCB included**	1.3×10^{-3}
25-30	**FCB included**	1.5×10^{-3}
< 25	**FCB included**	2.7×10^{-3}

Table 3.1: Momentum measurement precision for 45.6 GeV/c muons.

figure 3.6(a). As can be seen, the precision remains essentially constant over the barrel region for a given momentum but deteriorates in the forward regions of the detector. The variation of the average momentum precision for tracks in the barrel region as a function of momentum is shown in figure 3.6(b). Analogous plots for the precision in the azimuthal angle ϕ are shown in figures 3.6(c) and 3.6(d) while those for the polar angle θ are shown in figures 3.6(e) and 3.6(f).

3.3.2 Calorimeters

The **High-density Projection Chamber (HPC)**, the electromagnetic calorimeter of DELPHI, is a gas sampling calorimeter with high granularity (1 degree in ϕ and 9 samples in depth), composed of layers of lead absorber and gas (the active part of the detector). The HPC is a cylinder with inner and outer radii of 208 and 255 cm, respectively. The total length in z measures 500 cm. The detector is subdivided in 24 sectors in ϕ and 6 sectors in z, combining to a total of 144 independent modules. Each module consists of 41 layers of lead, spaced by 8 mm gaps. The volume between the lead layers is filled with an ionizing drift gas: an 80 % argon per 20 % methane mixture. The lead layers consist of a fiberglass-epoxy support on which thin lead wires are glued. A resistor chain is used to provide a voltage gradient between neighboring lead wires, yielding a drift field of about 100 V/cm in z. The ionization charges drift to readout chambers.These chambers are single plane Multi Wire Proportional Chambers (MWPC). The segmented cathode layer consists of 8 mm by 8 mm U-shaped brass elements. The sense wire is a 20 μm gold plated wire. The cathode elements are grouped into 128 pads. The detector has a total depth of about 18 radiation lengths.

Information about the z-coordinate is obtained by drift time measurements. The amplified charge is sampled with 15 MHz. The sampling frequency combined with an average drift velocity of 5.5 cm/μs gives a granularity of about 3.7 mm.

The HPC is aimed to measure the three dimensional charge distribution induced by electromagnetic showers and by hadrons. The sheets of lead cause the traversing particles to interact which results in a shower of particles. These particles ionize the

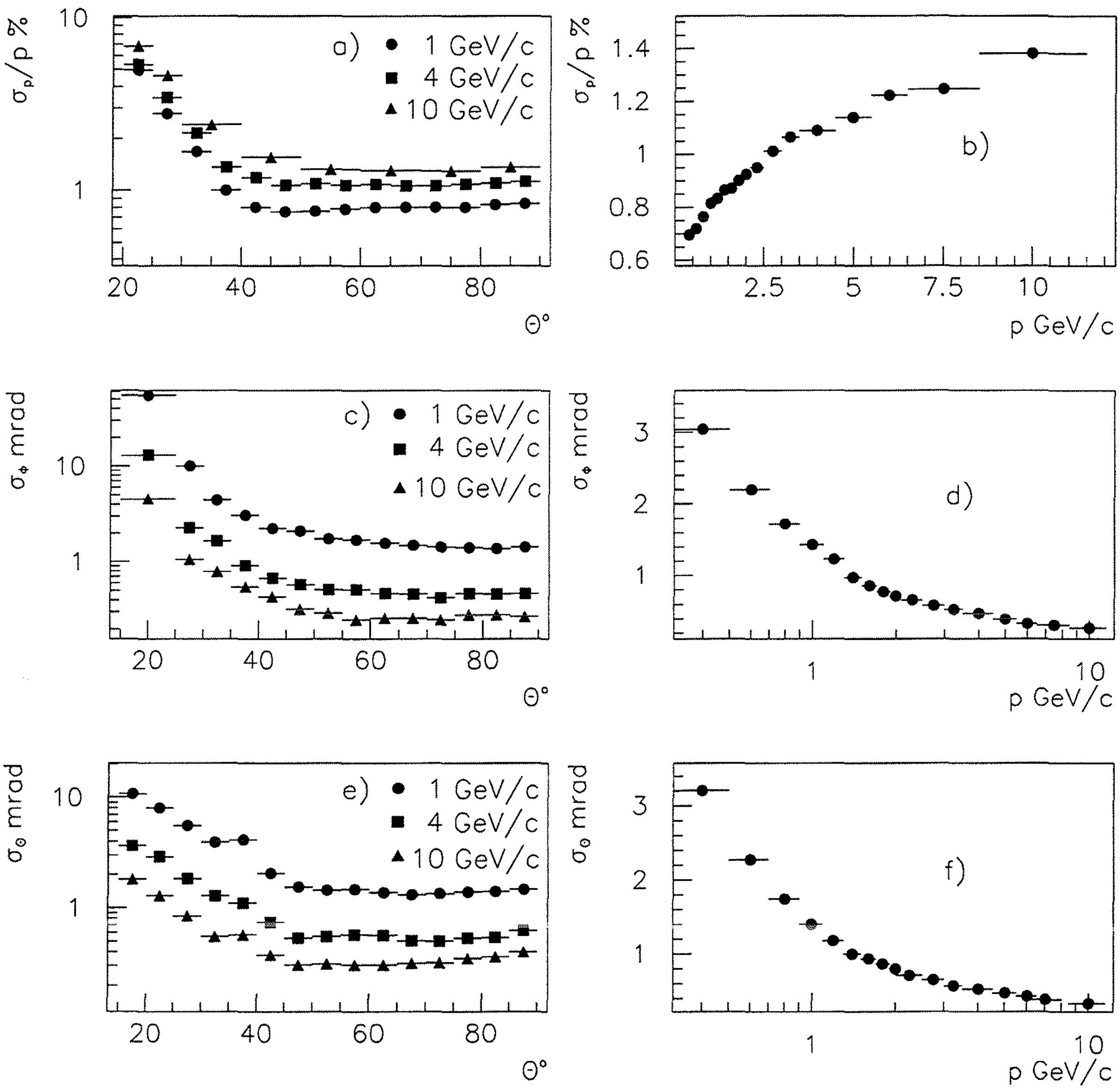

Figure 3.6: Track parameter precisions estimated by comparing simulated and reconstructed parameters: (a) momentum precision as a function of the polar angle θ, (b) momentum precision as a function of the momentum for barrel tracks, (c) azimuthal angle precision as a function of θ, (d) azimuthal angle precision as a function of the momentum for barrel tracks, (e) polar angle precision as a function of θ, (f) polar angle precision as a function of the momentum for barrel tracks.

gas molecules and the ionization charges drift towards the MWPC. The collected charge provides a measure of the energy of the incident particle.

The relative precision on the measured energy is parameterized as follows:

$$\frac{\sigma_E}{E} = 0.043 \oplus \frac{0.32}{\sqrt{E}} \tag{3.7}$$

where E is in GeV.

The **Forward ElectroMagnetic Calorimeter (FEMC)** covers polar angles between 10° and 36.5° and between 143.5° and 170°. The detector consists of two arrays of 4532 lead glass blocks shaped in truncated pyramids, pointing towards the interaction region.

The reconstruction of electromagnetic showers is performed in two stages.

The first stage is an iterative search for energy clusters. In each endcap, the glass with the largest energy deposit not yet associated with others is located and the eight adjacent ones are taken as part of the cluster if their energies exceed a threshold value. A flag is set if a glass had previously been attributed to a contiguous cluster and its energy is then shared between the clusters in proportion to the energies in their central glasses. The cluster energy is then evaluated by summing the energies assigned to it and its coordinates are calculated from their center of gravity. The energy sharing between contiguous clusters are then refined taking into account the computed energies and positions of the clusters. The process continues until all energies above threshold have been assigned to an energy cluster.

The second stage uses information from the tracking system to distinguish the clusters due to neutral particles from those coming from charged particles. A matching is performed based on a χ^2 comparison between the predicted impact point and the reconstructed shower position.

The relative precision on the measured energy can be parameterized as:

$$\frac{\sigma_E}{E} = 0.03 \oplus \frac{0.12}{\sqrt{E}} \oplus \frac{0.11}{E} \tag{3.8}$$

where E is expressed in GeV.

The **Small angle TIle Calorimeter (STIC)** is found in the forward direction. It is the luminosity monitor of DELPHI, which gives an accuracy at the permill level. The STIC is a sampling lead-scintillator calorimeter composed by two cylindrical detectors placed on each side of the DELPHI interaction region at a distance of 2200 mm, and covers an angular region between 29 and 185 mrad in θ (from 65 to 420 mm in radius). The light produced in the scintillator is read by wavelength shifting fibers placed perpendicularly to the scintillator planes. The geometry is quasi-projective, to avoid channeling of the incoming particles through the fibers. The total length of the detector is 27 radiation lengths. Each STIC arm is divided into 10 rings and 16 sectors, giving a $r\phi$ segmentation of 3 cm $\times$ 22.5°.

The relative precision on the measured energy can be parameterized as:

$$\frac{\sigma_E}{E} = 0.0152 \oplus \frac{0.135}{\sqrt{E}} \tag{3.9}$$

where E is in GeV.

The **HAdron Calorimeter (HAC)**, in both the barrel and endcap regions, uses iron as the absorber. The barrel calorimeter is incorporated in the return yoke of the magnet. Polar angle coverage extends from $11.2° - 48.5°$, $42.6° - 137.4°$ and $131.5° - 168.8°$. The detector is again a gas sampling calorimeter. It has 20 layers of limited streamer mode detectors of thickness 2 cm. The absorber layers are 5 cm thick iron plates. The resolution obtained with this detector is

$$\frac{\sigma_E}{E} = 0.21 \oplus \frac{1.12}{\sqrt{E}(\mathrm{GeV})} \tag{3.10}$$

3.3.3 Ring Imaging Čerenkov detectors

DELPHI is equipped with three Ring Imaging Čerenkov detectors. One in each endcap, the Forward RICH-es, and one in the barrel region of DELPHI, the Barrel-RICH (BRICH). In the analyses presented in this thesis only the BRICH was used.

The working principle of the detector is based on photo-ionization in a gaseous volume. Charged particles traversing a dielectric medium faster than the speed of light in that medium produce a cone of Čerenkov light. The Čerenkov photons create free electrons which drift towards a wire chamber. The measured drift time and the hit addresses of anode wires and cathode strips allow three dimensional reconstruction of the conversion point of each individual Čerenkov photon (the RICH detector in DELPHI obtains this measured position with an accuracy better than 1 mm).

As a photo-sensitive agent, TMAE [1] was chosen. Combined with a drift tube with quartz windows, this allows for a photo-sensitive energy range of about 5.6 - 7.4 eV. The lower limit corresponds to the ionization potential of the TMAE. The upper limit is due to photon absorption in the quartz.

Two radiator media, with different refractive indexes, are needed in order to provide particle identification over a large momentum range (0.7 to 45 GeV/c).

Important for the choice of the radiators is the UV transparency, so that a high number of Čerenkov photons is obtained per event, leading to a better Čerenkov

[1] Tetrakis-diMethylAmino-Ethylene; $C_2[(CH_3)_2N]_4$

angle resolution and consequently to a better particle separation. In the BRICH the fluorocarbon C_5 F_{12} was chosen as gaseous radiator and C_6 F_{14} as liquid radiator. These media show only small chromatic aberrations. In addition they are non-flammable, non-toxic, thermally stable and chemically inert.

The detector layout is shown in figure 3.7 [46]. The BRICH is a 3.5 m long cylinder with inner and outer radii of 124 cm and 197 cm. It is divided into two halves by a 6.4 cm thick wall, located at $z = 0$. The mid wall is made of a honeycomb structure clad by epoxy resin and glass fiber mat. Each half is divided into 24 sectors in azimuth. Each sector contains a liquid radiator, a drift tube with a multiwire proportional chamber (MWPC) and a set of six mirrors. The gas radiator fills the remaining volume.

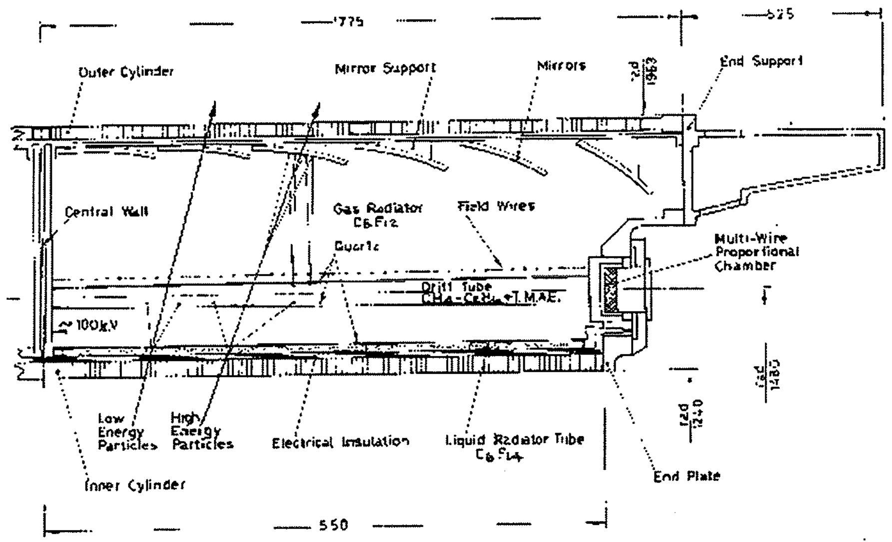

Figure 3.7: Cross section of the BRICH detector of DELPHI.

A particle coming from the interaction point enters the RICH through the inner cylinder wall. Immediately behind the inner cylinder, liquid radiator trays are located. A tray contains 1 cm of C_6 F_{14} and is closed by a 4 mm thick UV-grade quartz window. Around the tray there are 130 μm wide metallic strips with a pitch of 6 mm in z. They are there to help providing a well defined electrical field within the detector.

The rest of the BRICH volume is filled with C_5 F_{12} gas radiator (40 cm) and the drift tubes. The distance between liquid radiators and drift tubes is about 11 cm, in order to ensure the proper geometric resolution for the cones generated in the liquid radiator.

A drift tube measures about 155 cm in z, it is 34.5 cm wide and the depth varies from 4.2 to 6.2 cm, increasing away from the interaction point. The structure is made this way to avoid efficiency losses in electron transport close to the walls of the drift tube, due to diffusion. A resistor chain supplies the voltage gradient needed for the drift field. Single electrons drift maximally 155 cm to the MWPC's mounted on the end of the drift tubes.

Between the top of the drift tubes and the outer cylinder of the BRICH, there are 39 cm of $C_5\ F_{12}$. Parabolic mirrors are mounted on the outer cylinder. The mirrors project Čerenkov photons from the gas radiator back onto the drift tubes.

A particle enters the BRICH and traverses the liquid radiator. If the velocity of the particle, v, is such that $v > \frac{c}{n}$, where c is the light speed and n the refraction index, it will radiate off photons in a cone around its trajectory (see section 4.1.2 for details). The photons from the liquid radiator are directly incident onto the drift tube. Depending on the angle of the particle with respect to the beam axis, the cone section thus obtained varies from elliptic to hyperbolic. Photons radiated behind the drift tube are projected back onto the drift tube.

To determine the Čerenkov angle, the track position and direction have to be known. It is therefore essential to have track information coming from both the TPC (behind the BRICH) and the OD (beyond the BRICH).

The accuracy with which the Čerenkov angle is measured determines the particle identification power of the RICH. The refractive indices of the radiators depend on temperature and pressure variations, and as well may change due to different compositions of the fluids caused by leaks and diffusion. Therefore efficient monitoring, control and calibration systems are implemented. The BRICH operates at a temperature of 40° C. Fluctuations in the temperature will cause fluctuations in the drift velocity and this will consequently lead to mismeasurements of the Čerenkov angle. Furthermore, since thermal expansion directly leads to misalignment for all detector components within the BRICH, stability of temperature is necessary. For this reason, the BRICH is equipped with a sophisticated heating system. On both the outer and inner cylinder, heating strips are mounted. The temperature is monitored by 245 temperature probes. The detector is thermally isolated from the rest of DELPHI to avoid heat dissipation. Furthermore, a number a safety measures as alarm and interlock systems, automatic purges and several back-up computer systems are installed.

The BRICH is equipped with an online calibration system to monitor the drift velocity. A 9×5 matrix of quartz fibers is installed per each module. It consists of rows of nine fibers at five different locations in z. The fibers are driven by a UV-lamp located outside the DELPHI detector. The lamp is triggered by Bhabha events. The frequency is about 0.3 Hz and the accuracy on the drift velocity thus obtained is 0.02 %.

Chapter 4

Particle identification

The measurement of the production rate of several different particle species can provide an important tool for testing the predictions of QCD based models (as discussed throughout chapter 2). In particular, the study of the production rate and momentum spectrum of identified particles in jets initiated by different partons can provide detailed information on the fragmentation process.

The LEP detectors can select gluon jets in bbg events, by tagging the b quarks using selections based on the presence of particles with large impact parameters. This technique recently allowed conclusive measurements of the different behaviour of quark and gluon jets from LEP data (see for example ref. [9, 10, 11]). The DELPHI detector at LEP, equipped with a powerful system for particle identification, can provide information on the spectra of identified particles.

This chapter is organized as follows. In section 4.1 the identification of charged particles (π, K^+ and p) is described. The V^0 (K^0_S and Λ) selections are presented in section 4.2. Finally in section 4.3 the b-tagging technique used in DELPHI to select events with b (c) and light quark initiated jets is discussed.

4.1 Charged particle identification

The identification of charged hadrons in DELPHI relies on the specific energy loss per unit length (dE/dX) in the TPC and on the Čerenkov radiation in the RICH detectors. In section 4.1.1 the hadron identification and selection criteria using the energy loss per unit length in the TPC will be discussed. The RICH identification and selections is presented in section 4.1.2.

4.1.1 dE/dX identification

Charged particles can be identified by the simultaneous measurement of their momentum p and energy loss in the TPC. The energy loss is a statistical process: the charged particles undergo several interactions per unit length, and the total energy loss is given by the sum of the energy losses through the several individual interactions. The main processes for energy loss are:

- Inelastic collisions with the electrons in the medium traversed by the particles;
- Radiation emission (bremsstrahlung).

The energy loss per unit length due to inelastic collisions between the charged particles and the atomic electrons in the detector material is given by the Bethe-Bloch formula:

$$-\frac{dE}{dX} = 4\pi N_A r_e^2 m_e c^2 z^2 \frac{Z}{A}\frac{1}{\beta^2}[\log(\frac{2m_e c^2\gamma^2\beta^2 T_{max}}{I^2})^{1/2} - \beta^2 - \frac{\delta}{2}], \tag{4.1}$$

where r_e and m_e are respectively the classical radius of the electron (2.817×10^{-13} cm) and its mass, N_A is the Avogadro's number ($6.023 \times 10^{23} mol^{-1}$), I represents the average excitation and ionization potential, Z and A are, respectively, the atomic number and weight of the absorbing material, z represents the charge of the incident particle in units of e, and β its velocity, $\gamma = 1/\sqrt{1-\beta^2}$. δ is a correction due to the "screening" effect ($\sim 2\log\gamma + constant$ for high energy particles), $4\pi N_A r_e^2 m_e^2 c^2 = 0.3071$ MeVcm^{2}g^{-1}, dx is measured in units of gcm^{-2} and T_{max} is the maximum energy transferred in a collision:

$$T_{max} = \frac{2m_e c^2\gamma^2\beta^2}{1 + 2\gamma m_e/M + (m_e/M)^2}.$$

Besides this energy loss mechanism by ionization, charged particles also loose energy through radiation emission (bremsstrahlung). This emission is due to the dispersion in the magnetic field of the nucleus, and is in fact only relevant for electrons (positrons):

$$\sigma \sim (\frac{e^2}{mc^2})^2.$$

The cross section varies inversely with the square of the incident particle's mass (m): for instance it is 40000 times lower for muons (the particle with lowest mass after the electron) compared to electrons.

The dependence of dE/dX on the momentum p of the particle is measured from the data using various samples, and the final result is shown in figure 4.1 [45]. Clearly defined bands corresponding to electrons, pions, kaons and protons can be seen. The dE/dX is normalized such that minimum-ionizing pions have $< dE/dX > = 1$. The large statistical spread in dE/dX means that the bands overlap over a significant range of momentum - the separation between kaons and protons is less than two standard deviations for momenta greater than 3 GeV. In the regions where the bands of different particle species cross, their rates cannot be determined.

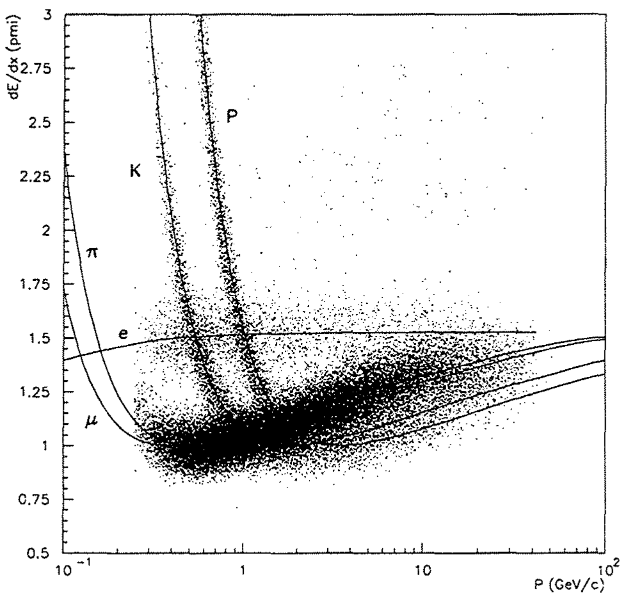

Figure 4.1: Specific energy loss $\frac{dE}{dX}$ in the TPC as a function of the momentum.

4.1.1.1 Pion, kaon and proton identification

The pion, kaon and proton identification is based on probabilities derived from the simultaneous measurement of the momentum of the particles, p, and ionization energy loss in the TPC.

A set of routines were developed in DELPHI, which use the information from the characteristic signals produced by the different particles in the TPC, mentioned in section 3.3.1, and combine these identification capabilities in an optimal way.

A likelihood is evaluated for a given mass hypothesis [47]. The calculations are performed in two stages.

In the first stage the "$PULL$" is computed for each signal, S, and background, B, hypothesis:

$$PULL = \frac{(dE/dX)_M - (dE/dX)_{EXP}}{\sigma_{EXP}} \tag{4.2}$$

where $(dE/dX)_M$ is the measured value of dE/dX, $(dE/dX)_{EXP}$ the value expected for the hypothesis considered and σ_{EXP} the expected error.

In the second stage, the likelihood ratio (L) is computed, according to:

$$L = \frac{Pb_S}{Pb_S + Pb_B} \tag{4.3}$$

with $Pb_S = exp(-0.5PULL^2(S))$ and $Pb_B = exp(-0.5PULL^2(B))$.

For each signal hypothesis as many likelihoods are evaluated as the number of background hypothesis the user wants to consider. In particular, in the present work four likelihood values are estimated per signal hypothesis, since the particles considered are the electron, the muon, the pion, the kaon and the proton. Among these four likelihood values the lowest is considered to characterize the signal hypothesis (*minimum likelihood*).

The separation between pion and muon is very poor and basically possible only for particle momenta below ~ 0.3 GeV/c. For this reason the *minimum likelihood* for the pion hypothesis is expected to be smaller compared to the values reached for the kaon and proton.

The thresholds on the *minimum likelihoods* used for the particle selections were estimated by the compromise between a *good efficiency* and a *low contamination.* The following selections were used in the analysis throughout this work:

- **PION TAG:** A particle is selected as pion if the pion *minimum likelihood* is larger than 10% and the kaon and proton *minimum likelihoods* are lower than 10%.
- **KAON TAG:** A particle is selected as kaon if the kaon *minimum likelihood* is larger than 40%, the pion lower than 20% and the proton lower than 40%.
- **PROTON TAG:** A particle is selected as proton if its *minimum likelihood* is larger than 50%, the pion lower than 10% and the kaon lower than 40%.

In figure 4.2 the efficiency ($efficiency = \frac{\sum XX \ selected \ and \ tagged \ as \ YY}{\sum XX \ selected}$, where XX (YY) = pion, kaon and proton) is presented for pion, kaon and proton tag. The results were obtained from events generated with the Monte Carlo program JETSET 7.3 Parton Shower (PS), which were afterwards passed through the full detector simulation program of the DELPHI detector (DELSIM [45]).

4.1.2 RICH identification

When a particle traverses a transparent medium with index of refraction n, and if the velocity of the particle, v, satisfies

$$\beta > \frac{1}{n}\ , \ \beta = \frac{v}{c}\ , \ c = light\ speed \tag{4.4}$$

it will radiate photons. This is called the Čerenkov effect.

Together with a measurement of the momentum of the particle, equation 4.4 leads to the following constraint on the mass of a particle which is observed to emit Čerenkov radiation:

$$m < p\sqrt{n^2 - 1} \tag{4.5}$$

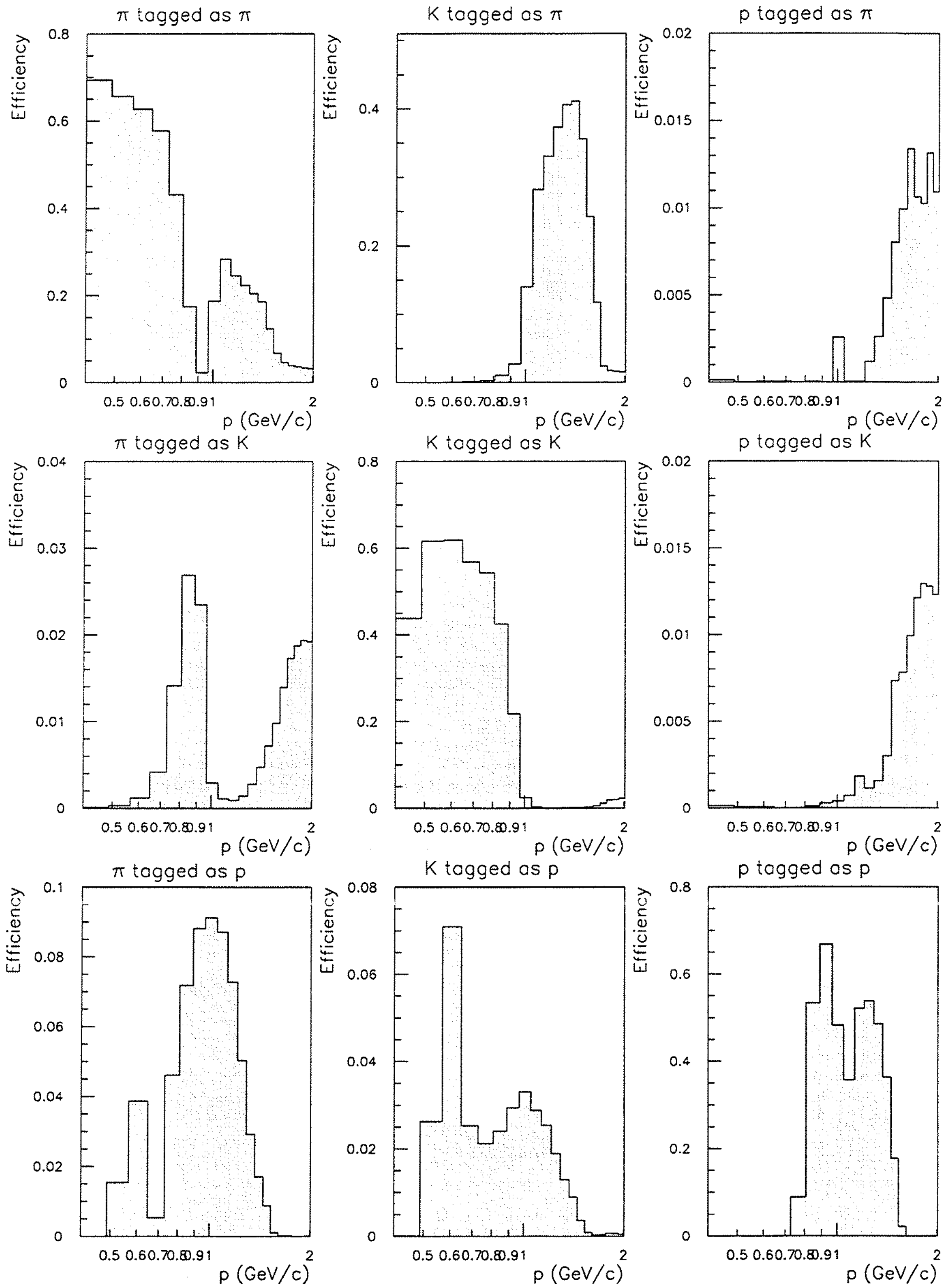

Figure 4.2: Efficiency obtained with the dE/dX selections (see text) as a function of momentum.

where the relations $p = \gamma m \beta$ and $\gamma = (1-\beta^2)^{-1/2}$ are used.

Different particles can be distinguished, in a certain momentum window, if one of them radiates Čerenkov photons while the other does not. In case the particle radiates, equation 4.5 is satisfied and leads to a mass indication in the form of a limit. Threshold Čerenkov counters operate under this principle. These momentum thresholds for pions, kaons and protons in the gas ($C_5\ F_{12}$; $n_{C_5\ F_{12}} = 1.0019$) and liquid ($C_6\ F_{14}$; $n_{C_6\ F_{14}} = 1.2718$) radiators of the BRICH detector of DELPHI are indicated in table 4.1.

Medium	π	K	p
$C_5\ F_{12}$	$p > 2.3$GeV/c	$p > 8.2$GeV/c	$p > 16.0$GeV/c
$C_6\ F_{14}$	$p > 0.2$GeV/c	$p > 0.7$GeV/c	$p > 1.2$GeV/c

Table 4.1: Momentum thresholds for pions, kaons and protons in the gas ($C_5\ F_{12}$) and liquid ($C_6\ F_{14}$) radiators of the BRICH detector of DELPHI.

It is important to notice that the Čerenkov photons are emitted under a well defined angle (θ_C) with respect to the direction of flight of the particle (they lie on a cone around the track). The relation is given by:

$$\cos\theta_C = \frac{1}{\beta n} \tag{4.6}$$

and the number of photons, N, depends on θ_C and on the length of the particle's track in the medium, L, through:

$$N = N_0 L sin^2\theta_C, \tag{4.7}$$

$N_0 = 370(\text{cm eV})^{-1} \int_\omega \epsilon(\omega) d\omega$, where $\epsilon(\omega)$ is the efficiency for detecting a photon of frequency ω.

By measuring the Čerenkov angle and combining this with the measurement of the momentum, equation 4.6 leads to a determination of the mass of the particle:

$$m = p\sqrt{n^2\cos^2\theta_C - 1}. \tag{4.8}$$

By projecting the cone onto a plane perpendicular to the track, a ring image is obtained.

If the light emission per unit track length from a charged particle travelling in a given radiator medium is sufficiently large it may be possible to determine the Čerenkov angle with satisfactory precision by measuring the light emitted from a thin layer of radiator by simply projecting the light onto a photon-detector surface at some distance. This is practicable when using dense radiators such as liquids. If, on the other hand, the light emission per unit length of radiator medium is low, as it is in gases, the radiator length has to be maximized. In this case the light has to be focused to retain a satisfactory geometric angular resolution, for details see for instance reference [48]. In the BRICH detector of DELPHI mirrors are used in the gas radiator, to focus the Čerenkov photons back onto a photon detector, while the light produced in the liquid radiator falls directly onto the photon detection plane (see figure 4.3). This geometry has the advantage of enabling the usage of the same photon detector by both the liquid and gas radiators.

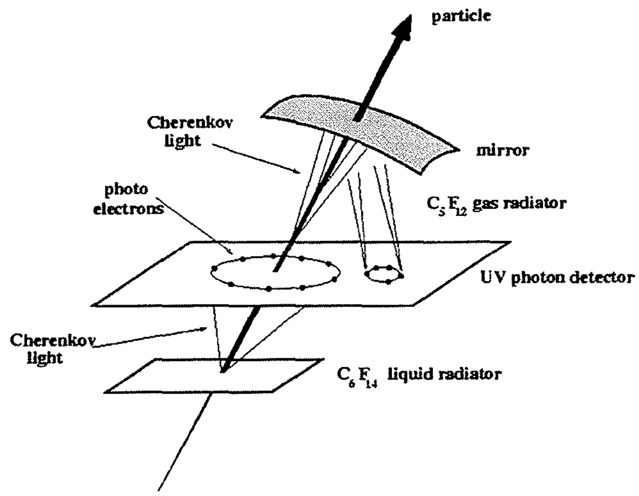

Figure 4.3: The Čerenkov effect as observed by the BRICH detector. Due to the parabolic shape of the mirrors, the focusing point on the photon detector for photons in the gas radiator does not depend on the emission point along the particle trajectory.

In figure 4.4 the average Čerenkov angle per track is given as a function of the momentum for pions, kaons and protons in multihadronic events collected by DELPHI in 1994 [45].

Considering, for instance, the separation of pions and kaons in the gas radiator, there are two distinct momentum regions.

Below 9 GeV the condition 4.4 is not satisfied for kaons (and protons), therefore a signal indicates the passage of a pion in the RICH. At about 9 GeV, kaons start to radiate. At this stage, the measured Čerenkov angle is compared with the expected angles for different particle hypotheses, and the closest hypotheses gives

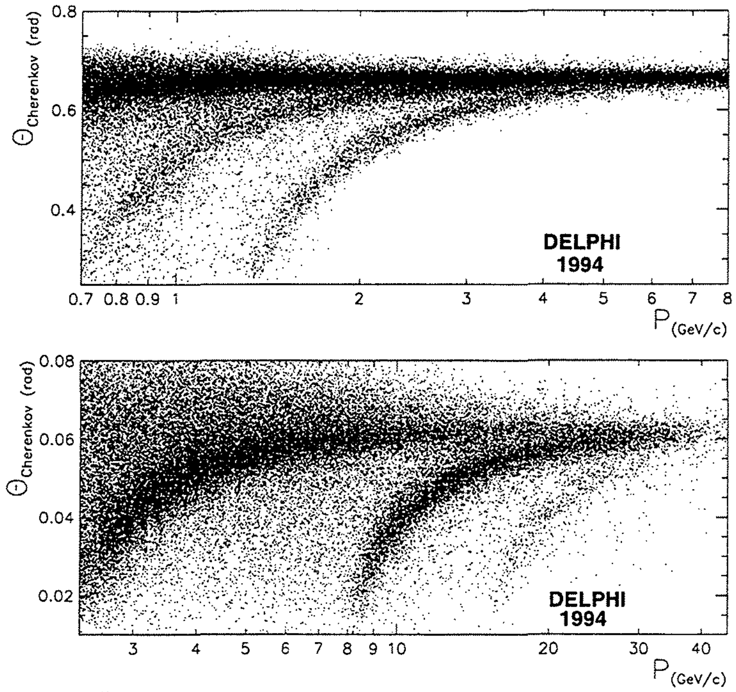

Figure 4.4: Average Čerenkov angle per track as a function of the momentum in multihadronic events in the Barrel RICH, for the liquid (top) and gas (bottom) radiators. The three bands on both plots correspond to pions (uppermost band), kaons (middle band) and protons (lowest band).

the particle identity. At around 25 GeV the Čerenkov angle for kaons is almost saturated, leaving almost no difference between pion and kaon Čerenkov angles. Here, the separation between pions and kaons ends. The same principle applies for the liquid radiator and for all combinations of particles (pions, kaons and protons); this will be detailed in the next section.

4.1.2.1 Pion, kaon and proton identification

The pion, kaon and proton identification is based on probabilities derived from the measured average Čerenkov angle and observed number of photons in the RICH detector.

A set of routines were developed in DELPHI, which use the information from the characteristic signals produced by the different particles in the RICH, mentioned in section 3.3.3, and combine these identification capabilities in an optimal way. Probabilities for each particle hypothesis are evaluated for the gas and liquid radiator, and according to criteria based on which particle type was attributed the highest probability, together with separation criteria between the particles, several levels of tagging selections are defined.

The Čerenkov angle reconstruction is performed by the RIBMEAN clustering algorithm [49]. The photoelectrons are grouped into clusters which are weighted according to quality criteria, such as measurement errors or possible ambiguities between several tracks [49]. The best cluster is retained and weights used to measure the average Čerenkov angle, its error and the estimated number of photoelectrons.

Pion, kaon and proton tagging is then achieved by means of the NEWTAG package [50] which combines information of the liquid and gas radiator with respect to different momentum windows. The basic philosophy of NEWTAG is to require a tagged particle to be inside 2.5 standard deviations of the closest hypothesis ($\sigma_{acc} = \frac{|\theta_c^{meas(i)} - \theta_c^{exp(i)}|}{\sigma_{ring}^{exp}} < 2.5$, θ_c^{meas} is the measured Čerenkov angle, θ_c^{exp} the Čerenkov angle expected, and σ_{ring}^{exp} the expected error; i, j=pion, kaon,proton) and at least 1 (*loose*), 2 (*standard*) or 3 (*tight*) standard deviations separated from the nearest neighbour hypothesis ($\sigma_{sep} = \frac{\theta_c^{meas(i)} - \theta_c^{exp(j)}}{\sigma_{ring}^{exp}} > 1, 2, 3$). These tag definitions (*loose*, *standard* and *tight*) are optimized, as will be specified below, for different momentum windows of the particles.

It should be noted here that the fact that a particle did not radiate light in a given momentum region also provides information on its possible flavor, as mentioned before. When a particle is in the momentum region where it emits Čerenkov radiation, we speak of "positive identification" or "band region". If the momentum of the particle is below the threshold we speak of "negative identification" or "veto region". The track veto requirement for the gas radiator is a number of detected photoelectrons (NP) lower than 2, and for the liquid lower than 4.

The specific particle tags, optimized for different momentum windows, are described in tables 4.2, 4.3 and 4.4. Further details about the selections can be found in reference [50].

PION TAG										
		loose			*standard*			*tight*		
p (GeV/c)	radiator	σ_{sep}	σ_{acc}	NP	σ_{sep}	σ_{acc}	NP	σ_{sep}	σ_{acc}	NP
$[0.7, 2.7]$	liquid	> 1 $j = K$	< 2.5	-	> 2 $j = K$	< 2.5	-	> 3 $j = K$	< 2.5	-
	gas	-	-	-	-	-	-	-	-	-
$[2.7, 8.5]$	liquid	-	-	-	-	-	-	-	-	-
	gas	-	< 3	> 3	-	< 2	> 4	-	< 1	> 5
$[8.5, 15]$	liquid	-	-	-	-	-	-	-	-	-
	gas	> 1 $j = K$	< 3	-	> 2 $j = K$	< 3	-	> 3 $j = K$	< 3	-
> 15	liquid	-	-	-	-	-	-	-	-	-
	gas	> 1 $j = K$	< 2.5	-	> 2 $j = K$	< 2.5	-	> 3 $j = K$	< 2.5	-

Table 4.2: Pion selections based on the NEWTAG package.

In figure 4.5 the efficiency ($efficiency = \frac{\sum XX \text{ selected and tagged as } YY}{\sum XX \text{ selected}}$, where

KAON TAG										
		loose			*standard*			*tight*		
p (GeV/c)	radiator	σ_{sep}	σ_{acc}	NP	σ_{sep}	σ_{acc}	NP	σ_{sep}	σ_{acc}	NP
$[0.7, 1.8]$	liquid	> 1 $j = (1)$	< 2.8	-	> 2 $j = (1)$	< 2.8	-	> 3 $j = (1)$	< 2.8	-
	gas	-	-	-	-	-	-	-	-	-
$[1.8, 2.7]$	liquid	> 1 $j = (1)$	< 2.5	-	> 2 $j = (1)$	< 2.5	-	> 3 $j = (1)$	< 2.5	-
	gas	-	-	-	-	-	-	-	-	-
$[2.7, 3.5]$	liquid	> 1 $j = p$	< 2.8 -	-	> 2 $j = p$	< 2.8 -	-	> 3 $j = p$	< 2.8 -	-
	gas	-	-	$2^{(2)}$	-	-	$1^{(2)}$	-	-	$0^{(2)}$
$[3.5, 5.5]$	liquid	> 1 $j = p$	< 2.5 -	-	> 1.5 $j = p$	< 2.5 -	-	> 2 $j = p$	< 2.5 -	-
	gas	-	-	$2^{(2)}$	-	-	$1^{(2)}$	-	-	$0^{(2)}$
$[5.5, 8.5]$	liquid	> 0.5 $j = p$	< 2.5	-	> 1 $j = p$	< 2.5	-	> 1.5 $j = p$	< 2.5	-
	gas	-	-	$2^{(2)}$	-	-	$1^{(2)}$	-	-	$0^{(2)}$
$[8.5, 15]$	liquid	-	-	-	-	-	-	-	-	-
	gas	> 1 $j = (3)$	< 3	-	> 2 $j = (3)$	< 3	-	> 3 $j = (3)$	< 3	-
> 15	liquid	-	-	-	-	-	-	-	-	-
	gas	> 1 $j = (3)$	< 2.5	-	> 2 $j = (3)$	< 2.5	-	> 3 $j = (3)$	< 2.5	-

Table 4.3: Kaon selections based on the NEWTAG package. (1) For $p < 1.3$ GeV/c, $j = \pi$. For $p > 1.3$ GeV/c the kaon hypothesis is sandwiched between the pion and proton hypothesis, therefore the tags are defined as the most conservative separation from the two. (2) K/p gas veto is used. (3) For $p < 17.5$ GeV/c $j = \pi$. For $p > 17.5$ GeV/c $j = \pi$ or $j = p$ (the most conservative hypothesis is taken).

PROTON TAG										
		loose			*standard*			*tight*		
p (GeV/c)	radiator	σ_{sep}	σ_{acc}	NP	σ_{sep}	σ_{acc}	NP	σ_{sep}	σ_{acc}	NP
$[0.7, 1.3]$	liquid	-	-	$< 2^{(1)}$	-	-	$< 1^{(1)}$	-	-	$< 0^{(1)}$
	gas	-	-	-	-	-	-	-	-	-
$[1.3, 1.5]$	liquid	> 1 $j = K$	< 3	-	> 2 $j = K$	< 3	-	> 3 $j = K$	< 3	-
	gas	-	-	-	-	-	-	-	-	-
$[1.5, 2.7]$	liquid	> 1 $j = K$	< 2.5	-	> 2 $j = K$	< 2.5	-	> 3 $j = K$	< 2.5	-
	gas	-	-	-	-	-	-	-	-	-
$[2.7, 4]$	liquid	> 1 $j = K$	< 2.8	-	> 2 $j = K$	< 2.8	-	> 3 $j = K$	< 2.8	-
	gas	-	-	$2^{(2)}$	-	-	$1^{(2)}$	-	-	$0^{(2)}$
$[4, 6.5]$	liquid	> 1 $j = K$	< 2.5	-	> 1.5 $j = K$	< 2.5	-	> 2 $j = K$	< 2.5	-
	gas	-	-	$2^{(2)}$	-	-	$1^{(2)}$	-	-	$0^{(2)}$
$[6.5, 9]$	liquid	> 0.5 $j = K$	< 2.5	-	$> 1.$ $j = K$	< 2.5	-	> 1.5 $j = K$	< 2.5	-
	gas	-	-	$2^{(2)}$	-	-	$1^{(2)}$	-	-	$0^{(2)}$
$[9, 17.5]$	liquid	-	-	-	-	-	-	-	-	-
	gas	-	-	$2^{(2)}$	-	-	$1^{(2)}$	-	-	$0^{(2)}$
$[17.5, 24.5]$	liquid	-	-	-	-	-	-	-	-	-
	gas	> 1 $j = K$	< 3	-	> 2 $j = K$	< 3	-	> 3 $j = K$	< 3	-
> 24.5	liquid	-	-	-	-	-	-	-	-	-
	gas	> 1 $j = K$	< 2.5	-	> 2 $j = K$	< 2.5	-	> 3 $j = K$	< 2.5	-

Table 4.4: Proton selections based on the NEWTAG package. (1) K/p liquid veto is used. (2) K/p gas veto is used.

XX (YY) = pion, kaon and proton) obtained with the three RICH tags (*loose*, *standard* and *tight*) is shown for a sample of events generated with the Monte Carlo program JETSET 7.3 PS, which were passed through the full simulation program of the DELPHI detector (DELSIM [45]).

4.2 V^0 Reconstruction

Neutral strange weakly decaying particles (i.e. $\Lambda = uds$ and $K^0_S = d\bar{s}$, see table 4.5), have average decay lengths ranging from cm to meters in the laboratory frame. They are detected by a secondary vertex in the tracking chambers. Two tracks being consistent with coming from a common point different from the primary e^+e^- collision point are selected with little background. A kinematic fit, which uses the fact that most of these light flavored hadrons originate from the primary vertex, may improve the signal to background ratio.

Particle	Mass (MeV/c^2)	lifetime (10^{-10} s)	quark composition
K^0_S	497.672 ± 0.031	0.8927 ± 0.0009	$d\bar{s}$
Λ	1115.684 ± 0.006	2.632 ± 0.020	uds

Table 4.5: Characteristics of the hadrons K^0_S and Λ.

The K^0_S and Λ candidates are detected by their decay in flight into $\pi^+\pi^-$ and $p\pi^-$, respectively. All oppositely charged pairs of particles in a hadronic event are tested for the hypothesis that they originate from a secondary vertex. The vertex defined by each pair is determined by minimizing the χ^2 obtained from the distances of the vertex to the extrapolated tracks.

The V^0 decay vertex candidates are required (in a *loose* selection [51]) to have in the xy plane an angle θ^{xy}, between the V^0 momentum and the line joining the primary to the secondary vertex, of less than 0.1 rad; a radial separation (R^{xy}) between the primary and the secondary vertices greater than 2 standard deviations; a probability of the χ^2 fit to the secondary vertex larger than 0.001; a transverse momentum of each charged particle from the V^0 decay with respect to its line of flight, greater than 0.02 GeV/c; an invariant mass in the e^+e^- hypothesis lower than 0.16 GeV/c^2 and when the reconstructed decay point of the V^0 is beyond the VD radius, it should not exist any signal in the VD consistent with association to the decay vertex.

A *standard* sample is defined by requiring $\theta^{xy} < (0.01 + 0.02/p_t{}^1)$ rad; $R^{xy} > 4\sigma$ and a probability of the χ^2 fit larger than 0.01.

[1] p_t is the transverse momentum of the V^0 candidate relative to the beam axis, in GeV/c.

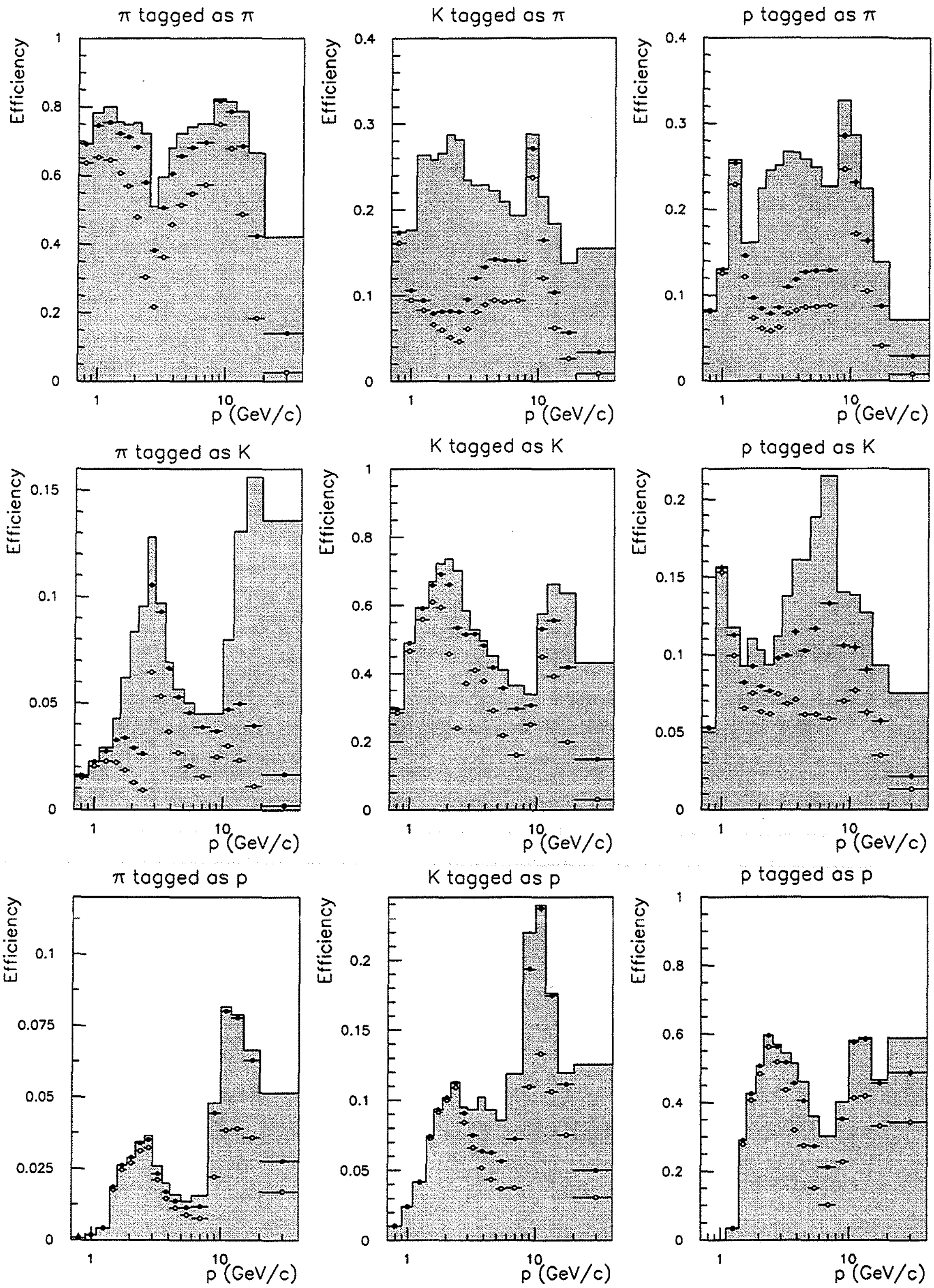

Figure 4.5: Efficiency matrix obtained with the NEWTAG flags: *loose* (full histogram); *standard* (closed circles) and *tight* (open circles) as a function of momentum.

The $\pi^+\pi^-$ and $p\pi^-$ ($\overline{p}\pi^+$) invariant masses (attributing the proton mass to the particle with larger momentum) are calculated. If more than one V^0 hypothesis is available for the same charged tracks within three standard deviations, the hypothesis corresponding to the smaller mass pull[2] is selected. In the following analysis these selections will be referred to as *tight* when the probability that the V^0 has decayed within the calculated distance is between 2% and 95%.

The efficiency and background fraction as a function of $-\log x_p = -\log 2p/\sqrt{s}$ for *tight* K^0_S and Λ are shown in figure 4.6.

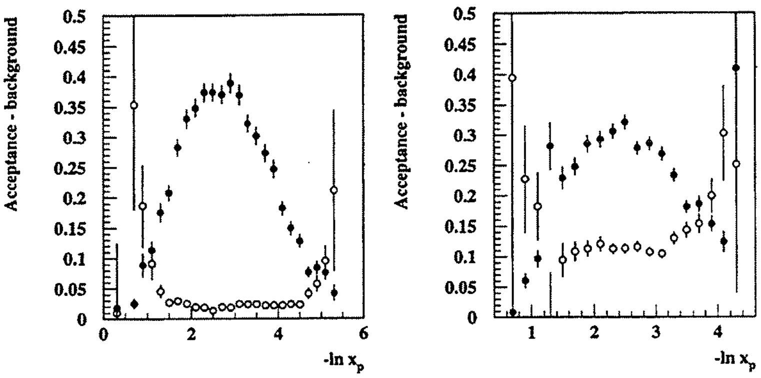

Figure 4.6: Efficiency (closed circles) and background fraction (open circles). The left hand side graph shows results for the K^0_S and the right hand side graph for the Λ.

All these selections for the V^0 reconstruction are provided by a package developed by the DELPHI collaboration [51]. The reconstructed invariant mass distributions for a sample of selected *tight* K^0_S and Λ are shown in figure 4.7. A Breit-Wigner with a linear background was fitted to these distributions in order to extract the mass resolution ($\sigma = \Gamma/2.35$) shown in the figures.

In figure 4.8 the mass spectra together with their contamination, at the level of the *tight* selections are shown for five different momentum windows ([0.0, 1.4]; [1.4, 6.0]; [6.0, 8.0]; [8.0, 12.0] and [12.0, 16.0]). These distributions were obtained for a sample of events generated with the Monte Carlo program JETSET 7.3 PS, which were passed through the full simulation program of the DELPHI detector (DELSIM [45]).

As seen from the figures, the contamination from misidentified particles in the selected samples of K^0_S and Λ is very small.

In figure 4.9 the mass resolution of the K^0_S and Λ is shown as a function of the momentum of the pion and proton, respectively. A Breit-Wigner with a linear

[2]Mass pull is the absolute value of mass shift with respect to the nominal mass, divided by the mass resolution.

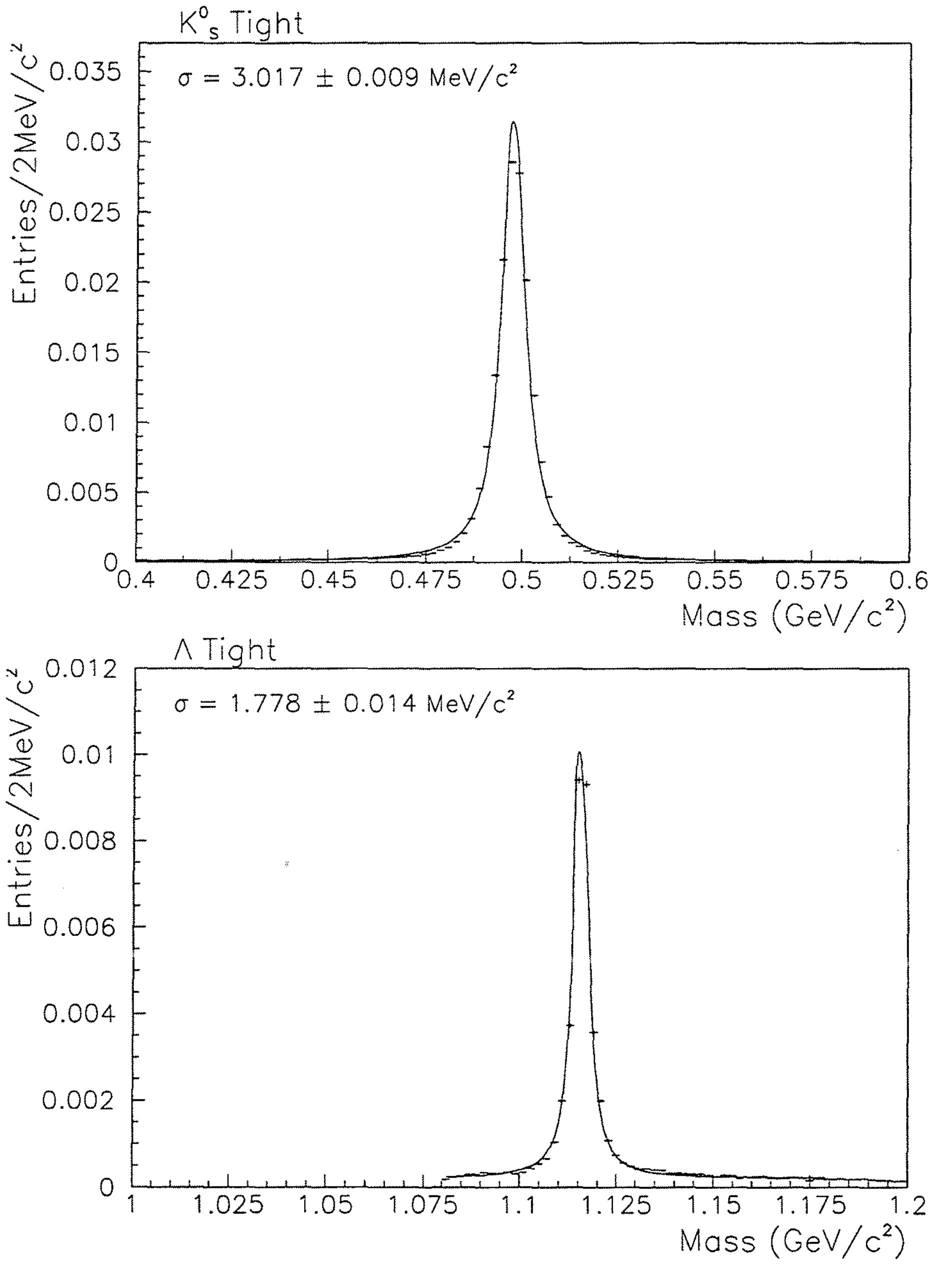

Figure 4.7: Reconstructed invariant mass distributions for K_S^0 and Λ selected as *tight*.

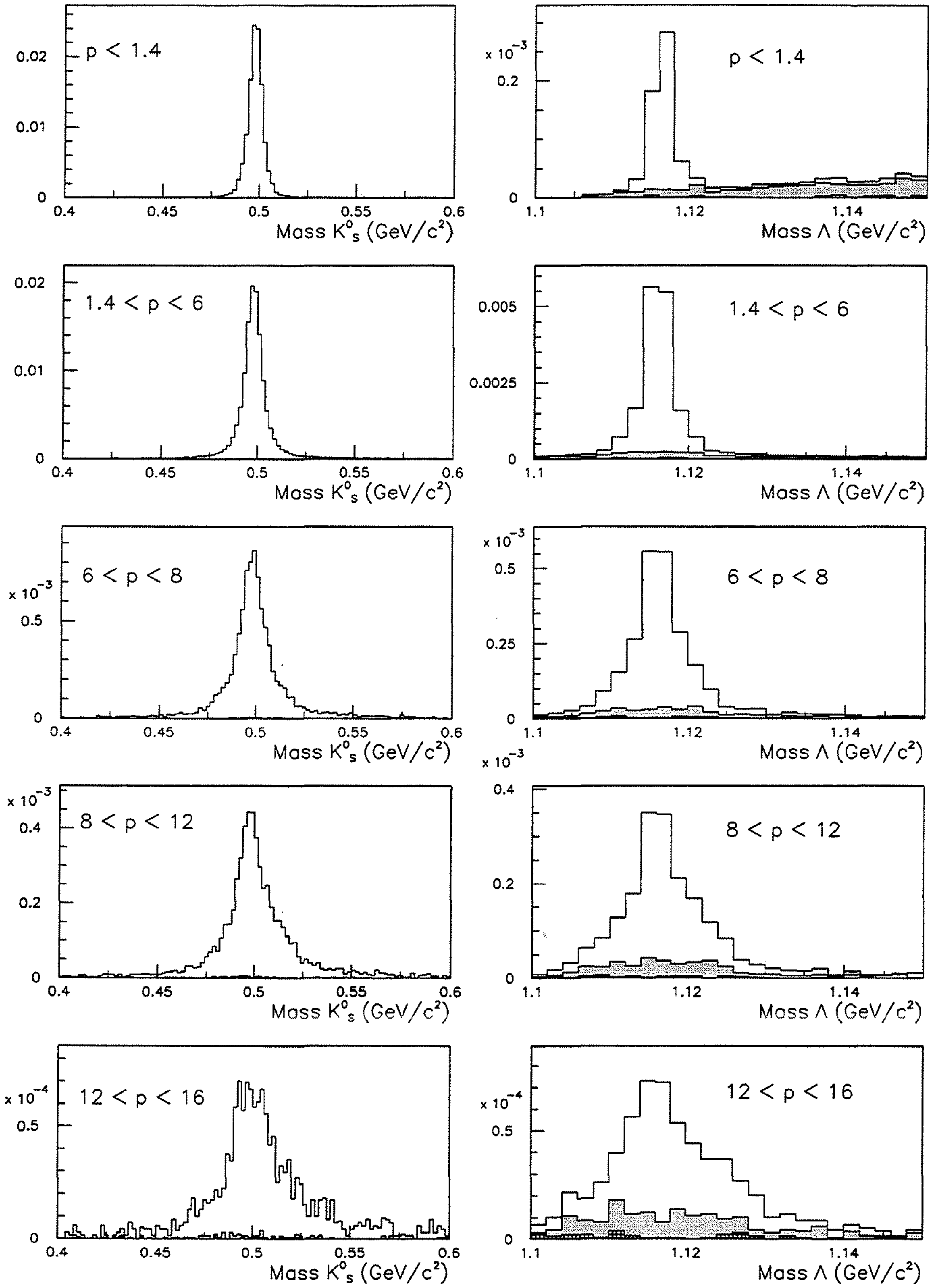

Figure 4.8: Mass distributions and background contributions under the K^0_S (left column) and Λ (right column) selected with the *tight* criteria described in the text. The light-grey histogram (dark) represents the background from misidentified protons (kaons) under the K^0_S, in the case of the Λ the background is given by the misidentified pions (kaons). All histograms were normalized to the total number of hadronic events selected. The momentum windows are indicated in the figures.

background was fitted to the distributions shown in figure 4.8 in order to extract the mass resolution ($\sigma = \Gamma/2.35$).

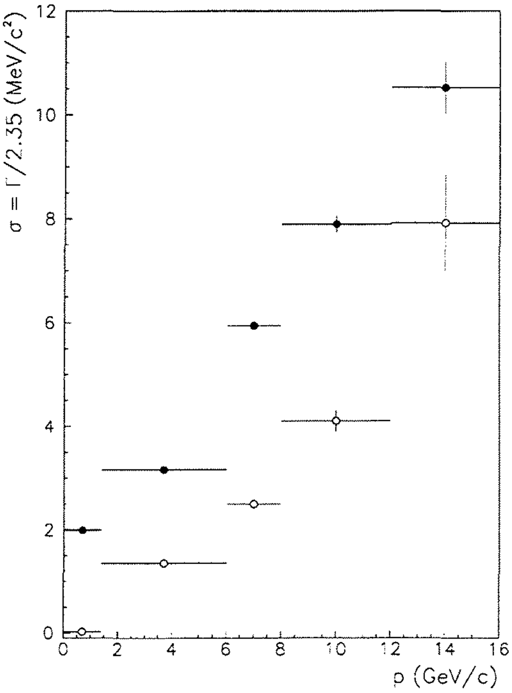

Figure 4.9: Mass resolution of the K^0_S (closed circles) and Λ (open circles), selected as *tight*, as a function of the momentum of the pion and proton, respectively.

In analysis using selected samples of K^0_S and Λ, the contamination under the invariant mass peaks is estimated, separately for each kinematical region, by linear interpolation between two sidebands in invariant mass: the regions between 0.40 and 0.45 GeV/c^2 and between 0.55 and 0.60 GeV/c^2 for the K^0_S, and the regions between 1.08 and 1.10 GeV/c^2 and between 1.14 and 1.18 GeV/c^2 for the Λ. This procedure is justified by the assumption that the background under the mass peaks is reasonably flat (see figure 4.8). In the evaluation of the background it is also estimated and rejected the contribution from the Λ reflections on the selected K^0_S sample and vice-versa.

4.2.1 Efficiency matrix from the data

Data samples of selected K^0_S and Λ were used to cross-check and re-evaluate, using the pions and the protons from their decay, the efficiency matrix previously obtained from simulation for the RICH selections using the NEWTAG package. The kaons were obtained from a selected sample of $\phi \to K^+K^-$.

The selection criteria for the ϕ are described next. All pairs of charged particles were used to built the invariant mass distribution, which was obtained by requiring that at least one of the particles from the decay would be selected with either the *standard* NEWTAG selections for kaons, or with the dE/dX kaon selections, previously described. The particle not tagged (unbiased sample) is used for this study.

In figure 4.10 the mass spectra together with the contamination from misidentified pions and protons, are shown for five different momentum windows ([0.0, 1.4]; [1.4, 6.0]; [6.0, 8.0]; [8.0, 12.0] and [12.0, 16.0]). These distributions were obtained for a sample of events generated with the Monte Carlo program JETSET 7.3 PS, which were passed through the full simulation program of the DELPHI detector (DELSIM [45]).

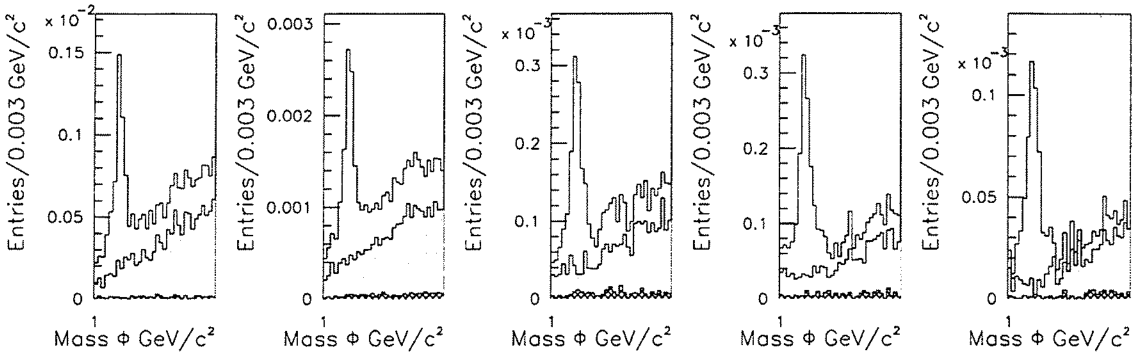

Figure 4.10: Mass distributions and background contributions under the ϕ mass distributions. In the first column are presented the results for kaon momenta below 1.4 GeV/c, the second column for momenta between 1.4 and 6 GeV/c, third column for momenta between 6 and 8 GeV/c, the fourth column between 8 and 12 GeV/c and fifth column between 12 and 16 GeV/c. The dark histogram (light-grey) represents the background from misidentified pions (protons). All histograms were normalized to the total number of hadronic events selected.

The background under the invariant mass peaks is not negligible (figure 4.10), since in the ϕ selections used in this study are not restrictive; only one particle from its decay is obliged to verify the RICH tag selections. This background is estimated by fitting the invariant mass distributions with a Breit-Wigner with a linear background. The (*background regions*) considered for the ϕ are: the regions from 0.99 to 1.00 GeV/c^2 and from 1.03 to 1.06 GeV/c^2.

The efficiency matrix was determined as follows :

$$\varepsilon_{ij} = \frac{N_{ij}^{tag}}{N_j}$$

where ε_{ij} is the efficiency to tag a real particle of type j as i, N_{ij}^{tag} is the number of particles tagged of type i in an environment of real particles of type j and N_j the total number of real particles of type j.

The main problem about estimating N_{ij}^{tag} from the data, using the particles from the decay of the resonances K_S^0, Λ and ϕ, relies on the fact that these resonances are themselves not completely background free. In order to estimate and subtract their background, it was considered, and checked via Monte Carlo, that the background composition under the peak region does not differ from the background composition under the tails of the resonances (*background region*). It was also assumed, that the tagging efficiencies are the same under the *signal* and *background regions*. This last assumption has intrinsic limitations, due to the fact that the efficiency depends on the momentum, and the charged particles from the V^0 decays have different momenta inside different mass regions of the resonances. Via Monte Carlo it was checked that the limitations from this assumption are mainly relevant only for low momenta, and for the case of the Λ and ϕ (figure 4.11). For the Λ there is an additional constraint due to the fact that its reconstruction efficiency is very poor for low momenta [52].

To calculate the efficiency, the number of particles tagged of type i in the V^0 *background region* was determined and normalized to the estimated background under the V^0 *signal region*. This number was then subtracted from the total number of particles tagged of type i in the *signal region*. N_j was estimated, as mentioned before, by subtracting from the *signal region* a background which was estimated by linearly interpolating the two background sidebands considered.

The comparison between the efficiency obtained for data and Monte Carlo, treating the simulation as equal to the real data is shown in figure 4.12. In this figure it is also shown the efficiency obtained from a pure sample of real pions, protons and kaons from the Monte Carlo.

The results for real protons were estimated only for momenta above 1 GeV/c, since the proton is taken as the highest momentum particle from the Λ decay, and this assumption limits it is momentum distribution towards low values (below $\sim$ 1 GeV/c). Moreover, the Λ reconstruction efficiency is very poor for low momenta. There is a 5% discrepancy between data and Monte Carlo for the efficiency obtained from the V^0 sample, which is observed for the higher statistics sample of pions. The Monte Carlo results on the kaon contamination on a pure sample of real pions and protons also does not reproduce well the contamination obtained using the V^0 sample. In the low momentum region there is a discrepancy between data (and simulation treated as the real data) and Monte Carlo, for the pion contamination in kaons. As mentioned before, this results from the fact that in the efficiency calculations from the data, the tagging efficiencies are assumed to be the same under the *signal* and *background regions*. This assumption however leads to an overestimation of the efficiency at low momentum for kaons from ϕ decays (see figure 4.11).

The dE/dX and Čerenkov angle distributions for the selected pion ($K^0_S \to \pi^+\pi^-$), proton ($\Lambda \to p\pi^-$) and kaon ($\phi \to K^+K^-$) candidates is shown in figure 4.13. In order to further reduce the background from misidentified kaons from ϕ, in the figure the kaon candidates were selected for invariant masses of the resonance within the restricted interval $[1.018, 1.022]$. To obtain the gas Čerenkov angle distributions also kaons from D^0 decays ($D^0 \to K\pi$) were used.

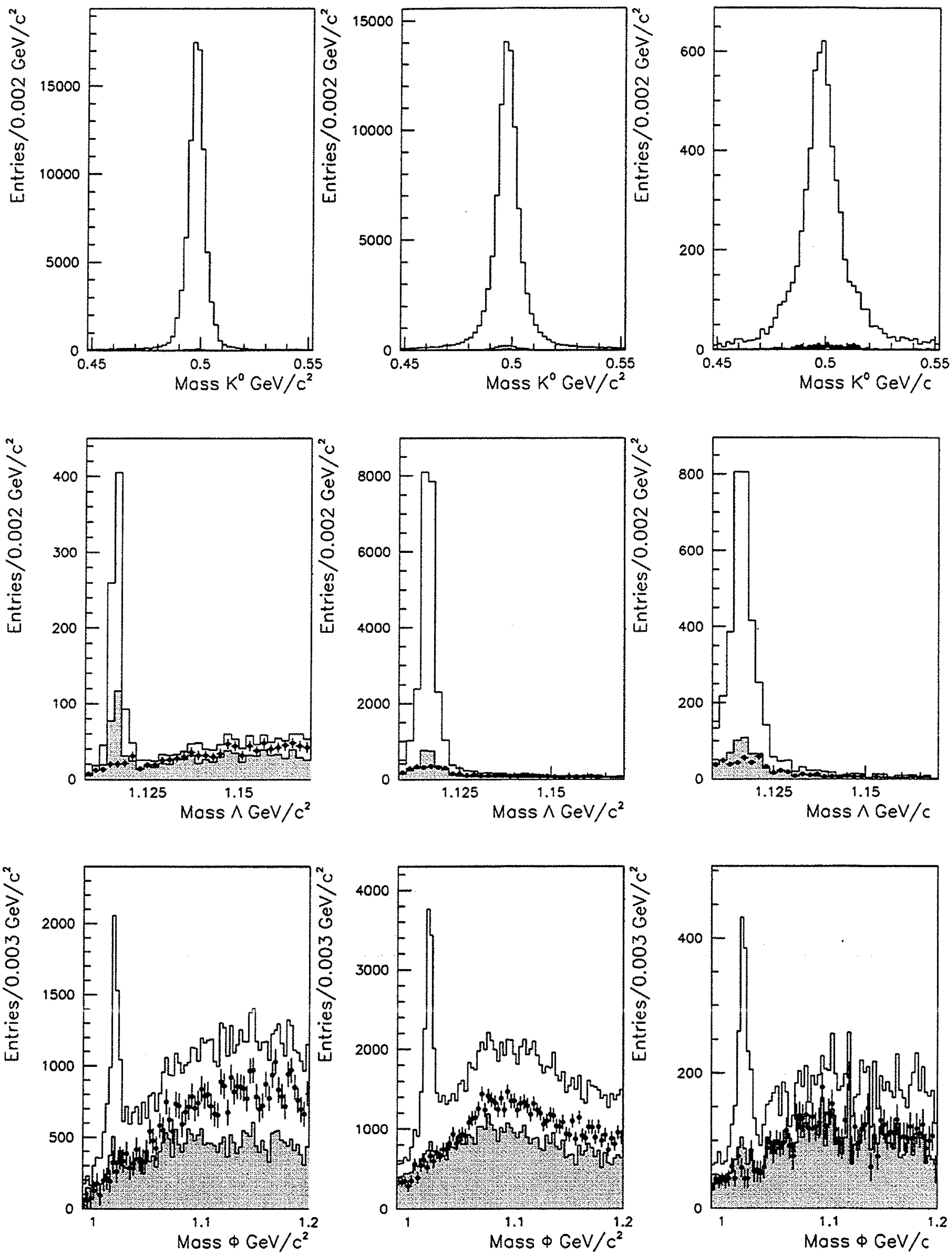

Figure 4.11: Mass distributions for K_S^0, Λ, and ϕ (solid lines). The grey histograms (points) represent the same mass distributions as before, for the case in which the pion under the K_S^0 is tagged as a proton (is a real proton), the proton under the Λ is tagged as a pion (is a real pion) and the kaon under the ϕ is tagged as a pion (is a real pion). The histograms on the left side represent the results for particle (pion, proton and kaon) momenta below 1.4 GeV/c, the histograms in the middle concern the momentum region from 1.4 to 6 GeV/c and the right side histograms were obtained for particle momenta between 6 to 8 GeV/c.

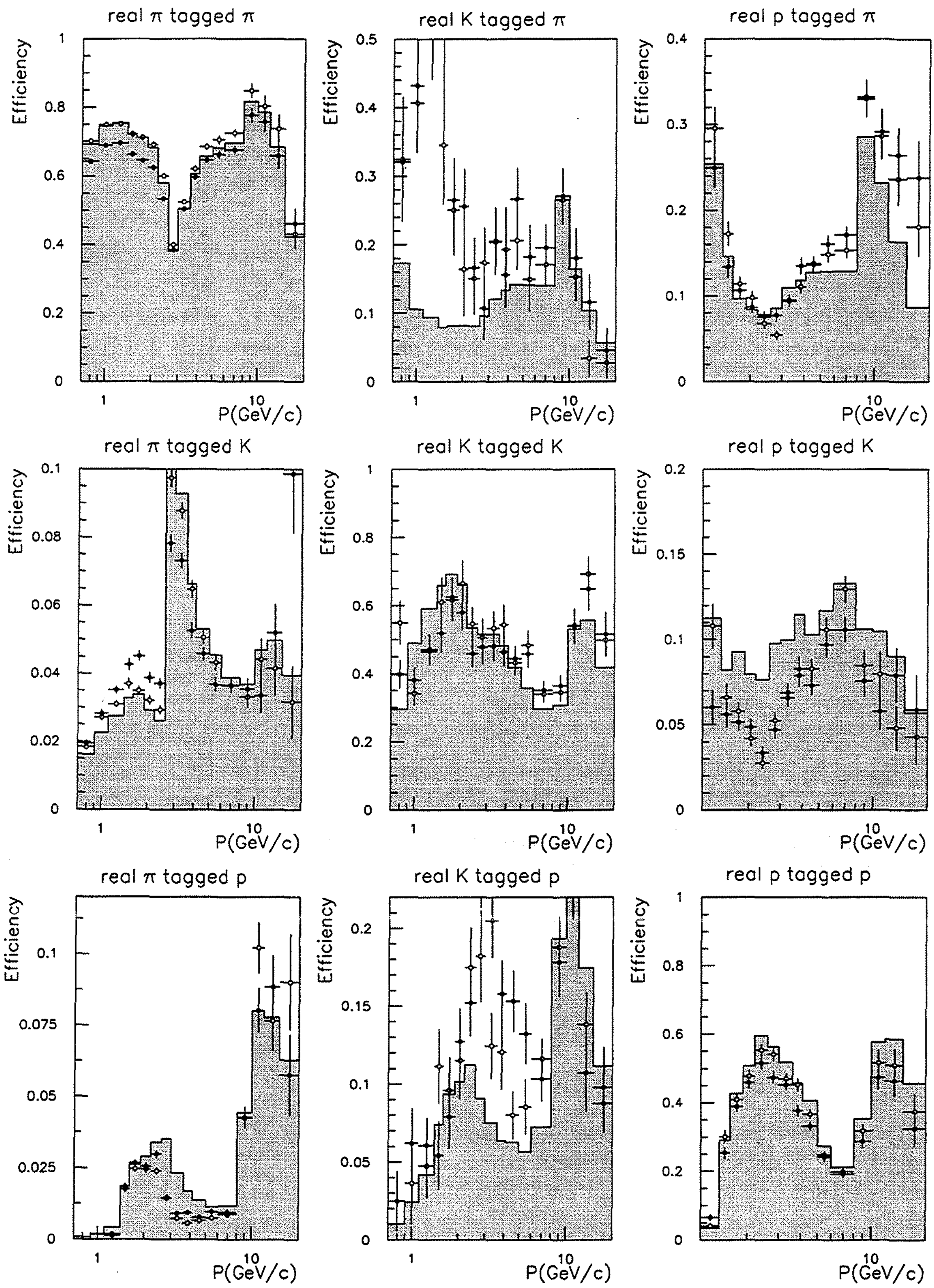

Figure 4.12: Efficiency matrix for the π, p and K selected from K_S^0, Λ, and ϕ, respectively. The black circles represent the results for the data, the open circles for Monte Carlo. The full line represents the efficiency obtained from a normal sample of pions, protons and kaons from the Monte Carlo.

The D^0 was selected through the decay $D^* \to D^0\pi$. All oppositely charged particles were considered for the reconstruction of the D^0 candidate invariant mass. For each combination both the pion and kaon mass hypothesis were tested and the right combination considered as the one for which the reconstructed D^0 mass was between 1.54 and 2.14 GeV$/c^2$. The particles were fitted to a common vertex and the D^0 flight distance was required to be between -0.5 and 2.5 cm. The D^0 was afterwards attached to the slow pion candidate. This was required to have a momentum from 0.3 to 4.5 GeV$/c$ and the mass difference between the D^0 and D^* candidates for a given slow pion hypothesis should be lower than 0.18 GeV$/c^2$. In figure 4.13 the kaon candidates displayed for the gas RICH Čerenkov angle distributions were selected for D^0 candidates in the mass range from 1.74 to 1.94 GeV$/c^2$, and for a mass difference between the D^* and D^0 candidates in the interval $[0.143, 0.149]$.

In figure 4.14 results are presented on the dE/dX and Čerenkov angle distributions for selected pions, kaons and protons from a simulation sample (JETSET 7.3 PS). From the comparison between figures 4.13 and figure 4.14 it is seen that the distributions obtained from the data and from the Monte Carlo are in good agreement. The low momentum region is constrained in the data (seen in the dE/dX distributions) due to the several quality and selection cuts applied to the particles K^0_S, Λ and ϕ, described previously.

4.3 b-Tagging

Particles containing bottom quarks have lifetimes of the order of $\sim 10^{-12}$ seconds, it is thus possible to use their finite decay length as a tagging mechanism. To achieve this goal it is necessary to identify both the position in space of the primary Z^0 decay vertex and the decay position of the heavy quark with high accuracy. As these two points are not possible to instrument (this region is inside the vacuum pipe of the storage ring), they must be deduced indirectly from very accurate measurements made as near as possible to the interaction region. This is achieved with the vertex detector. As an example it is shown in figure 4.15 a candidate $Z^0 \to b\bar{b}b\bar{b}$ seen by DELPHI, together with the result after fitting the decay vertices of the B hadrons produced.

4.3.1 Primary vertex fit

The primary vertex is reconstructed for every hadronic event, using the beamspot position (interaction region of the electron and positron beams) as a constraint.

To follow possible fluctuations, the beamspot position is determined for every 200 hadronic events collected. A common vertex is fitted, using tracks with at least 2 hits in the vertex detector, and the horizontal (x) and vertical (y) position of the beam and its horizontal width are determined. The x and y positions are

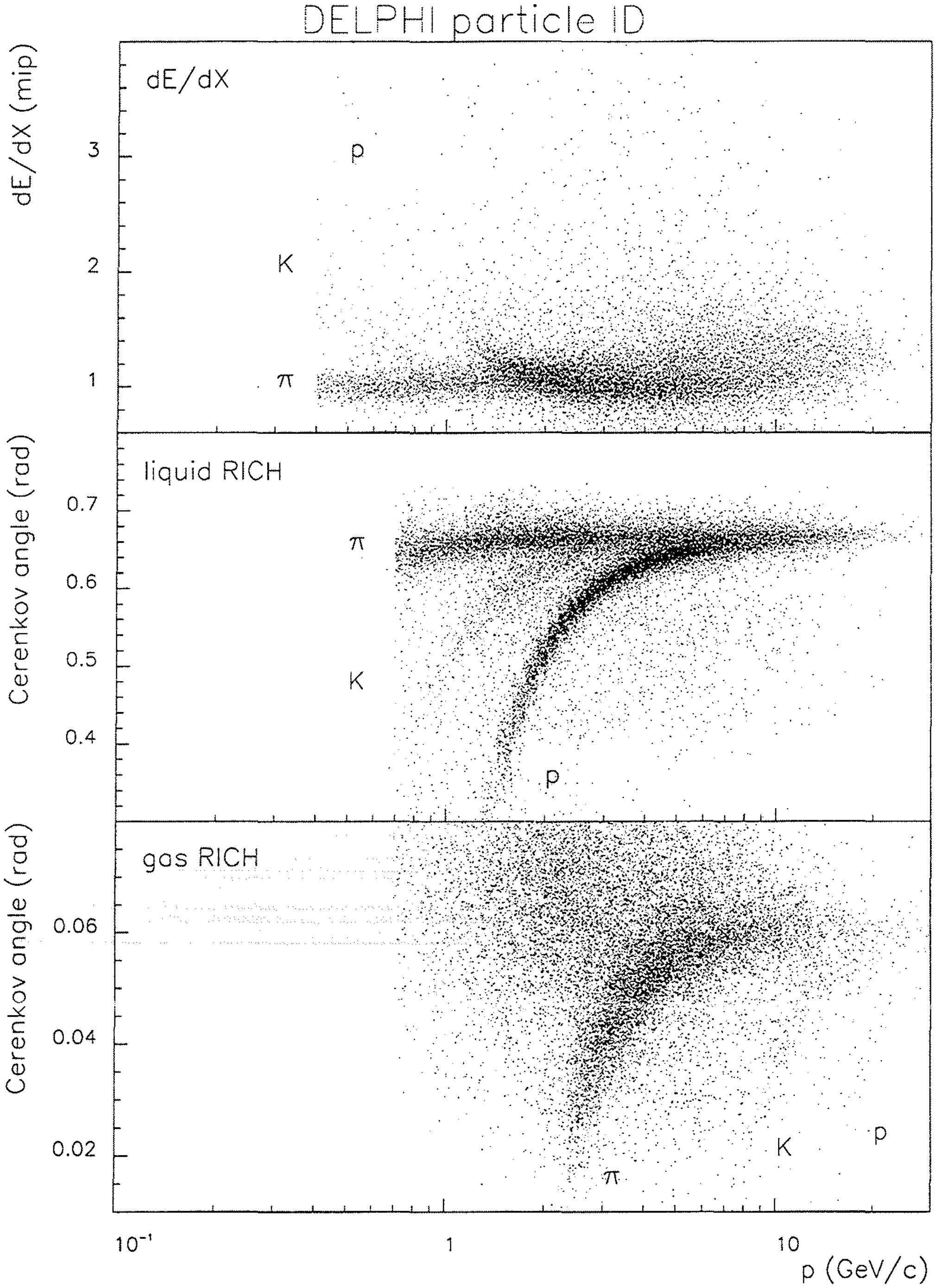

Figure 4.13: Specific energy loss dE/dX in the TPC as a function of the momentum (uppermost plot) and Čerenkov angle per track as a function of the momentum in the Barrel RICH, for the liquid (middle plot) and gas (lowest plot) radiators. The three bands on both RICH plots correspond to pions (uppermost), kaons (middle band) and protons (lowest band). These results were obtained from the data (see text).

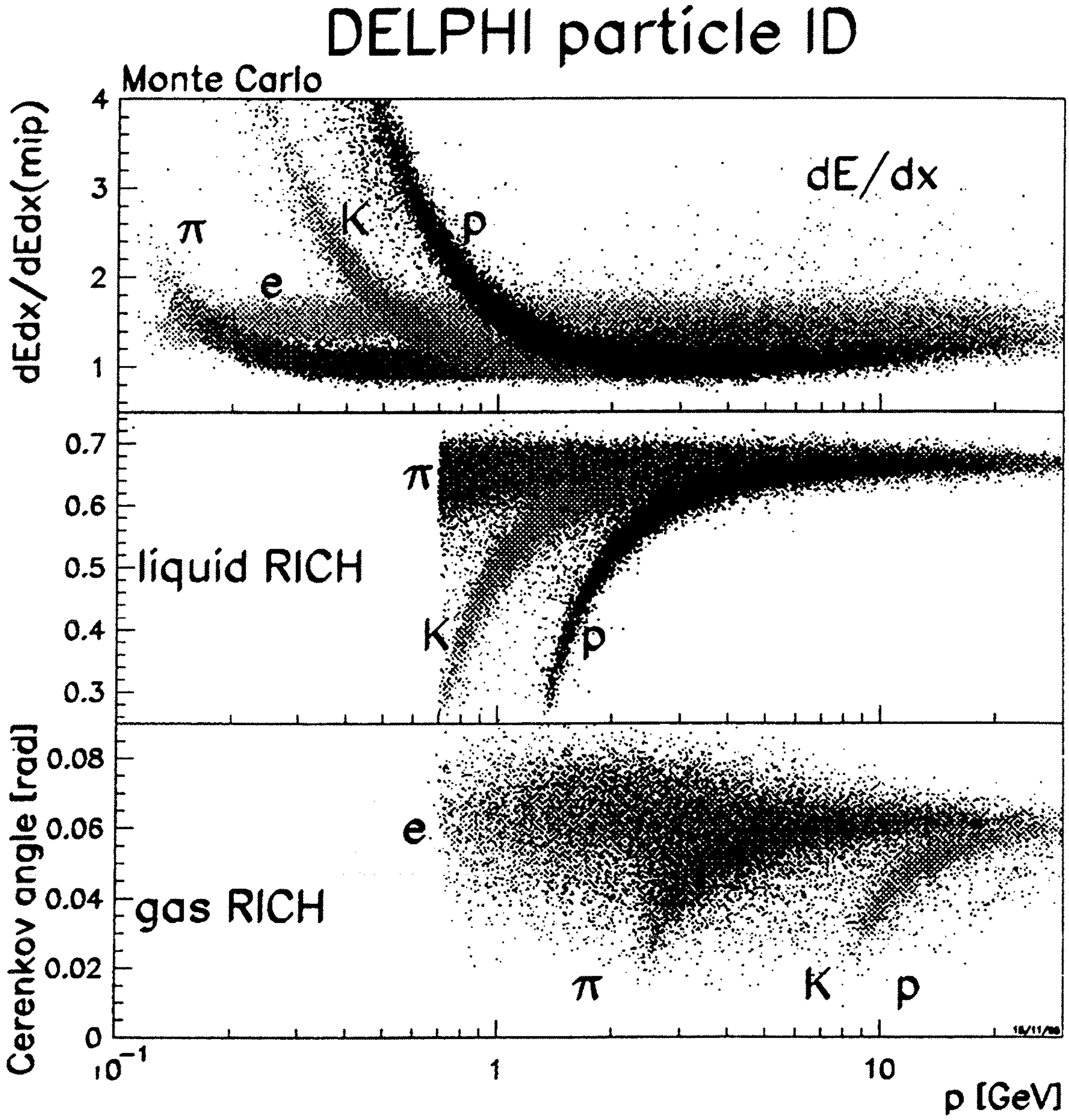

Figure 4.14: Specific energy loss dE/dX in the TPC as a function of the momentum (uppermost plot) and Čerenkov angle per track as a function of the momentum in the Barrel RICH, for the liquid (middle plot) and gas (lowest plot) radiators. The three bands on both RICH plots correspond to pions (uppermost), kaons (middle band) and protons (lowest band). These results were obtained from the simulation (see text).

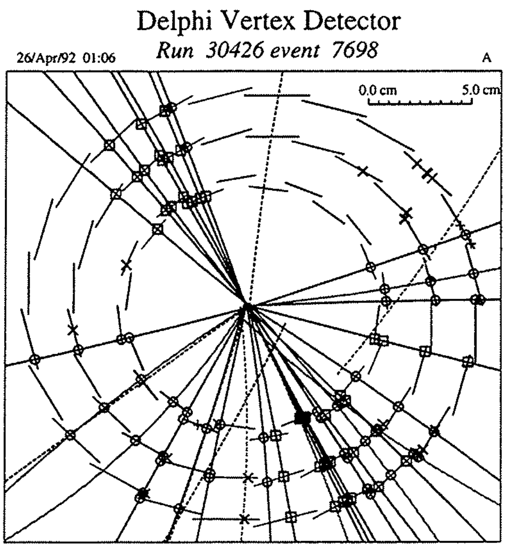

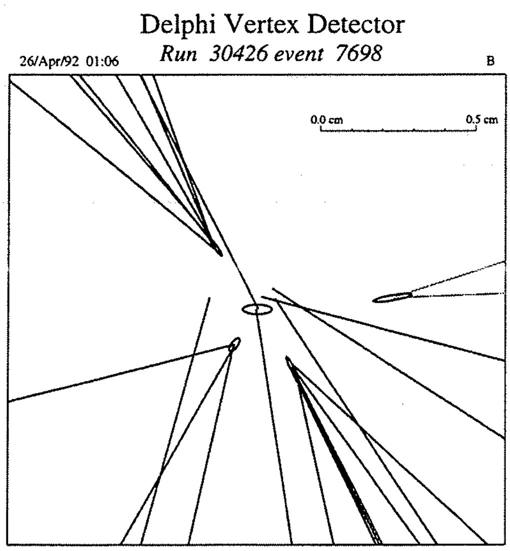

Figure 4.15: In the upper display is shown an event $Z^0 \to b\bar{b}b\bar{b}$ with the tracks measured by the microvertex detector. In the lower display are indicated the adjusted vertices.

determined with typical uncertainties of about 9 μm and 4 μm respectively. The width along the x coordinate varies with time but a typical value is 100 to 120 μm with an error of 7 μm.

Only tracks with 2 to 3 hits in the vertex detector, and which fulfill the condition $\frac{\sum(d_i^2/\sigma_{VD}^2)}{N_{VD}} \leq 4$, are used to determine the primary vertex. The sum is over all the N_{VD} hits in the vertex detector associated to the track, d_i is the distance of closest approach of the track to the VD hit and σ_{VD} is the accuracy of the VD hits. In addition, tracks should be close to the beamspot in terms of δ/σ, where δ is the distance from the track to the beamspot and σ is the corresponding error, including the track error and the beamspot size (the confidence level computed for a given δ/σ is required to be greater than 0.05).

Using these tracks, and the above definition of beamspot, the primary vertex position is determined by minimizing the χ^2 function given by:

$$\chi^2(V_i) = \sum_a \frac{\overline{d_a^2}}{\sigma_a^2} + \sum_{i=x,y,z} \frac{(b_i - V_i)^2}{(\sigma_i^b)^2} \tag{4.9}$$

where $\overline{d_a}$ is the distance of the track a to the fitted vertex, σ_a the corresponding error, V_i is the coordinate of the primary vertex and b_i, σ_i^b are the beamspot position and size. The fit is done iteratively, excluding after every iteration the track giving the largest difference $\chi^2(N_{tr}) - \chi^2(N_{tr} - 1)$ if it exceeds a cutoff value Δ_{max}. The beamspot is used as the starting reference point. If all tracks are rejected from the fit (which happens in about 1% of the cases), then the beamspot centre is taken as the primary vertex. In figure 4.16 is shown the difference between the reconstructed and generated vertex position in a simulated event sample [45].

The width of the distributions is about 22 μm in the x and z directions for light quark events and 35 μm for b quark events. The distributions for b quark events show non-Gaussian tails due to the inclusion of tracks coming from secondary vertices.

The impact parameter can be obtained from the above information. In the $R\phi$ plane it is defined as the distance of closest approach of a charged particle track to the reconstructed primary vertex. In the z direction, it is defined as the difference between the z coordinate of the primary vertex and the z coordinate of the point used to calculate the impact parameter in $R\phi$. Its sign is defined with respect to the jet direction, it is positive if the vector joining the primary vertex to the point of closest approach of the track is less than 90° from the direction of the jet to which the track belongs.

The impact parameter error is due to the track extrapolation error on the point of closest approach and the error on the primary vertex; consequently it depends on the beamspot size. After subtracting the vertex position uncertainty in quadrature, the extrapolation errors in the $R\phi$ and Rz planes can be parameterized as:

$$\sigma_{R\phi} = \left(\frac{\alpha_{MS}}{p sin^{3/2}\theta}\right) + (\sigma_{0,R\phi})^2$$
$$\sigma_{Rz} = \left(\frac{\alpha'_{MS}}{p sin^{5/2}\theta}\right) + (\sigma_{0,Rz})^2$$

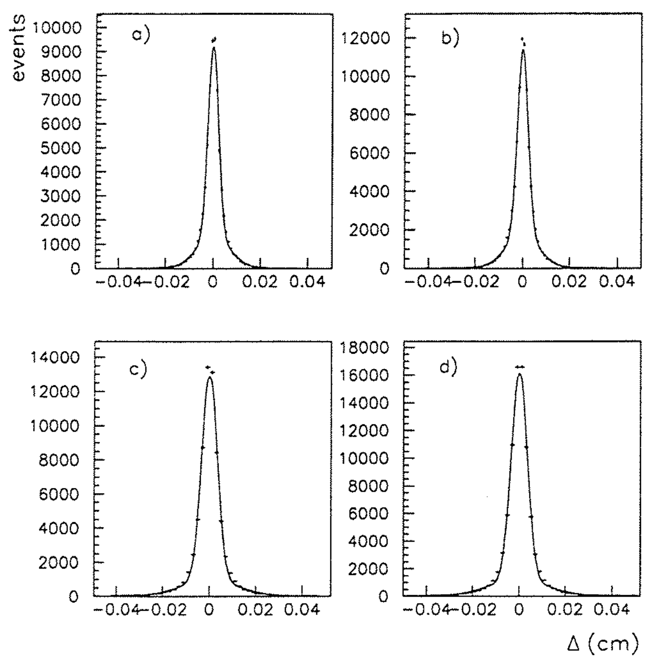

Figure 4.16: Difference between the reconstructed and generated vertex position in a simulated event sample for (a) x-coordinate for light quarks, (c) x-coordinate for b quarks, (b) z-coordinate for light quarks and (d) z-coordinate for b quarks. The full lines show a fit to the data with the sum of two Gaussians.

where α_{MS} (α'_{MS}) is a multiple scattering coefficient (in μmGeV/c) and p is the track momentum. In both expressions, the first term is the multiple scattering contribution and the second is due to the measurement error. Using a sample enriched in light quark events, the above coefficients were estimated [45]: $\alpha_{MS} =$ 65 μmGeV/c and $\sigma_{0,R\phi} = 20$ μm. The extrapolation error in the Rz plane depends strongly on the polar angle of the track [45], therefore σ_{Rz} was estimated separately for $80° < \theta < 90°$ and $45° < \theta < 55°$, $\sigma_{Rz} = (71/p \oplus 39)\mu$m and $\sigma_{Rz} = (151/p \oplus 96)\mu$m, respectively.

4.3.2 Secondary vertex fit

Hadrons containing b quarks have long lifetimes and large masses, therefore they have many decay products with large impact parameters. This feature can be used to separate between events with produced b quarks from other hadronic events. An alternative method uses the identification of B hadron semileptonic decays. Here the leptons' transverse momentum signature is used to identify and select B hadrons. This last method however, is less pure than the first referred, moreover it is limited by lower statistics (the decay rate of B hadrons into semileptonic modes is only 20%). In the present studies only the impact parameter technique is used.

The tracks are initially selected as for the vertex fit (see section 4.3.1) and only those with positive impact parameter are used. The reason being the fact that the tracks from the decay of B hadrons should have positive impact parameter, as defined in section 4.3.1, whereas non-zero impact parameters arising from inaccurate track reconstruction, should be equally likely to be positive or negative (the tracks with negative impact parameter are used as a control sample to determine the experimental resolution).

A probability function $P(S_i)$, representing the probability for a track from the primary interaction to have a significance S_i or greater, is built for each track (i). The significance is defined by:

$$S = \frac{IP}{\sigma_{IP}} \tag{4.10}$$

where IP is the value of the tracks' impact parameter and σ_{IP} the corresponding error. Tracks coming from a secondary vertex have low values of $P(S_i)$, whereas tracks from the primary vertex have high $P(S_i)$.

Using the track probability function, a global variable is constructed, combining the individual track probabilities. For events with N tracks this combined probability (the N-track probability) is defined as:

$$P_N = \coprod \times \sum_{j=0}^{N-1} \left(-\log \coprod\right)^j / j! \ , \ \textit{where} \ \coprod \equiv \prod_{i=1}^{N} P(S_i) \tag{4.11}$$

This variable gives the probability for a group of N tracks with the observed values of significance all to come from the primary vertex. By construction, the distribution of P_N should be flat for groups of tracks from the primary vertex, while for b-quarks it should have a sharp peak at 0 (reflecting the presence of secondary vertices).

The event probability, P_E, is defined as P_N but using all the tracks in the event. Similarly, the hemisphere (P_H) and jet (P_j) probabilities are the probabilities computed from the tracks belonging to a given hemisphere and jet, respectively. In figure 4.17 the event and jet probabilities are displayed, for a sample of simulated $b\bar{b}$, $c\bar{c}$ and light-quark (uds) events. The distributions for b quarks show a clear peak for low values of P_E and P_j. In the case of c quarks, there exists as well an accumulation of events at low probability values (reflecting the presence of secondary vertices from charmed particles' decays), although this is one order of magnitude lower than the accumulation of events observed for b quarks. For uds type events, the distribution is fairly flat. To select b quarks a cut is used on the probability value (in the present analysis on both P_E and P_j).

The efficiency as a function of the purity is shown for the event and hemisphere probabilities in figure 4.18.

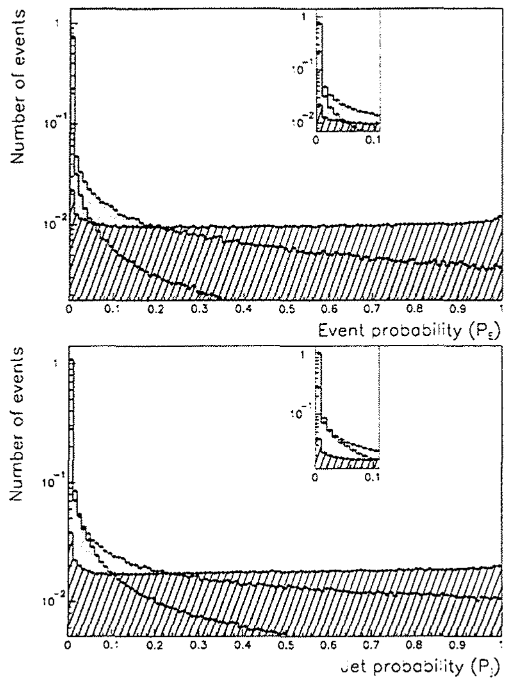

Figure 4.17: P_E (upper) and P_j (lower) distributions for b (white histogram), c (light-grey histogram) and uds (hatch histogram) quarks in two jet events. Each distribution is normalized to the respective number of two jet events.

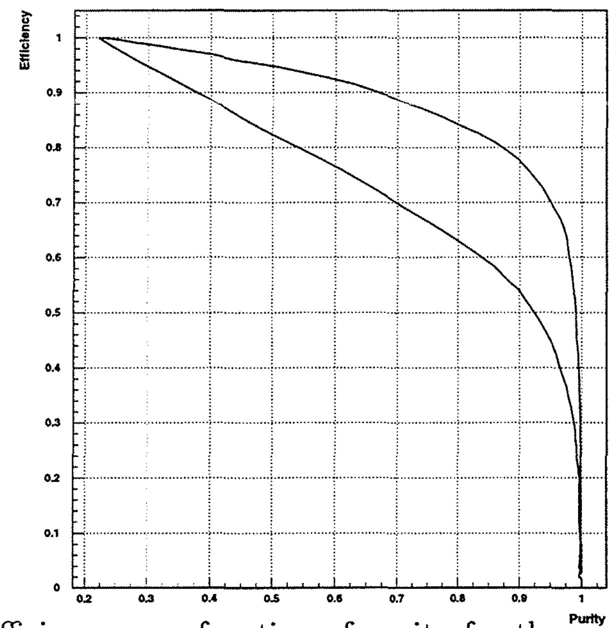

Figure 4.18: Efficiency as a function of purity for the event (upper curve) and hemisphere probabilities (lower curve).

Chapter 5

Analysis

A measurement of the composition of the hadronic final states in e^+e^- annihilation is fundamental to an understanding of the fragmentation of quarks and gluons into hadrons. While no calculable theory yet exists to describe this process, a number of phenomenological models have evolved, falling, as mentioned in section 2.3, in the two main broad classes: *string fragmentation* and *cluster fragmentation*, as exemplified by the JETSET and HERWIG Monte Carlo programs, respectively.

In the present work several measurements related to the production rates, momentum distributions and KNO scaling of protons, kaons, K^0_S and Λ in jets from hadronic decays of the Z^0 will be presented. The multiplicity of identified particles at the Z^0 and at higher energies (up to 183 GeV) have also been measured. The criteria applied to the data in order to select hadronic events at the various center of mass energies (91 GeV, 130 GeV, 136 GeV, 140 GeV, 161 GeV, 172 GeV and 183 GeV); the selection of quark and gluon jet samples and the particle identification selections will be described in the present chapter. In section 5.1 these selections will be specified for the analysis at 91 GeV and in section 5.2 for the analysis at energies above the Z^0 peak.

5.1 Event selections - LEP I

In this section the general framework of the analysis will be described, including the selection of hadronic events, jet and particle selections.

5.1.1 Hadronic event selections

A sample of hadronic events was selected by demanding:

- a multiplicity of particles (with $p > 100$ MeV/c, $20° < \theta < 160°$, a track length of at least 30 cm in the TPC and consistent with coming from the interaction vertex) larger than four. p is the particle's momentum and θ the polar angle with respect to the beam axis,

- a total charged energy ($E_{ch} = \sum_i E_i = \sum_i \sqrt{p_i^2 + m_\pi^2}$) greater than $0.12 \times E_{cm}$, where E_{cm} is the center of mass energy and m_π the pion mass.

The distribution of multiplicity and visible energy, for the events fulfilling the above selection criteria is presented in figure 5.1.

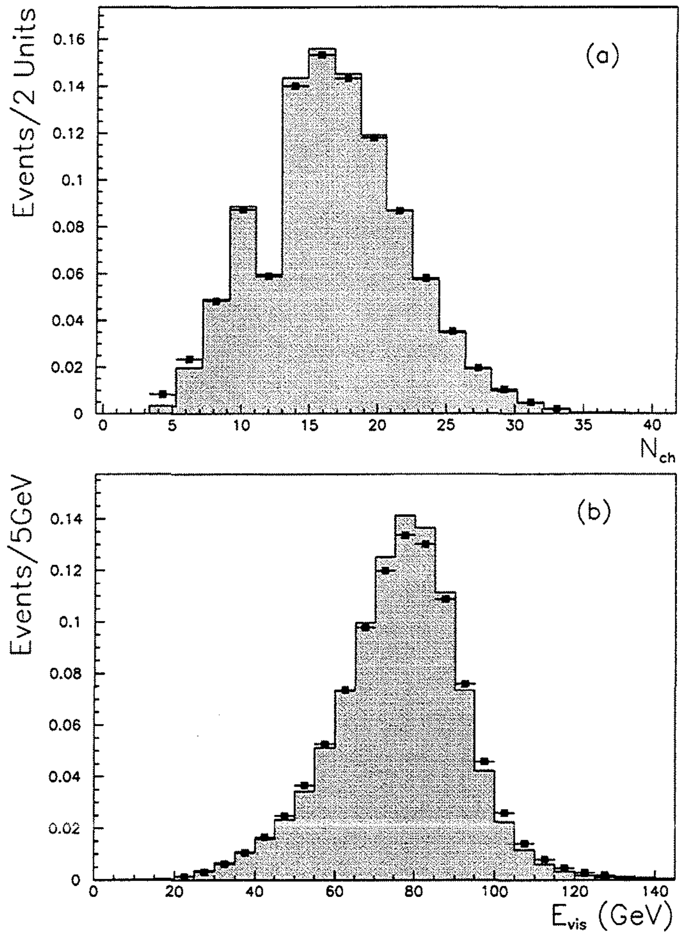

Figure 5.1: Multiplicity (a) and visible energy (b) distributions. The grey histogram represents the Monte Carlo results, and the data is represented by the closed squares. Data and Monte Carlo were normalized to the number of hadronic events (events passing the cuts mentioned in the text).

The selection efficiency is of the order of 95 % for hadronic Z^0 decays. For the data taken by the DELPHI detector in 1994[1] these cuts result in 1418260 selected events.

[1]At the Z^0 peak only the data collected during 1994 was used in this analysis, to profit from the full operation of the main particle identification detector of DELPHI (RICH [45]).

The largest background contribution is from events of the type $e^+e^- \to \tau^+\tau^-$ (beam-gas scattering and $\gamma\gamma$ interactions contribute with a smaller amount to the total background [45]), which are estimated to make up at most ~ 0.7 % of the selected events. This background can be safely neglected in the analysis reported below.

The influence of the detector in the several steps of the analysis was studied with the full DELPHI simulation program, DELSIM [45]. Events were generated with the JETSET 7.3 PS Monte Carlo program (see section 2.3.5) with parameters tuned by DELPHI [53]. The particles were followed through the detailed geometry of DELPHI giving simulated digitizations in each detector. These data were processed with the same reconstruction and analysis programs as the real data. Simulations based on JETSET 7.4 PS Monte Carlo with default parameters and HERWIG 5.8 with parameters tuned by DELPHI [53] were also used throughout the analysis reported below.

5.1.2 Three-jet event selections

Particle clustering into jets was performed by means of the Durham jet reconstruction algorithm (see section 2.2.3.1). The jet resolution parameter, y_{cut}, was optimized by maximizing the statistics available and the purity attained in the three-jet event sample.

In figure 5.2 the measured jet rates as a function of y_{cut} are shown. The results were obtained from events generated with the Monte Carlo program JETSET 7.3 Parton Shower (PS), which were afterwards passed through the full detector simulation program of the DELPHI detector (DELSIM [45]).

In the present work, $y_{cut} = 0.015$ was used. The number of 3-jet events selected in the data was 360216.

In order to compare jets initiated by different partons (quarks and gluons) in an identical environment, events are selected in which the gluon and at least one quark jet have the same energy. Two types of 3-jet events with different geometries were used:

- Y events, two-fold symmetrical events with each of the two angles θ_2 and θ_3 in figure 5.3 in the interval between 135° and 165°. The polar angle of the jets was required to be between 30° and 150° (this cut ensures that the event is well contained within the barrel region of the DELPHI detector). The condition of planarity $\theta_1+\theta_2+\theta_3 \geq 355°$, and the condition $|\theta_2-\theta_3| \leq 15°$ (to limit the energy difference between jet 2 and jet 3, in order to allow a direct comparison between them) were required in addition. Only the symmetric jets (jets 2 and 3 in figure 5.3) were used in the analysis. Jet 1 in figure 5.3 has a high probability of originating from a quark or anti-quark. The Monte Carlo estimate is that in only 3% of the events is jet 1 a gluon jet.

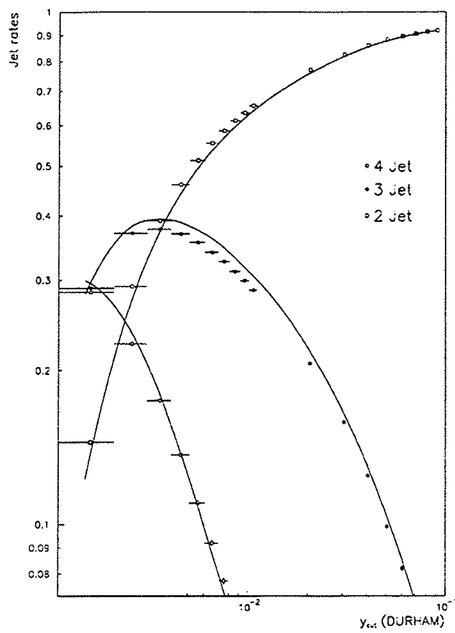

Figure 5.2: Measured jet rates as a function of y_{cut}. The points represent the data and the lines the Monte Carlo simulation.

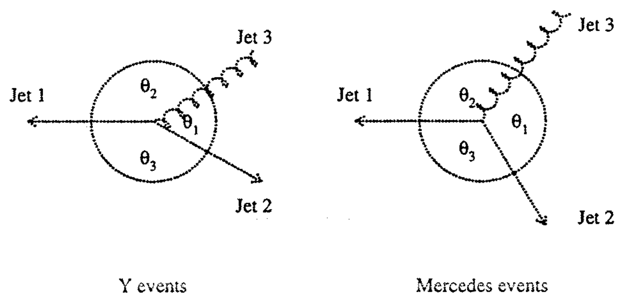

Figure 5.3: Geometry of Y and Mercedes type events.

- Mercedes events, three-fold symmetrical events with each of the three angles θ_1, θ_2 and θ_3 in figure 5.3 in the interval between 100° and 140°. The polar angle of the jets was required to be between 30° and 150°. The condition of planarity $\theta_1 + \theta_2 + \theta_3 \geq 355°$ was required in addition. All jets were used in the analysis.

The advantage of Mercedes and Y events (discarding the cases in which the gluon jet is the most isolated: jet 1 in figure 5.3 left) is that the gluon and at least one quark jet are symmetrical, thus removing phase space effects. The disadvantage is a severe limitation of the statistics and of the parton energies spanned. The number of 3-jet events selected in the Mercedes and Y samples was 10008 and 59296 respectively.

To each of the jets a calculated energy was assigned as derived from the jet directions and the angles between them. Assuming massless kinematics, the jet energy can be expressed as:

$$p_j^{calc} = E_j^{calc} = \frac{sin\theta_j}{sin\theta_1 + sin\theta_2 + sin\theta_3}\sqrt{s}, \quad j = 1,2,3 \tag{5.1}$$

where θ_j is the inter-jet angle as defined in figure 5.3. This expression corrects for the energy shift towards low values due to particle loss.

In figure 5.4 the calculated energy distribution of the jets in the Y and Mercedes configurations is shown for the data and the simulation.

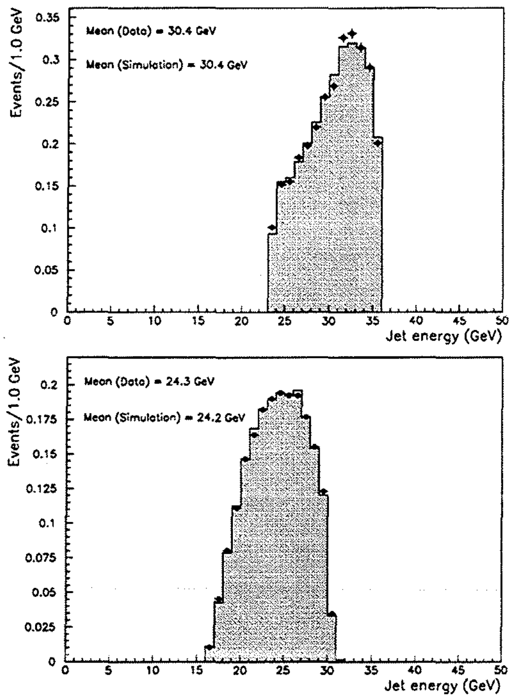

Figure 5.4: Energy distribution of the three jets in events selected as "Mercedes" (upper plot), and of the two lowest energy jets in events selected as "Y" (lower plot). The points represent the data and the full line the simulation (JETSET 7.3 PS). The distributions were normalized to the number of events selected in each topology.

5.1.3 Selection of gluon and b jets

Less than 1% of the gluon jets are expected to contain particles originating from the fragmentation of b quarks [54]. Gluon jets can thus be collected from a sample of reconstructed bbg three-jet events, by directly identifying the two quark jets as originating from b quarks. The identification of b-jets is achieved by means of the b tagging as described in section 4.3.2.

The selection was performed in two stages. In the first stage bbg events were selected via a cut on the event probability, P_E (section 4.3.2). The events were tagged as bbg if P_E was lower than a certain cutoff. The value choose for the cut was estimated according to criteria based on the compromise between a good efficiency and a good purity of the selected sample.

In figure 5.5 the efficiency and purity as a function of the cutoff on P_E, for selected events in the Y and Mercedes topologies, are shown.

The purity and efficiency calculations were performed using events generated with JETSET 7.3 PS Monte Carlo, which were passed through the full simulation program of the DELPHI detector. In order to assign the reconstructed jets to the generated jets, the partons were clustered in three jets and reconstructed jets were associated to the parton jet closest in angle.

In order to select bbg events it was required, in the present work, P_E to be smaller than 2×10^{-2}. The efficiency (purity) attained in the Mercedes and Y topologies was 78% (70%) and 79% (73%) respectively (see figure 5.5).

In the second stage, a cut on the jet probability, P_j (see section 4.3.2), is applied in order to tag b and gluon jets in the events selected in the first stage. The events are tagged as bbg if two of the jets have P_j lower than a certain cutoff value (the b jets) and the remaining jet has P_j higher than a certain cutoff value (the gluon jet).

In figure 5.6 and figure 5.7 the jet purity and efficiency as a function of the cutoff value on P_j are shown for the events already preselected using the cutoff: $P_E < 2 \times 10^{-2}$.

In the sample of Mercedes events, the gluon jet was selected as the jet with largest P_j, provided it was greater than 0.1, and that the two other possible candidates verify $P_j \leq 0.1$. In Y events, a candidate gluon jet was selected as the jet with largest P_j, provided it was greater than 0.1. If this is the most isolated (jet 1 in figure 5.3 left), the event is discarded. It was required in addition that the nearest jet had $P_j \leq 0.1$.

After b tagging, the number of 3-jet events in the Mercedes and Y samples was equal to 1265 and 8072, respectively.

The average energy and RMS spread of the jets selected as b and gluon, are shown in table 5.1 for both the Mercedes and Y events.

With these selections, three classes of jets were considered in the analysis:

- A g-enriched class, including the gluon candidates selected as described in the previous paragraph.

- A b-enriched class. This was constructed from the two jets not selected for the g-enriched class in the Mercedes sample, and from the non-gluon jet among jet 2 and jet 3 in the Y sample.

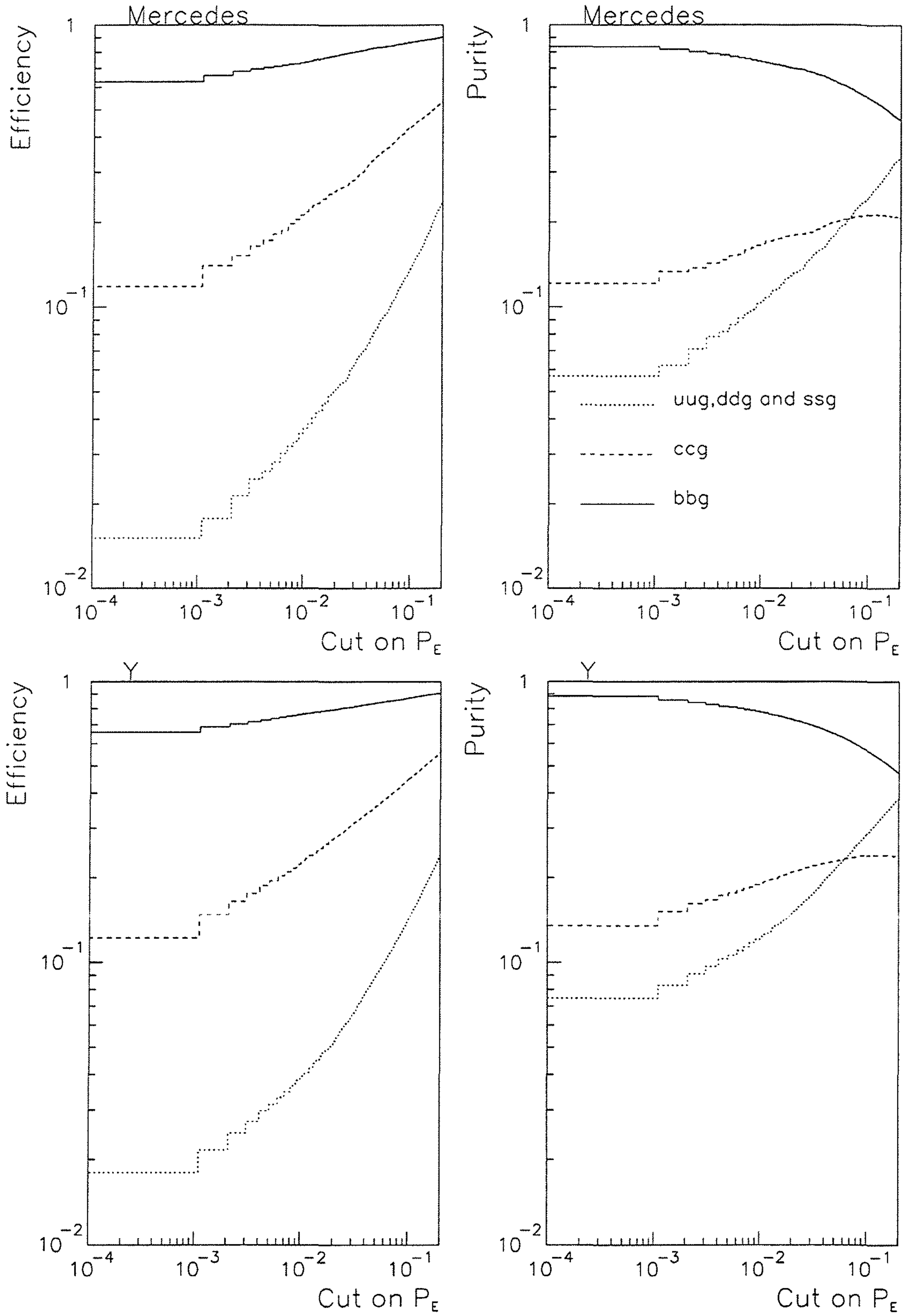

Figure 5.5: Efficiency and purity of the $q\bar{q}g$ events selected with $P_E < cutoff$ as a function of the cutoff. The upper plots represent the results for Mercedes events, the lower plots for Y events.

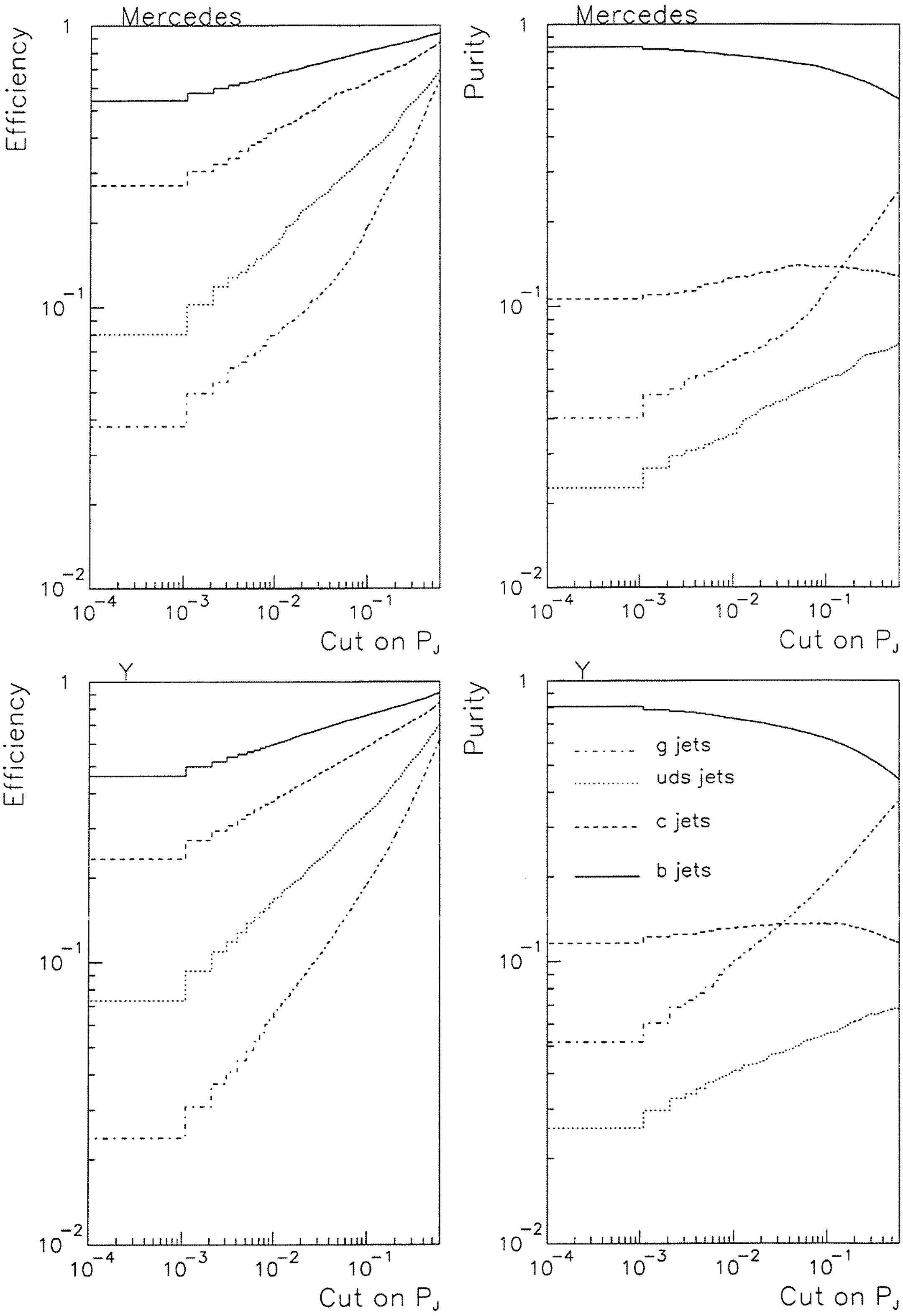

Figure 5.6: Efficiency and purity of the jets selected with $P_j < cutoff$ as a function of the cutoff. The upper plots represent the results for Mercedes events, the lower plots for Y events.

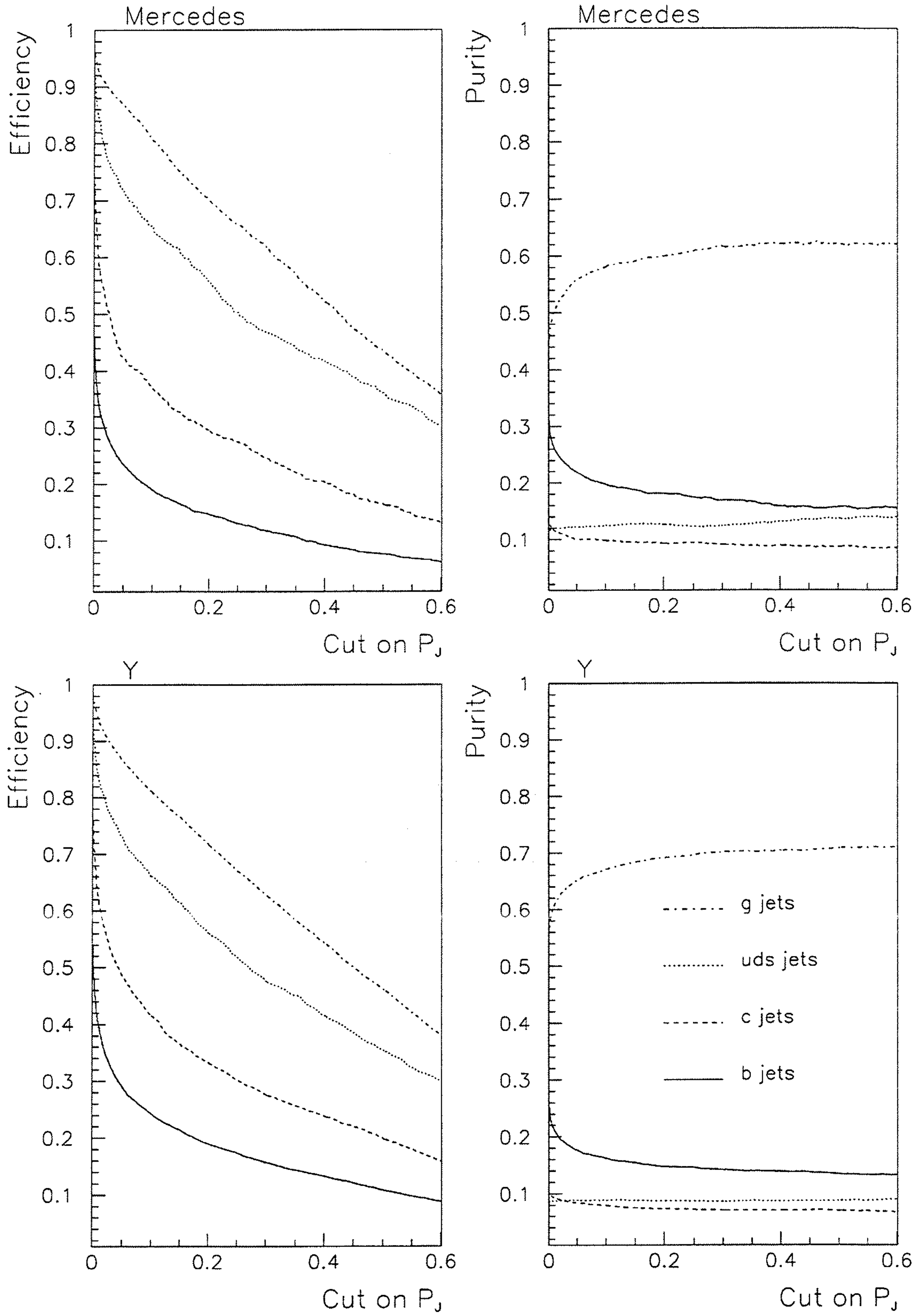

Figure 5.7: Efficiency and purity of the jets selected with $P_j > cutoff$ as a function of the cutoff. The upper plots represent the results for Mercedes events, the lower plots for Y events.

Class	gluon	b
Mercedes Events		
Average energy (GeV)	29.4	30.9
RMS spread (GeV)	3.4	3.2
Y Events		
Average energy (GeV)	23.5	25.0
RMS spread (GeV)	3.3	3.2

Table 5.1: Average energy and RMS spread of b and gluon selected jets of the Mercedes and Y events.

- A reference class, which included all jets before b tagging. In order to reduce the bias in the Y class, for Y events only jet 2 and jet 3 were used.

The compositions of the three jet classes are summarized in table 5.2 for Mercedes and Y events.

Class	g	b	$udsc$
Mercedes Events			
g-enriched	81.79%	7.87%	10.12%
b-enriched	7.72%	76.15%	15.22%
Reference	32.98%	14.21%	52.47%
Y Events			
g-enriched	81.93%	6.75%	10.92%
b-enriched	10.12%	71.00%	17.66%
Reference	45.71%	10.62%	43.22%

Table 5.2: Fractional composition of the three jet classes for Mercedes and Y events.

5.1.4 Selection of particle flavors

5.1.4.1 Pion, kaon and proton selections

To select pions, kaons and protons a tagging procedure based on the Čerenkov angle measurement in the RICH detector and on the ionization energy loss (dE/dX) in the TPC has been applied (the detailed procedure is specified in sections 4.1.1.1 and 4.1.2.1).

The dE/dx information was used together with the RICH tagging for momenta below 2 GeV/c and only RICH was used above 2 GeV/c. The analysis is restricted to the barrel RICH region ($41° \leq \theta_{track} \leq 139°$).

The specific particle selections applied throughout this work were the following:

- ***dE/dX* selections**: The pion kaon and proton tagging was performed as described in section 4.1.1.1.
- **RICH selections**: The particles were tagged as π, K^+ or p if they were selected as *standard* (as described in section 4.1.2.1) and if both the OD and TPC had been used for the track reconstruction.

The efficiency and contamination of these selections in the samples of tagged quark and gluon jets, and in the Mercedes and Y topologies, will be specified in the subsection 5.1.5.2.

5.1.4.2 K^0_S and Λ selections

The K^0_S and Λ candidates are detected by their decay in flight into $\pi^+\pi^-$ and $p\pi^-$, respectively (section 4.2). The particles were tagged as K^0_S or Λ if they fulfilled the *tight* criteria described in detail in section 4.2.

The efficiency and contamination of these selections in the samples of tagged quark and gluon jets, and in the Mercedes and Y topologies, will be specified in section 5.1.5.2.

5.1.5 Correction method

In this section the correction of measured quantities for various detector related effects and bias from jet flavour selections will be described. Since gluon jets differ from quark jets (gluon jets are expected to be broader, to have a higher multiplicity and a softer energy spectrum, see section 2.2) the particle identification efficiency was evaluated separately for each type of jet.

5.1.5.1 Unfolding of the jet flavors

Particle distributions for pure quark and gluon jets (generator level) can be extracted from the three classes of jets, as selected in section 5.1.3, via a simple unfolding procedure. This unfolding is based on the knowledge of the quark flavour and gluon composition of these classes (table 5.2) and it is computed via an algebraic method applied to the particle's distribution in question. The procedure followed is described below.

If $\mathrm{X}_{g-enriched}(m_i)$, $\mathrm{X}_{b-enriched}(m_i)$ and $\mathrm{X}_{reference}(m_i)$ are the distributions of the measured quantity X constructed from the g-enriched class, b-enriched class and reference class, respectively, where m_i is the content of bin i, then:

$$\left|\begin{array}{c} X_{g-enriched}(m_i) \\ X_{b-enriched}(m_i) \\ X_{reference}(m_i) \end{array}\right| \begin{array}{c} = \\ = \\ = \end{array} \left|\begin{array}{c} P_g(g-enriched)\ P_b(g-enriched)\ P_q(g-enriched) \\ P_g(b-enriched)\ P_b(b-enriched)\ P_q(b-enriched) \\ P_g(reference)\ P_b(reference)\ P_q(reference) \end{array}\right| \begin{array}{c} \cdot \\ \cdot \\ \cdot \end{array} \left|\begin{array}{c} G(m_i) \\ B(m_i) \\ Q(m_i) \end{array}\right|$$

where $P_g(j)$, $P_b(j)$ and $P_q(j)$ are the fractions of g, b and $q = udsc$ in the enriched class j ($j=$ g-enriched, b-enriched and reference). From the above system of equations the corresponding distributions for pure jets are extracted; $G(m_i)$ for pure gluon, $B(m_i)$ for pure b and $Q(m_i)$ for pure $q = udsc$.

The distributions for a pure quark mixture including all quarks, $q = udscb$, are obtained from the distributions for $udsc$ and b in the enriched classes and reference class of table 5.2, considering the quark compositions in the proportion predicted by the standard model for the decay $Z^0 \to q\bar{q}$.

5.1.5.2 Efficiency and contamination of the particle tagging

In order to compare the particle distributions, already corrected for the jet contamination, with the theoretical predictions or with the results from other experiments they must first be corrected for various detector effects, such as geometrical acceptance, efficiency, particle interactions with the material of the detector and effects of event and track selections. In the present work these corrections are applied via multiplicative correction factors, C, relating the distribution X (already corrected for the jet contamination), to the fully corrected distribution $X_{corrected}$ (corrected for both the jet contamination and the detector effects):

$$X_{corrected} = X \times C \tag{5.2}$$

The correction factors are computed individually for each bin. The bin size is chosen to be always at least twice as large as the detector resolution, and depending on the analysis and the distribution under study, it is chosen such as the bin content is not limited by low statistics thus enabling any reliable conclusions.

The correction factors are computed in the following way. First, hadronic events are generated with the Monte Carlo program JETSET 7.3 PS and the observable in question is evaluated at this level ($X_{generator}$), separately for the gluons and for the different quark flavors. These events are afterwards processed through the detector simulation program (DELSIM [45]) to produce simulated raw data, which are then processed by the same reconstruction and analysis programs as used for the real data. From these data the value of the corresponding observable, in the pure quark and gluon jet samples, is computed yielding $X_{fullsim}$. The correction factor is the ratio of the two quantities,

$$C = \frac{X_{generator}}{X_{fullsim}}. \tag{5.3}$$

In figure 5.8 the reconstruction efficiency as a function of momentum (given by $1/C$) and the contamination are shown for the protons, kaons, Λ and K_S^0 in pure quark and gluon jets and for the two topologies, Mercedes and Y. The momentum bins are the same as the ones used in the analysis pursued next (section 6.1).

5.1.5.3 Multiplicity matrix unfolding

In order to compare the multiplicity distributions, already corrected for the jet contamination, with the theoretical predictions or with the results from other experiments they must first be corrected for various detector effects, such as geometrical acceptance, efficiency, particle interactions with the material of the detector and effects of event and track selection.

The relation between the multiplicity M_i obtained for a given jet [2] and the underlying true distribution T_j can be described by a matrix equation:

$$T_j = \sum_j G_{ij} M_i. \tag{5.4}$$

The response matrix G_{ij} describes the detector effects. It is defined as the probability of an event with "observed" multiplicity (already corrected for the jet contamination) i to have an underlying true multiplicity j. The matrices G_{ij} were determined with the Monte Carlo simulation program JETSET 7.3.

The rms spread of the true multiplicity distributions (n_{true}) around the range of "observed" values: $n = 1$ to $n = 8$, are indicated in table 5.3 for quark (in particular b quark) jets and gluon jets in the Mercedes and Y samples (see figure 5.9).

Class	Mercedes Events		Y events	
	$n=1$	$n=8$	$n=1$	$n=8$
q jets	2.2	2.6	2.2	2.7
b jets	2.3	2.7	2.4	2.7
g jets	3.1	2.8	2.5	2.7

Table 5.3: RMS spread of the true multiplicity distributions around the range of "observed" values: $n = 1$ to $n = 8$.

From the "observed" multiplicity distributions in the data, the true distributions are estimated by multiplying the first by the matrix G_{ij}.

[2]Unless otherwise stated it is assumed throughout this subsection (5.1.5.3) that the distributions were already corrected for the effects of jet contamination.

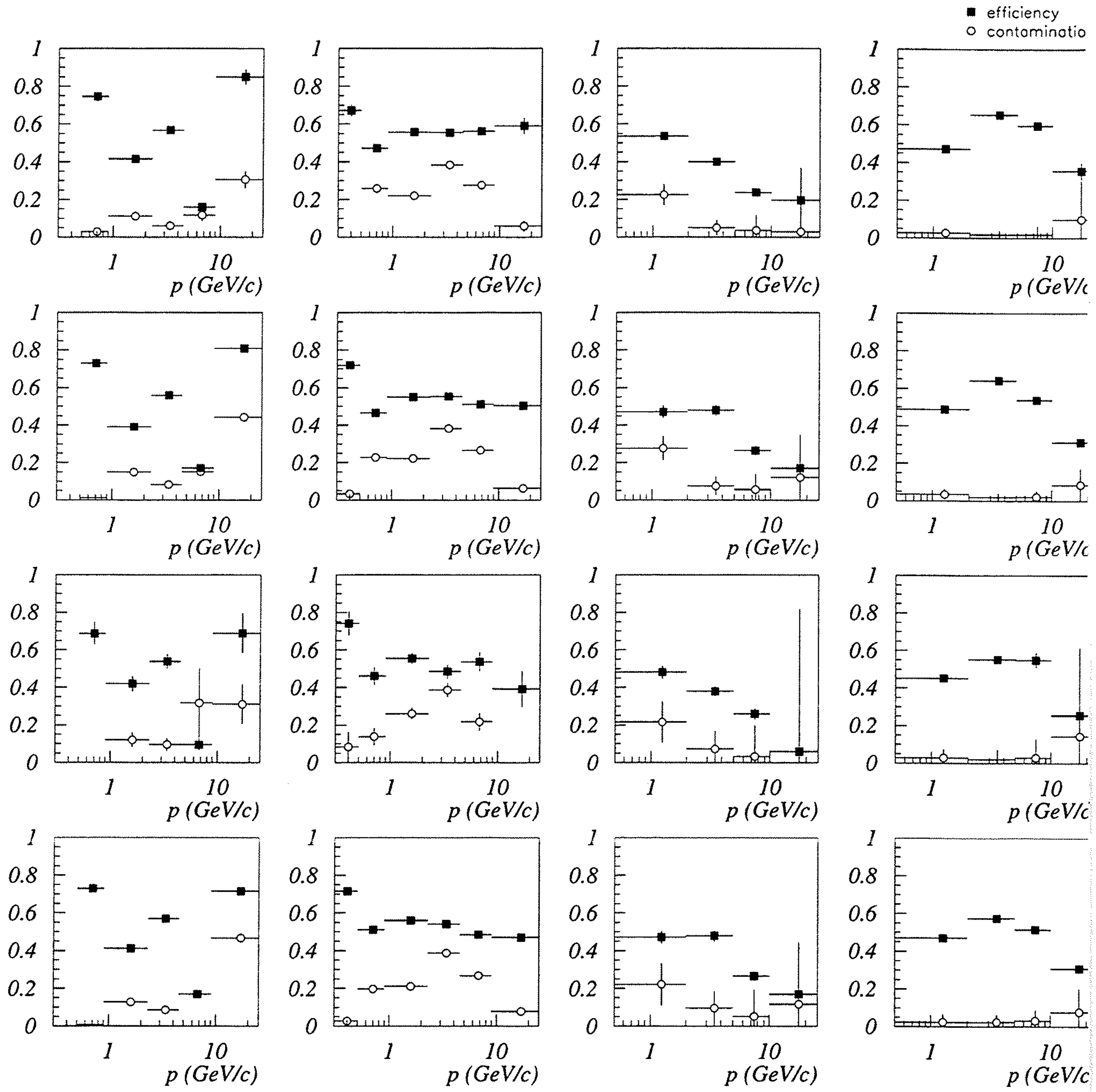

Figure 5.8: Efficiency (squares) and contamination (open circles) as a function of momentum for Y events and Mercedes events for different types of particle: the histograms in the 1st, 2nd, 3rd and 4th columns correspond to particle types p, K^+, Λ and K^0_S respectively. The 1st and 2nd rows of histograms refer to Y events, the 1st row for gluon jets and the 2nd row for quark jets. The 3rd row corresponds to gluon jets in Mercedes events and the 4th row to quark jets in Mercedes events.

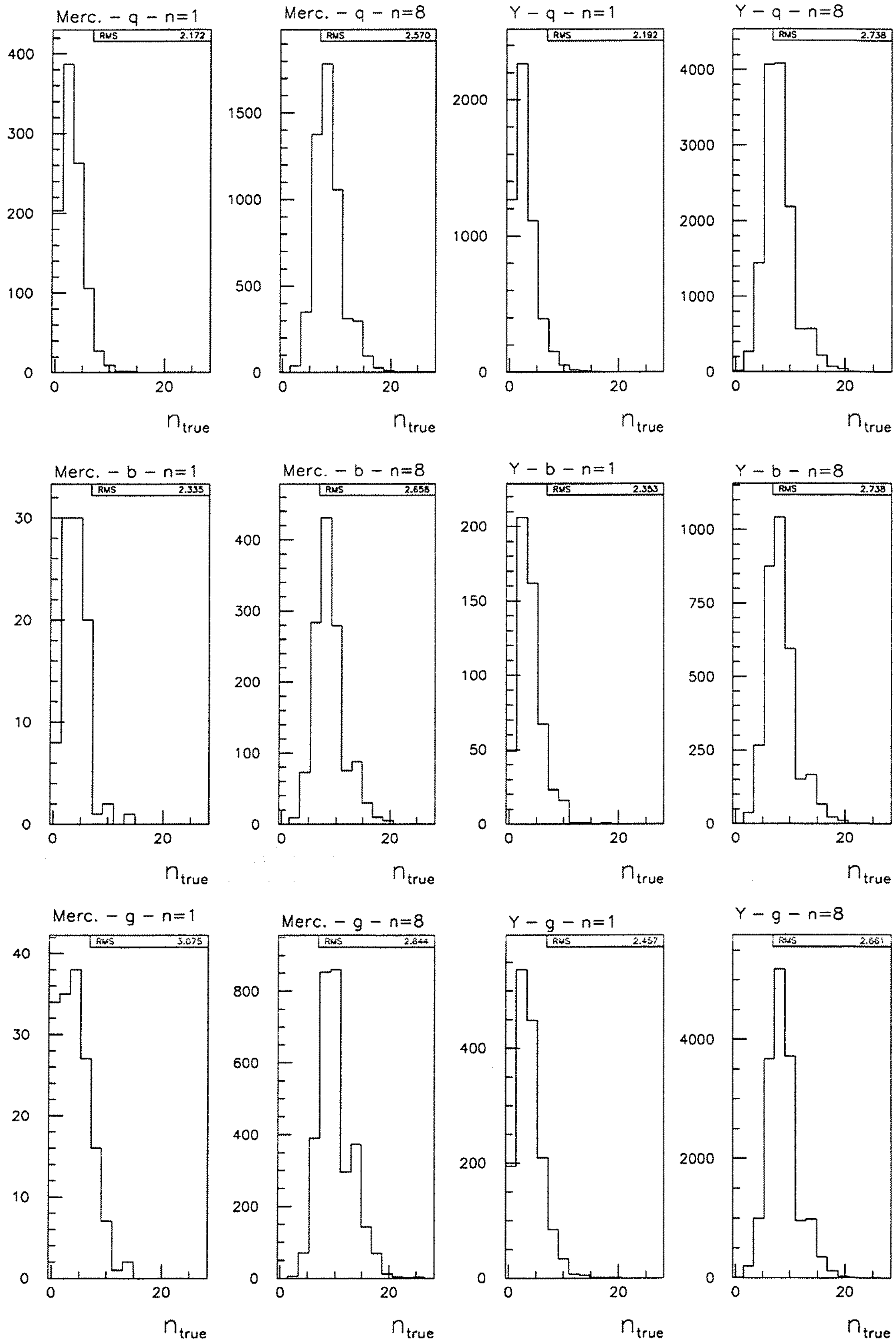

Figure 5.9: True multiplicity distributions (n_{true}) under the "observed" values $n = 1$ and $n = 8$ in quark jets (first row), b jets (second row) and gluon jets (third row) selected in Y events (third and forth columns) and in Mercedes events (first and second columns).

5.2 Event selections - LEP II

In this section the general framework of the analysis pursued at energies above 91 GeV (hereafter referred as the "LEP II" period) will be described, in particular the main differences relative to the event selections previously specified in section 5.1 will be focused.

In this context special emphasis is given to the reduction of the effective center of mass energy of the e^+e^- collision (section 5.2.1) due to the Initial State Radiation photons, and to the background from W^+W^- pair production. Above the W^+W^- production threshold (the measured W mass is $m_W = 80.35 \pm 0.12$ GeV [1]) the decay $W^+W^- \to q\bar{q}q\bar{q}$ ($\sim$ 50% of all W pairs produced decay hadronically) contributes as a considerable background to the process $e^+e^- \to (Z^0/\gamma)^* \to q\bar{q}$. The cross section for W boson pair ($(Z^0/\gamma)^* \to q\bar{q}$) production at 161 GeV is only 3.7 pb (147 pb) but it rapidly rises to 12 pb at 172 GeV (121 pb) and 15 pb (110 pb) at 183 GeV. The selection of hadronic events above 91 GeV and the method used to reduce the background from fully hadronic decays of the produced W pairs is detailed in section 5.2.2.

The data sample analysed corresponds to a period of data taking during the years of 1995: 130 GeV, 136 GeV and 140 GeV, with integrated luminosities: 2.85, 2.98 and 0.04 pb^{-1}, respectively; 1996: 161 GeV and 172 GeV, with integrated luminosities: 9.96 and 10.14 pb^{-1}, respectively; and 1997: 130 GeV and 183 GeV, with integrated luminosities of 6 pb^{-1} and 50.15 pb^{-1}, respectively.

The influence of the detector in the several steps of the analysis was studied with the full DELPHI simulation program, DELSIM [45]. Events were generated with the JETSET 7.4/PYTHIA 5.7 Parton Shower (PS) Monte Carlo program [31] with parameters tuned to fit LEP I data from DELPHI [53] [3]. The particles were followed through the detailed geometry of DELPHI giving simulated digitizations in each detector. These data were processed with the same reconstruction and analysis programs as the real data. The sizes of the simulated samples at the several energies analysed and for the two channels: $e^+e^- \to (Z^0/\gamma)^* \to q\bar{q}$ ($QQPS$) and $e^+e^- \to W^+W^-$ (WW) are presented in table 5.4. In addition, 100,000 events were generated with JETSET 7.4/PYTHIA 5.7 and HERWIG 5.8 [30] for each energy, in order to compare the data distributions, corrected for all detector effects, with the model predictions.

5.2.1 Initial state radiation

The radiation of initial state photons lowers the energy available for the e^+e^- collision and this effect is particularly important at LEP II energies.

[3] The Monte Carlo program PYTHIA 5.7 was used to generate the processes $e^+e^- \to (Z^0/\gamma)^* \to q\bar{q}$ (*or* W^+W^-) and the parton shower was introduced via the generator JETSET 7.4, with parameters tuned by DELPHI [53]

OVERAL STATISTICS				
Channel	133 GeV	161 GeV	172 GeV	183 GeV
$QQPS$	20,310	24,811	45,186	29,186
WW	-	11,031	27,546	14,475

Table 5.4: Sizes of the simulation samples analyzed.

The photons from Initial State Radiation (hereafter called ISR photons) tend to move along the beam directions and their energy tend to $E_{\gamma R} = (s - M^2_{Z^0})/(2\sqrt{s})$, where $\sqrt{s}$ is the center of mass energy and M_{Z^0} stands for the Z^0 mass. The events with such hard Initial State Radiation have the energy in the center of mass of the e^+e^- collision reduced to the Z^0 mass ("Z^0 radiative return" events).

By measuring or estimating the energy and momentum of the initial state ISR photon(s) DELPHI has developed a method (hereafter referred by the name of the package in which it is implemented: "SPRIME") to evaluate the effective center of mass energy, $\sqrt{s'}$, in e^+e^- annihilations into hadrons [55]. A brief resume of the method is given below, for details see reference [55].

First showers are searched for in the calorimeters and are considered as candidate ISR photons, if they fulfill the following criteria:

- energy deposition higher than 10 GeV;
- isolation angle with respect to any charged particle with momentum, p, greater than 1 GeV higher than 0.3 radians;
- if the shower energy is lower than 70% of $E_{\gamma R}$, the isolation angle with respect to any charged particle, with $p > 1$ GeV, is required to be between 0.6 and 1.5 radians (the upper limit is raised to 1.8 radians if the shower is in the STIC).

These selected showers are grouped together if their distance in space does not exceed 5 degrees (the association is done adding the energies but keeping the direction of the sum of the momenta).

In a second step all particles, excluding the ISR candidates, are clustered using the DURHAM algorithm (see section 2.2.3.1 for details) until two jets remain.

Energy and momentum conservation is applied in order to obtain, through the directions of the jets and of the candidate photons, the energy of the ISR photon(s). If there is no candidate ISR photon or if there is only one candidate which is not able to balance the energy and momentum of the jets, the method assumes an hypothetical photon along the beam pipe (in the z direction).

Finally the effective energy in the e^+e^- center of mass is computed as the mass of the system recoiling from all the ISR photons.

The method fails if three or more candidate ISR photons are found, in this case the e^+e^- center of mass effective energy, $\sqrt{s'}$, is computed from the sum of the ISR photon measured energies and momenta.

The method can overestimate the true energy in the case of double hard radiation in the initial state. For instance, if the two ISR photons are emitted back-to-back, the remaining two jets may also be back-to-back, but with energy much smaller than the beam energy. Cutting on the total energy measured in the detector reduces the contamination from such events.

The estimated distributions of $\sqrt{s'}$ for hadronic events at the center of mass energies: 130 GeV to 140 GeV, 161 GeV, 172 GeV and 183 GeV, are presented in figure 5.10 [55, 56]. The upper left histogram of figure 5.10 corresponds to the data collected in 1995 at energies between 130 GeV and 140 GeV.

In figure 5.11 [55] the efficiency and purity for selecting "high energy" events (defined as those with effective center of mass energy above $0.85{\cdot}2E_b$, E_b is the beam energy) using a cut on $\sqrt{s'}/2E_b$, as a function of the cut are presented.

5.2.2 Hadronic event selections

The criteria applied in order to select a sample of hadronic events from the data collected at the several LEP II center of mass energies, were based on the following cut variables:

- N_{ch}: number of charged particles with $p >$ 100 MeV/c, $20^\circ < \theta < 160^\circ$, a track length of at least 30 cm in the TPC and consistent with coming from the interaction vertex. p is the particle's momentum and θ the polar angle with respect to the beam axis (see figure 5.12),
- E_{vis}/E_{cm}: E_{vis} is visible energy (sum over all particles, charged and neutral, in the event) and E_{cm} is the center of mass energy (see figure 5.13).
- SPRIME: SPRIME$=\sqrt{s'}$, is the effective center of mass energy (see section 5.2.1)
- EVBN is the narrow jet broadening defined as follows: for each hemisphere $j = 1, 2$ with respect to a plane perpendicular to the thrust axis $B_j = \frac{1}{2\cdot p_{tot}} \sum_i p_i \cdot sin\theta_{i-T}$, where p_{tot} is the sum of the module of the momenta of all the particles in the j-th hemisphere, p_i is the momentum of the particle i and θ_{i-T} is the angle between the direction of the particle and the thrust axis. The narrow jet broadening is the minimum between B_1 and B_2.

In table 5.5 the selection criteria applied to select hadronic final states in the process $e^+e^- \to (Z^0/\gamma)^* \to q\bar{q}$ are shown. The distributions of the charge multiplicity and E_{vis} are presented in figures 5.12 and 5.13 for the 4 energies analysed. The excess of events in the data, compared to the Monte Carlo simulations, for low

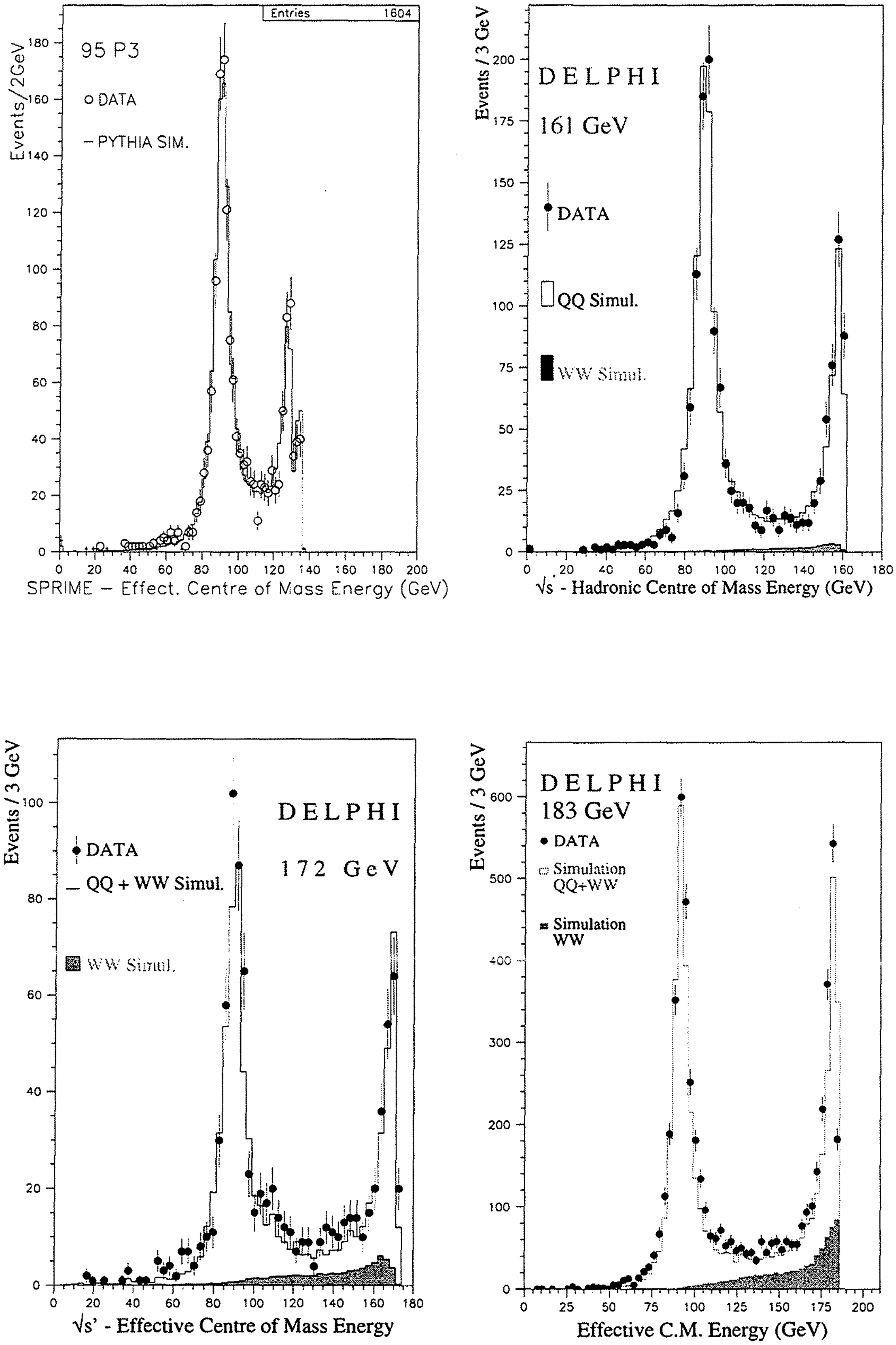

Figure 5.10: Distribution of the effective center of mass energy (SPRIME) for the different center of mass energies. The data is indicated by the points, the dark histogram represents the results obtained from the W^+W^- simulation, and the white histogram is the result of the sum of the simulations: $q\overline{q}$ and W^+W^- (only $q\overline{q}$ simulation for the data collected in 1995).

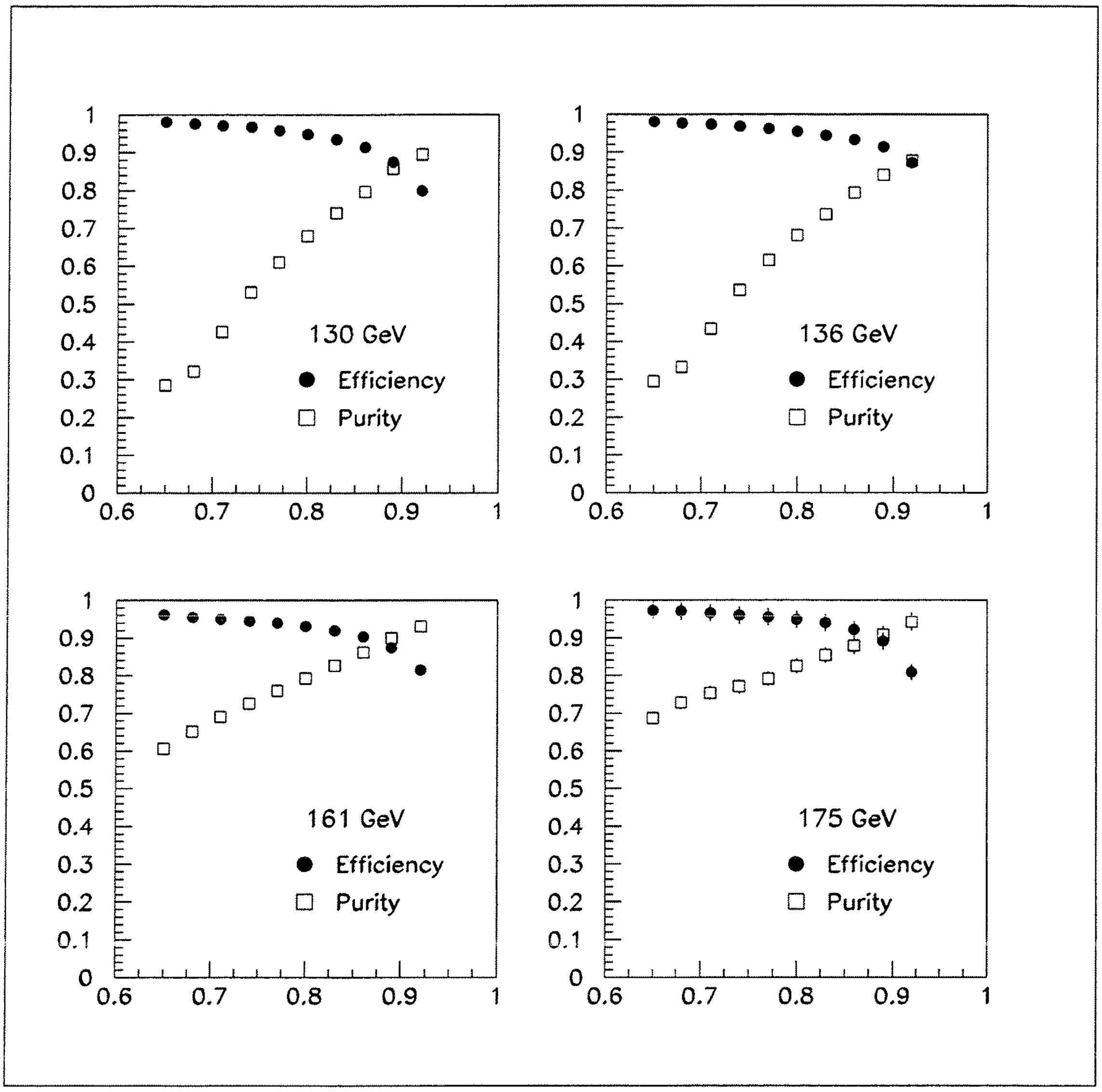

Figure 5.11: Efficiency (black circles) and purity (white squares) for selecting events with generated effective center of mass energy above $0.85{\cdot}2E_b$ as a function of the cut on the ratio of the SPRIME result to the LEP center of mass energy (horizontal axis). The top left figure corresponds to simulated events at center of mass energies of 130 GeV, the top right figure corresponds to 136 GeV, the bottom left corresponds to 161 GeV and the bottom right figure corresponds to 175 GeV.

values of N_{ch} and E_{vis} is due to the contribution of Bhabha events ($e^+e^- \to e^+e^-$) and events of the type: $e^+e^- \to \gamma^*\gamma^* \to e^+e^-X$, which are not accounted for in the present Monte Carlo simulations. The cuts applied (see figures 5.12 and 5.13) reduce this background contributions to less than $\sim 1\%$.

The distribution of the "narrow jet broadening" for the data collected at 172 GeV and 183 GeV is presented in figure 5.14, for the events selected after applying the cuts on N_{ch}, E_{vis}/E_{cm} and SPRIME shown in table 5.5.

Energy (GeV)	N_{ch}	E_{vis}/E_{cm}	SPRIME (GeV)	EVBN
130/136/140	≥ 7	$\geq 15\%$	≥ 122	-
161	≥ 9	$\geq 20\%$	≥ 150	-
172	≥ 10	$\geq 20\%$	≥ 155	≤ 0.1
183	≥ 10	$\geq 20\%$	≥ 160	≤ 0.1

Table 5.5: Cuts applied to select hadronic final states in the process $e^+e^- \to (\mathrm{Z}^0/\gamma)^* \to q\bar{q}$.

5.2.3 Selection of particle flavors

As in section 5.1.4.

5.2.4 Correction method

In order to compare the particle distributions with the theoretical predictions or with the results from other experiments they must first be corrected for various detector effects, such as geometrical acceptance, efficiency, particle interactions with the material of the detector and effects of event and track selection.

In the present work these corrections are applied via multiplicative correction factors, F, obtained from the comparison between the Monte Carlo distributions at generator level, $X_{generator}$, with the corresponding distributions after the detector simulation and analysis (as for the real data), X_{final}:

$$Data(corrected) = \frac{Data(uncorrected)}{F}; \tag{5.5}$$

where:

$$F = \frac{X_{final}}{X_{generator}} \tag{5.6}$$

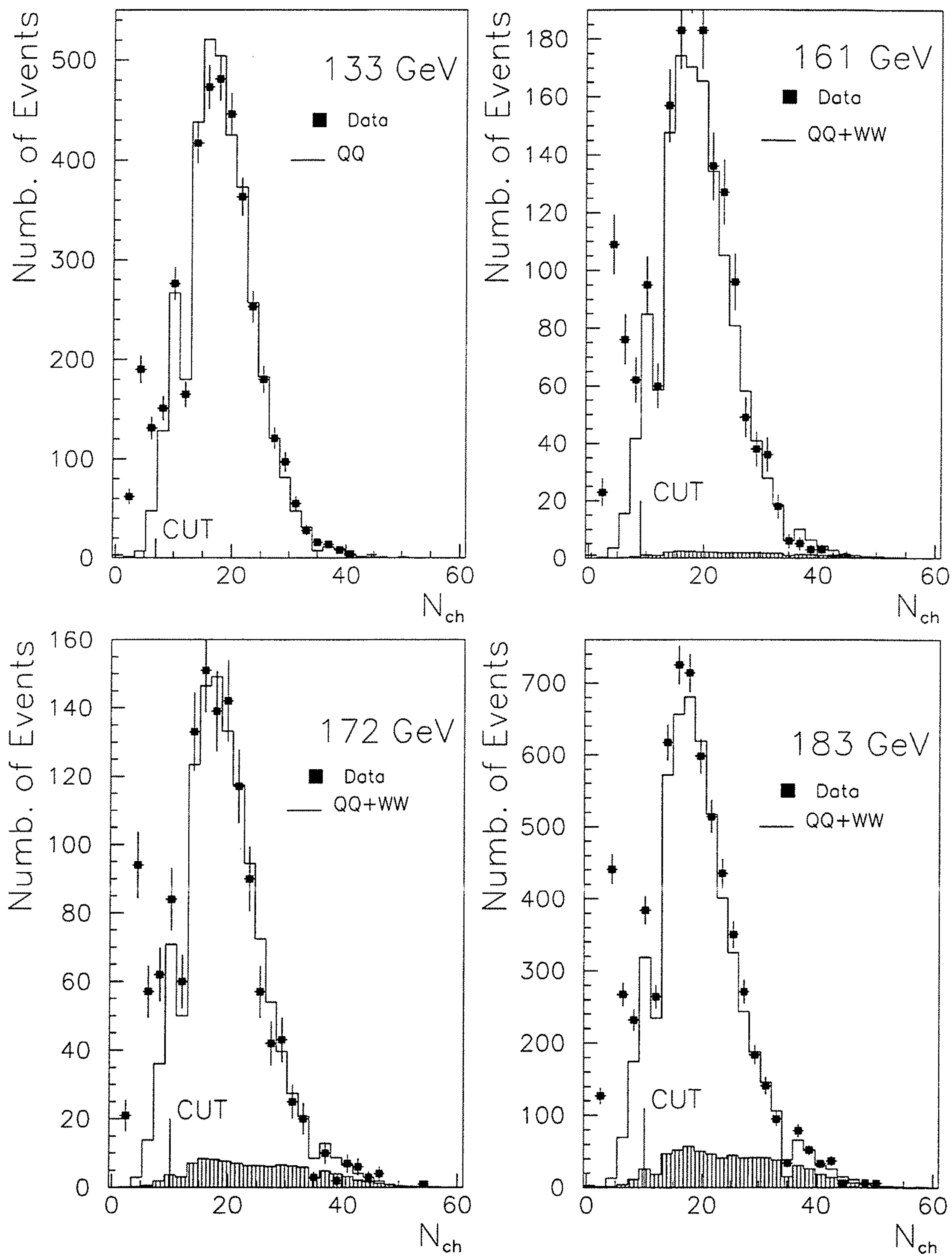

Figure 5.12: Multiplicity distribution. The data is indicated by the points (black squares), the dark histogram represents the results obtained from the W^+W^- simulation, and the white histogram is the result from the sum of the simulations: $q\bar{q}$ and W^+W^-. The straight line denotes the cut value applied to select hadronic events using the variable N_{ch}.

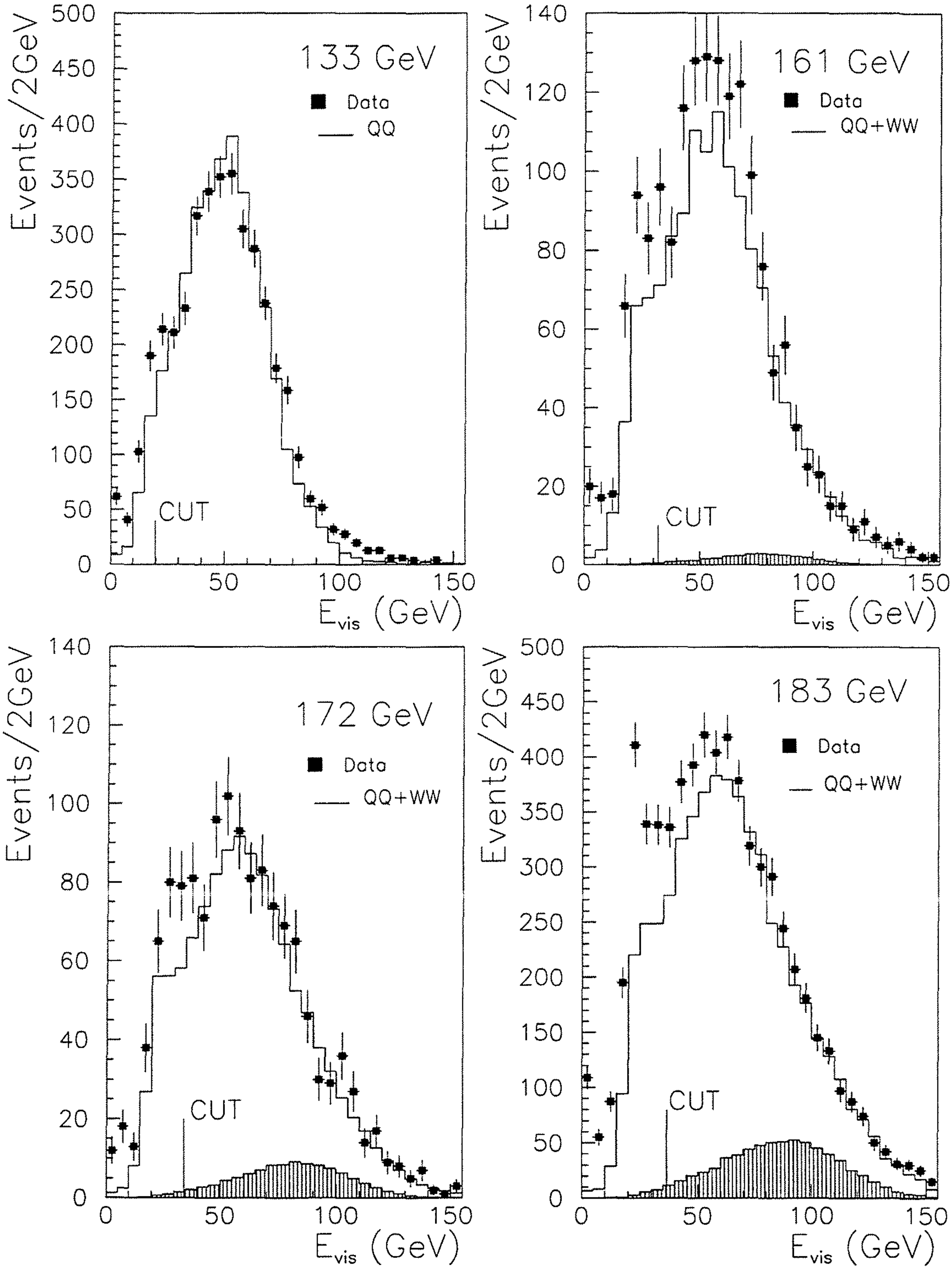

Figure 5.13: Distribution of the visible energy. The data is indicated by the points (black squares), the dark histogram represents the results obtained from the W^+W^- simulation, and the white histogram is the result from the sum of the simulations: $q\bar{q}$ and W^+W^-. The straight line denotes the cut value applied to select hadronic events using the variable E_{vis} (or E_{vis}/E_{cm}).

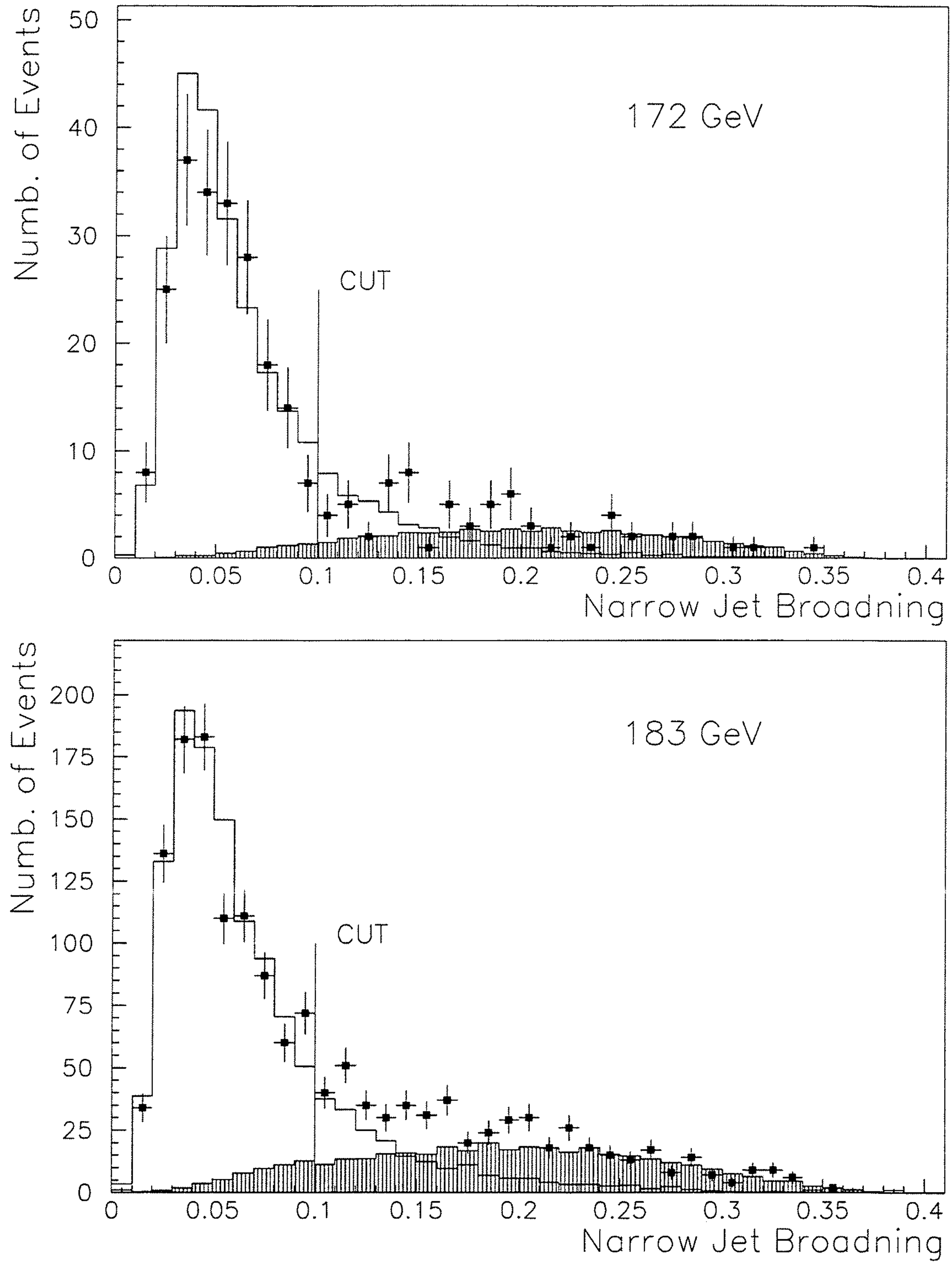

Figure 5.14: Narrow Jet broadening distribution, for the selected events. The data is indicated by the points (black squares), the dark histogram represents the results obtained from the W^+W^- simulation, and the white histogram is the result from the sum of the simulations: $q\bar{q}$ and W^+W^-. The straight line denotes the cut value applied to select hadronic events using the variable $EVBN$.

In figure 5.15 these correction factors are presented as a function of the variable $\xi_p = -\log x_p$, where $x_p = 2\frac{p}{E_{cm}}$, p is the momentum of the particle and E_{cm} the center of mass energy.

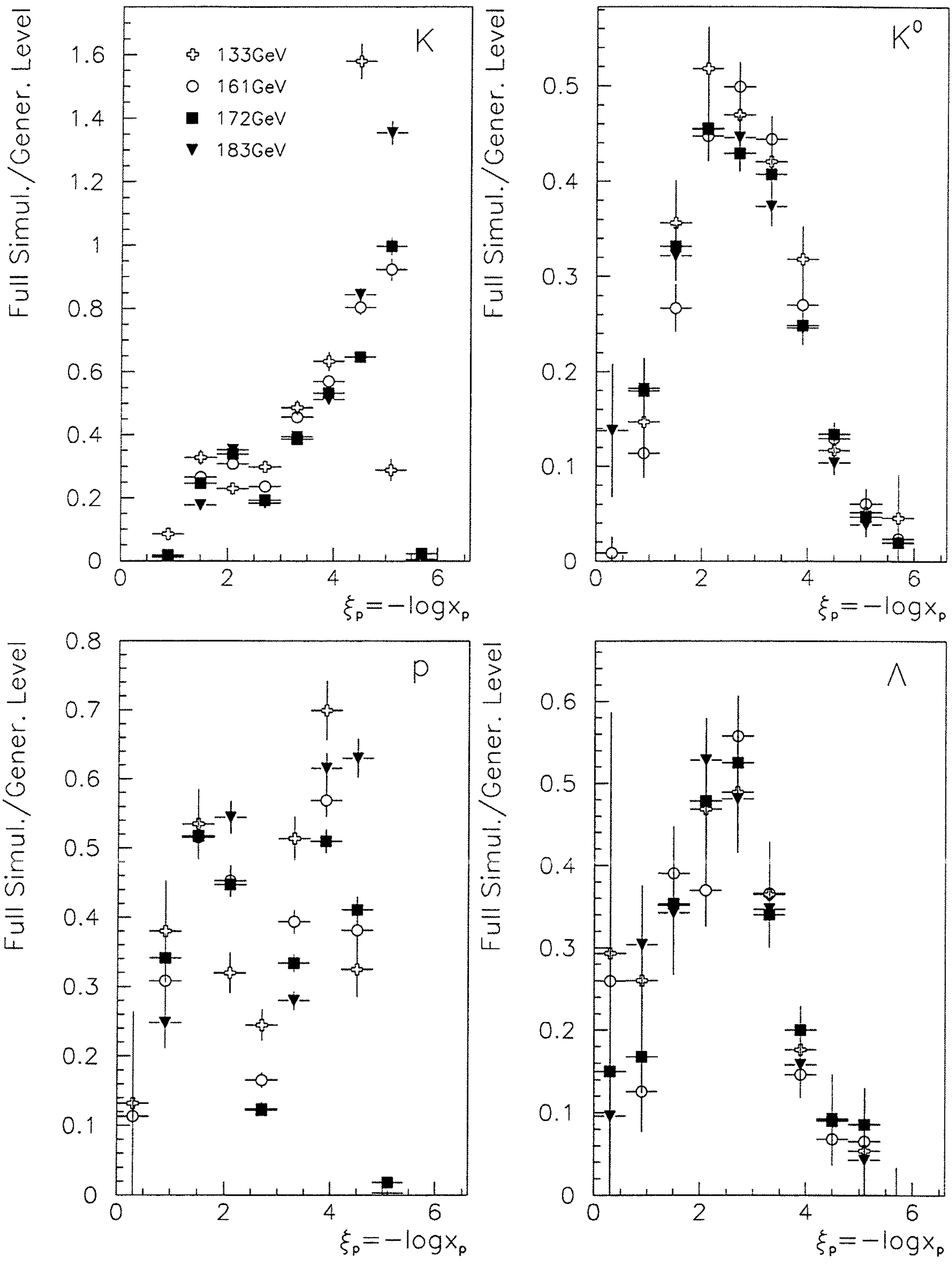

Figure 5.15: Correction factors F, as a function of ξ_p (see text).

Chapter 6

Results

The way quarks and gluons transform into hadrons is complex and not entirely understood by present theories; the most satisfactory description is given by Monte Carlo simulations. In the picture implemented in Monte Carlo simulations, the hadronization of a $q\overline{q}$ pair is split into phases. In a first phase, gluon emission and parton branching of the original $q\overline{q}$ pair take place. In a second phase, at a certain virtuality Q_0, quarks and gluons produced in the first phase transform into mesons and baryons. Only phenomenological models, which need to be tuned to the data, are available to describe this process of fragmentation; the models most frequently used in e^+e^- annihilations are based on string and cluster fragmentation. In the third phase the unstable states decay into hadrons which can be observed or identified by the detector (see chapter 2 for a review).

These models account correctly for the average multiplicity and the momentum spectrum of identified particles in $q\bar{q}$ events up to the Z^0 energy; with LEP II, the energy range spanned in e^+e^- interactions is doubled. It is interesting to check the validity of these models through the analysis of observables which might probe certain aspects of the fragmentation of quarks and gluons into hadrons, and their evolution with the center of mass energy.

In section 6.1 quark and gluon jets will be compared in terms of their hadron content; the KNO distribution for charged particles in quark and gluon jets is presented for LEP I data in section 6.2 and in section 6.3 the momentum distribution for identified hadrons at high energies (above 91 GeV) and the evolution of the average hadron multiplicity with the center of mass energy will be presented.

6.1 Identified particles in jets at LEP I

The production of identified particles in the final state was studied in 4 momentum bins for K^0_S's and Lambdas and in 8 momentum bins for charged kaons and protons, as indicated in table 6.1.

The ratios of the momentum distributions, not yet corrected for the contami-

Particle	K^0_S, Λ							
Momentum bins (GeV/c)	bin 1 0.5-2.0		bin 2 2.0-5.0		bin 3 5.0-10.0		bin 4 10.0-25.0	
Particle	K, p							
Momentum bins (GeV/c)	bin 1 0.3-0.5	bin 2 0.5-0.7	bin 3 0.7-0.9	bin 4 0.9-1.3	bin 5 1.3-2.3	bin 6 2.3-4.5	bin 7 4.5-9.0	bin 8 9.0-35

Table 6.1: Energy bins used for the study of identified particles.

nation of the different jet classes or for the reconstruction efficiency of the particles in those jets, are shown in figure 6.1 for the g-enriched class relative to the reference class, together with the same ratios for charged particles. The simulation sample used consisted of about $4.6 \cdot 10^6$ hadronic Z^0 decays generated with the JETSET 7.3 PS model, with JETSET 7.4 PS and with HERWIG 5.8. The spectra of identified particles in the class enriched in gluon jets appear to be softer than the corresponding spectra in the reference class.

The effects of the contaminations in the jet classes were unfolded by applying the algebraic correction method described in section 5.1.5.1. The reconstruction efficiencies were determined as described in section 5.1.5.2.

The ratios obtained, after unfolding the contamination of the jet classes and correcting for the reconstruction efficiencies of the particles in the pure jet classes, are shown in figure 6.2, together with the corresponding ratios for charged particles.

Normalized ratios $R'_X(p)$ were then defined by :

$$R'_X(p) = \frac{r_X(p)}{r_{ch}(p)}, \tag{6.1}$$

where $r_X(p)$ is the fully corrected ratio of the average multiplicity of the identified particle X ($X = K^0$, Λ, K, proton) measured in gluon jets relative to quark jets in a given bin of the momentum p, and $r_{ch}(p)$ is the corresponding ratio for all charged particles. These normalized ratios, which are shown in figure 6.3, are computed from the ratios in figure 6.2.

To further test the model predictions, the normalized ratios

$$R'_X = r_X / r_{ch}, \tag{6.2}$$

were also defined, where r_X is the fully corrected ratio of the average multiplicities of the identified particles X ($X = K^0$, Λ, K, proton) in gluon jets relative to quark jets in the momentum range $0.5 < p < 25.0$ GeV/c, and r_{ch} is the corresponding ratio for all charged particles. These normalized ratios are shown and compared with the predictions from the simulation in table 6.2. The values of r_{ch} were found to be $r_{ch} = 1.22 \pm 0.01$ and $r_{ch} = 1.30 \pm 0.03$ for the Y and Mercedes events

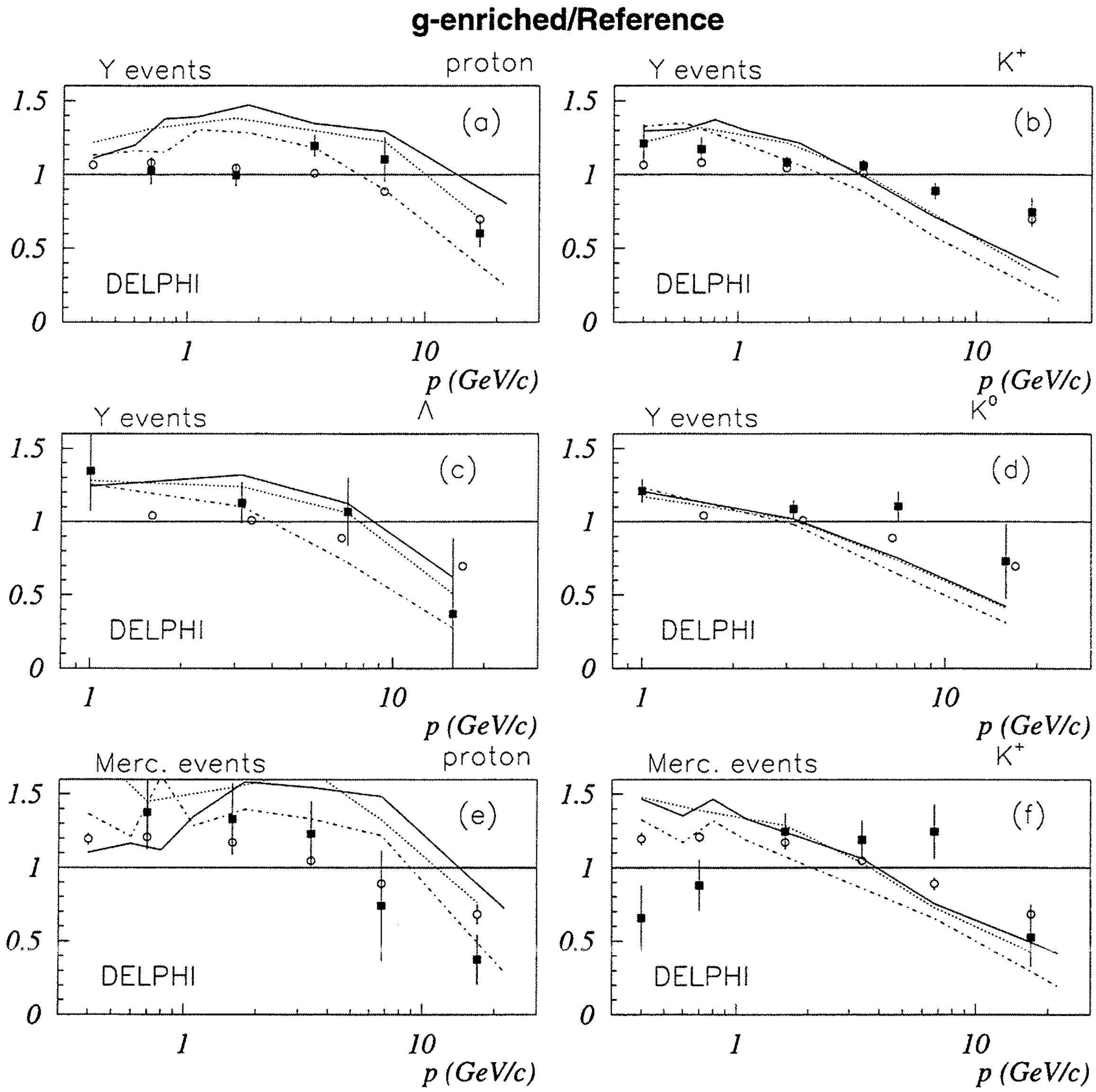

Figure 6.1: Observed uncorrected ratios of the yields of (**a**) protons, (**b**) kaons, (**c**) Λ, and (**d**) K_S^0 in the g-enriched class with respect to the reference class (black squares), for Y events; (**e**) and (**f**) for Mercedes events correspond to (a) and (b) respectively. The open circles represent the observed ratios of the yields of charged particles in the g-enriched class with respect to the reference class. The predictions from the JETSET 7.3 PS model are shown as a dotted line, the full line represents the predictions from the JETSET 7.4 PS model, and the dash-dotted line represents the predictions from HERWIG 5.8.

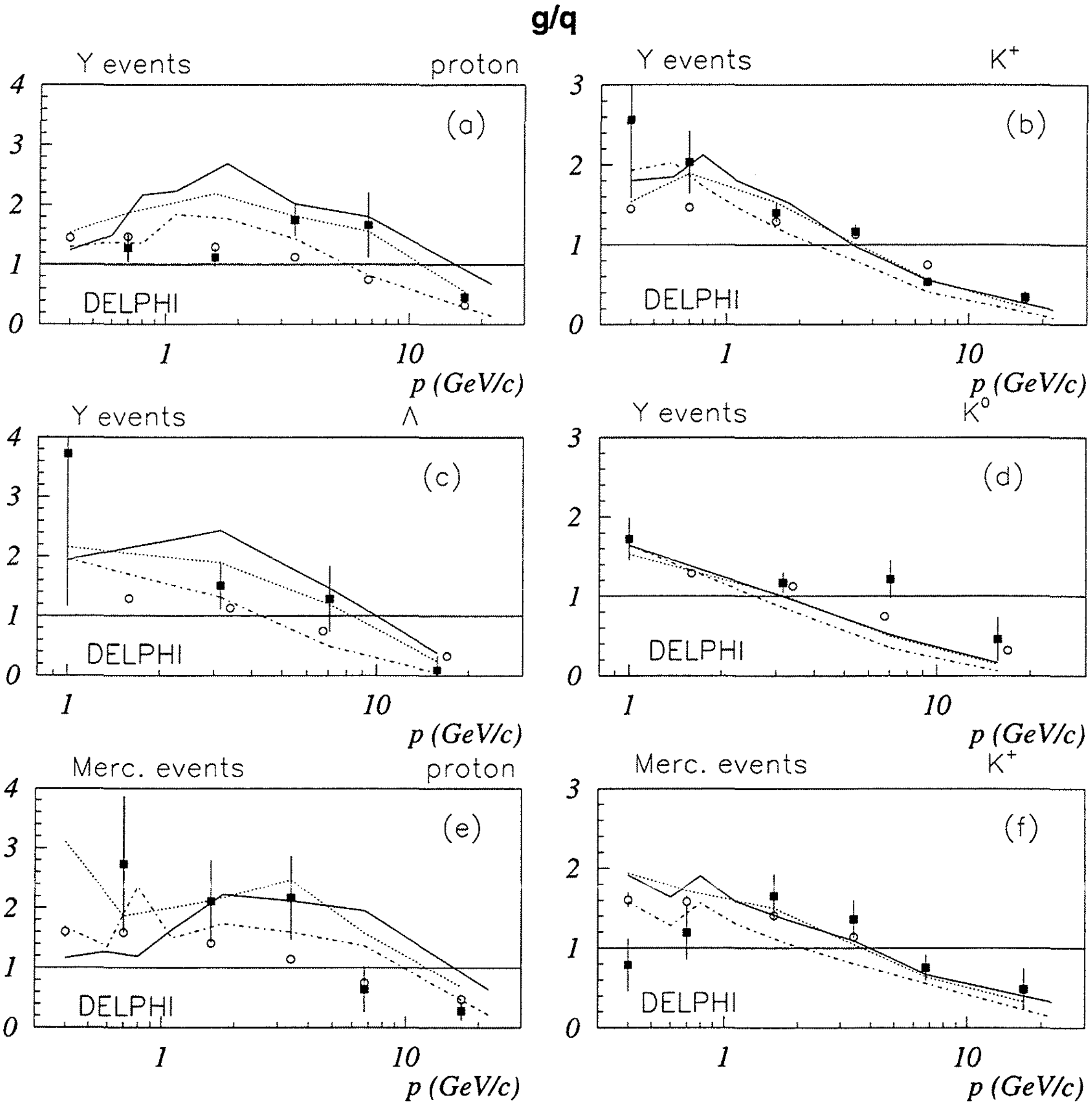

Figure 6.2: As in figure 6.1, but for the fully corrected ratios of yields in gluon jets with respect to quark jets (black squares), and the corresponding model predictions. The corresponding values for all charged particles are shown as open circles.

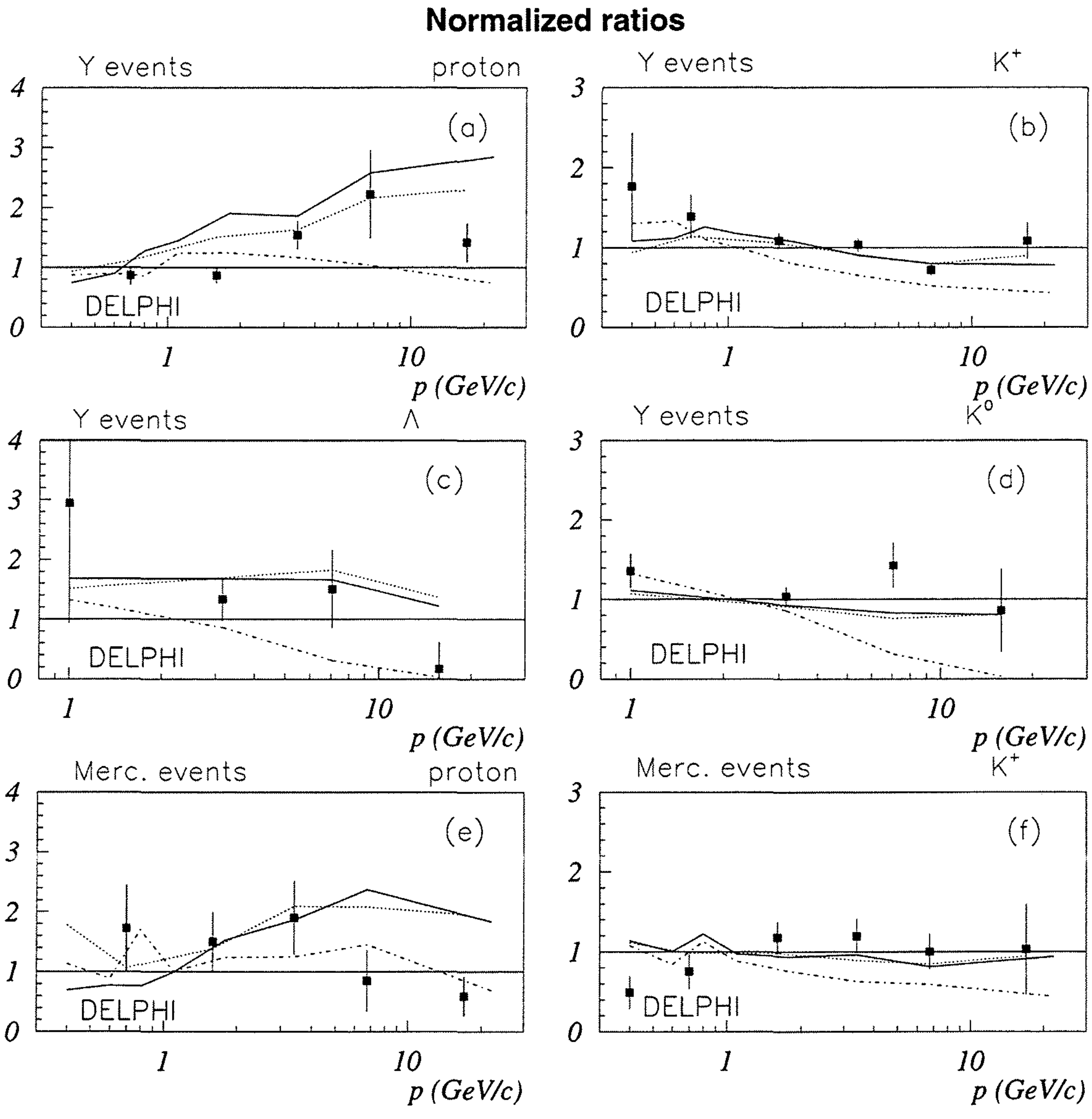

Figure 6.3: As in figure 6.1, but for the normalized ratio, $R'_X(p)$ defined in the text (black squares), and the corresponding model predictions.

respectively, consistent with the dependence of this ratio on the jet energy observed previously [11] (see section 2.2).

R'_X	Measured	JETSET 7.3 PS	JETSET 7.4 PS	HERWIG 5.8
Y Events				
R'_p	1.12 $\pm$ 0.11 $\pm$ 0.04	1.36$\pm$0.03	1.53 $\pm$0.05	0.94$\pm$0.02
R'_K	0.93 $\pm$ 0.04 $\pm$ 0.02	0.83$\pm$0.01	0.84 $\pm$0.01	0.70$\pm$0.01
R'_Λ	1.40 $\pm$ 0.30 $\pm$ 0.23	1.40$\pm$0.06	1.53 $\pm$0.07	1.02$\pm$0.03
R'_{K^0}	1.13 $\pm$ 0.09 $\pm$ 0.13	0.94$\pm$0.02	0.98 $\pm$0.02	0.93$\pm$0.01
Mercedes Events				
R'_p	1.25 $\pm$ 0.22 $\pm$ 0.05	1.43$\pm$0.05	1.35 $\pm$0.06	1.07$\pm$0.04
R'_K	0.92 $\pm$ 0.09 $\pm$ 0.03	0.82$\pm$0.02	0.84 $\pm$0.02	0.68$\pm$0.02

Table 6.2: Normalized ratios $R'_X = r_X/r_{ch}$ of the ratio r_X of the average multiplicities of the identified particles X in gluon jets relative to quark jets with momentum $0.5 < p < 25.0$ GeV/c normalized to the corresponding ratio r_{ch} for all charged particles in data and in simulation. For the data, the first error quoted is statistical, the second is systematic.

The systematic uncertainties on these ratios were estimated by summing in quadrature the following sources.

1. An overall uncertainty of $\pm5\%$ was used for the kaon and proton identification, deduced from the simulation by comparing the results from loose, standard and tight tagging (see section 4.1.2.1). For K^0 and Λ, this systematic uncertainty was taken as $\pm15\%$.

2. The uncertainties on the flavour compositions in table 5.2 was estimated from the effect of considering all c quarks as b's in the g-enriched and b-enriched classes. In addition, the gluon purity was varied by 5%. The difference between the normalized rations of table 6.2 and the results obtained with these new flavour compositions was estimated and the larger of the two variations was taken as a conservative estimate of this systematic uncertainty.

3. The effect of neglecting the c-enrichment in the b-enriched class when unfolding the effect of the contamination of the jet classes was estimated from the effects of considering all c quarks as b's, and all uds quarks as b's. The half distance between the two results was taken as a conservative estimate of this systematic uncertainty.

The effects of these sources of systematic uncertainty on the normalized ratios are summarized in table 6.3.

R'_X	Source 1	Source 2	Source 3	Total
Y Events				
R'_p	0.011	0.010	0.038	0.041
R'_K	0.014	0.001	0.014	0.020
R'_Λ	0.139	0.130	0.123	0.227
R'_{K^0}	0.112	0.074	0.008	0.134
Mercedes Events				
R'_p	0.013	0.003	0.050	0.052
R'_K	0.014	0.020	0.015	0.029

Table 6.3: Systematic uncertainties on the normalized ratios R'_X.

It can be seen in table 6.2 that all the R'_X values are consistent with unity, *i.e.* the ratios of the average multiplicities in g jets and q jets for all identified particles are consistent with the corresponding ratios for charged particles. The value of R'_p in Y events is about 1.5 standard deviations higher than predicted by HERWIG, and 2 to 3 standard deviations lower than predicted by JETSET. The value of R'_K is higher than predicted by HERWIG 5.8 by about 5 standard deviations in Y events, and by about 2.5 standard deviations in Mercedes events.

6.2 KNO distribution in jets at LEP I

The KNO distribution ($< n > P$ versus $z = n/ < n >$, where P is the probability to have an hadronic Z^0 decay with n charged particles and $< n >$ is the average multiplicity, see section 2.4.1) was obtained for charged particles in quark and gluon jets (and in particular in b jets) from events selected in the Mercedes and Y symmetric topologies.

The multiplicity distributions, **uncorrected** for the contamination of the different jet classes and for the reconstruction efficiency of the charged particles in those jets are presented for quark jets (in particular b jets) and gluon jets in figure 6.4.

The effects of the contaminations in the jet classes were unfolded by applying the algebraic correction method described in section 5.1.5.1. The reconstruction efficiencies were determined as described in section 5.1.5.3. The corrected multiplicity distributions are presented in figure 6.5.

From figure 6.5 the KNO distributions were obtained, they are presented in figure 6.6.

The shape of the distributions in the data is well reproduced by the Monte Carlo predictions.

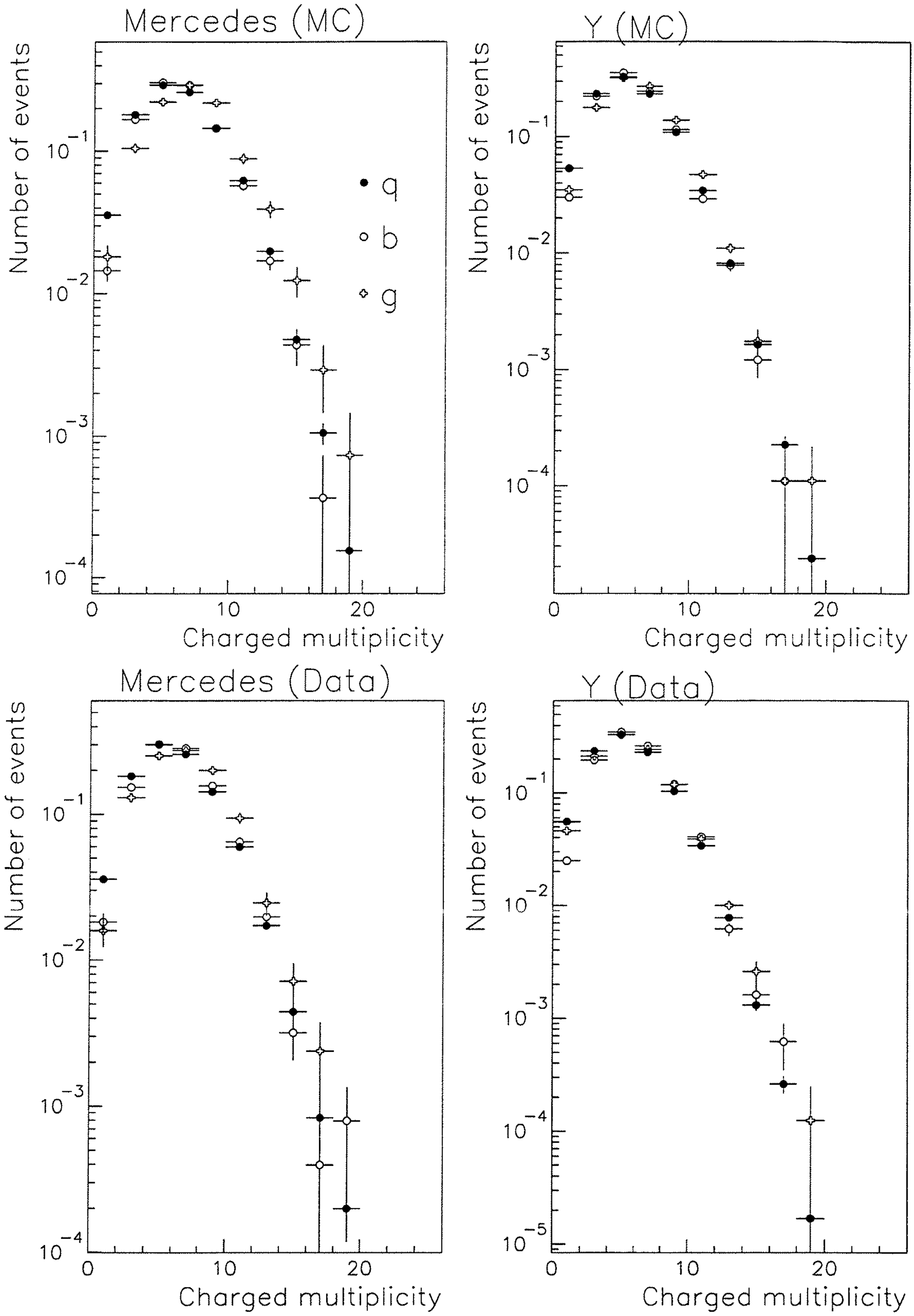

Figure 6.4: **Uncorrected** multiplicity distribution in quark jets (closed circles), b jets (open circles) and gluon jets (open crosses) for the data (lower plots) and the JETSET 7.3 Monte Carlo simulation (upper plots). The distributions were normalized to the number of events in the Mercedes and Y topologies.

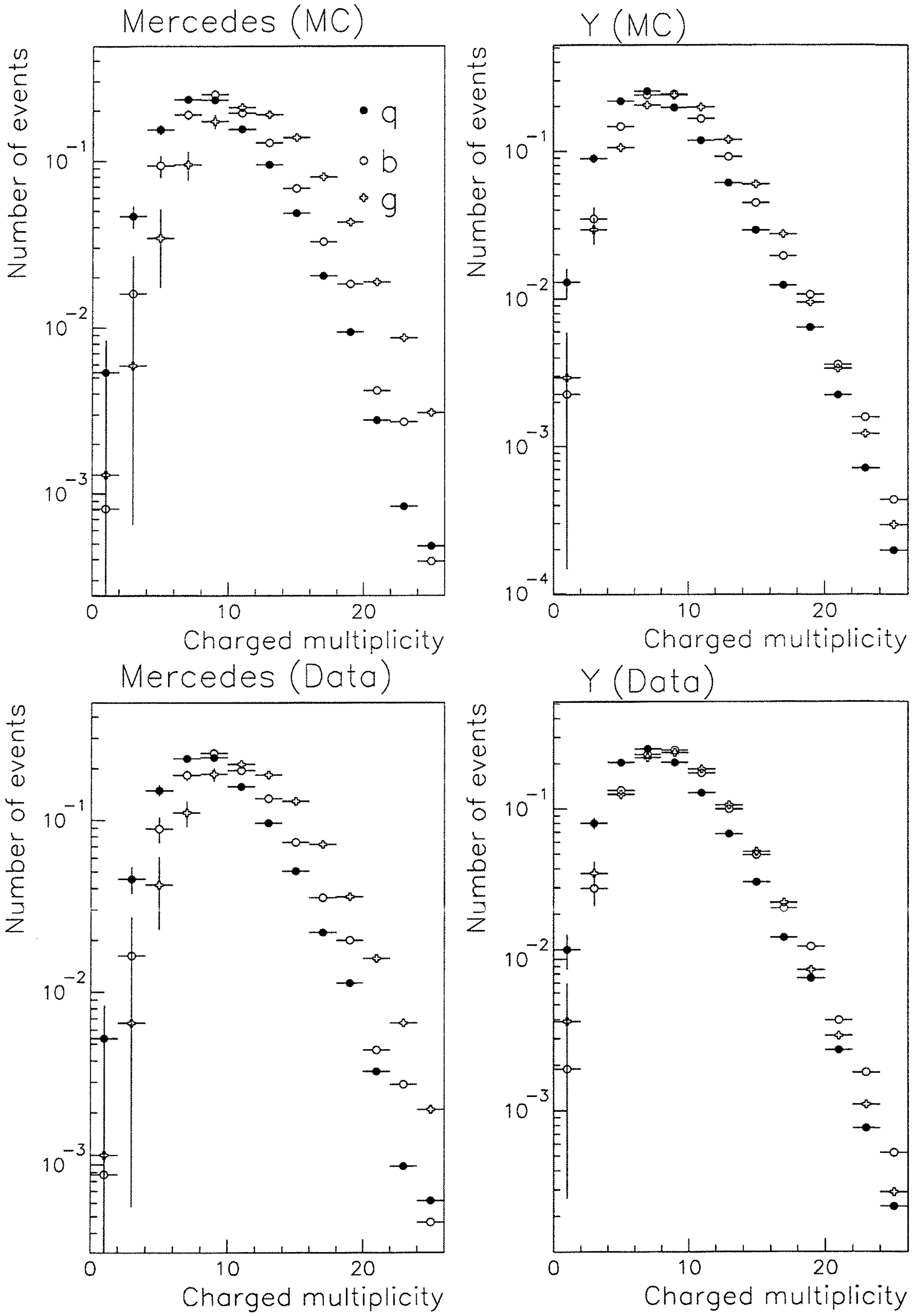

Figure 6.5: **Corrected** multiplicity distribution in quark jets (closed circles), *b* jets (open circles) and gluon jets (open crosses) for the data (lower plots) and the JETSET 7.3 Monte Carlo simulation (upper plots). The distributions were normalized to the number of events in the Mercedes and Y topologies.

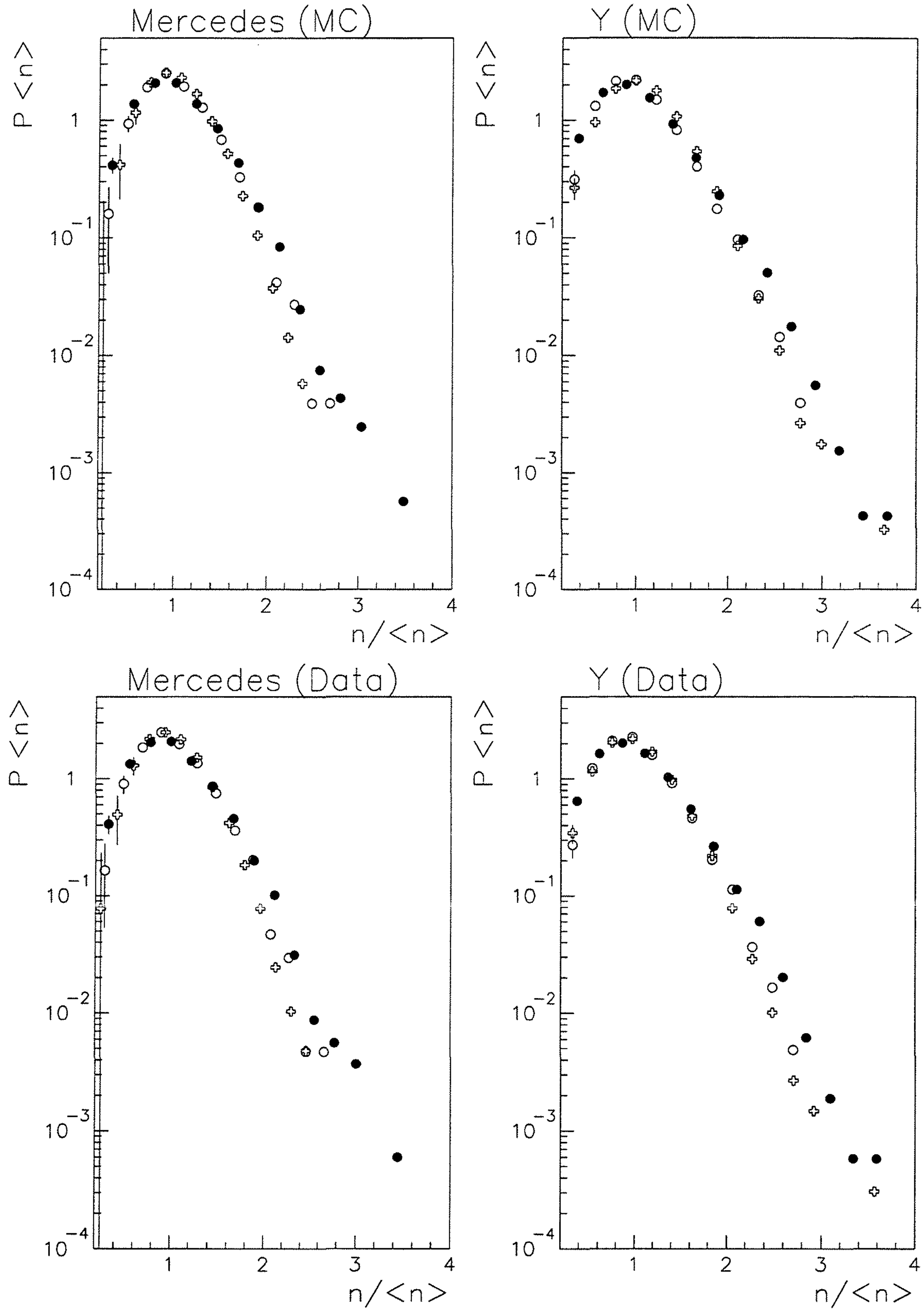

Figure 6.6: The KNO distribution for charged particles in quark jets (closed circles), b jets (open circles) and gluon jets (open crosses) for the data (lower plots) and the JETSET 7.3 Monte Carlo simulation (upper plots). N represents the multiplicity and n the average multiplicity.

A relevant outcome of these distributions is the ratio:

$$\frac{D}{<n>} = \frac{\sqrt{<n^2> - <n>^2}}{<n>}, \tag{6.3}$$

in table 6.4 this ratio is presented for q jets, b jets and gluon jets.

Geometry	Class	$\frac{D}{<n>}$ (DATA)	$\frac{D}{<n>}$ (JETSET 7.3)
Mercedes Events	g	0.028 ± 0.001	0.027
	b	0.035 ± 0.001	0.035
	q	0.044 ± 0.001	0.044
Y Events	g	0.040 ± 0.001	0.042
	b	0.040 ± 0.001	0.042
	q	0.053 ± 0.001	0.056

Table 6.4: $\frac{D}{<n>}$ for gluons, quarks and in particular b quarks.

It has been proposed [57] that the KNO distribution of b jets differ from the corresponding distribution in quark jets (not resolved) due to the decay of (virtual, time-like) $W^{\pm}$ bosons, which produce approximately always one extra charged particle per W. In this situation [58]:

$$P_b(n) \approx P_q(n - \nu), \tag{6.4}$$

where ν is a fixed parameter of the order of 1.5 [57]; P_q is the distribution for quarks and P_b the distribution for b jets. It follows [57]:

$$<n>_b = <n>_q + \nu, \tag{6.5}$$

(in agreement with QCD calculations [59]) and

$$\frac{D_b}{<n>_b} = \frac{D_q}{<n>_q}\left(\frac{1}{1+\nu/<n>_q}\right), \tag{6.6}$$

where $<n>_b$ is the average multiplicity in b jets, $<n>_q$ the average multiplicity in q jets, D_b is the dispersion of the KNO distribution in b jets and D_q the dispersion of the KNO distribution in q jets. For $\nu \sim 1.5$, as expected, and a multiplicity per jet $<n> \sim 8-9$[1] it is predicted $\frac{D_b}{<n>_b} \sim 0.8 \cdot \frac{D_q}{<n>_q}$, as observed (table 6.4).

The difference in the KNO distributions for gluon jets and quark jets, comes from the different branching processes they exhibit (see the introductory chapters).

[1] For Y events the value measured was $<n>_q = 8.08 \pm 0.15$ and for Mercedes events $<n>_q = 9.00 \pm 0.24$.

In the limit $N_c \to \infty$, N_c being the number of colours, a gluon behaves essentially as a quark-antiquark pair. Based on this approach it was proposed [60] that the width of the KNO distribution $(\frac{D^2}{<n>^2})$ for quark and gluon jets is given by:

$$\left(\frac{D^2}{<n>^2}\right)_{quark} = \frac{1}{(1+\alpha)(1+2\alpha)}\left[\frac{\alpha}{\overline{\alpha}}(2+\alpha)+(1+2\alpha)\right]-1 \tag{6.7}$$

and

$$\left(\frac{D^2}{<n>^2}\right)_{gluon} = \frac{2+\alpha}{1+2\alpha}-1 \tag{6.8}$$

respectively. The parameter α is related to the probability for a gluon to emit additional gluons [60] and $\overline{\alpha}$ is the $q \to qg$ transition probability. At low energies one expects $\alpha < \overline{\alpha}$. In the limit $\alpha = \overline{\alpha}$ it follows: $R_D \equiv (\frac{D^2}{<n>^2})_{quark}/(\frac{D^2}{<n>^2})_{gluon} = 2$. This result, however, overestimates our observations: $R_D = 1.6$ for Mercedes events and $R_D = 1.3$ for Y events. In the situation [60]:

$$1 \geq \frac{\alpha}{\overline{\alpha}} > 1 - \frac{1-\alpha^2}{2+\alpha}, \tag{6.9}$$

we have $(\frac{D^2}{<n>^2})_{quark} > (\frac{D^2}{<n>^2})_{gluon}$, as observed (table 6.4).

6.3 Identified hadrons at LEP II

In this section the analysis of the K^+, p, K^0 and Λ spectra in e^+e^- interactions recorded by LEP in the years 1995 to 1997 at energies above the Z^0 (around 133, 161, 172 and 183 GeV) were measured. The measurements were compared to the MLLA+LPHD calculations and to the JETSET 7.4/PYTHIA 5.7 and HERWIG 5.8 model predictions. In particular, the results concerning the measurement of the ξ_p distribution, where $\xi_p = -\log(\frac{2p}{\sqrt{s}})$ (p is the momentum of the particle and $\sqrt{s}$ is the center of mass energy), average hadron multiplicity ($< n >$) in hadronic final states and the evolution of $< n >$ and ξ^*, where ξ^* is the position of the maximum of the differential cross-section as a function of ξ_p, with $\sqrt{s}$ will be presented.

The models most frequently used in e^+e^- annihilation to describe the fragmentation process, are those using string and cluster fragmentation implemented, for instance, via the JETSET/PYTHIA and HERWIG Monte Carlo models, as referred in section 2.3.

A different and purely analytical approach ([59]) giving quantitative predictions of hadronic spectra are QCD calculations using the so-called Modified Leading Logarithmic Approximation (MLLA) under the assumption of Local Parton Hadron Duality (LPHD). In this picture the particle yield is described by a parton cascade, and the virtuality cut-off Q_0 is lowered to values of the order of 100 MeV, comparable to the hadron masses; at the end of the parton cascade it is assumed that a calculated spectrum for partons can be related to the spectrum of real hadrons by simple normalization constants (see section 2.2 for more details).

The momentum spectra of particles produced can be calculated as a function of the variable ξ_p, where $\xi_p = -\log(\frac{2p}{\sqrt{s}})$ (p is the momentum of the particle and $\sqrt{s}$ is the center of mass energy):

$$\frac{1}{\sigma}\frac{d\sigma}{d\xi_p} = K_{LPHD} \cdot f(\xi_p, X, \lambda) \tag{6.10}$$

with

$$X = \log\frac{\sqrt{s}}{Q_0} \quad ; \quad \lambda = \log\frac{Q_0}{\Lambda_{eff}} . \tag{6.11}$$

These MLLA+LPHD predictions involve three parameters: an effective scale parameter Λ_{eff}, a momentum cut-off Q_0 in the evolution of the parton cascade and an overall normalization factor K_{LPHD}. The function 6.10 has the form of a "humped-backed plateau", which is approximately Gaussian in ξ_p [61]. It can be approximated by a distorted Gaussian over the entire spectrum, as proposed in [62, 63]:

(6.12)
$$D(N, <\xi_p>, \sigma, \delta, s, k) = \frac{N}{\sigma\sqrt{2\pi}} \exp(\frac{1}{8}k - \frac{1}{2}s\delta - \frac{1}{4}(2+k)\delta^2 + \frac{1}{6}s\delta^3 + \frac{1}{24}k\delta^4)$$

where N is the average multiplicity, $\delta = \frac{\xi_p - <\xi_p>}{\sigma}$ with $<\xi_p>$ being the mean of the ξ_p distribution ($<\xi_p>$ coincides with the peak position up to the next-to-leading order only [59]), σ is the width, s the skewness and k the kurtosis of the distribution. For a pure Gaussian s and k vanish.

To check the validity of the MLLA+LPHD approach, it is interesting to study the evolution with the center of mass energy of the maximum, ξ^*, of the ξ_p distribution. In the framework of the MLLA+LPHD the dependency of ξ^* on the center of mass energy can be expressed as [59, 62, 64]:

$$\xi^* = Y\left(\frac{1}{2} + \sqrt{C/Y} - C/Y\right) + F_h(\lambda), \tag{6.13}$$

where

$$Y = \log\frac{E_{beam}}{\Lambda_{eff}} \; , \; C = \left(\frac{11N_c/3 + 2n_f/(3N_c^2)}{4N_c}\right)^2 \cdot \left(\frac{N_c}{11N_c/3 - 2n_f/3}\right),$$

with N_c being the number of colours and n_f the active number of quark flavors in the fragmentation process. $F_h(\lambda)$ depends on the hadron type through the ratio $\lambda = \log\frac{Q_0}{\Lambda_{eff}}$ [59]:

$$F_h(\lambda) = -1.46\lambda + 0.207\lambda^2 \pm 0.06. \tag{6.14}$$

6.3.1 ξ^* distribution

The ξ_p distributions for charged kaons, neutral kaons, protons and Λs at the various center of mass energies above the Z^0 peak are shown in figures 6.7 to 6.10. These distributions were afterwards subtracted from the W^+W^- background (see figures 6.7 to 6.10) and corrected for the tagging efficiency and detector effects, as described in section 5.2.4.

The corrected ξ_p distributions are shown for charged kaons, neutral kaons, protons and Λs in figure 6.11, figure 6.12, figure 6.13 and figure 6.14 respectively. In the figures the predictions from the generators JETSET 7.4/PYTHIA 5.7 and HERWIG 5.8, and the fit to expression 6.12, are also shown. In the fit to the data distributions, s and k were fixed to the values obtained by fitting equation 6.12 to the corresponding JETSET 7.4/PYTHIA 5.7 Monte Carlo distributions. Within the statistics of the data samples analysed the shape of the ξ_p distribution is well described by both generators, JETSET 7.4/PYTHIA 5.7 and HERWIG 5.8.

The fit of the data points to expression 6.12 was used to extract the peak position of the ξ_p distribution, ξ^*.

In figure 6.15 and table 6.5 the results on the evolution of ξ^* with the center of mass energy are presented. The data up to center of mass energies of 91 GeV was taken from previous measurements [64]. The fit to expression 6.13, where F_h and Λ_{eff} were taken as free parameters, is superimposed to the data points (solid line). Figure 6.15 shows that the fitted functions follow the data points rather well.

From table 6.5 and figure 6.15 it is shown that there is good agreement between the data and the predictions from the generators JETSET 7.4 and HERWIG 5.8.

The systematic errors on ξ^* were obtained as the sum in quadrature of the following contributions:

- From the original $dN/d\xi_p$ distribution two "distorted" distributions were obtained: one of them by adding 1σ to the values below ξ^* and subtracting 1σ to the values above, and the other by subtracting 1σ to the values below ξ^* and adding 1σ to the values above. From these distributions, two new values were obtained for ξ^*. These were compared to the values obtained from the normal distribution, and the larger difference was taken for the systematic error.

- The difference between the maximum fitted using a distorted Gaussian and the maximum fitted using a simple Gaussian.

The parameters F_h and Λ_{eff} obtained from the fit (figure 6.15) are presented in table 6.6. The values obtained for F_h agree within the errors with the results from [64], in which data with center of mass energies varying from 14 GeV to 91 GeV was used.

This Λ_{eff} corresponds to a value of $\alpha_s \sim 0.1$ when plugged in the evolution equation at leading order [64] (see section 2.2.2):

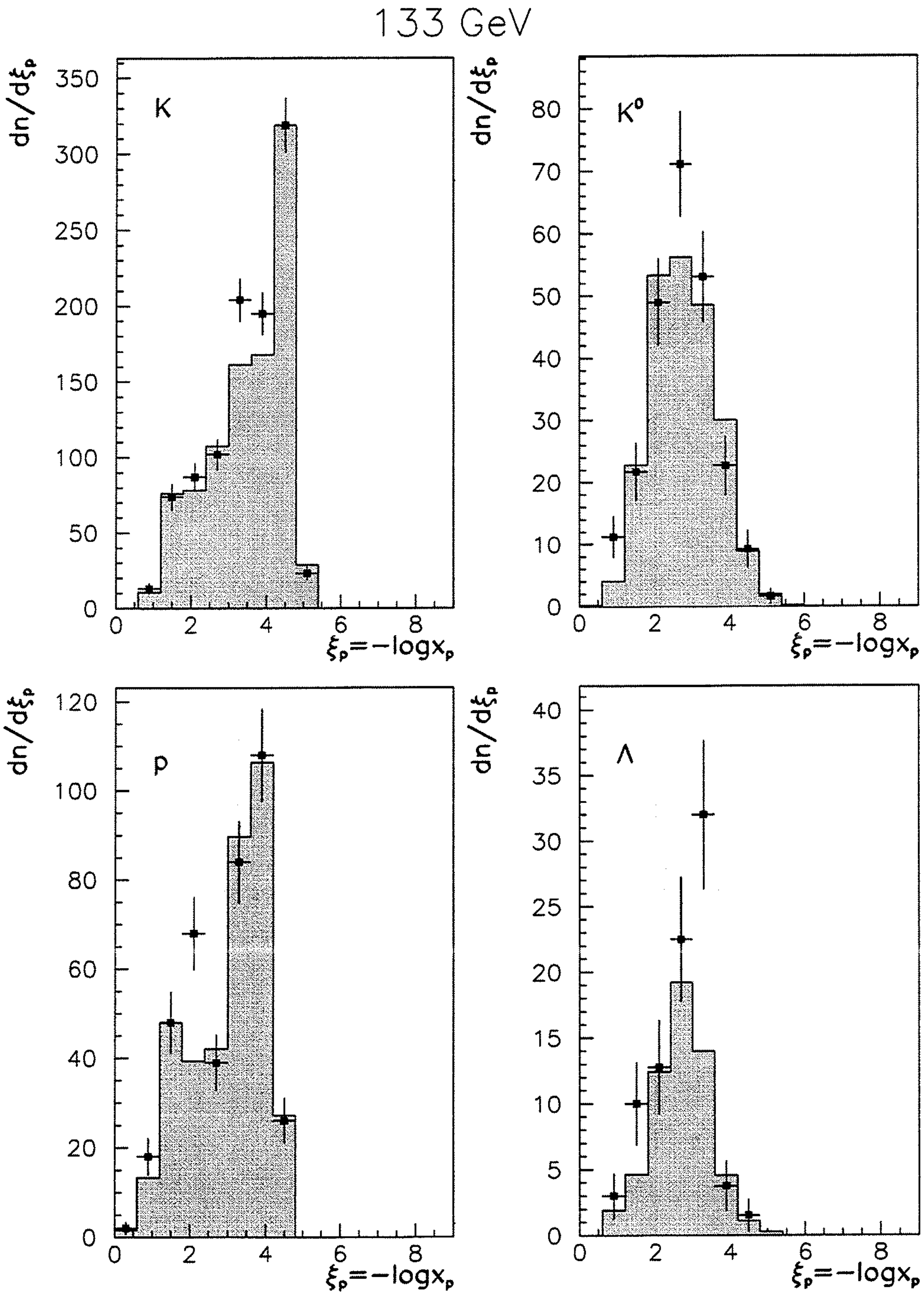

Figure 6.7: ξ_p distributions for K^+, K^0, p and Λ, as indicated in the figures, at 133 GeV/c: data (points). The grey histogram represents the $q\overline{q}$ simulation.

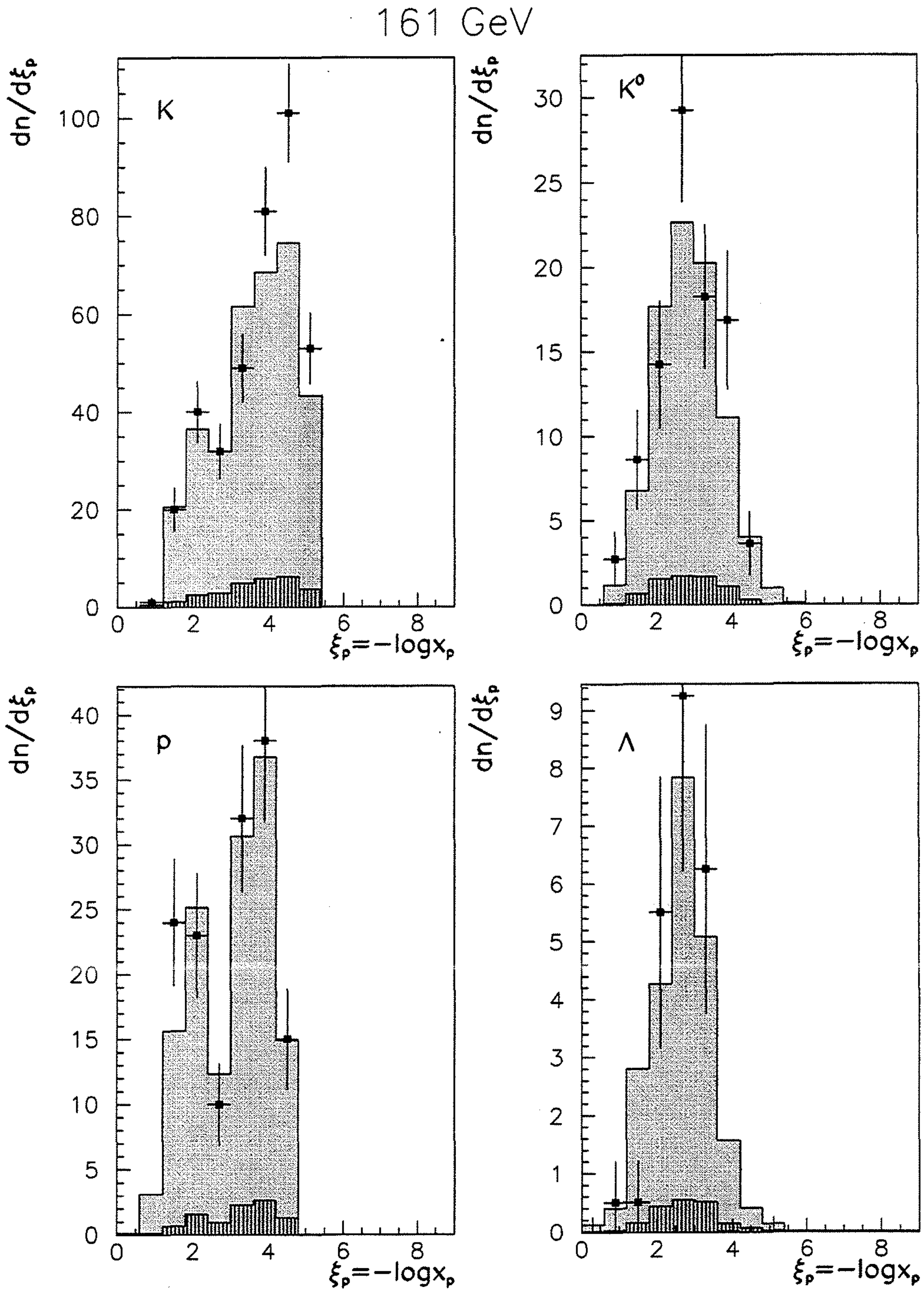

Figure 6.8: ξ_p distributions for K^+, K^0, p and Λ, as indicated in the figures, at 161 GeV/c: data (points). The grey histogram represents the $q\bar{q}$ simulation and the dark histogram represents the $\mathrm{W}^+\mathrm{W}^-$ simulation.

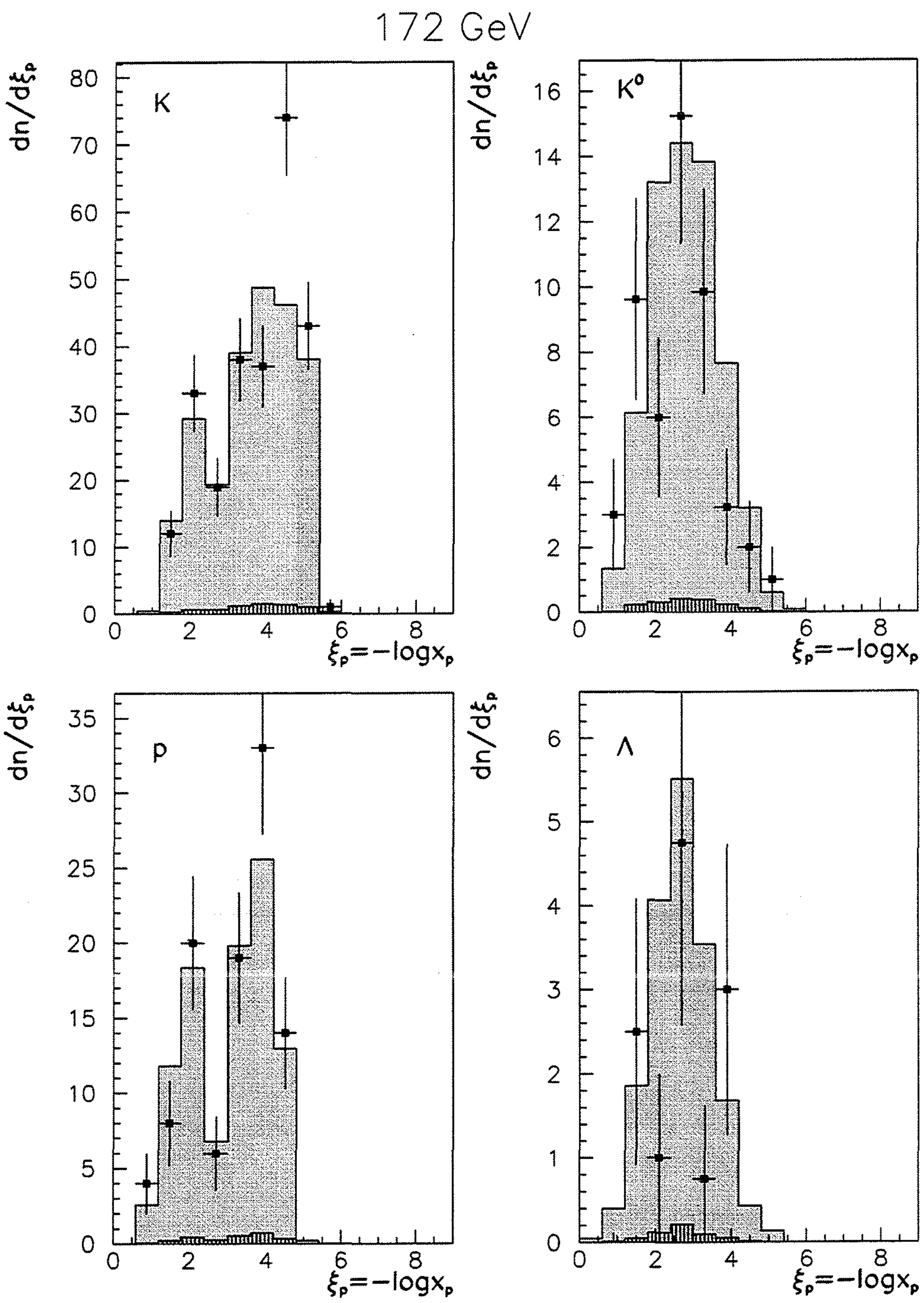

Figure 6.9: ξ_p distributions for K^+, K^0, p and Λ, as indicated in the figures, at 172 GeV/c: data (points). The grey histogram represents the $q\bar{q}$ simulation and the dark histogram represents the W^+W^- simulation.

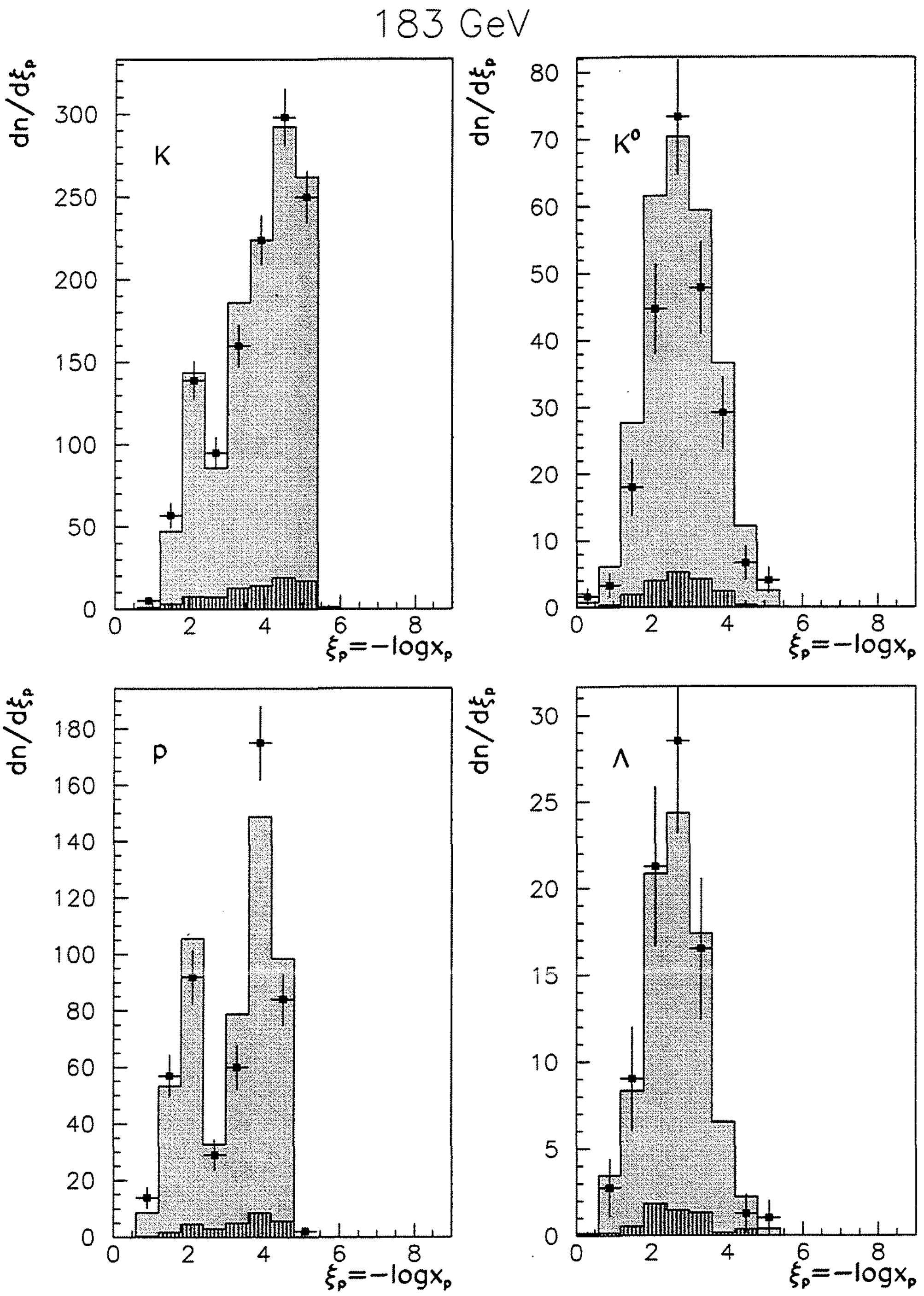

Figure 6.10: ξ_p distributions for K^+, K^0, p and Λ, as indicated in the figures, at 183 GeV/c: data (points). The grey histogram represents the $q\bar{q}$ simulation and the dark histogram represents the W^+W^- simulation.

$$\frac{\alpha_s}{2\pi} = \frac{1}{b \cdot \log(E_{beam}/\Lambda_{eff})} \tag{6.15}$$

where

$$b = 11N_c/3 - 2n_f/3, \tag{6.16}$$

N_c is the number of colours and n_f the active number of quark flavors in the fragmentation process.

This suggests that MLLA+LPHD could possibly give a quantitative description of the observed particle spectra. The MLLA+LPHD approach is presented here as an attempt to understand some properties of multihadron production in terms of perturbative QCD, namely to test the possibility within this framework to determine hadron properties based on the corresponding parton distributions. It was shown that this approach can give predictions for properties of the momentum spectra that can be compared with experimental data.

6.3.2 Average multiplicity

The multiplicity of the identified final states per hadronic event was obtained from the integration of the distributions shown in figures 6.11 to 6.14 inside a range varying according to the particle type and energy; outside this range the fraction of particles was extrapolated using the JETSET 7.4 prediction. The results are shown in figure 6.16 and table 6.7 and they are compared with the predictions from JETSET 7.4 and HERWIG 5.8. In figure 6.16 the results shown for energies below 133 GeV (open squares) were extracted from [65].

The systematic uncertainties on the multiplicity were obtained as the sum in quadrature of the following contributions:

- The difference between the JETSET and HERWIG predictions in the unseen region.
- The uncertainty coming from the particle identification efficiency. A relative systematic error of 2% was assumed for protons and charged kaons as in [66]; a relative error of 3% for K^0 [67] and a relative error of 5% for Λ [68].

The Monte Carlo programs JETSET 7.4 and HERWIG 5.8 display in general a fair agreement with the data. However the K^0 multiplicity at 183 GeV is 3.4 standard deviations (2.4 standard deviations) below the HERWIG (JETSET) predictions; HERWIG underestimates the results for protons at 133 GeV and overestimates the results for charged kaons at 161 GeV by 2 standard deviations.

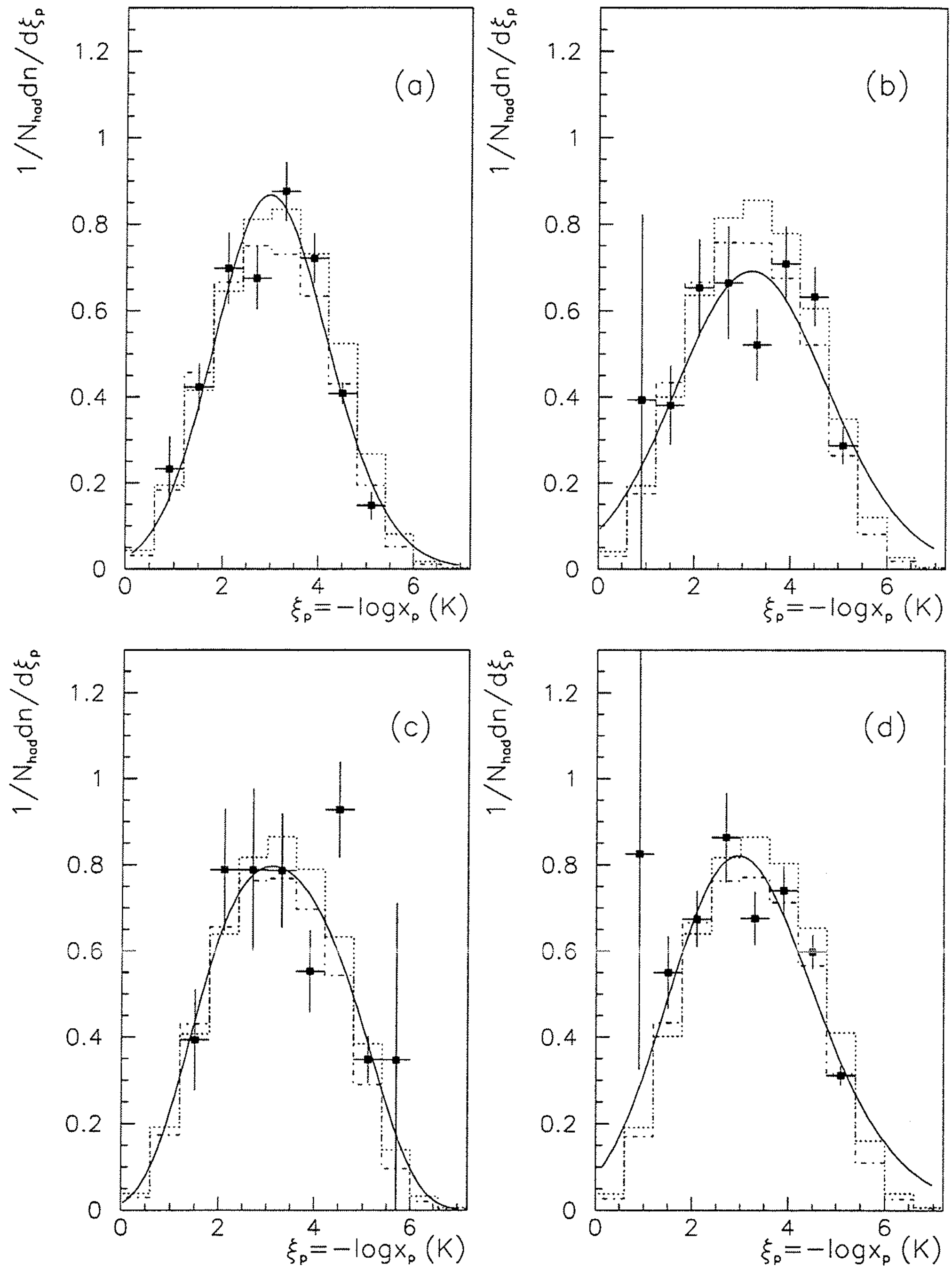

Figure 6.11: ξ_p distributions (efficiency corrected) for charged kaons at 133 GeV/c (a), 161 GeV/c (b), 172 GeV/c (c) and 183 GeV/c (d): data (points), simulation using JETSET (dashed-dotted line) and HERWIG (dotted line). The full curves show the fit of the data to the distorted Gaussian.

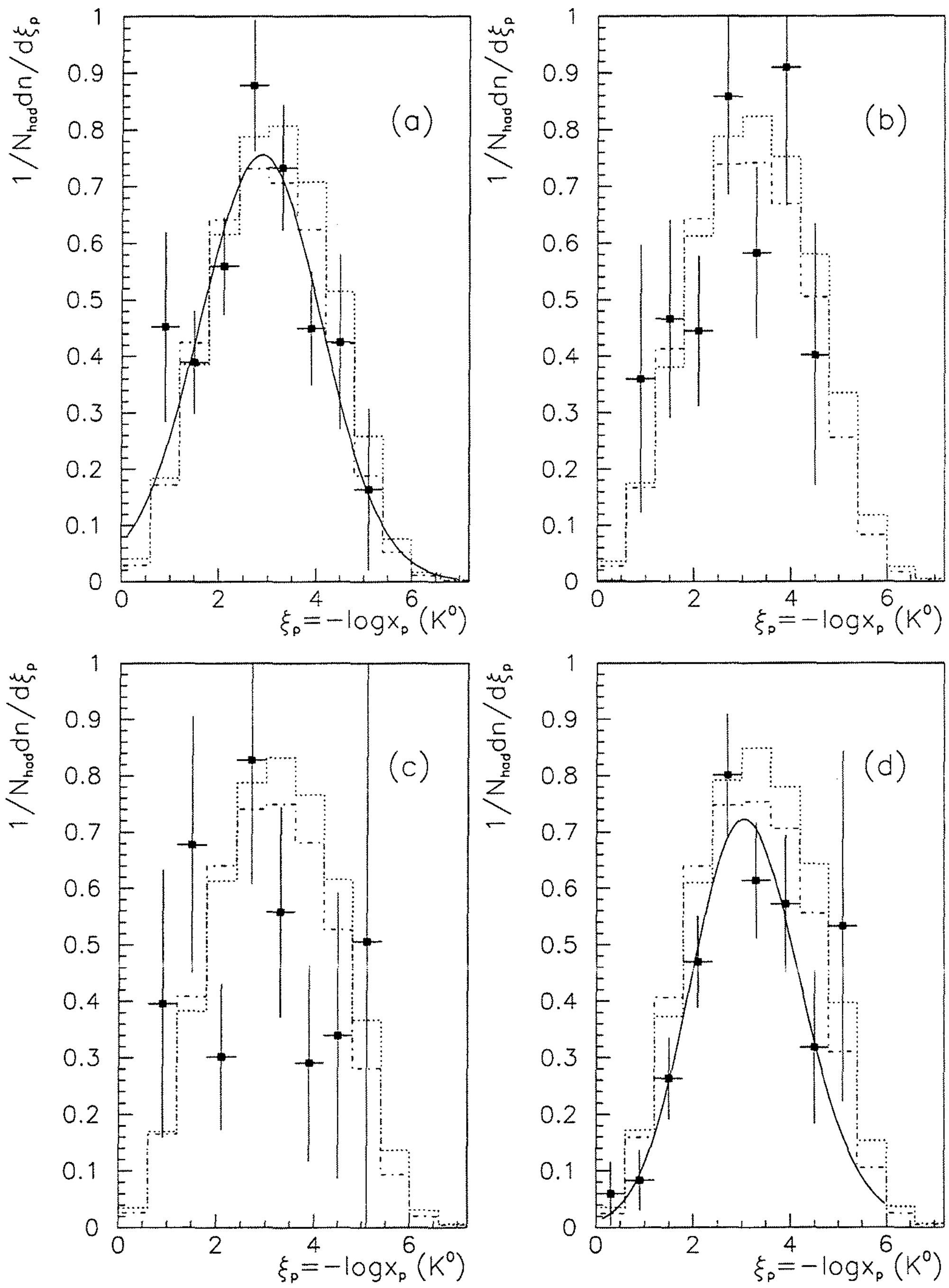

Figure 6.12: ξ_p distributions (efficiency corrected) for neutral kaons at 133 GeV/c (a), 161 GeV/c (b), 172 GeV/c (c) and 183 GeV/c (d): data (points), simulation using JETSET (dashed-dotted line) and HERWIG (dotted line). The full curves show the fit of the data to the distorted Gaussian.

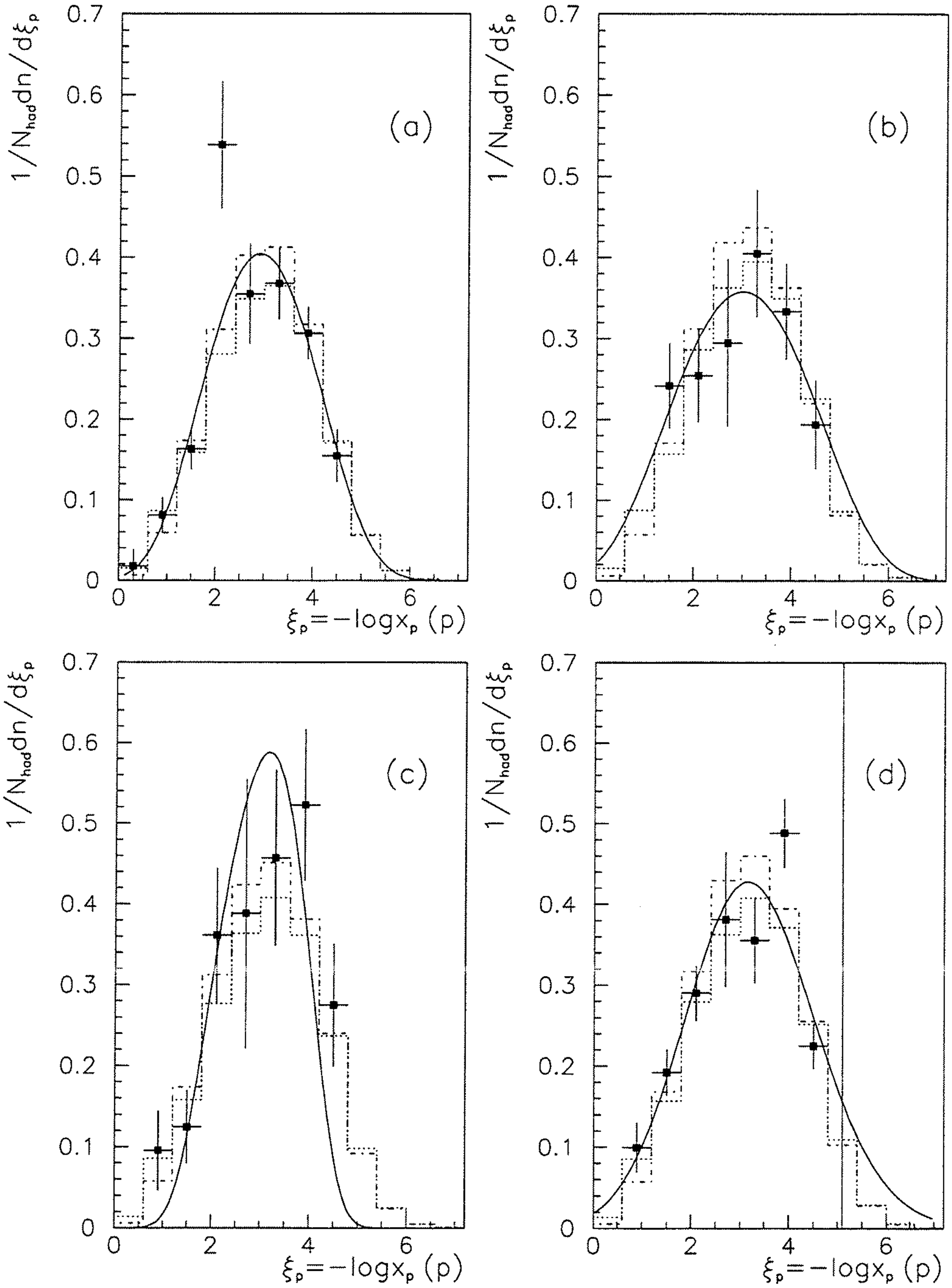

Figure 6.13: ξ_p distributions (efficiency corrected) for protons at 133 GeV/c (a), 161 GeV/c (b), 172 GeV/c (c) and 183 GeV/c (d): data (points), simulation using JETSET (dashed-dotted line) and HERWIG (dotted line). The full curves show the fit of the data to the distorted Gaussian.

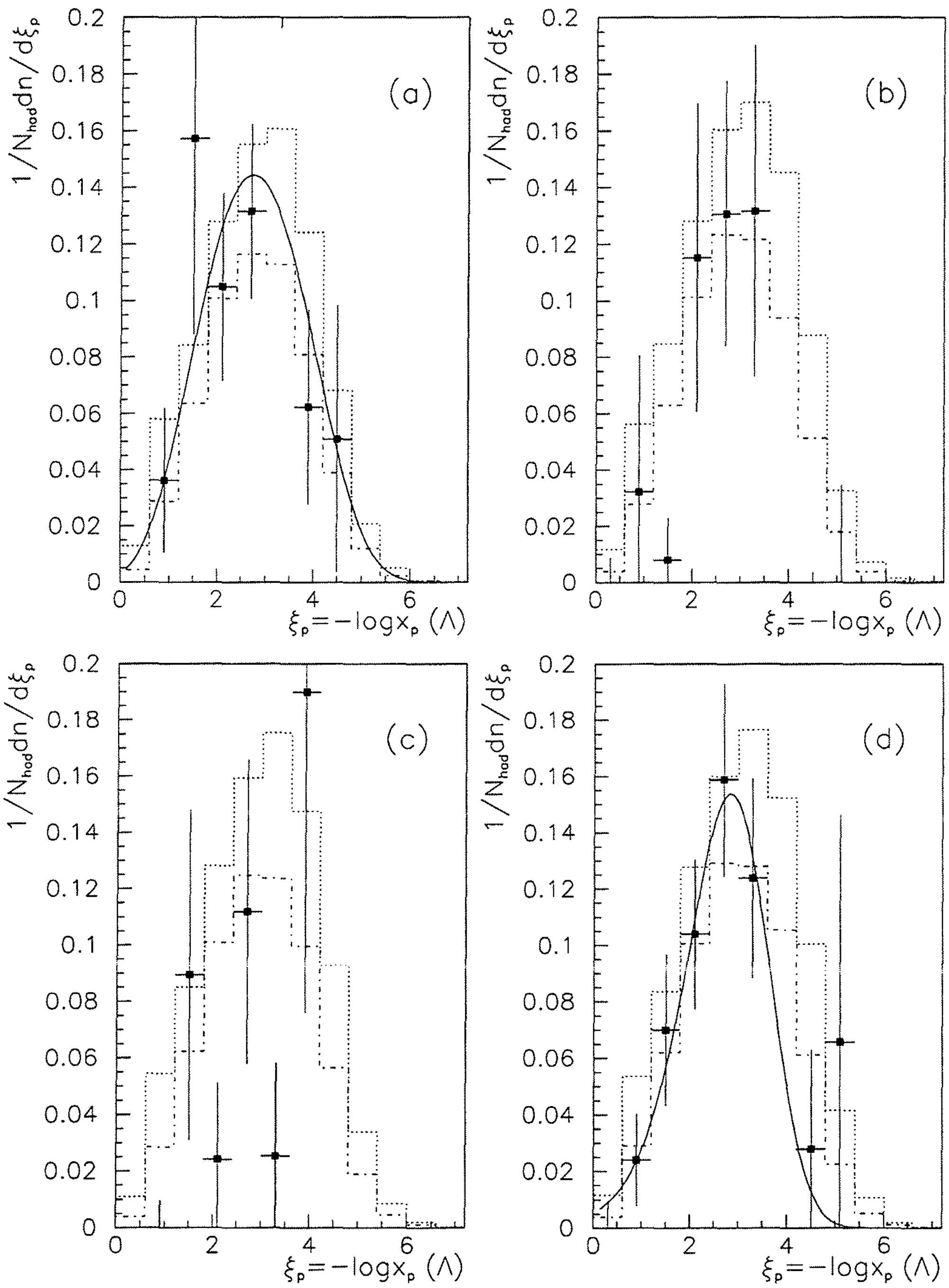

Figure 6.14: ξ_p distributions (efficiency corrected) for Λ at 133 GeV/c (a), 161 GeV/c (b), 172 GeV/c (c) and 183 GeV/c (d): data (points), simulation using JETSET (dashed-dotted line) and HERWIG (dotted line). The full curves show the fit of the data to the distorted Gaussian.

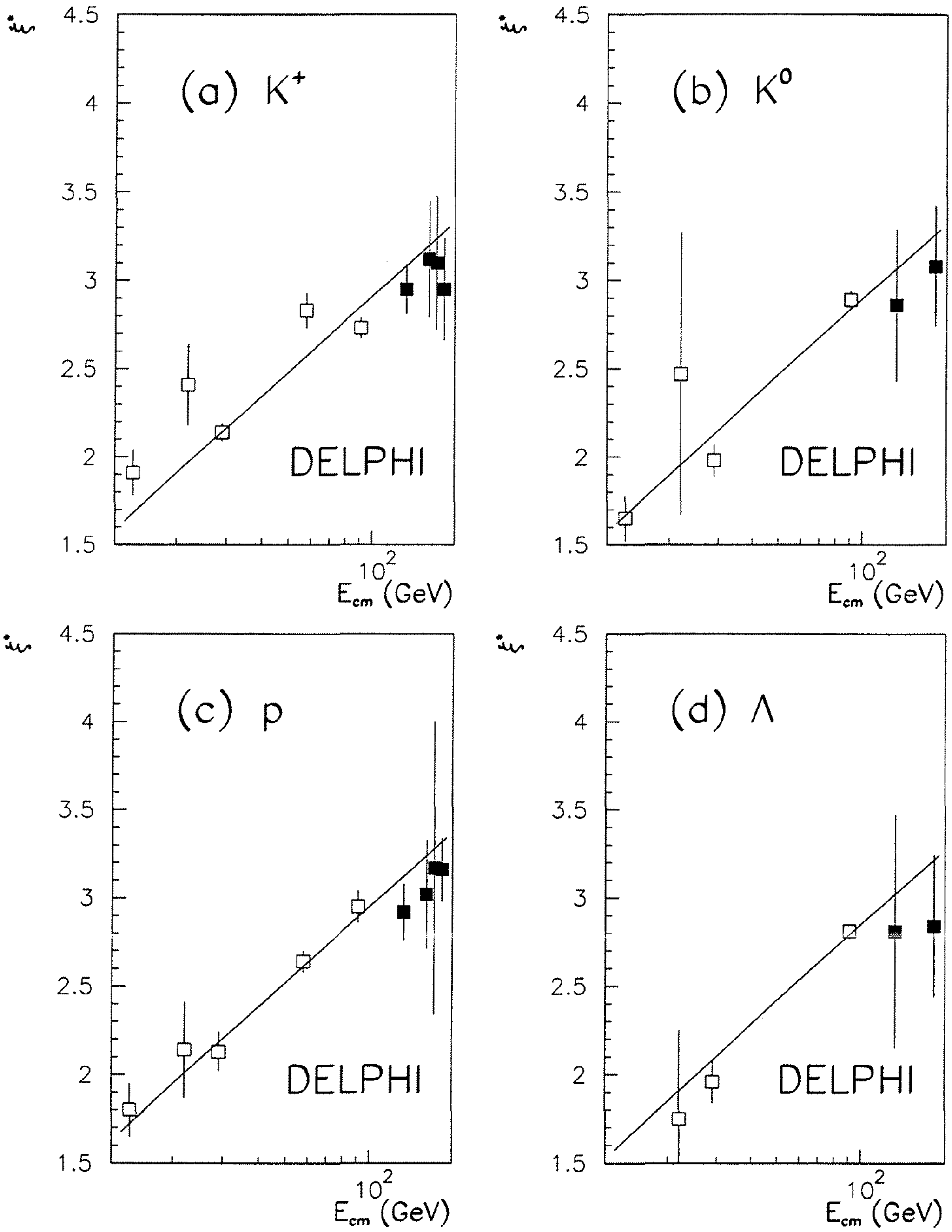

Figure 6.15: The maximum ξ^* of the ξ_p-distribution is shown for K^+ (a), K^0 (b), p (c) and Λ (d) as function of the center-of-mass energy (closed squares). The fit (solid line) is superimposed to the data points (see text).

$\sqrt{s}$ (GeV)	Particle	Fitting range (GeV)	ξ^* (Data)	JETSET 7.4	HERWIG 5.8
133	K^+	1.2-5.4	$2.95 \pm 0.06 \pm 0.13$	2.84	3.12
	K^0	0.6-5.4	$2.86 \pm 0.14 \pm 0.41$	2.87	3.15
	p	0.0-4.8	$2.92 \pm 0.08 \pm 0.14$	2.98	3.10
	Λ	0.6-4.8	$2.81 \pm 0.24 \pm 0.62$	2.79	2.99
161	K^+	1.2-4.8	$3.12 \pm 0.22 \pm 0.25$	2.96	3.25
	K^0	-	-	-	-
	p	1.2-4.8	$3.02 \pm 0.17 \pm 0.26$	3.08	3.23
	Λ	-	-	-	-
172	K^+	1.2-5.4	$3.10 \pm 0.09 \pm 0.37$	3.02	3.27
	K^0	-	-	-	-
	p	0.6-4.8	$3.17 \pm 0.11 \pm 0.82$	3.12	3.26
	Λ	-	-	-	-
183	K^+	1.2-5.4	$2.95 \pm 0.11 \pm 0.27$	3.01	3.30
	K^0	0.6-5.4	$3.08 \pm 0.15 \pm 0.30$	3.07	3.34
	p	0.6-4.8	$3.16 \pm 0.08 \pm 0.16$	3.15	3.30
	Λ	0.6-4.2	$2.84 \pm 0.14 \pm 0.38$	2.99	3.20

Table 6.5: ξ^* for charged kaons, K^0, protons and Λ at 133 GeV, 161 GeV, 172 GeV and 183 GeV. In the data the first uncertainty is statistical, the second is systematic.

Hadron	F_h	Λ_{eff}	$\chi^2/n.d.f$
K^+	-1.57 ± 0.09	0.06 ± 0.02	1.37
K^0	-1.45 ± 0.10	0.08 ± 0.01	0.62
p	-1.49 ± 0.13	0.07 ± 0.01	0.28
Λ	-1.49 ± 0.27	0.08 ± 0.01	0.41

Table 6.6: Results of the fit of the evolution of ξ^* with the center of mass energy.

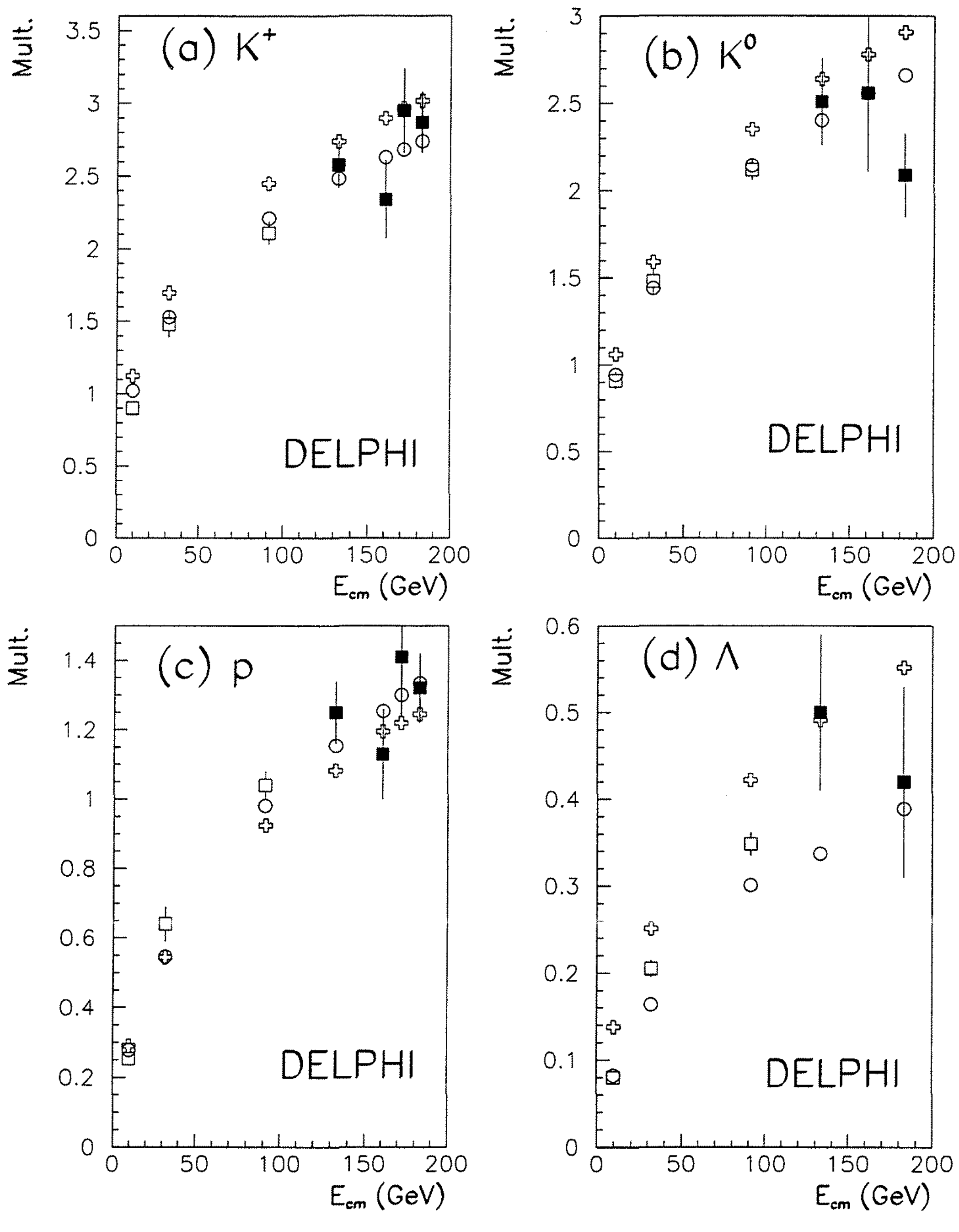

Figure 6.16: Average multiplicity of $K^{\pm}$(a), K^0(b), p (c) and Λ (d) as function of the center-of-mass energy (black squares). Simulation using JETSET 7.4 (open circles) and HERWIG 5.8 (open crosses) are superimposed.

$\sqrt{s}$ (GeV)	Particle	Integration range (GeV)	$< n >$ (Data)	JETSET 7.4	HERWIG 5.8
133	K^+	1.2-5.4	$2.58 \pm 0.10 \pm 0.13$	2.49	2.74
	K^0	0.6-5.4	$2.51 \pm 0.21 \pm 0.14$	2.40	2.64
	p	0.0-4.8	$1.25 \pm 0.08 \pm 0.03$	1.15	1.08
	Λ	0.6-4.8	$0.50 \pm 0.07 \pm 0.05$	0.34	0.49
161	K^+	1.2-4.8	$2.34 \pm 0.18 \pm 0.20$	2.63	2.90
	K^0	0.6-4.2	$2.56 \pm 0.38 \pm 0.25$	2.56	2.78
	p	1.2-4.8	$1.13 \pm 0.12 \pm 0.05$	1.25	1.19
	Λ	-	-	-	-
172	K^+	1.2-5.4	$2.95 \pm 0.23 \pm 0.17$	2.68	2.97
	K^0	-	-	-	-
	p	0.6-4.8	$1.41 \pm 0.17 \pm 0.04$	1.30	1.22
	Λ	-	-	-	-
183	K^+	1.2-5.4	$2.87 \pm 0.12 \pm 0.17$	2.74	3.02
	K^0	0.6-5.4	$2.09 \pm 0.18 \pm 0.16$	2.66	2.91
	p	0.6-4.8	$1.32 \pm 0.09 \pm 0.03$	1.33	1.24
	Λ	0.6-4.2	$0.42 \pm 0.06 \pm 0.09$	0.39	0.55

Table 6.7: Average multiplicity for charged kaons, K^0, protons and Λ at 133 GeV, 161 GeV, 172 GeV and 183 GeV. In the data the first uncertainty is statistical, the second is systematic.

Chapter 7

Conclusions

The transition from the quark and gluon degrees of freedom, appropriate in perturbative theory, to the hadrons observed by real world experiments is complex and a complete perturbative expansion is impossible. To describe this region of phase space non-perturbative phenomenological models, mostly relying on mathematical constructs such as clusters and strings, were developed. In these models, implemented via Monte Carlo programs, the process which leads the initial quark-antiquark pair in the process: $e^+e^- \rightarrow \gamma^*/Z^0 \rightarrow q\overline{q}$, to the final hadrons we observe, is described in steps. First, gluon emission and parton branching of the original $q\overline{q}$ pair take place. In the second phase, at a certain virtuality Q_0, quarks and gluons produced in the first phase transform into mesons and baryons. In the third phase the unstable states decay into hadrons.

A different and purely analytical approach giving quantitative predictions of hadronic spectra are QCD calculations using the so-called Modified Leading Logarithmic Approximation (MLLA) under the assumption of Local Parton Hadron Duality (LPHD). In this model the particle yield is described by a parton cascade and at the end of the parton cascade it is assumed that a calculated spectrum for partons can be related to the spectrum of real hadrons by simple normalization constants.

In this thesis final states of charged particles (unresolved) and of hadrons (protons, charged kaons, K^0 and Λ) identified with the DELPHI detector at LEP were analysed. The final states were selected in quark and gluon jets from the symmetric topologies Mercedes and Y (at LEP I energies), and in $q\overline{q}$ events (at higher energies). The particle identification profited from the tracking detectors and mainly from the RICH detectors (Ring Imaging Čerenkov detectors) of DELPHI.

The aim was to test some of the phenomenological models proposed, in particular the JETSET and HERWIG models, based on string and cluster fragmentation, respectively, and to check, using the distribution ξ^* versus $\sqrt{s}$ for identified hadrons, the validity of the MLLA+LPHD approach in this context.

At 91 GeV the following analysis have been performed:

- The measurement of the multiplicity ratio of identified particles (protons, charged kaons, K^0 and Λ) in gluon jets relative to quark jets and its evolution with momentum.
- The KNO distribution ($< n > P$ versus $z = n/ < n >$, where P is the probability to have an hadronic Z^0 decay with n charged particles and $< n >$ is the average multiplicity) for charged particles in quark and gluon jets (and in particular in b jets).

Both JETSET and HERWIG give a satisfactory description of the evolution with momentum of the multiplicity ratio of identified particles (protons, charged kaons, K^0 and Λ) in gluon jets relative to quark jets.

The enhancement of identified particles' production (protons, charged kaons, K^0 and Λ) in gluon jets relative to quark jets is consistent with the corresponding enhancement observed for all charged particles (unresolved). This is in disagreement with HERWIG predictions for protons in Y events (1.5σ difference) and charged kaons in both Y (5σ difference) and Mercedes (2.5σ difference) events. Also JETSET is in disagreement with the proton results in Y events by 2 to 3σ.

The width of the KNO distribution $\frac{D^2}{<n>^2}$ was measured for gluon jets, quark jets and b jets in particular. The ratio of the width of the KNO distribution for gluon jets relative to quark jets and the ratio of the width of the KNO distribution for b jets relative to quark jets were compared with theoretical predictions [57, 58, 60].

Based on the difference between light quarks and b's, due to the decay of virtual $W^{\pm}$ bosons, it was predicted $\frac{D_b}{<n>_b} \sim 0.8 \cdot \frac{D_q}{<n>_q}$ [57, 58], reproduced by the present results. Due to the different branching processes for gluons and quarks, it is expected [60] $(\frac{D^2}{<n>^2})_{quark} > (\frac{D^2}{<n>^2})_{gluon}$, as observed. In the present analysis we have obtained $R_D \equiv (\frac{D^2}{<n>^2})_{quark}/(\frac{D^2}{<n>^2})_{gluon} = 1.6$ (1.3) for Mercedes (Y) events.

At energies above the Z^0 resonance, the multiplicity of identified hadrons (protons, charged kaons, K^0 and Λ) and the peak of the ξ_p distribution ($\xi_p = -\log(\frac{2p}{\sqrt{s}})$), ξ^*, were measured in $q\bar{q}$ events.

The Monte Carlo programs JETSET 7.4 and HERWIG 5.8 display in general a fair agreement with the data. However the K^0 multiplicity at 183 GeV is 3.4 standard deviations (2.4 standard deviations) below the HERWIG (JETSET) predictions; HERWIG underestimates the results for protons at 133 GeV and overestimates the results for charged kaons at 161 GeV by 2 standard deviations.

Within the statistics of the data samples analysed the shape of the ξ_p distribution is well described by both generators, JETSET and HERWIG.

The parameter $\Lambda_{eff} \sim 0.07$ was obtained from the data by fitting the evolution ξ^* versus $\sqrt{s}$ to the MLLA+LPHD predictions. This Λ_{eff} corresponds to a value of $\alpha_s \sim 0.1$ when plugged in the evolution equation at leading order. This suggests that MLLA+LPHD could possibly give a quantitative description of the observed particle spectra. The MLLA+LPHD approach is presented here as an attempt to understand some properties of multihadron production in terms of perturbative QCD, namely to test the possibility within this framework to determine hadron properties based on the corresponding parton distributions. It was shown that this approach can give predictions for properties of the momentum spectra that can be compared with experimental data.

The phase of qualitative studies of perturbative and non-perturbative QCD has evolved to reliable quantitative testes of its predictive power, mainly with LEP. Until 1995 LEP has worked at center of mass energies ($\sqrt{s}$) of 91 GeV and since 1995, with the increase of $\sqrt{s}$ to values up to 183 GeV, the window available for QCD testes has greatly enlarged. This enabled high precision testes of QCD parameters and their evolution with $\sqrt{s}$ (namely α_s), and to test the hadronization models. Our knowledge about the detailed process which leads the final state partons in the process $e^+e^- \to \gamma^*/Z^0 \to q\bar{q}$ to the hadrons observed by real world is still not complete. However, the hadronization models predict and describe satisfactorily well the observed particle distributions (as for instance the momentum and multiplicity distributions and their evolution with $\sqrt{s}$), although some parameters of these models have to be adjusted to the data output. The future increase of the LEP center of mass energy to $\sim$ 190 GeV will contribute to a better precision of the QCD analysis (perturbative and non-perturbative), and introduce an extra data point to the evolution with $\sqrt{s}$.

Bibliography

[1] R.M.Barnett *et al.*, Phys. Rev. **D54** (1996) 1,
and 1997 off-year partial update for the 1998 edition available on the PDG WWW pages ($URL: http://pdg.lbl.gov/$).

[2] G.Altarelli, R.Kleiss and C. Verzegnassi (editors), "Z Physics At LEP 1", volume 1, CERN 89-08 (1989).

[3] G.Altarelli, T.Sjöstrand and F.Zwirner (editors), "Physics At LEP 2", volume 2, CERN 96-01 (1996).

[4] A. De Angelis, "Hadronic Physics in e^+e^- interactions at LEP", to be published in the Proceedings of the Gleb Watagnin School on High-energy phenomenology, Campinas (1996).

[5] F.Halzen and A.D.Martin, "Quarks & Leptons", John Wiley & Sons (1984).

[6] Review of Particle Properties 1992.

[7] J.B.Gaffney and A.H.Mueller, Nucl. Phys. **B250** (1985) 109.

[8] I.M.Dremin *et al.*, Phys. Lett. **B324** (1994) 477.
I.M.Dremin *et al.*, Mod. Phys. Lett. **A9** (1994) 1471.

[9] OPAL Collab., G.Alexander *et al.*, Phys. Lett. **B265** (1991) 462;
OPAL Collab., P.D.Acton *et al.*, Z. Phys. **C58** (1993) 387;
OPAL Collab., R.Akers *et al.*, Z. Phys. **C68** (1995) 179.

[10] ALEPH Collab., D.Buskulic *et al.*, Phys. Lett. **B346** (1995) 389.

[11] DELPHI Collab., P. Abreu *et al.*, Z. Phys. **C70** (1996) 179.
(and references therein)
DELPHI Collab., P.Abreu *et al.*, 1996 preprint CERN-PPE/96-193, submitted to Phys. Lett. B.

[12] S. Marti, private communication.

[13] ALEPH Collab., R.Barate *et al.*, 1997 preprint CERN-PPE/97-003, submitted to Z. Phys. C.

[14] OPAL Collab., G.Alexander *et al*, Phys. Lett. **B388** (1996) 659.

[15] R.K.Ellis *et al.*, Nucl. Phys. **B178** (1981) 421.

[16] G. Altarelli, Phys. Rep. **81** (1982) 1.

[17] G.Altarelli and G.Parisi, Nucl. Phys. **B126** (1977) 298.

[18] K.J.Peach, L.L.J.Vick and P.Osborne (editors), S.Berthke, "Hadronic Physics in Electron-Positron Annihilation", Proceedings of the Forty Second Scottish Universities School in Physics, St. Andrews (1993).

[19] Mark II Collab., G.Hansen *et al.*, Phys. Rev. Lett. **35** (1975) 1609.

[20] DELPHI Collab., P.Abreu *et al.*, Z. Phys. **C73** (1997) 229.

[21] R.K.Ellis *et al.*, Nucl. Phys. **B178** (1981) 421.

[22] DELPHI Collab., P.Abreu *et al.*, Z. Phys. **C70** (1996) 179.

[23] K.Hamacher *et al.*, DELPHI note 95-146 PHYS-571 (1995).

[24] R.D.Field *et al.*, Nucl. Phys. **B136** (1978) 1.

[25] B.Andersson *et al.*, Z. Phys. **C1** (1979) 105.
B.Andersson *et al.*, Z. Phys. **C3** (1980) 33.

[26] B.Anderson *et al.*, Phys. Rep. **97** (1983) 31.

[27] B.Anderson *et al.*, Z. Phys. **C20** (1983) 317.

[28] C.Peterson *et al.*, Phys. Rev. **D27** (1983) 105.

[29] T.Gottschalk, Nucl. Phys. **B239** (1984) 325.

[30] G.Marchesini *et al.*, Comp. Phys. Comm. **67** (1992) 465.

[31] T.Sjostrand, Comp. Phys. Comm. **82** (1994) 74.

[32] B.Foster, "Electron-Positron Annihilation Physics", Adam Hilder (1990).

[33] TASSO Collab., W. Braunschweig *et al.*, Z. Phys. **C45** (1989) 193.

[34] B.R.Webber, Phys. Lett. **B143** (1984) 501 and references therein.

[35] P.Abreu *et al*, DELPHI note 97-21 PHYS-677 (1997).

[36] H.B.Nielsen, Z.Koba and P.Olesen, Nucl. Phys. **B40** (1972) 317.

[37] A.Bohrer, 1996 preprint CERN-OPEN/97-021, submitted to Phys. Rep.

[38] B.R.Webber, "QCD Cascade Approach to Jet Fragmentation", in *Proc. XV Int. Symp. on Multiparticle Dynamics*, LUND 1984, Eds. G. Gustafson and C. Peterson (World Scientific, Singapore, 1984).

[39] DELPHI Collab., P. Abreu *et al.*, Z. Phys. **C50** (1991) 185.

[40] A.H.Chan and C.K.Chew, Z. Phys. **C55** (1992) 503.

[41] A.Giovannini, Nucl. Phys. **B161** (1979) 429.

[42] S.Hegyi, Phys. Lett. **B387** (1996) 642.

[43] DELPHI Collab., P. Abreu *et al.*, Z. Phys. **C68** (1995) 353.

[44] ALEPH Collab., D. Buskulic *et al.*, Z. Phys. **C62** (1994) 1.

[45] DELPHI Collab., P. Abreu *et al.*, Nucl. Instr. Meth. **A378** (1996) 57.

[46] DELPHI Collab., P. Abreu *et al.*, Nucl. Instr. Meth.

[47] P.Antilogus, "DST Analysis Libraries Writeup", internal note from the DELPHI Collaboration.

[48] T.Ekelof, DELPHI note 85-11 RICH-5 (1985).

[49] DELPHI Collab., P. Abreu *et al.*, Phys. Lett. **B334** (1994) 435.

[50] E.Schyns, "NEWTAG, $\pi^{\pm}$, $K^{\pm}$ and $p\bar{p}$ tagging for DELPHI RICHes", DELPHI 96-103 RICH-89.

[51] B.De Lotto, L.Vitale, "The V^0 identification", internal note from the DELPHI Collaboration.

[52] L.Vitale. PhD thesis, Trieste University, November 95.

[53] DELPHI Collab., P. Abreu *et al.*, Z. Phys. **C73** (1996) 11.

[54] M. L. Mangano, P. Nason, Phys. Lett. **B285** (1992) 160;
M. H. Seymour, Z. Phys. **C63** (1994) 99;
M. H. Seymour, Nucl. Phys. **B436** (1995) 163.

[55] P.Abreu *et al.*, DELPHI note 96-124 PHYS-632 (1996)

[56] DELPHI Collab., P. Abreu *et al.*, 1997 preprint CERN-PPE/97-113, submitted to Phys. Lett. B.

[57] J. Dias de Deus, private communication.

[58] J.Dias de Deus, Phys. Lett. **B355** (1995) 539.
J. Dias de Deus, Phys. Lett. **B338** (1994) 80.

[59] V.A. Khoze and W. Ochs, Int. J. Mod. Phys. **A12** (1997) 2949.

[60] P. Brogueira, J. Dias de Deus and I.P. da Silva, Phys. Lett. **B389** (1996) 608.

[61] A.H. Mueller, in Proc. 1981 Intern. Symp. on Lepton and Photon Interactions at High Energies ed. W.Pfeil (Bonn 1981) 689;
Yu.L. Dokshitzer, V.S.Fadin and V.A Khoze, Phys. Lett. B 115 (1982) 242.

[62] Yu.L. Dokshitzer, V.A. Khoze and S.I. Troyan, Int. J. Mod. Phys. **A7** (1992) 1875.

[63] C.P. Fong and B.R. Webber, Phys. Lett. **B229** (1989) 289.

[64] N.C.Brummer, Z. Phys. **C66** (1995) 367.

[65] Review of Particle Properties 1994.

[66] DELPHI Collab., E. Schyns *et al.*, Contribution n.541 to the Jerusalem Conference on HEP (1997).

[67] DELPHI Collab., P. Abreu *et al.*, Z. Phys. **C65** (1995) 587.

[68] DELPHI Collab., P. Abreu *et al.*, Phys. Lett. **B318** (1993) 249.